ISSN 2423-9992

JAEA R&D Review

2018-19

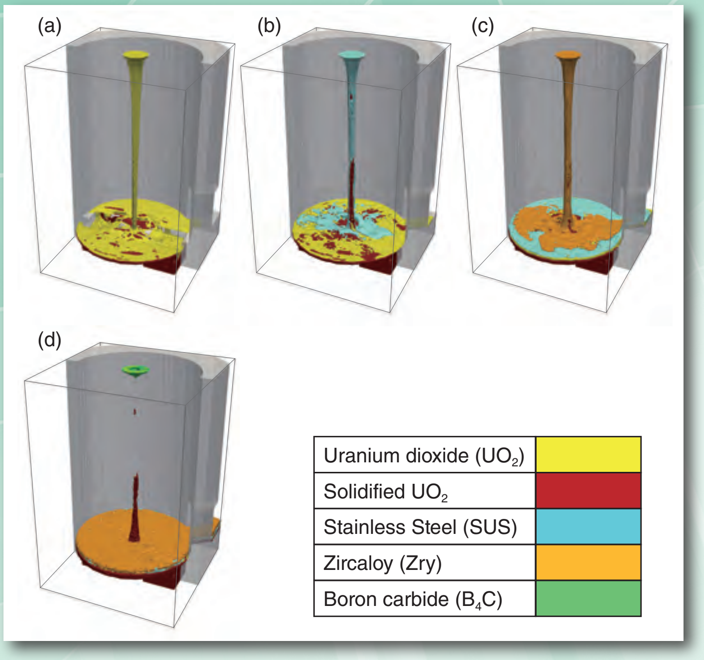

Detailed molten materials accumulation behavior inside the pedestal by mechanistic numerical simulation method, JUPITER, for molten materials behavior (Topic 1-1)

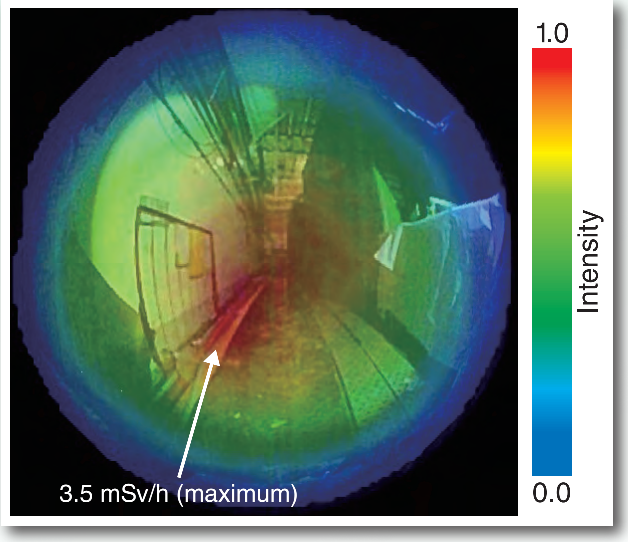

Visualization result of radioactive substances inside 1F3's turbine building (Topic 1-7)

Message from the President

児玉 敏雄

President Toshio KODAMA

We sincerely thank you for your understanding and continued support regarding the Japan Atomic Energy Agency (JAEA)’s research and development (R&D) activities.

JAEA’s mission as the only comprehensive nuclear R&D institution in Japan is to contribute to the welfare and prosperity of human society through nuclear science and technology. To realize this, we undertake R&D in active cooperation and collaboration with industries and universities. Our studies include cases such as the accident at the Fukushima Daiichi Nuclear Power Station operated by the Tokyo Electric Power Company Holdings, Inc.; research on nuclear-safety improvement; R&D toward the establishment of nuclear-fuel-recycling technologies such as fast reactors and reprocessing; and the development of technology for the treatment and disposal of radioactive waste. Furthermore, to support these R&D activities and create new technologies, we have implemented nuclear science and engineering research and human-resources development.

In response to the accident at Fukushima Daiichi Nuclear Power Station, as of last year, we have started full-scale operation of the International Collaborative Research Building of the Collaborative Laboratories for Advanced Decommissioning Science (CLADS), which is located in Tomioka Town, Fukushima Prefecture: our aim there is to solve problems related to the decommissioning of nuclear-reactor facilities and restoration of its environment. Remarkable results have been obtained in basic foundational research, such as a study on treatment methods for radioactive waste by nuclear transmutation, which received the 21st Century Invention Award. For research reactors, we have been responding to the new regulatory standards of the Nuclear Regulation Authority, and in June of this year, we resumed operation of the Nuclear Safety Research Reactor (NSRR).

Meanwhile, the Nuclear Regulation Authority has approved the decommissioning plans for the Prototype Fast Breeder Reactor Monju and the Tokai Reprocessing Plant and these plants entered the full-scale decommissioning stage. We will continue to work on safe and steady decommissioning measures in accordance with this plan in the future.

In this publication, we will introduce representative topics related to the latest achievements obtained by R&D, on which JAEA is working daily.

We are pleased that you will gain further understanding of JAEA’s accomplishments through this publication, and we appreciate your continued encouragement and cooperation for our R&D activities.

1 *Research and Development Related to the Accident at the TEPCO's Fukushima Daiichi NPS*

2 *Nuclear Safety Research*

3 *Advanced Scientific Research*

4 *Nuclear Science and Engineering Research*

5 Applied Neutron and Synchrotron-Radiation Research and Development

6 HTGR Hydrogen and Heat Application Research

7 *Research and Development of Fast Reactors*

8 *Research and Development on Fuel Reprocessing, Decommissioning, and Radioactive Waste Management*

9 Computational Science and E-Systems Research

10 Development of Science & Technology for Nuclear Nonproliferation

About This Publication and the Outline of the Organization of JAEA

This publication introduces our latest research and development (R&D) results in each field. Each chapter presents the activities of one R&D Sector. The various R&D Sectors perform their activities through R&D centers or institutes. Depending on the R&D activities, some of these centers or institutes comprise only one site, whereas others comprise two or more sites. The R&D centers and institutes are located throughout Japan, as shown on the map below. The following brief introduction outlines the research undertaken by each R&D Sector at various R&D centers and institutes.

1. **The Sector of Fukushima Research and Development** is promoting R&D towards the decommissioning and the environmental restoration to correspond to the accident of the Fukushima Daiichi Nuclear Power Station (1F) of Tokyo Electric Power Company Holdings, Inc. (TEPCO). The Sector is also preparing the research bases that are essential to the 1F decommissioning.

2. **The Nuclear Safety Research Center, Sector of Nuclear Safety Research and Emergency Preparedness,** is in charge of safety research that supports the national nuclear safety bodies that regulate nuclear power plants, nuclear fuel cycle facilities, and radioactive waste-disposal facilities. This work is being conducted at the Nuclear Science Research Institute.

3. **The Advanced Science Research Center, Sector of Nuclear Science Research,** explores yet-undiscovered disciplines and studies advanced atomic energy sciences via the Nuclear Science Research Institute to develop new theories and investigate novel phenomena, materials, and technologies. In particular, six research themes have been organized under the two divisions “advanced actinides science” and “advanced nuclear materials science”.

4. **The Nuclear Science and Engineering Center, Sector of Nuclear Science Research,** is carrying out fundamental research on various key technologies for the use of nuclear energy at the Nuclear Science Research Institute.

5. **The Materials Sciences Research Center, Sector of Nuclear Science Research,** is engaged in research using neutrons at the Nuclear Science Research Institute and the Japan Proton Accelerator Research Complex (J-PARC). Research using synchrotron radiation is being performed at the Harima Area.

6. **The Reactor Systems Design Department, and the HTGR Research and Development Center, Sector of Fast Reactor and Advanced Reactor Research and Development,** conduct R&D on High Temperature Gas-cooled Reactor (HTGR) technology, technology for hydrogen production through high-temperature water-splitting, and technology for helium gas turbines at the Oarai Research and Development Institute.

Japan Atomic Energy Agency -Outline of Organization-

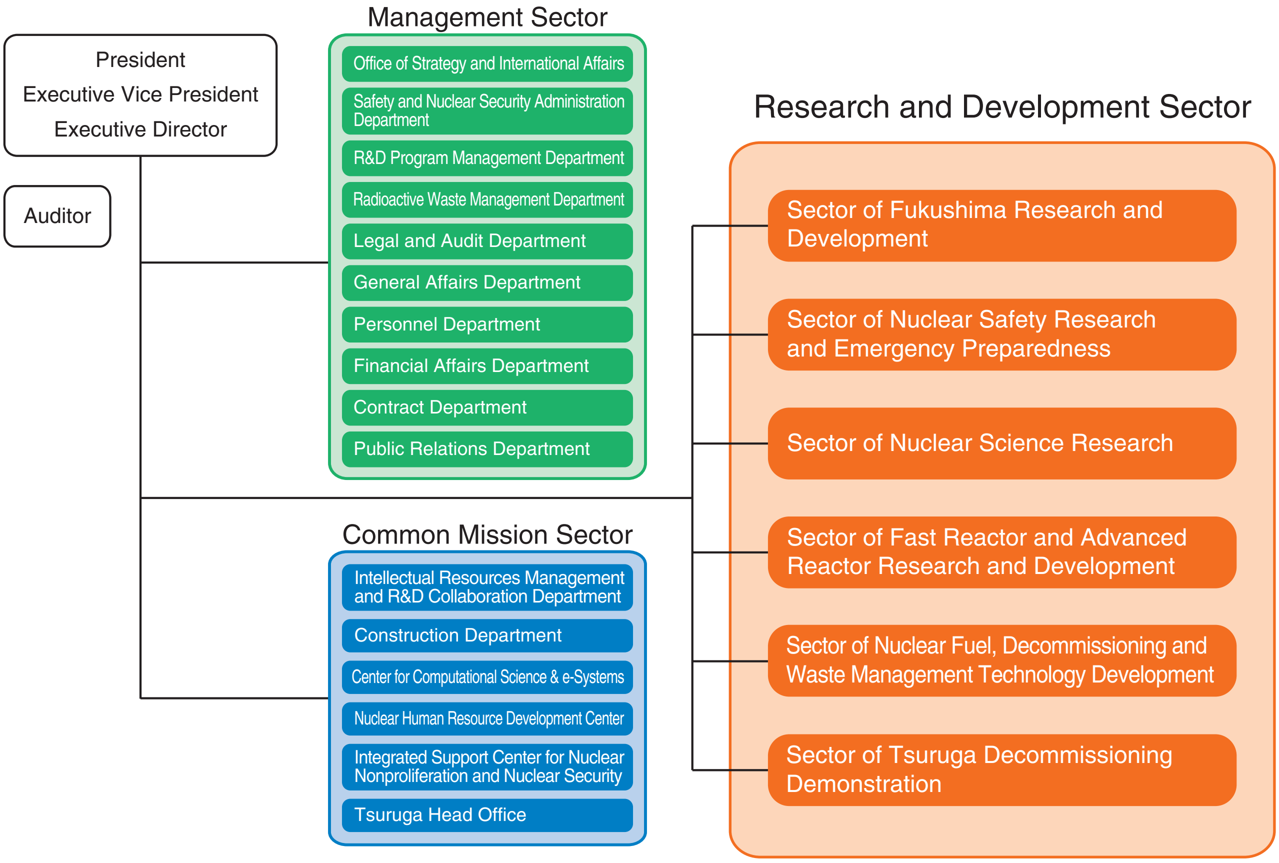

As of October, 2018

7. **The Reactor Systems Design Department, Fuel Cycle Design Department, Fast Reactor Cycle System Research and Development Center, and Tsuruga Comprehensive Research and Development Center, Sector of Fast Reactor and Advanced Reactor Research and Development** are conducting R&D toward the establishment of fast reactor (FR) cycles to address long-term energy security and global environmental issues. R&D activities are aimed at enhancing the safety of the FR system at the Oarai Research and Development Institute, at compiling the results on the Prototype Fast Breeder Reactor Monju (MONJU) and attaining the inspection and repair technologies for the FR system at Tsuruga Comprehensive Research and Development Center, and at manufacturing plutonium fuel and reprocessing spent FR fuel at the Nuclear Fuel Cycle Engineering Laboratories in cooperation with the Sector of Nuclear Fuel, Decommissioning and Waste Management Technology Development.

8. **The Sector of Nuclear Fuel, Decommissioning and Radioactive Waste Management** develops technologies for the safe and rational decommissioning of nuclear power facilities as well as measures for processing and disposing of radioactive waste in their R&D centers or institutes. This sector also conducts multidisciplinary R&D aimed at improving the reliability of geological disposal of high-level radioactive waste in Japan. A particular focus involves establishing techniques for investigating the deep geological environment through R&D at the Tono Geoscience Center and the Horonobe Underground Research Center. At the Nuclear Fuel Cycle Engineering Laboratories, the focus is on improving the technologies for disposal facility design and safety assessment. Furthermore, the development of nuclear fuel cycle technology for light water reactors (LWRs) is in progress at the Nuclear Fuel Cycle Engineering Laboratories.

9. **The Center for Computational Science & e-Systems** performs research on advanced simulation technology and on basic technology in computational science, and also operates and maintains computer systems. These efforts are mainly conducted at the Nuclear Science Research Institute and the Kashiwa Office.

10. **The Integrated Support Center for Nuclear Nonproliferation and Nuclear Security (ISCN)** plays an active role in technology development to support activities of the international organizations such as the International Atomic Energy Agency (IAEA), and other countries to strengthen nuclear non-proliferation and nuclear security, activities to contribute to ensuring transparency in nuclear material management and peaceful uses, and policy research. Moreover, ISCN continues to support human resources development activities of the Asian countries. These efforts are carried out mainly at the Head Office and the Nuclear Science Research Institute.

R&D Institutes/Centers of JAEA

1 Research and Development Related to the Accident at the TEPCO's Fukushima Daiichi NPS

Providing Advanced Scientific Knowledge to Promote Environmental Restoration and Decommissioning by Concentrating Expertise

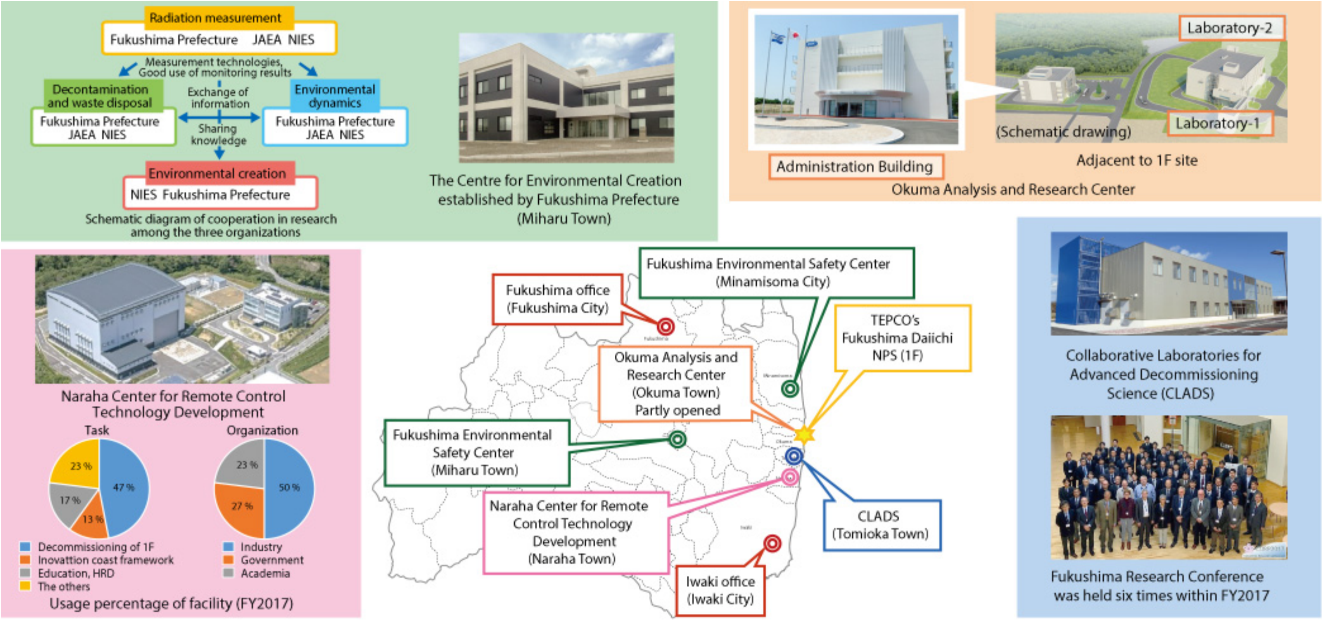

Fig.1-1 Sector of Fukushima Research and Development: R&D bases and activities

As Japan's sole comprehensive R&D institute in the field of nuclear energy, we are conducting R&D to promote the decommissioning of the TEPCO's Fukushima Daiichi NPS (1F), as well as environmental restoration after the 1F accident (Fig.1-1). Our research results are described below.

Towards the decommissioning of 1F, the Collaborative Laboratories for Advanced Decommissioning Science (CLADS), as an international research hub based on the Mid- and Long-term Roadmap formulated by the Inter-Ministerial Council for Contaminated Water and Decommissioning Issues, is promoting research and development on: 1) clarification of 1F-accident-progression scenarios (Topics 1-1 and 1-2); 2) retrieval of fuel debris from nuclear reactors (Topics 1-3 and 1-4); 3) treatment and disposal of radioactive wastes generated by the decommissioning work (Topics 1-5 and 1-6); and 4) remote-controlled instrumental technologies (Topics 1-7–1-9).

The CLADS main building began operation in Tomioka Town in FY2017 (Fig.1-1, right), and has integrally promoted R&D and human-resource development by industry, academia and government. Also, we have held many Fukushima research conferences attended by domestic and international researchers in Fukushima prefecture (Fig.1-1, bottom right). The Research Fund for Promoting Projects on Decommissioning Research was founded by the Ministry of Education, Culture, Sports, Science and Technology (MEXT) in FY2018. The purpose of this fund is to promote fundamental R&D and human-resources development (HRD), mainly at CLADS. With this fund, we will reinforce cooperation with universities and research institutes so that we can continuously achieve a more stable environment for R&D and HRD.

The Naraha Center for Remote Control Technology Development, which began operation in FY2016 in Naraha Town, is available for external users who are interested in the development of the remote-control devices to be used in decommissioning work and nuclear disasters (Fig.1-1, left). The number of facility users from industry, academia, and government exceeded one hundred (38 in FY2016 and 64 in FY2017) (Fig.1-1, bottom left). We are improving the test equipment by developing robot simulators and robot test methods to encourage facility use.

The Okuma Analysis and Research Center is intended to analyze radioactive wastes and fuel debris for development of long-term waste management. The Center consists of three buildings: an Administration Building, Laboratory-1, and Laboratory-2 (Fig.1-1, top right). The Administration Building, which consists of office rooms, meeting spaces, workshop, etc., was opened in March 2018 in Okuma Town. Laboratory-1, which is now under construction, will be used for analyzing low-to-medium-radiation-level rubbles and secondary waste. Laboratory-2, which is at the design phase, will be used to analyze high-radiation-level material, such as fuel debris.

These three centers described above are regarded as decommissioning-related facilities that will play a part in the Fukushima Innovation Coast Framework, and will therefore contribute ever more to 1F decommissioning.

For environmental restoration, the Fukushima Environmental Safety Center is carrying out R&D in accordance with the Medium- and Long-Term Activities of the Centre for Environmental Creation (CEC), in collaboration with Fukushima Prefecture and the National Institute for Environmental Studies (NIES) (Fig.1-1, top left). We have cooperated with Fukushima Prefecture and the NIES of the CEC to investigate and analyze the environmental impact due to the forest fire that occurred inside the difficult-to-return zone of Namie Town in April 2017. The Fukushima Environmental Safety Center has been developing technologies for environmental monitoring and mapping (Topics 1-10 and 1-11) in order to establish methods for monitoring contaminated forests, river areas, inshore areas and so on. Moreover, the Center conducts research on environmental dynamics (Topics 1-12–1-15) to predict and resolve the migration of radioactive materials in the environmental, as well as research on decontamination and volume reduction (Topics 1-16–1-18). The Center is disseminating R&D results with a web-based system that will meet a wide variety of needs for researchers, municipalities, local residents, and so on (Topic 1-19).

We will continue to offer technical expertise to promote environmental restoration and decommissioning of 1F by concentrating expertise. We are contributing to Fukushima's revitalization through development of regional industries and HRD by network buildings and cooperation with regional industries, research institutes, and educational institutes.

1–1 How is Debris Distributed?

— Evaluation of the Detailed Debris Distribution and Re-Criticality by Large-Scale Simulation —

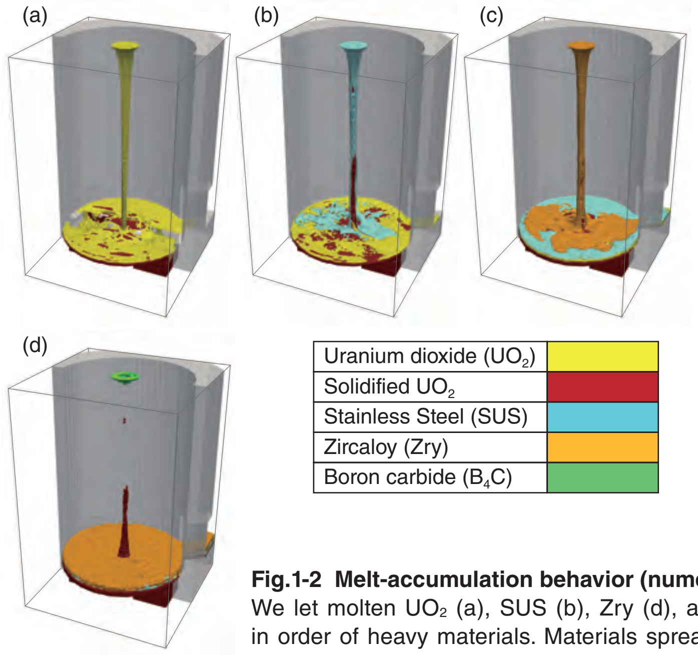

Uranium dioxide (UO_2)	🟨
Solidified UO_2	🟥
Stainless Steel (SUS)	🟦
Zircaloy (Zry)	🟧
Boron carbide (B_4C)	🟩

Fig.1-2 Melt-accumulation behavior (numerical result)
We let molten UO_2 (a), SUS (b), Zry (d), and B_4C (d) flow at the center of the top boundary in order of heavy materials. Materials spread in a complicated fashion and accumulate in the pedestal. Since the amount of inflowing B_4C is less than that of the other materials and it solidifies at the top boundary, its accumulation onto the pedestal was very limited.

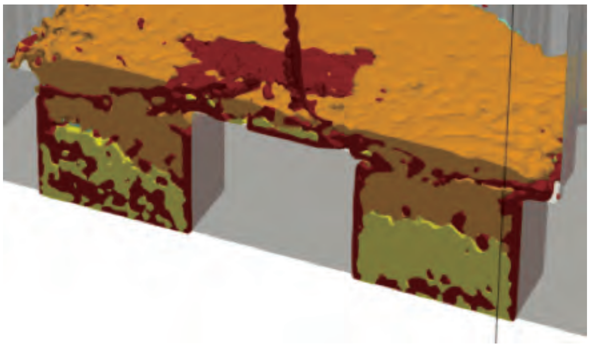

Fig.1-3 Interior distribution of accumulated debris (numerical result)
Molten and solidified uranium and Zry are distributed complicatedly inside the accumulated debris (Component shown by colors is same as Fig.1-2).

During severe accidents (SAs), fuel debris (a mixture of fuel and the other materials) is generated by melting of reactor cores and is relocated to the lower part of reactors. Information concerning fuel debris, including its distribution, composition, and re-criticality, is required for its removal. Therefore, obtaining this information is important for decommissioning of the TEPCO's Fukushima Daiichi NPS (1F). However, melting and relocation of fuel debris are complicated phenomena, making this information quite difficult to obtain. Numerical simulations are effective tools, but conventional SA-analysis codes are of little use because they include various assumptions about phenomena and simplify the shapes of reactor-core structures to shorten the computational time.

Therefore, the fuel-debris-melting and relocation process must be simulated precisely. To this end, we have developed a numerical-simulation code for melting and relocation behavior called JUPITER, based upon a mechanistic methodology. JUPITER can simulate melting and relocation without assumptions or simplification using basic equations governing the thermal-hydraulic behavior of the fluids.

We numerically simulated melt-relocation behavior to the lower part of the primary containment vessel (pedestal) using JUPITER. In this simulation, we decided the largest-density material, molten UO_2, should be poured first, followed by the lower-density materials SUS, Zry, and B_4C. As shown in Fig.1-2(a), UO_2 spreads over the pedestal and is accumulated in two cavities (sump pits) with solidification. Then, fuels and other materials mix in a complicated fashion (Fig.1-2(b)–(d)). Fig.1-3 shows a cross-sectional view of the pedestal along its center to illustrate the accumulation state inside the sump pits. As shown in Fig.1-3, the melt near wall of the pedestal is solidified by heat transfer to the wall. The heavier material, UO_2, is located at the bottom and the lighter material, Zry, is located at the upper layer. This distribution is given by mechanistic estimation for melt relocation and solidification based upon the physical governing equations.

In addition, we try to evaluate the re-criticality of fuel debris in the pedestal using the continuous-energy-neutron-transport Monte Carlo code MVP. The required fuel-debris distribution for re-criticality analysis is evaluated using the above-mentioned fuel-debris-relocation simulation of JUPITER. In a normal re-criticality analysis, it is assumed that the fuel debris is uniformly mixed. Here, with the distribution given by JUPITER, re-criticality can be calculated using a more realistic condition. If water exists in fuel debris, re-criticality occurs readily in theory. In this simulation, we calculated re-criticality with and without water in the fuel debris. It is found that re-criticality does not occur except where an unrealistic amount of water exists in the fuel debris.

In the near future, we will validate the applicability of JUPITER to the relocation and accumulation of fuel debris by comparing simulation results with experimental ones and perform debris-accumulation simulation under several parameters. In addition, we will contribute to the decommissioning of 1F by evaluating the characteristics and re-criticality of fuel debris.

Reference

Yamashita, S. et al., Coupled Analysis of Fuel Debris Distribution and Recriticality by both Multiphase/Multicomponent Flow and Continous Energy Neutron Trasport Monte Carlo Simulations, Transactions of the Atomic Energy Society of Japan, vol.17, issues 3-4, 2018, p.99–105 (in Japanese).

1–2

Two Types of Insoluble Cesium Particles Emitted at the Early Stages of the Accident

— Investigation of the Generation Process of Mainly Silicate Particles —

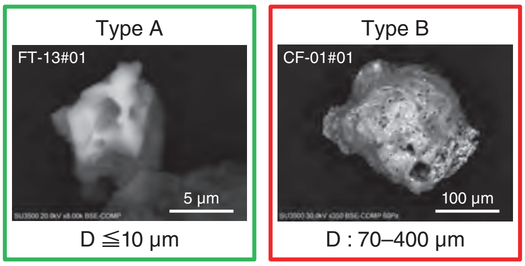

Fig.1-4 Two types of radioactive insoluble cesium particles
Type A is a few μm in diameter and has been observed extensively in eastern Japan, including the Tokyo Metropolitan Area. Type B has a larger mean diameter and is found mainly in the vicinity of the 1F.

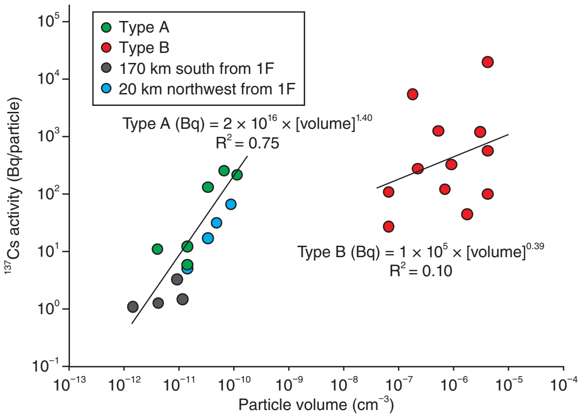

Fig.1-5 Particle volume vs. cesium concentration
The specific radioactivity of Type A is larger than that of Type B.

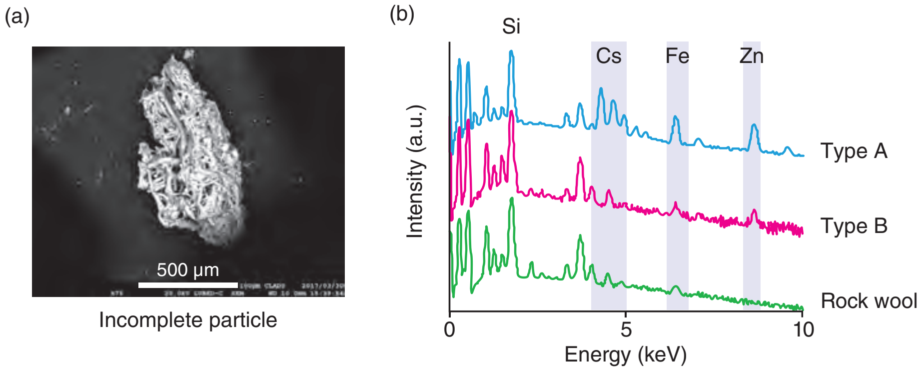

Fig.1-6 Intermediate type-B particles and the results of energy-dispersive X-ray spectrometry (EDS)
(a) Attached fiber-silicate materials and melted fibers were observed. (b) EDS spectra of the standard type of heat insulator and the Type B particle were consistent.

Emission of insoluble cesium (Cs) particles was detected in environmental samples collected during the early stage of the TEPCO's Fukushima Daiichi NPS (1F) accident. Particles with diameters of 1 μm to 1 mm were particular ejecta of the accident.

There were at least two types of particles of which the main element is silicate (Fig.1-4). This silicate makes the particles insoluble in water. Type A is a few μm in diameter and contains a small amount of radioactive Cs within it. However, the concentration of Cs is so large that characteristic X-rays can be detected using energy-dispersive X-ray spectrometry (EDS), which has a much higher detection limit than other methods. By contrast, Type B particles are hundreds of microns in size and can be see with the naked eye, but the concentration of Cs is lower than in Type A. The radioactivity concentration per unit volume is called the specific radioactivity, but in order to clarify the above relationship, when two kinds of particles are illustrated by the particle volume and the Cs concentration contained, the inclination of Type B is smaller than that of Type A. The results of previous studies (● and ● in Fig.1-5) of particles considered to have been released at the same time (midnight on March 14) as Type A also agreed with specific radioactivity relationships.

Type-B particles with low specific radioactivity were confirmed to have been released by the 1F Unit 1 reactor hydrogen explosion on March 12. Moreover, Type-B particles were deposited over a limited region north of the polluted nuclear plant immediately after the explosion took place. Observing Type B, fibrous silicate compounds were confirmed to adhere surface (Fig.1-6(a)). Based on this discovery, we investigated the silicate compounds used around the reactor building. The elemental composition of the heat-insulating material used inside the building and the constituent elements of Type B nearly agreed (Fig.1-6(b)). This result shows that cesium filled in the reactor building, adsorbed onto fibrous insulation made of silicate compounds, shrunk, spread due to the hydrogen-explosion heat and the blast, and scattered as Type-B particles into the environment. On the other hand, Type-A particles, whose generation process has many unknown features due to their high specific activity, are a subject for further study.

Reference

Satou, Y. et al., Analysis of Two Forms of Radioactive Particles Emitted during the Early Stages of the Fukushima Dai–Ichi Nuclear Power Station Accident, Geochemical Journal, vol.52, issue 2, 2018, p.137–143.

1–3 Chemical Reaction between Stainless Steel and Cesium

— Estimation of the Cesium Distribution within the TEPCO's Fukushima Daiichi NPS —

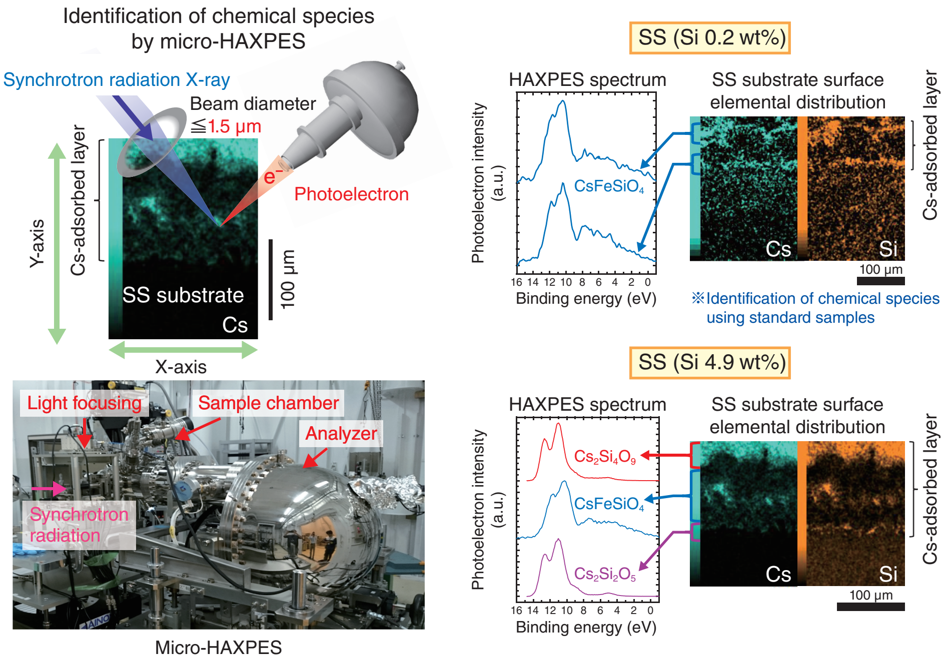

Fig.1-7 Result of identification of chemical species by micro-HAXPES for Cs-adsorbed stainless steel
Cross-sectional observation of stainless steel reacted with cesium-hydroxide vapor (right figure) showed similar distributions of Si and Cs in the Cs-adsorbed layer. This suggests that Si and Cs can form compounds. Furthermore, the identification of chemical species by micro-HAXPES (lower-left figure) indicated that the chemical forms of Cs compounds depended upon the Si content in the SS (right figures). In the future, we will try to improve estimates of the Cs distribution within nuclear reactors by establishing a model that considers the chemical properties of the identified Cs compounds.

At the TEPCO's Fukushima Daiichi NPS, information on cesium (Cs) distributions within the nuclear reactors is necessary for managing the radiation exposures of workers, because Cs is a major source of γ ray. In particular, evaluation of Cs-chemisorption behavior, which is a reaction between Cs vapor and the stainless steel (SS) used in structural materials, is essential. Thus, such Cs-chemisorption amounts are estimated using severe-accident-analysis codes with Cs-chemisorption models. However, there is a large discrepancy among the analytical codes. One reason for this is that the chemical forms treated in their models differ.

Since Cs has various compounds with differing vapor pressures and water solubilities, the revaporization and transport behaviors of Cs from structural materials to gaseous and aqueous phases significantly depend upon which Cs compounds are formed. Therefore, clarification of the chemical forms of Cs adsorbed onto SS, which is widely used inside reactors, or clarification of reactions between SS and Cs vapor, is important for improving the estimation of Cs distributions within nuclear reactors. However, although Cs has been found to react with silicon (Si) impurities in SS, various Cs silicates have been reported and the major chemical form remains unclear, possibly due to the micron sizes of the reaction products.

Thus, we aim to develop an analytical technique to identify the chemical forms of micro-sized compounds by combining micro-hard-X-ray photoelectron spectroscopy (HAXPES) with scanning electron microscopy (SEM). Furthermore, since the chemical forms may depend upon the Si contents in SS, Cs chemisorption tests were performed using different Si-content samples. As a result, the compounds formed by chemical reaction between SS and Cs vapor were successfully identified, and their distributions were clarified (Fig.1-7). In particular, complicated chemical reactions were found to occur since not only iron (Fe)-containing Cs compounds ($CsFeSiO_4$), but also $Cs_2Si_2O_5$ and $Cs_2Si_4O_9$, were formed when the Si content of SS increased.

In the future, we will try to elucidate the chemical properties of the identified Cs compounds such as vapor pressure and water solubility, and contribute to improving estimation of the Cs distribution within nuclear reactors by establishing a chemisorption model considering the chemical factors influencing the revaporization and transport behaviors of Cs.

Reference

Kobata, M., Nakajima, K. et al., Chemical Form Analysis of Reaction Products in Cs–Adsorption on Stainless Steel by Means of HAXPES and SEM/EDX, Journal of Nuclear Materials, vol.498, 2018, p.387–394.

1–4 Zirconium Hinders the Oxidative Dissolution of Nuclear Fuel

— Effect of Zirconium Incorporation in Uranium Oxide upon Inhibiting Oxidative Dissolution —

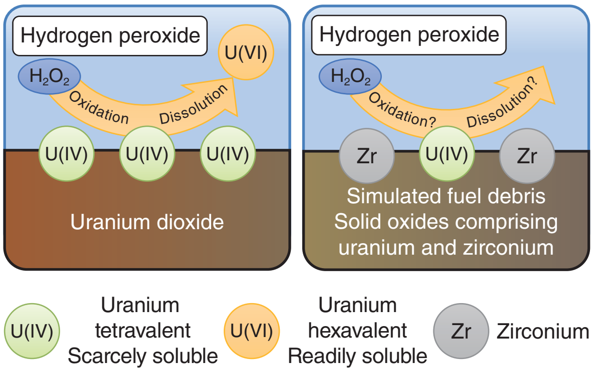

Fig.1-8 Reaction scheme of U dissolution by H_2O_2
Oxidative dissolution by H_2O_2 is a well-known degradation process for UO_2, but little is known about the process for fuel debris. Thus, the oxidative U dissolution was examined through experiments with simulated fuel debris.

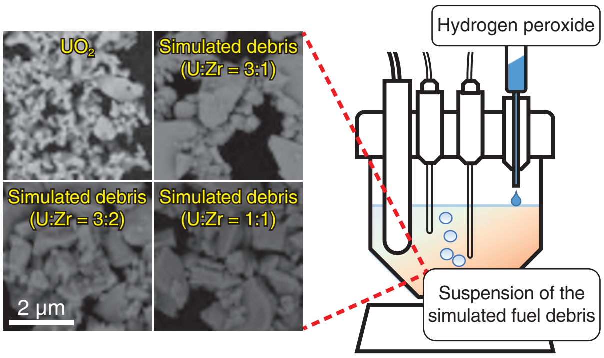

Fig.1-9 Scanning-electron-microscope (SEM) images of the U oxide samples and a schematic illustration of the setup for the H_2O_2 reaction experiment
The reactions of H_2O_2 with UO_2 and with the simulated fuel debris in aqueous solution were examined.

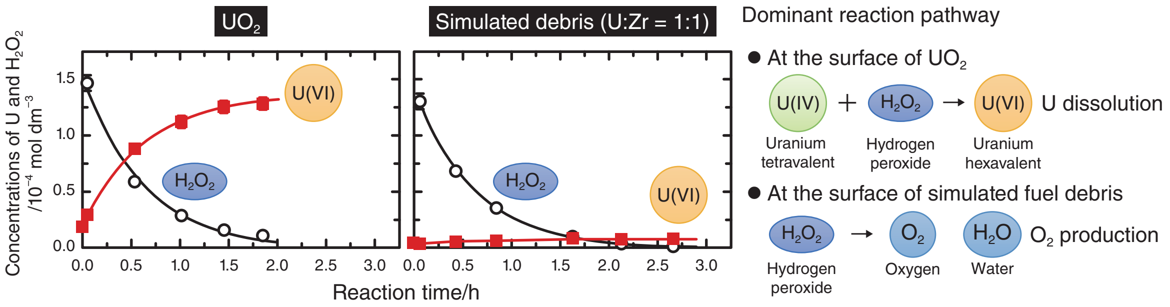

Fig.1-10 Comparison of the H_2O_2 reaction kinetics between UO_2 and the simulated fuel debris
The reaction of H_2O_2 with UO_2 results in the dissolution of U. However, the reaction with the simulated fuel debris scarcely caused the U dissolution and resulted in catalytic decomposition of H_2O_2, producing oxygen and water molecules.

We have shown that uranium dioxide (UO_2) becomes chemically stable by forming solid solution containing zirconium (Zr). The stabilization by Zr indicates that the molten fuel debris in the TEPCO's Fukushima Dai-ichi NPS (1F) would be stable against dissolution by chemical reactions and would remain in the reactors until it is retrieved.

Our research on the chemical reaction of the molten fuel debris is based on an understanding of the chemical degradation of spent nuclear fuel under the conditions of deep geological disposal. The spent fuel emits intense ionizing radiation and produces hydrogen peroxide (H_2O_2) by decomposing water molecules. In the case of direct contact of the fuel with water, H_2O_2 consequently reacts with the fuel, inducing dissolution of uranium (U). The U dissolution is induced by oxidation of U at the surface of the fuel (Fig.1-8). In the UO_2 matrix of the fuel, U is mainly in tetravalent state that is scarcely soluble in water. However, if tetravalent U is oxidized into hexavalent state, its solubility drastically increases. This sequence of chemical reactions is expected to occur for the fuel debris in 1F. However, little is known about the chemical behavior of the fuel debris in water, because the composition of fuel debris is far different from that of the usual UO_2 fuel due to melting with the materials in the reactor core.

We have performed experiments regarding the dissolution of U by H_2O_2, and shown that it is significantly inhibited by the incorporation of Zr (Fig.1-9). U oxide containing Zr was used as simulated fuel debris, because the fuel debris is expected to contain Zr by melting with the fuel-cladding material. When the simulated debris was exposed to H_2O_2, the reaction of H_2O_2 proceeded at a rate comparable with that of UO_2. However the dissolution of U was significantly inhibited (Fig.1-10). For example, the U dissolution from the simulated debris containing 50 % Zr in atomic ratio was only 4 % of that from UO_2. This inhibited dissolution resulted from the effect of Zr promoting H_2O_2 decomposition on the surface. This reaction mechanism was confirmed by analysis of gaseous products of the reaction. The reaction of H_2O_2 with the simulated debris produced nearly the stoichiometric amount of oxygen (O_2).

We are going to further investigate the basic chemistry of molten fuel in order to support technological development for the safe retrieval and management of the fuel debris in 1F.

Reference

Kumagai, Y. et al., Reaction of Hydrogen Peroxide with Uranium Zirconium Oxide Solid Solution–Zirconium Hinders Oxidative Uranium Dissolution, Journal of Nuclear Materials, vol.497, 2017, p.54–59.

1-5 Characterization of Waste Generated by Contaminated Water Treatment

— Analysis of Carbonate Slurry —

Fig.1-11 Appearance of the carbonate slurry sample

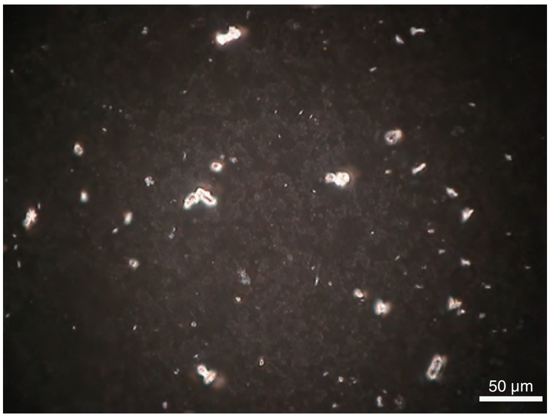

Fig.1-12 Enlarged image of the carbonate slurry sample
The particle-size distribution measurements revealed many particles with sizes of several μm.

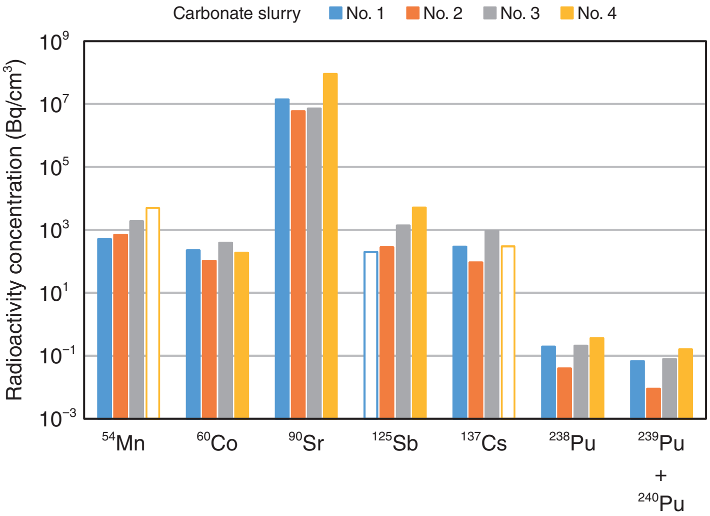

Fig.1-13 Radioactivity analysis results
Radiochemical analysis results of the carbonate slurry sample. In the slurry, ^{90}Sr was present at a concentration higher than those of other radionuclides (white bar denotes the lower detection limit, which varies among the nuclides).

The Multiple Radio-nuclides Removal System (MRRS^{TM}) is a contaminated water treatment facility that decontaminates the radioactive water at the TEPCO's Fukushima Daiichi NPS (1F). The treatment generates secondary wastes, e.g., slurry and used adsorbent. Since such secondary waste is not generated during the operation of a normal nuclear power plant, a method of safely storing, processing, and disposing this waste is imperative. For this purpose, the properties of this waste must be investigated.

The carbonate slurry must be characterized preferentially because it contains highly concentrated radionuclides and is generated abundantly by the MRRS. We collected and analyzed four samples of the waste generated at different times from different sampling positions in the High Integrity Container (HIC), which stores the carbonate slurry generated by the MRRS of 1F.

We found high dose rates (surface dose rates of the vial) in the sampled carbonate slurry (10–100 mSv/h from a 10-mL sample in the polyethylene terephthalate vial (Fig.1-11)).

Fig.1-12 is a micrograph of the carbonate slurry. As a result of measuring the particle size distribution in this slurry, there were many particles of several μm.

As a result of the element concentration analysis using inductively coupled plasma atomic emission spectrometry, magnesium and calcium were each approximately 20mass% in the solid component of the carbonate slurry. It was found that magnesium and calcium which are removal targets in the carbonate precipitation process could be removed.

A radiochemical analysis of the carbonate slurry revealed eight main nuclides (Fig.1-13), among which ^{90}Sr was present at the highest concentration. Moreover the high-radiation dose emitted from the carbonate slurry was attributable to the radiation derived from ^{90}Sr and ^{90}Y (its daughter nuclide).

These results will be used to find suitable methods for the disposal and treatment of the slurry.

This work includes part of the results of the "Development of technology for treatment and disposal of accident waste", funded by the Ministry of Economy, Trade and Industry (METI), Japan.

Reference

Fukuda, Y. et al., Characterization of Carbonate Slurry Generated from Multiple Radio-Nuclides Removal System in Fukushima Daiichi Nuclear Power Station, Proceedings of 2017 International Congress on Advances in Nuclear Power Plants (ICAPP 2017), Fukui and Kyoto, Japan, 2017, paper 17077, 10p., in CD-ROM.

1–6 Safe Long-Term Storage of Secondary Wastes after Decontamination of Radioactive Water

— Evolution of Radiolysis Studies to Support Practical Issues in the Decommissioning of 1F —

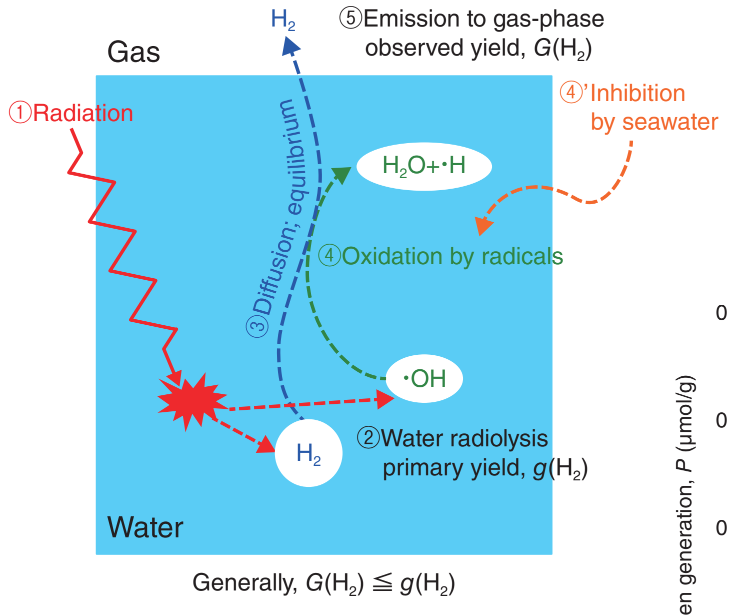

Fig.1-14 Diagram of radiolytic-H_2 formation and reaction in water
H_2 would be emitted into the air in the open condition in a severe accident but dissolved into water in the closed condition typical of reactors. H_2 ② formed by radiation ① is scavenged by radicals ④ on the way to the water surface ③, but the scavenging can be blocked by seawater salts ④'.

Table 1-1 H_2-generation factors relevant to the decommissioning of 1F

Effect factor	Main phenomenon (this work)
Seawater salt (halide ions, X^-)	X^- scavenging of oxidizing •OH radical in its H_2 oxidation
Zeolites; solid oxides	Surface interaction with (binding to) oxidizing products including •OH
Liquid depth; viscosity	H_2 escaping from reactions in liquid phase (water) dependent on time for reaching gas phase
Liquid flow	
Dose rate	Reaction between H_2 and •OH present in different isolated spurs

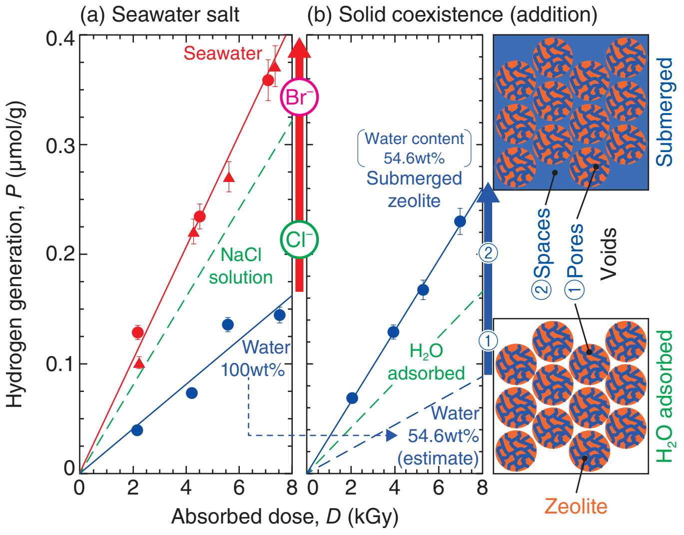

Fig.1-15 Effects of seawater salt (a) and solid coexistence (b) upon H_2 generation (constant-height (1-cm) condition)
In seawater (a), Cl^- and Br^- ions affect H_2 generation, making its amount larger than in pure water (PW). In submerged zeolites (b), pores and spaces affect H_2 generation, leading to an enhancement that cannot be explained only by the water content within the zeolites.

Following the accident at the TEPCO's Fukushima Daiichi NPS (1F), we have focused upon water decontamination and secondary-waste storage, and performed R&D on cesium adsorption, hydrogen (H_2) generation, corrosion of structural materials, and gas and heat flows. We then provided the data obtained as information indispensable for safety measures to TEPCO and 1F-related companies. Moreover, according to the medium- and long-term roadmap for decommissioning 1F, we have quickly complied with requests for studying and solving urgent problems and events in cooperation with TEPCO and the companies.

R&D upon H_2 generation is related to the explosion of this gas just after the accident; it is considered to be the most dangerous phenomenon in the management of radioactive materials. Since water radiolysis in H_2-generation sources is brought about by ionizing radiations emitted from radioactive materials, the temperature need not be higher than several hundred degrees centigrade; this process takes place continuously anywhere the materials for it exist. Thus, studies on water radiolysis have been performed at every step of the roadmap.

Unlike that derived from other sources, H_2 formed from water decomposition by radiation is emitted into the air through numerous processes and reactions (Fig.1-14). H_2 generation is complexly affected by many conditions and factors. Using practical materials under real conditions, several effects upon the generation have been investigated in detail and determined to be important for 1F decommissioning (Table 1-1).

Fig.1-15 shows representative experimental results. Seawater supplied at the accident works as a coolant as well as pure water (PW), while more H_2 was generated in seawater than in PW (a). This was because chloride (Cl^-) and bromide (Br^-) ions in seawater suppress H_2 consumption. The full amount of H_2 generation in zeolites submerged by PW could not be explained only by their water content (b). This enhancement indicates an interaction between the radiolysis products of water and the solid surface of zeolite, giving useful information for improvement in conventional safety analysis of the generation without solids.

In these radiolysis studies, hydrogen peroxide (H_2O_2) and its decomposed product of oxygen (O_2) are also studied.

Reference

Nagaishi, R., Evolution of Water Radiolysis Studies for Measures against Post-Severe Accidents, Radioisotopes, vol.66, no.11, 2017, p.601–610 (in Japanese).

1–7 Understanding the Radioactive-Contamination Situation Inside the TEPCO's Fukushima Daiichi NPS Building

— Development of 3D-Visualization Technology for Radioactive Substances —

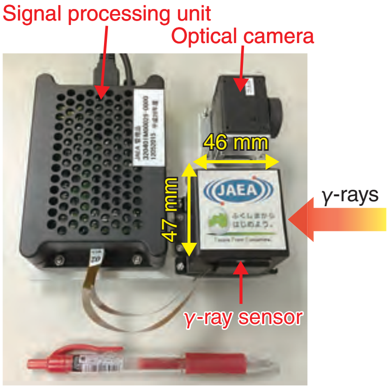

Fig.1-16 Photograph of a compact Compton camera
A compact Compton camera consists of a γ-ray sensor, signal-processing unit, and an optical camera.

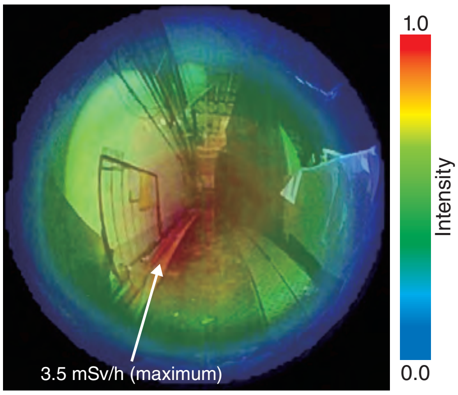

Fig.1-17 Visualization result of radioactive substances inside 1F3's turbine building
Strong contamination was detected on the hose located on the floor surface.

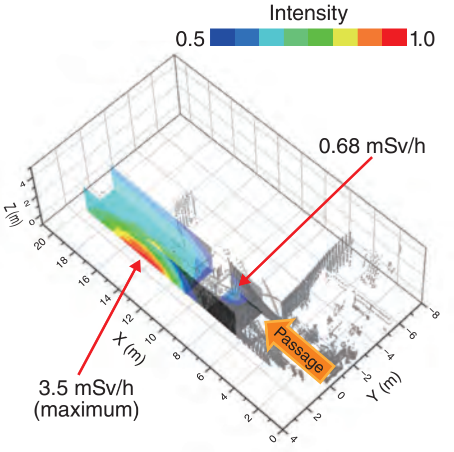

Fig.1-18 3D-radiation-distribution map
A radiation-distribution map was created by superimposing visualized images of radioactive substances onto a 3D-structural model of the measurement environment.

Seeing invisible radiation is important not only for protecting workers from radiation exposure, but also for understanding the contamination situation inside the TEPCO's Fukushima Daiichi NPS (1F). Inside its buildings, radioactive substances are adhering to various objects such as floors, walls, equipment, and scattered rubble, and the contamination due to radioactive substances exists in three dimensions (3D). There is also an area with such a high dose rate that workers cannot enter or remain there. Drawing a radiation-distribution map indicating the distribution condition of radioactive substances inside 1F is extremely important for predicting the risk to workers and decreasing the amount of radiation exposure for performing decommissioning tasks. Such a map would help workers to easily recognize the locations of radioactive substances in the work environment. In addition, the information would be effective for establishing detailed decontamination plans. We have newly developed a method for visualizing the radioactive substances scattered inside the 1F building in 3D.

To this end, we fabricated a compact Compton camera that could be installed in remote equipment such as a drone or crawler robot, as shown in Fig.1-16. This camera weighs about 680 g and was fabricated based on handheld-Compton-camera technology jointly developed by Waseda University and Hamamatsu Photonics. In high-dose-rate environments, it was necessary to equip the γ-ray sensor with a large and heavy shield for radiation measurements using a conventional Compton camera. On the other hand, since our Compton camera is compact, it is possible to perform measurements with a compact shield while maintaining portability within the 1F buildings. Using this Compton camera, we conducted a measurement of the distribution of radioactive substances inside 1F3's turbine building. We succeeded in detecting a high-dose-rate region (up to 3.5 mSv/h) inside the turbine building with an air dose rate of 0.4 to 0.5 mSv/h. Fig.1-17 shows the result of the radiation measurement, which visualizes the radioactive substances (mainly ^{137}Cs) by superimposing their image onto a photograph of the measurement environment. The measurement time required for visualization was under 1 minute.

In addition, we also succeeded in drawing a 3D-radiation-distribution map by superimposing the image of the radioactive substances obtained by the Compton camera onto a 3D-structural model acquired using a scanning-laser range finder, as shown in Fig.1-18. Two contaminated regions with a higher dose rate than the surroundings are displayed at the wall and floor surfaces of the measurement environment. Since this map reflects the dimensions and appearance of the actual work environment, workers can easily recognize dangerous regions at a glance. We believe that it will be useful for reducing worker exposure and planning decontamination.

We are currently installing this system on a small crawler robot, and we are also developing a radiation-imaging system to understand the contamination situation inside the 1F reactor buildings.

Reference

Sato, Y. et al., Radiation Imaging Using a Compact Compton Camera Inside the Fukushima Daiichi Nuclear Power Station Building, Journal of Nuclear Science and Technology, vol.55, issue 9, 2018, p.965–970.

1–8 Remote Laser-Sampling Technologies

— Development of Concrete-Sampling Technologies Using High-Power Lasers —

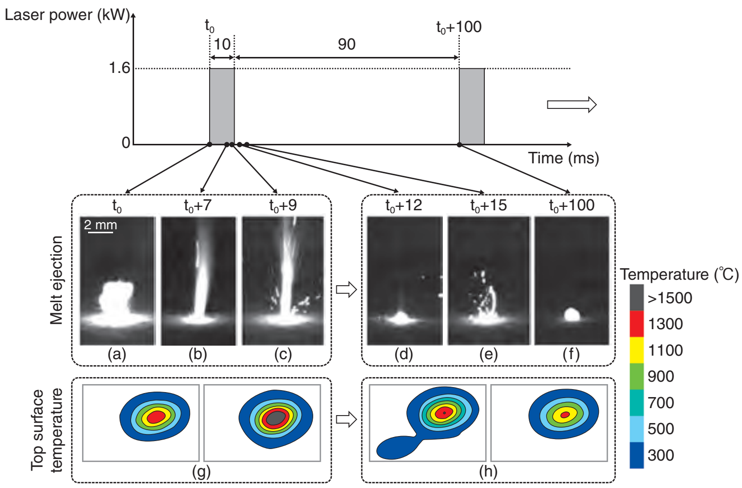

Fig.1-19 Images of melt ejection and temperature profiles on the top surface during QCW laser irradiation
The laser was set to a 10-ms pulse width, 1.6-kW peak power, 10-Hz repetition rate, and 1.1-mm beam-spot diameter. t_0 indicated the instant of laser irradiation. (a)–(f): High-speed images were taken by a high-speed camera. (g) and (h): Temperature profiles at the top surface were taken by thermography.

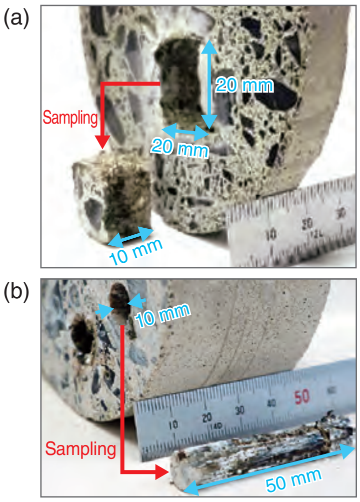

Fig.1-20 Sampling test of concrete
(a) High-performance square-shaped sampling by a 2-kW fiber laser. The areal sizes were 20 × 20 mm with a depth of 10 mm. The total sampling time was 32 s. (b) Circularly shaped sampling with a diameter of 10 mm and depth of 50 mm was demonstrated with a 6-kW fiber laser.

Safe and secure decommissioning of the TEPCO's Fukushima Daiichi NPS is a national issue. To evaluate the soundness of the reactor-pressure vessel and the primary containment vessel over the long period of decommissioning, we should develop suitable inspection technologies. On the other hand, maintaining safe and reliable conditions for aging public infrastructure such as roads and tunnels built during rapid economic growth is also a national issue. Thus, securing worker safety and enabling efficient inspection by workers are common shared issues. Therefore, we should develop remote technologies such as robots that incorporate advanced inspection technologies to overcome a high-dose environment or perform high-elevation works.

High-power fiber lasers are an attractive technology for material processing due to their advantages over mechanical-removal technologies, such as the capability to work over long distances with noncontact processing and ease of coupling with remote control. In this study, we have developed remote-sampling technology using a quasi-continuous wave (QCW) fiber laser. The advantages of the QCW fiber laser with a high peak power include a smaller heat-affected zone (HAZ) and a higher controllability with a smaller and lighter processing head than a continuous-wave laser. The results of melt ejection and the temperature profile during the QCW laser sampling are shown in Fig.1-19. When a laser pulse interacts with concrete, the surface is quickly heated to high temperature via the absorption of laser energy, causing the concrete to be melted and vaporized. A vapor plume was created immediately at the beginning of the laser-sampling process. As the surface temperature reached the vaporization point, part of the molten concrete was further vaporized by the pressure created by the beam upon the molten concrete's surface. Figs.1-19(d) and (e) show the melt-ejection process, which continued even after the laser. Fig.1-19(f) shows the concrete surface kept at a sufficiently high temperature to control the molten phase until the next laser pulse.

Fig.1-20 shows that increasing the peak power to 6 kW enables us to sample a piece of concrete up to 50 mm with a laser-spot diameter, pulse width, and repetition rate of 1.1 mm, 10 ms, and 10 Hz, respectively.

We will further characterize and minimize the HAZ to use laser-sampling techniques to prevent the degradation of concrete.

The present study was supported, in part, by the Cross-ministerial Strategic Innovation Promotion Program (SIP), funded by the Japan Science and Technology Agency (JST).

Reference
Nguyen, P. L., Yamada, T. et al., Experimental Characterization of Concrete Removal by High–Power Quasicontinuous Wave Fiber Laser Irradiation, Journal of Laser Applications, vol.29, issue 4, 2017, p.041501–1–041501–11.

1–9 Development of a Robot Simulator for Nuclear Decommissioning

— Operator-Proficiency Training and Performance Evaluation of the Robot by Simulation —

Fig.1-21 Developed robot simulator
A robot simulator utilizing a 3D digital model inside the 1F reactor building was developed to support robot-operator-proficiency training and performance evaluation of the robot.

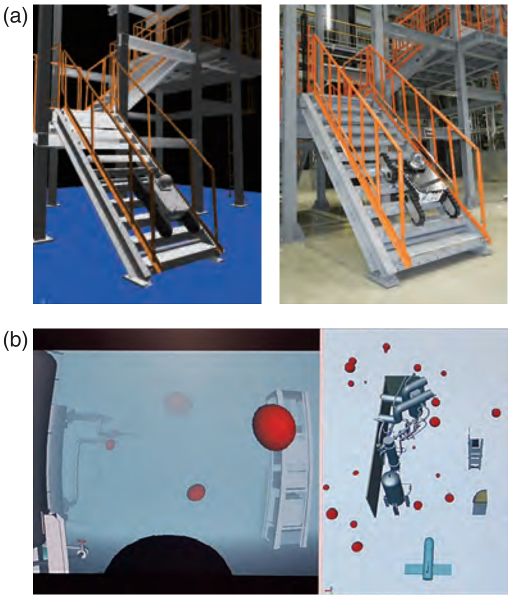

Fig.1-22 Examples of the simulation model and simulated effect
(a) a real mockup stair and a robot (right) and their simulated models (left). (b) This snapshot shows an example of camera-view-disturbance effects (distortion noise and the appearance of the obstacles) during underwater simulation.

After the accident at the TEPCO's Fukushima Daiichi NPS (1F), areas within 1F have high radiation-dose rates, so remotely operated robots need to be deployed there for physical and radiation surveys. It is difficult to remotely maneuver the robots inside reactor buildings due to natural obstacles that include staircases and obstacles created by debris from the accident. Remote robot operation is complicated by frequent difficulties with signal transmission between the operator site and the robots. Therefore, it is necessary to develop robots for specific tasks and to train skilled robot operators. To meet these needs, we are developing a robot-simulator system to support performance evaluation of remotely operated robots and to improve robot-operator skills (Fig.1-21 and Fig.1-22(a)).

As the basis of the robot simulator, we used a Choreonoid that was developed by the National Institute of Advanced Industrial Science and Technology (AIST). Additional functions can be designed and implemented on the Choreonoid as plug-ins. Therefore, we developed required functions and installed a 3D digital model inside the 1F reactor building to realistically simulate remotely operated robot-operational cases in the decommissioning process.

We developed a plug-in function for simulating the submerged behavior of underwater remotely operated vehicles (ROVs). The plug-in calculates the effects of buoyancy, hydrodynamic-lifting force, and fluid resistance upon the ROV's body in response to motion commands.

A plug-in function for camera-view-disturbance effects was also developed. We designed these functions to add the effects of magnification, distortion, noise, and view-blocking obstacles. Distortion effects occur in the underwater environment due to refraction. Fisheye distortion is a typical example of image distortion. Noise on the image is simulated to present an unclear-visual-recognition situation to the operators (Fig.1-22(b)).

Another function that we developed simulates the effects of signal- and data-transmission trouble that occurred during past missions of remotely operated robots at 1F. This function is implemented by installing a computer called the communication-traffic controller, between the computer that runs the robot simulator and the computer used to operate the simulated robot. The communication-traffic controller manages the communication states and can vary bandwidth limitations, communication delay, packet loss, and jitter effect both upstream and downstream. The developed simulation functions are implemented in the robot simulator and a 3D digital model is installed inside the 1F reactor building. The user can experience realistic remote operations by the robot (Fig.1-21).

We will continue to develop and implement the required functions to the robot simulator to promote robot development and operator training to contribute to the decommissioning of 1F.

Reference

Kawabata, K. et al., Development of a Robot Simulation System for Remotely Operated Robots for Operator Proficiency Training and Robot Performance Verification, Proceedings of 14th International Conference on Ubiquitous Robots and Ambient Intelligence (URAI 2017), Jeju, Korea, 2017, p.561–564, in USB Flash Drive.

1–10 Detection of Radionuclide Depth in Soil by Aerial Radiation Monitoring

— Technology for Estimating the Vertical Distribution of Radionuclides in Soil Based on the γ-ray Spectrum —

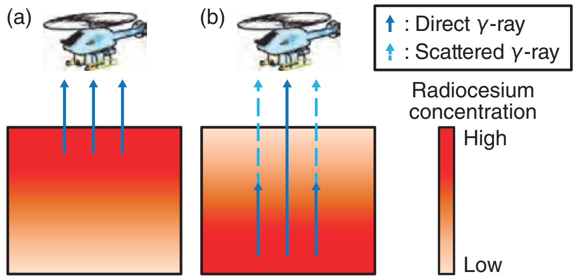

Fig.1-23 Aerial radiation monitoring using an unmanned helicopter
(a) The contribution ratio of direct γ-rays to scattered γ-rays is large when radiocesium is distributed in surface soil; (b) it is small when radiocesium is distributed in deeper soil layers because direct γ-rays are attenuated by soil particles in the upper soil layer.

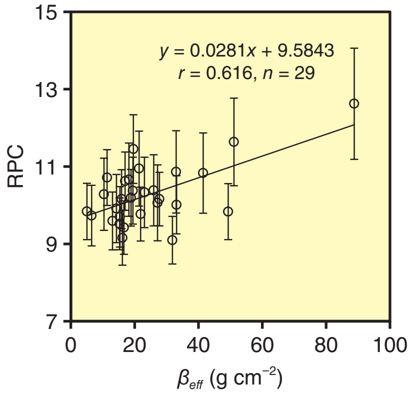

Fig.1-24 Relationship between the result of aerial radiation monitoring and the collection of core soil
It is estimated that the contribution ratio of scattered γ-rays to direct γ-rays obtained by aerial radiation monitoring varies with the distribution depth of radiocesium in the soil. The error bars are the standard deviation of the count rate.

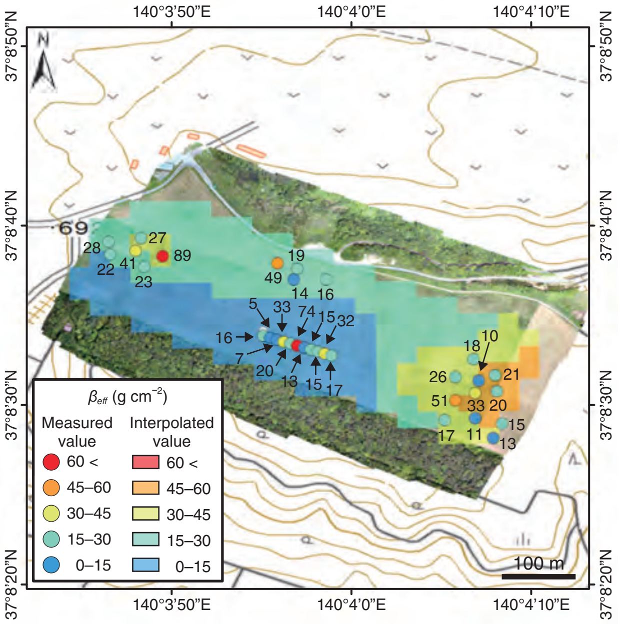

Fig.1-25 Comparison between the estimated value of β_{eff} and actual β_{eff}
The estimated β_{eff} value calculated by the equation in Fig.1-24 was well fitted to the actual result. This figure implies that the estimated β_{eff} value is the average vertical distribution of radiocesium in soil in the selected area.

Seven years have passed since the accident at the TEPCO's Fukushima Daiichi NPS (1F). It has been reported that radiocesium deposited by the accident was transferred into deeper soil with rainfall, inversion tillage (a type of decontamination work) and disturbance by wild animals. It is necessary to readily detect radiocesium depth in the soil from the ground surface. This method would be helpful for determining the depth of decontamination. We have developed an aerial-radiation-monitoring method using an unmanned helicopter (R-Max G1, YAMAHA Co., Ltd.), which is used to rapidly and easily investigate the spread status of radiocesium on a wide scale.

In the present study, we succeeded in developing a method for acquiring radiocesium soil depth based on the characteristics of the γ-ray spectrum obtained by aerial radiation monitoring. To validate the theory in Fig.1-23, the contribution ratio of scattered γ-rays to direct γ-rays is compared to the vertical distribution of radiocesium in core soil at the same point in the farmland (Fig.1-25). Inversion tillage was performed in the farmland, except in the southern area. The value of the ratio of peak to Compton-scatter peak heights (RPC) is calculated based on the ratio of the counting rate of scatted γ-rays (50–450 keV) to that of direct γ-rays (450–760 keV) for γ-rays obtained by aerial radiation monitoring. We used the $LaBr_3$(Ce) detector that showed good energy resolution for ^{137}Cs. The vertical distributions of radiocesium in the core samples (0–60 cm) were obtained by random soil sampling using a core sampler in farmland. The vertical distribution of radiocesium in soil was expressed as a parameter, effective relaxation mass depth (β_{eff}). As β_{eff} increased, radiocesium distributed more deeply into the soil.

As shown in Fig.1-24, good agreement was observed between the RPC and β_{eff}. The map of estimated β_{eff} in the entire field in Fig.1-25 was created based on the above-mentioned equation. The result of core soil sampling is shown as a black circle in the result for aerial radiation monitoring over all farmland. The vertical distribution of radiocesium from farmland on a wide scale was investigated by aerial radiation monitoring using an unmanned helicopter. This method would be helpful for performing decontamination in the difficult-to-return zone over a wide scale.

This research was supported by grants from the Project of the NARO Bio-oriented Technology Research Advancement Institution “the special scheme project on regional developing strategy”.

Reference

Ochi, K. et al., Estimation of the Vertical Distribution of Radiocesium in Soil on the Basis of the Characteristics of Gamma-Ray Spectra Obtained via Aerial Radiation Monitoring Using an Unmanned Helicopter, International Journal of Environmental Research and Public Health, vol.14, issue 8, 2017, p.926-1–926-14.

1–11 Highly Accurate Measurement of Radiation-Dose Distributions

— Realization of Highly Accurate Radiological Airborne Monitoring on Rugged Terrain —

(a) Radiological airborne monitoring

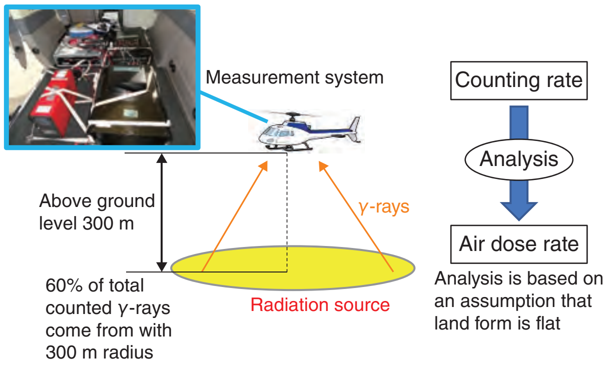

(b) Influence of terrain

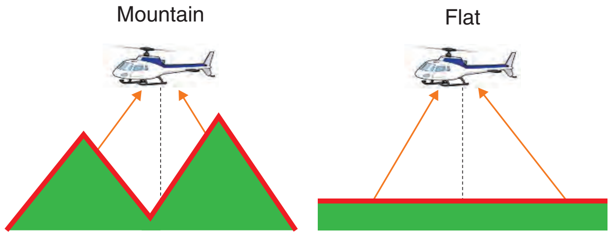

Flight path of γ-rays change depending on the land form

Fig.1-26 Effects of topographical relief upon radiation measurement
Counting rates measured by radiological airborne monitoring are converted into air dose rates based on the assumption that terrain is flat. Measured counting rates are different due to topographical relief, even if the contamination level is the same.

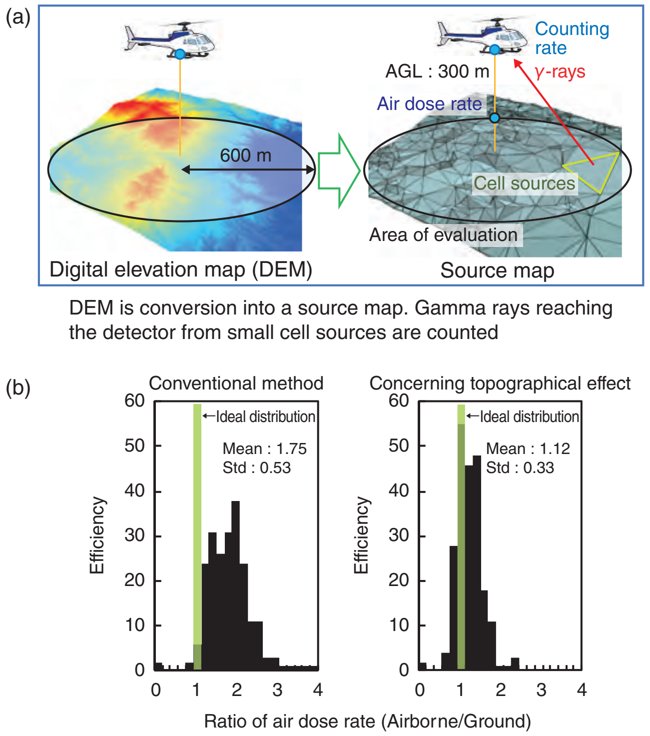

DEM is conversion into a source map. Gamma rays reaching the detector from small cell sources are counted

Fig.1-27 Data-analysis method incorporating terrain effect, and the results
Air dose rates were obtained based on the calculated results of counting rate for each terrain. Air dose rates obtained by the traditional method and by this method were compared to those obtained by ground measurement.

Radiological airborne monitoring is one radiation-monitoring tool that can measure air dose rates and radionuclide deposition rapidly over a wide area by measuring radiation at 300 m above the ground (Fig.1-26(a)). In radiological airborne monitoring, not only manned helicopters, but also unmanned helicopters, drones, and other flying objects are used. Measurement results collected by radiological airborne monitoring are employed for a number of purposes including assessment of the contamination situation. Recently, the measurement result has also been used to estimate inhabitants' exposure dose. Therefore, improvement of data accuracy is regarded as one of the most important issues.

In radiological airborne monitoring employed to date in Japan, the terrain of a target area has been regarded as flat in the process of data analysis. However, due to topographical relief, the air dose rates may potentially be overestimated or underestimated, because the measured counting rates change depending on the terrain effect in spite of having the same contamination level (Fig.1-26(b)). Unlike Europe and the United States, most of Japan's land area is covered by mountains. Therefore, we evaluate the effects of terrain upon data accuracy and develop a new method to decrease the error.

In the analytical process, an air dose rate (μSv/h), D, can be obtained by dividing a counting rate (cpm), C , by a conversion factor (cpm/(μSv/h)), CD, according to the following equation:

$$\mathrm{D} = C/CD$$

CD changes depending on the terrain. We performed data analysis considering the terrain effect. CD values for arbitrary terrain were obtained based on the calculated results of γ-ray flux at 300-m height. Gamma-ray flux was calculated as shown in Fig.1-27(a). First, a triangle-surface map was created from a digital elevation map. Then, small triangles in this map were regarded as small radiation sources and generated γ-rays. In the end, by summation of the number of γ-rays that reach to the detector position at a height of 300 m, the counting rate was obtained.

For 217 points in Fukushima prefecture, we compared D obtained with the traditional method and D obtained with the new method including the terrain effect to D obtained by ground measurement and evaluated the conversion accuracy. In the evaluation, the frequency distributions of the ratio between the radiological-airborne-monitoring and ground-measurement D values were used. If the two D values were equivalent, the distribution shows as a green bar in Fig.1-27(b). From the frequency distribution, the average was improved from 1.75 to 1.12 and the standard deviation was improved from 0.53 to 0.33 using a new analysis method considering terrain effect. By considering the terrain effect in data analysis, we succeeded in improving conversion accuracy.

We are going to apply this method to the regular operation of radiological airborne monitoring in Japan.

Reference

Ishizaki, A. et al., Application of Topographical Source Model for Air Dose Rates Conversions in Aerial Radiation Monitoring, Journal of Environmental Radioactivity, vol.180, 2017, p.82–89.

1–12 How is Radiocesium Distributed in a Town?

— Investigation of the Radiocesium Distribution in Residential Areas —

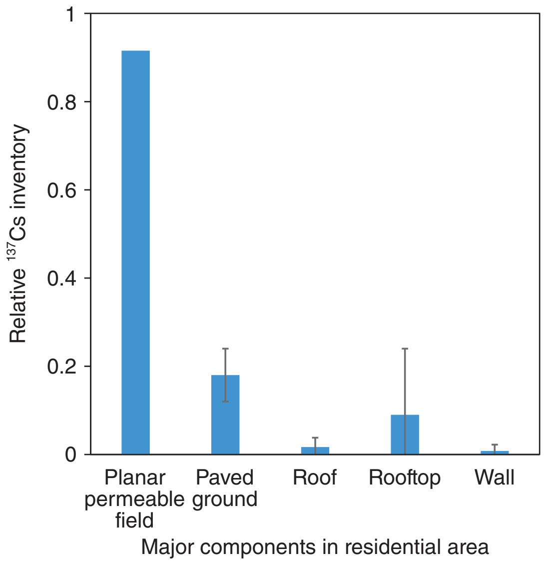

Fig.1-28 Relative ^{137}Cs inventory on studied components in urban areas during January 13–23, 2015
The error bar indicates the standard deviation of the relative ^{137}Cs inventory. Residential-area-specific components such as paved ground, roofs, and walls showed obviously lower ^{137}Cs-relative inventories than planar permeable fields in January 2015.

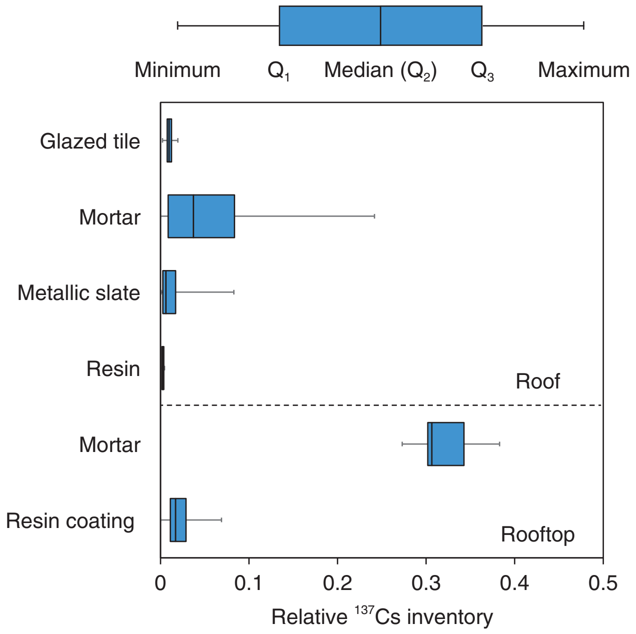

Fig.1-29 Box-and-whisker plot of the relative ^{137}Cs inventory for surface materials of roofs and rooftops
The relative ^{137}Cs inventory varied largely among the materials of roofs and rooftops. Porous materials, such as mortar, showed significantly higher relative ^{137}Cs inventories than others, and glazed tile and metallic slate showed obviously smaller values, indicating that ^{137}Cs deposited on smooth materials were easily removed from the surface during the first four years after the accident.

The distribution and migration of radiocesium in diverse terrestrial environments has been well-studied; however, there has been little analysis of its behavior in residential areas. Since residential areas comprise diverse components such as paved ground, roofs, walls, and permeable ground, the radiocesium dynamics should be different from other terrestrial environments. To evaluate the dynamics of radiocesium in a residential area, ^{137}Cs inventories (activity per unit area) were measured on major components (i.e., roofs, rooftops, walls, planar permeable fields, and paved ground) for 11 building lots in the evacuation zone in January 2015. The ^{137}Cs inventories were converted to relative ^{137}Cs inventories, which are defined as the relative values of the ^{137}Cs inventory on each component to the initial ^{137}Cs inventory on a nearby planar permeable field, enabling comparison of ^{137}Cs inventories among sites with different initial deposition amounts. The initial ^{137}Cs inventory on planar permeable fields on March 23, 2011 was estimated by only physical-decay correction, since the ^{137}Cs inventory on planar permeable fields has been reported to decrease almost as predicted by its physical-decay constant, without any detectable wash-off effects.

The average relative ^{137}Cs inventories on the components are shown in Fig.1-28. The value on paved ground accounted for about 20% of that on the planar permeable field. Other components, such as roofs, rooftops, and walls also showed values less than 10% of that on the planar permeable field. This study was carried out in the evacuation zone in which decontamination had not been conducted. Therefore, these results indicate that large amounts of radiocesium deposited in the residential area were removed by initial run-off and the following wash-off effects due to rainfall over the four years following the accident, even without decontamination.

The average relative ^{137}Cs inventories on roofs and rooftops showed large coefficients of variation over 100%. Studies in Europe reported that porous materials such as unglazed tiles have larger absorption capacities for ^{137}Cs than other materials. Variations in the relative ^{137}Cs inventories depending on roof and rooftop materials were also observed in this study (Fig.1-29); smooth-surface materials such as glazed tile, metallic slate, and resin showed low relative ^{137}Cs inventories, while unglazed mortar showed large values. Since the roof and rooftop are major components in residential areas, these results indicate that the migration of radiocesium deposited in the area largely depended upon the materials of roofs and rooftops.

The results in this study are expected to contribute to decontamination planning and exposure-dose simulations in residential areas.

Reference

Yoshimura, K. et al., Distribution of ^{137}Cs on Components in Urban Area Four Years after the Fukushima Dai–Ichi Nuclear Power Plant Accident, Journal of Environmental Radioactivity, vols.178–179, 2017, p.48–54.

1–13 Prediction of Radiocesium Behavior in Upstream Catchment

— Sediment and Radiocesium-Transport Simulation during Approximately Five Years Following the 1F Accident —

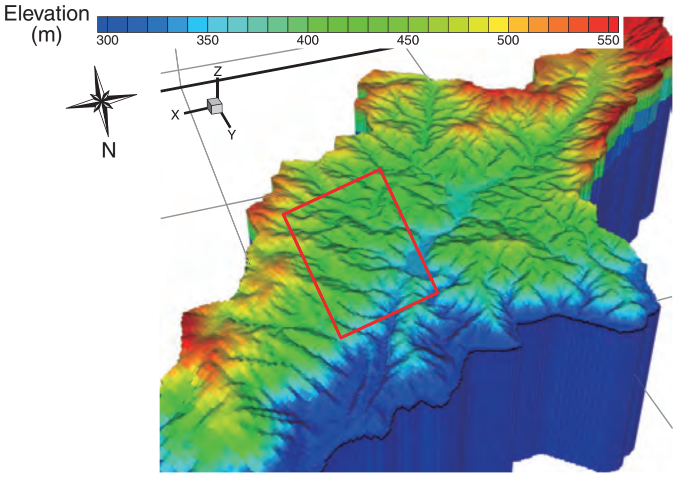

Fig.1-30 3-D-structure model developed for the study area
The red frame shows the boundary of Fig.1-31. In GETFLOWS, parameters such as the hydraulic coefficient and Manning's roughness coefficients are set for each grid described as Fig.1-30 and both surface and subsurface water flow are simulated simultaneously. Sediment and radiocesium transport are simulated based on the water fluxes of whole area and radiocesium behavior is predicted for the environment.

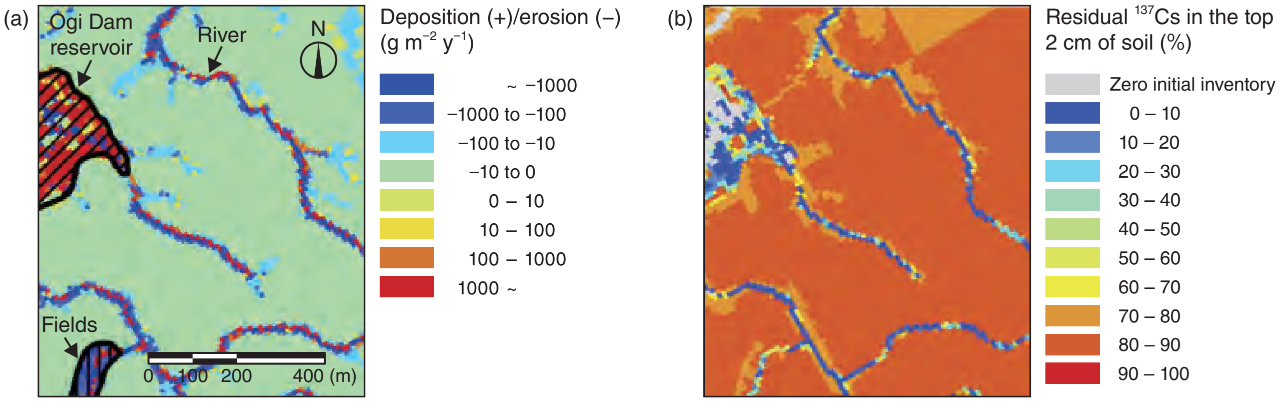

Fig.1-31 The amount of sediment erosion and deposition (a) and the fraction of residual ^{137}Cs (b) from May 2011 to December 2015
These maps show spatial redistribution of the sediment and radiocesium discharge through rivers from forested areas including crop and paddy fields. The area in the vicinity of river channel and forest gullies experience a large amount of sediment erosion, thus resulting in a reduction of residual ^{137}Cs.

Due to the accident at the TEPCO's Fukushima Daiichi NPS, significant amounts of radiocesium (RCs) remain in the top surface soil because RCs have the characteristic of adsorbing strongly to soil particles including clay minerals. Surface-soil erosion by heavy rainfalls such as typhoons is important for predicting RCs behavior in the watershed; however, we need to describe both surface and subsurface water flow to simulate this behavior with and without precipitation periods. In this study, we applied the watershed model GETFLOWS, which can describe sediment and RCs transport to an Oginosawa river catchment (Fig.1-30) in Fukushima.

Fig.1-31 shows the amount of sediment erosion/deposition and the fraction of the residual ^{137}Cs inventory from May 2011 to December 2015. Sediment erosion was found to have occurred significantly and the ^{137}Cs inventory decreased in the vicinity of the river channel and forest gullies. On the other hand, sediment erosion did not occur much in the forested area far from the rivers, with the result that the ^{137}Cs inventory remained. Therefore, the physical decay of ^{137}Cs is the most important factor in forested areas far from rivers. Calculation of ^{137}Cs sources supplied to the river at this catchment showed that contributions from the vicinity of the river channel were an order of magnitude higher than that from the forested area far from rivers. This is because surface-water flow during heavy-rainfall events can cause high sediment-erosion rates. In the future, ^{137}Cs discharge to the river is expected to decrease due to the decreasing ^{137}Cs inventory in the vicinity of the river and the migration of ^{137}Cs from top-surface soil to deeper soil. We need to watch the downstream influence of ^{137}Cs discharge by decontamination or starting cultivation in the future.

Verification and improvement of this study, especially dissolved RCs which is high bioavailability, can be used to understand mechanisms of dissolved RCs behaviors in environment in the future.

Reference

Sakuma, K. et al., Evaluation of Sediment and ^{137}Cs Redistribution in the Oginosawa River Catchment near the Fukushima Dai-Ichi Nuclear Power Plant Using Integrated Watershed Modeling, Journal of Environmental Radioactivity, vol.182, 2018, p.44–51.

1–14 Research on the Distribution of ^{137}Cs in Seabed Sediments

— Relationship between the ^{137}Cs Inventory and Seafloor Topography —

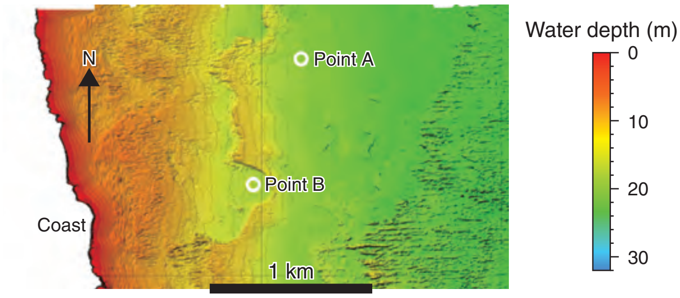

Fig.1-32 Bathymetric map and sample locations
A semicircular depression (diameter: ~ 200 m; depth: ~3 m) was observed around location B.

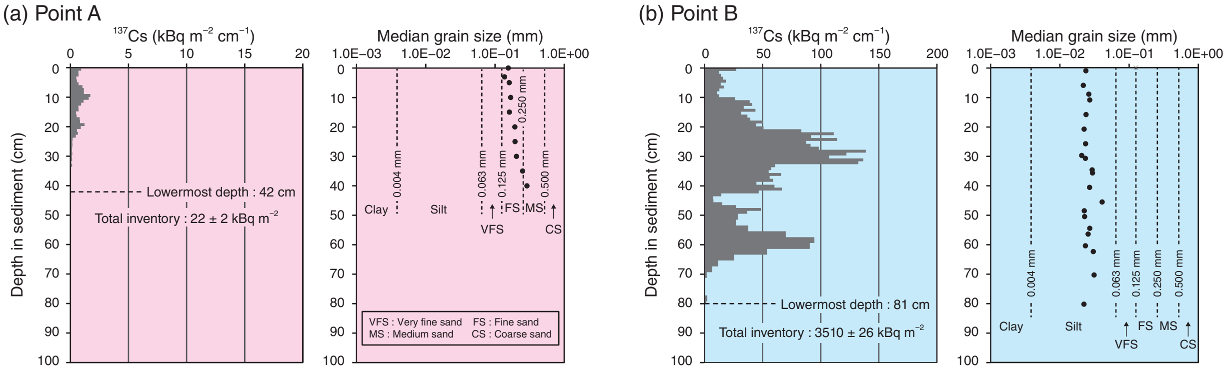

Fig.1-33 Vertical distribution of ^{137}Cs activities (kBq m^{-2} cm^{-1}), total inventory per unit (kBq m^{-2}), and median grain size (D50) of samples collected via core-sampling method
Size class of D50 value are described according the Wentworth grain-size scale.

The accident at the TEPCO's Fukushima Daiichi NPS that occurred following the Great East Japan Earthquake and the resulting tsunami in March 2011 resulted in extensive release of radioactive cesium into the Pacific Ocean. Understanding the features of ^{137}Cs transport from contaminated mountain forests to coastal sinks is key to the revitalization of marine industries. The ^{137}Cs distribution in shallow seas, which are major settlement areas for particle-sorbed ^{137}Cs, is very important when studying ^{137}Cs transport from contaminated mountain forests to coastal sinks. Therefore, we examine the heterogeneity of the ^{137}Cs distribution in seabed sediments at sea depths <30 m. A bathymetric survey and sonic prospecting were conducted to map the occurrences of seabed sediments, and core sampling of such sediments was performed to describe the vertical profile of the ^{137}Cs distribution therein.

The bathymetric map shown in Fig.1-32 indicates that terrace-like seafloors consisting of gently descending slopes opposite to the coastal sides (dip side; around point A, Fig.1-32) and steeper ascending slopes on their coastal sides (up-dip side) extend in the investigation area. In particular, point B is located in a semicircular depression surrounded by steep sides. According to the results of sonic prospecting, the surface ratio of bedrocks (Pliocene sedimentary rocks) is 52%, suggesting that the ^{137}Cs distribution on the seafloor is less than half of that in the investigation area. Seabed sediments tend to accumulate at the base of the steeper ascending slopes. Fine-to-medium sand is the main constituent of the seabed sediments (Fig.1-33(a)) and the distribution of the finer fraction (silt) is limited to a quite narrow zone of semicircular depression (point B).

The ^{137}Cs-inventory values collected at point B are greater than those at point A, and the grain sizes (D50 values) at point B are homogeneously silt (Fig.1-33). The current velocities of the bottom layer at point B, which were observed using current profilers towed by ships, were lower than those at point A. These results suggest that the steep slope around the semicircular depression area appears to play a major role as a topographic barrier in reducing the current velocity, prompting the settlement of fine-grained particles. In other words, the features of the seafloor topography are determined to be significant factors controlling the horizontal and vertical distributions of ^{137}Cs in the seabed sediments. Areas with similar seafloor topographies of the semicircular depression were not identified in the investigation area, suggesting that distributions with remarkably large ^{137}Cs inventories (more than several thousands of kBq m^{-2}) are strictly limited.

Our research also revealed the continuous ^{137}Cs distribution at depths greater than 81 cm (Fig.1-33(b)). Vertical ^{137}Cs profiles in seabed sediments obtained in previous studies have been insufficient to evaluate ^{137}Cs concentrations because information about the distribution of ^{137}Cs at the lowermost depths of these sediments is lacking, owing to short core-sampler lengths (almost less than 20 cm).

Therefore, these results indicate that estimation of the ^{137}Cs inventory in shallow seas should be performed carefully, considering the extent of the ^{137}Cs distribution along the vertical depth and the surface ratio of the seabed sediments.

Reference

Tsuruta, T. et al., Horizontal and Vertical Distributions of ^{137}Cs in Seabed Sediments around the River Mouth Near Fukushima Daiichi Nuclear Power Plant, Journal of Oceanography, vol.73, issue 5, 2017, p.547–558.

1–15 Prediction of the Dispersion of Radionuclides Released into the Ocean

— Dispersion Simulation of Radionuclides from Coastal Regions to the Open Sea —

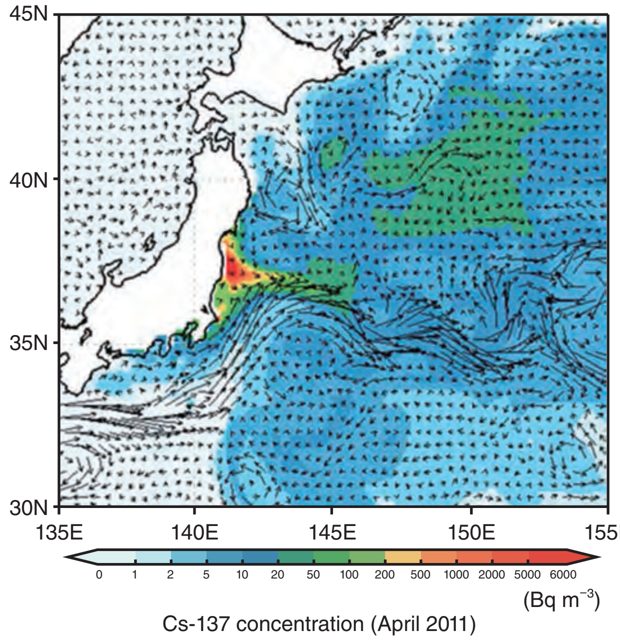

Fig.1-34 Averaged surface ^{137}Cs concentrations in April
Simulation results suggested that the ^{137}Cs concentrations in the coastal and offshore oceans were influenced by the Kuroshio Extension.

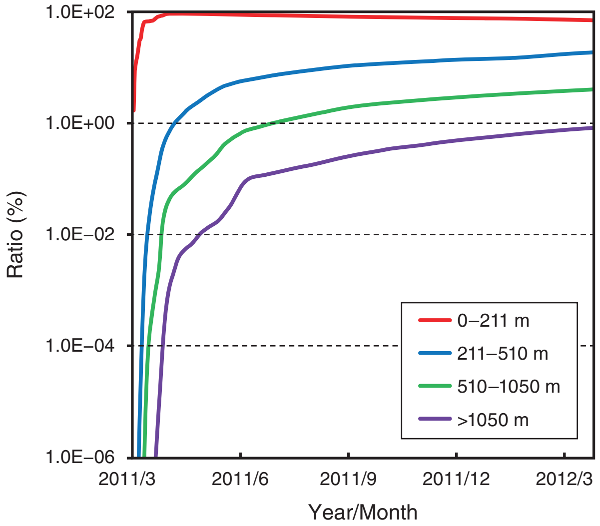

Fig.1-35 Time series of the ratios (%) of ^{137}Cs amounts in the surface, intermediate, deep, and bottom layers to the total release amount of ^{137}Cs
Simulation results suggested that one year after the 1F accident, the accident-derived ^{137}Cs was transported to layers below a depth of 200 m.

Cesium-137 (^{137}Cs) was released to the ocean by the accident at the TEPCO's Fukushima Daiichi NPS (1F). Many observational and simulation studies have been carried out to clarify the oceanic dispersion. Numerical simulation is a powerful methodology for understanding the spatiotemporal characteristics of oceanic dispersion of accident-derived radionuclides. Unfortunately, the quality of oceanic-dispersion simulations is degraded by uncertainties in the source term and simulated ocean currents. In this study, oceanic-dispersion simulations were carried out by an oceanic-dispersion model using output data from five oceanic general-circulation models. By comparing these simulation results, we objectively analyzed the effect of different oceanic data upon the ^{137}Cs-dispersion simulation. Then, we analyzed the ^{137}Cs dispersion from the coastal region of Fukushima to the North Pacific Ocean.

In this study, we applied the SEA-GEARN oceanic-dispersion model developed at JAEA. Input oceanic data were calculated by oceanic general-circulation models of the Japan Marine Science Foundation (JMSF), the Japan Agency for Marine-Earth Science and Technology (JAMSTEC), the Meteorological Research Institute (MRI) of the Japan Meteorological Agency (JMA), and the National Oceanic and Atmospheric Administration (NOAA). The data-assimilation method was applied to these oceanic general-circulation models to assimilate observed data into numerical simulations. The direct-release rate of ^{137}Cs into the ocean was estimated by means of the observed sea surface ^{137}Cs concentrations near the northern and southern discharge channels of 1F. To provide the ^{137}Cs-deposition amounts at the sea surface, we conducted an atmospheric-dispersion simulation using the latest-estimated ^{137}Cs release rate into the atmosphere.

Compared to the simulation with a lower horizontal resolution, the higher-resolution simulation reproduced well the ^{137}Cs concentration observed in the coastline and offshore of Fukushima prefecture. The ^{137}Cs was suggested to have been spread along the coast in the north–south direction during the first few months after the 1F accident. The simulations for the western part of the North Pacific and the whole North Pacific reproduced the main ocean current favorably using the data-assimilation method, despite the relatively low resolution. This suggests that the Kuroshio Extension plays a large role in the transport process of ^{137}Cs from the coast to the outer ocean (Fig.1-34).

Analysis of the depth distribution of ^{137}Cs by the dispersion simulation showed that most of that transferred to the ocean by direct release or deposition from the atmosphere existed in the surface layer (0–211 m from the sea surface) shortly after the accident. However, as time passed, it was transported from the surface layer to deeper layers (Fig.1-35). The ^{137}Cs amounts in the surface, intermediate (211–510 m), deep (510–1050 m), and bottom layers (deeper than 1050 m) one year after the 1F accident were 71, 19, 4, and 0.8% of the total release amount, respectively.

This study suggests that the accident-derived ^{137}Cs was dispersed widely into the North Pacific and gradually dispersed from the surface to the deeper layers by simulations, regardless of the different ocean-current data. A future task is to carry out oceanic-dispersion simulations over the whole North Pacific for several decades to quantify the time-series change of ^{137}Cs abundance.

Reference

Kawamura, H., Kobayashi, T. et al., Oceanic Dispersion of Fukushima–Derived Cs–137 Simulated by Multiple Oceanic General Circulation Models, Journal of Environmental Radioactivity, vol.180, 2017, p.36–58.

1–16 Determining the Conditions for Effective Forest Decontamination

— Simulation of the Effect of Reducing Air-Dose Rate by Decontamination —

	Evaluation points 1A	Evaluation points 1B	Evaluation points 1C
1 m in height	1A1	1B1	1C1
4 m in height	1A4	1B4	1C4

1A : Forest edge
1B : 5 m to the residential area
1C : 10 m to the residential area

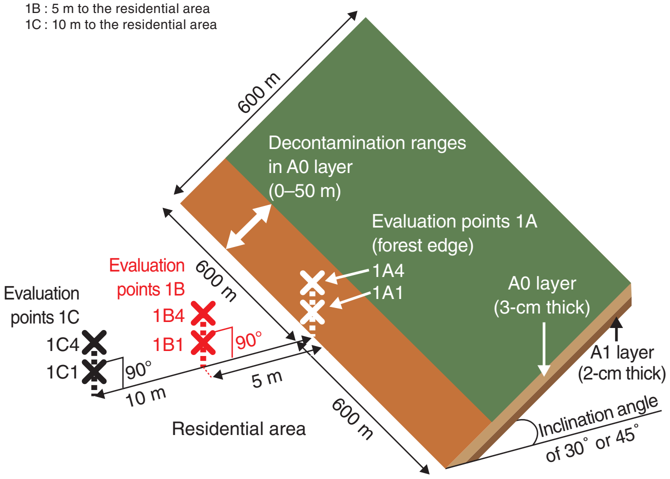

Fig.1-36 Evaluation system when there is a single slope of forest soil
At the forest edge (1A), which is the boundary between the forest and the residential area, the points 5 m (1B) and 10 m (1C) distant from the forest edge on the residential-area side were given as the evaluation points of the air-dose rate. Then, at these three points, elevations of 1 m and 4 m from the ground were given: the 1-m height was assumed to be an adult staying outside; the other was a two-story house.

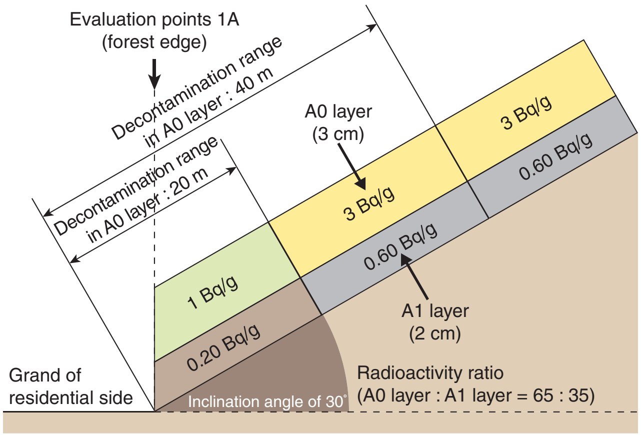

Fig.1-37 Cutaway view showing a case where a large amount of radioactive Cs is present in the A0 layer and the contamination has a planarly non-homogeneous source distribution
Assuming that almost double the amount of radioactive Cs is present in the A0 layer compared with the A1 layer and that the concentration of radioactive Cs in the forest soil away from the residential area is tripled that nearby, an example in which the contamination present in over 20 m distant from the forest edge is 3-times higher than that within 20 m is shown.

In the accident at the TEPCO's Fukushima Daiichi NPS, forests were polluted by radioactive-cesium (Cs) release. Radioactive Cs remains in forest soil. The decontamination of such Cs is expected to reduce the air-dose rate. However, if decontamination is applied to the forest as a whole, a huge amount of soil will have to be removed. Therefore, there will be a tremendous burden on its management and expenses. In addition, such decontamination increases the possibility that forest soil will leak out, damaging the multifaceted functions of forests such as water-source protection and disaster prevention. Thus, as a method of forest decontamination, the Forestry Agency has recommended gradually removing the surface layer of fallen leaves and forest soil.

In this research, the A0 and A1 layers were assumed to be radiation sources. The A0 layer is the surface of the forest soil including sedimentary organic materials such as fallen leaves. The A1 layer contains the soil. The air-dose rate in a residential area was analyzed using the three-dimensional transport calculation code MCNP on the condition that only the A0 layer was decontaminated. The shapes of radiation sources were given as one or three forest slopes. Fig.1-36 shows the shape of the radiation source for a single forest slope. The three forest slopes were assumed for the case of a house surrounded by three forests. For each radiation-source shape, cases where an inclination angle of the forest soil and the amount of radioactive Cs in the soil were changed–and also a case where the contamination of the forest soil was planarly non-homogeneous–were analyzed. For all of those cases, we analyzed the extent to which the air-dose rate at that point in the residential area was reduced when the range of the A0 layer was removed.

It was found that, even if the A0 layer was removed, the air-dose rate in the residential area (especially the second floor of the residence) was hard to lower compared with the forest edge, regardless of the number of slopes or the inclination angle.

Also, if there is more radioactive Cs in the A0 layer and the contamination is planarly homogeneous, it is effective to remove the A0 layer up to 20 m from the forest edge. But, for instance, as shown in Fig.1-37, in the case where the concentration of radioactive Cs included in the forest soil at over 20 m distant from the forest edge was tripled compared with its concentration included in the forest soil from the forest edge up to 20 m, the decontamination of the A0 layer from the forest edge up to 40 m was revealed to be needed to effectively reduce the air-dose rate in the residential area.

This simulation has made it possible to effectively determine the forest-decontamination method according to the distribution of contamination.

Reference

Henmi, K. et al., Analysis on the Effect of Forest Decontamination on Reducing the Air Dose Rate Using the Three-Dimensional Transport Code MCNP, Journal of Nuclear Fuel Cycle and Environment, vol.24, no.1, 2017, p.3–14 (in Japanese).

1–17 Nanoscale Visualization of Cesium Adsorption to Clay Minerals

— Chemical Mapping Using Synchrotron-Radiation-Photoemission Electron Microscopy —

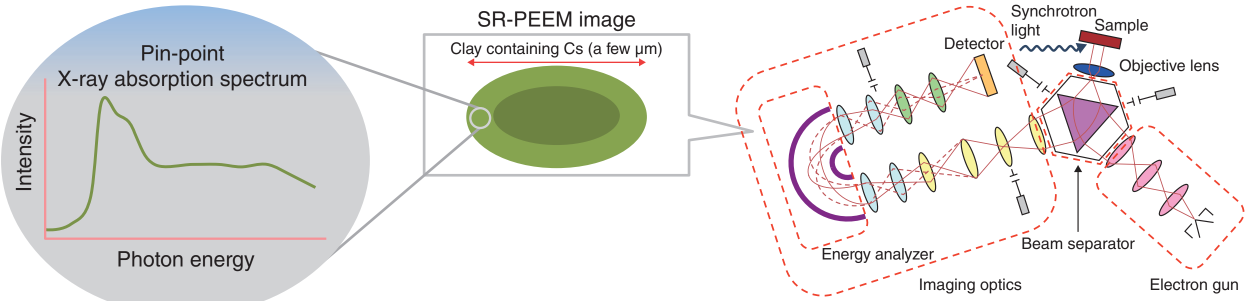

Fig.1-38 Diagram of nanoscale chemical analysis for Cs in clay particles
Images and pin-point X-ray-absorption spectrum obtained for each recorded position.

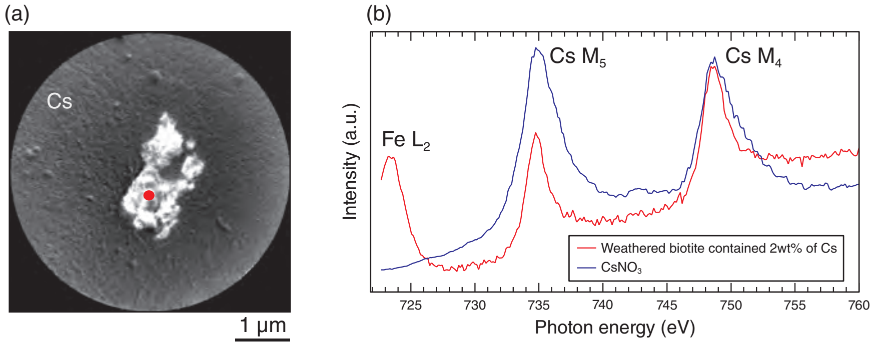

Fig.1-39 (a) SR-PEEM image of weathered biotite containing 2wt% Cs and (b) Comparison of the X-ray-absorption spectrum between weathered biotite containing Cs and $CsNO_3$
(a) The white portion shows the high-Cs concentration. (b) We found that the chemical state of Cs in clay is similar to $CsNO_3$ and that Fe with a trivalent-oxidation state (Fe^{3+}) is present.

It is known that radioactive cesium (^{137}Cs) is present at the soil surface and strongly adsorbed to clay minerals following the accident at the TEPCO's Fukushima Daiichi NPS. A basic understanding of Cs adsorption and removal is required to develop a decontamination method with a low environmental load. However, it is not easy to study the adsorption behavior of Cs because the clay contains an extremely small amount of Cs with an irregular size of less than several microns. Synchrotron-radiation-photoemission electron microscopy (SR-PEEM) is an analytical technique that can visualize the chemical state of individual elements with nanoscale spatial resolutions (Fig.1-38). Despite its superiority to other methods, a significant problem called charging arises for an insulator sample, e.g., clay. In this study, we developed an effective way to avoid this problem with a thin-carbon-film deposition to the particle surface. Here, the results of nanoscale chemical analysis of weathered-biotite clay particles containing Cs are shown.

In Fig.1-39(a), a clear Cs-distribution image was obtained for a clay mineral about several microns in size. We found that Cs was not localized at the particle surface. In addition to the information on particle identification and element distribution, the chemical state of Cs at a specific position indicated by a red full-circle could be visualized in Fig.1-39(b). We found that the Cs chemical state is similar to that of $CsNO_3$. The presence and distribution of Fe^{3+} were also revealed. The real-space information on the chemical states would deepen our understanding of Cs-adsorption mechanism.

Nanoscale visualization of chemical states can be applied to nuclear-research fields such as analysis of decontamination soil and mock samples of fuel debris contributing to decommission of the reactor. Our new approach to analyzing insulating materials using SR-PEEM is expected to be used for the development of many advanced materials in nanotechnology, environmental, and new-energy studies.

Reference

Yoshigoe, A. et al., Nanoscale Spatial Analysis of Clay Minerals Containing Cesium by Synchrotron Radiation Photoemission Electron Microscopy, Applied Physics Letters, vol.112, issue 2, 2018, p.021603-1–021603-5.

1–18 Strongest Cesium-Adsorption Site on Clay Minerals

— Numerical Simulations of Cesium Adsorption on Microscopic Surface Structures —

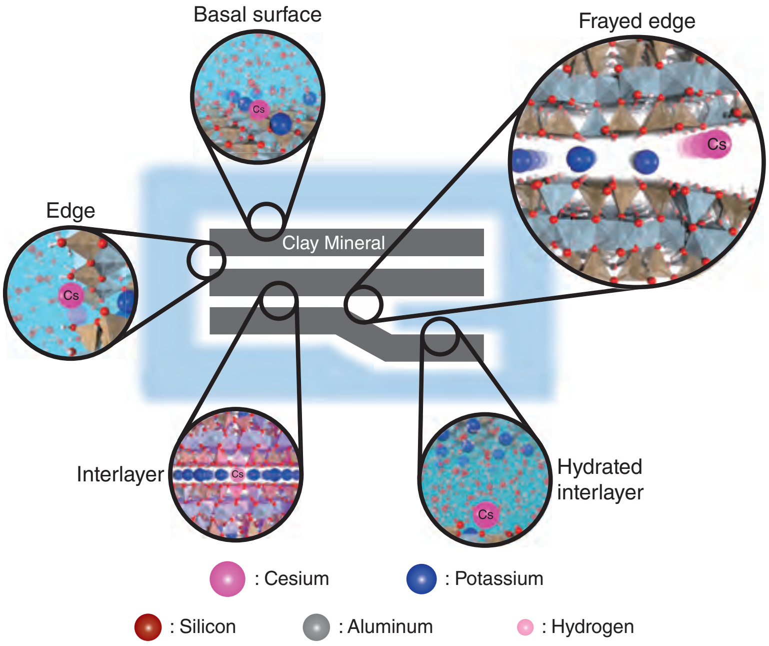

Fig.1-40 Microscopic models of surface structures on clay minerals
There are several different surface structures on clay minerals, including basal surfaces, edges, interlayers, hydrated interlayers, and frayed edges. Models of these structures were built at atomic scales and are shown in each circle.

Table 1-2 Adsorption Energies
The adsorption energies of cesium on each surface are obtained by numerical simulations. Smaller values correspond to stronger adsorption. The "frayed edge" shows the strongest adsorption.

Adsorption sites	Energy (kJ/mol)
Frayed edge	−27
Hydrated interlayer	−4
Edge	−2
Basal surface	Grater than −19

Radioactive cesium was released into the environment due to the accident at the TEPCO's Fukushima Daiichi NPS in March 2011. Part of it was strongly adsorbed onto the topsoil and became the main cause of the evacuation of residents. Decontamination was carried out on a large scale, and the radioactivity and air-dose rate were successfully reduced. However, a huge amount of waste soil was produced by the decontamination due to the use of a method that removes contaminated topsoil. Therefore, processing and management of the waste soil are emerging as problems.

For the development of volume reduction technology and risk assessment for long-term management, it will be helpful to know how cesium is adsorbed onto the soil. It is known that radioactive cesium strongly adsorbs to clay minerals in soil. However, its adsorption mechanism is unknown. One reason for which it is difficult to investigate this mechanism is that adsorption occurs over a small area that cannot be observed, even with the latest experimental equipment. As shown in Fig.1-40, clay minerals have several surface structures, each of which has been thought to exhibit different adsorption strengths. However, it is very difficult to observe the details.

Computer simulation is a powerful tool for research on such a small area. We collaborated with research institutes in the United States and the National Institutes for Quantum and Radiological Science and Technology to model the atomic-scale surface structures shown in Fig.1-40. The adsorption energies of cesium on the surfaces were evaluated using the supercomputer by changing the distance between cesium and the model surfaces at the atomic scale (Table 1-2). Based on the results of this systematic numerical simulation, it was shown that a wedge-shaped structure called "frayed edge" with a size of about a nanometer gouged by weathering adsorbs cesium most strongly (Table 1-2). A hypothesis concerning the strongest adsorption by the frayed edges was proposed about 50 years ago, but experimental proof was difficult to obtain due to the difficulty of directly observing atomic-scale structures. We succeeded in validating this hypothesis by investigating the adsorption on each surface through numerical simulations.

Based on the above results and the findings obtained from previous experimental studies, we also evaluated promising volume reduction technologies and risks during long-term management. In the future, based on the adsorption mechanism revealed in this research, we will continue research and development to contribute to reducing the volume of waste soil.

Reference

Okumura, M. et al., Radiocesium Interaction with Clay Minerals: Theory and Simulation Advances Post–Fukushima, Journal of Environmental Radioactivity, vol.189, 2018, p.135–145.

1–19 Becoming Familiar with Research Related to Environmental Recovery in Fukushima

— Development of a Comprehensive-Evaluation System and Clarification of Scientific Grounds and Insights —

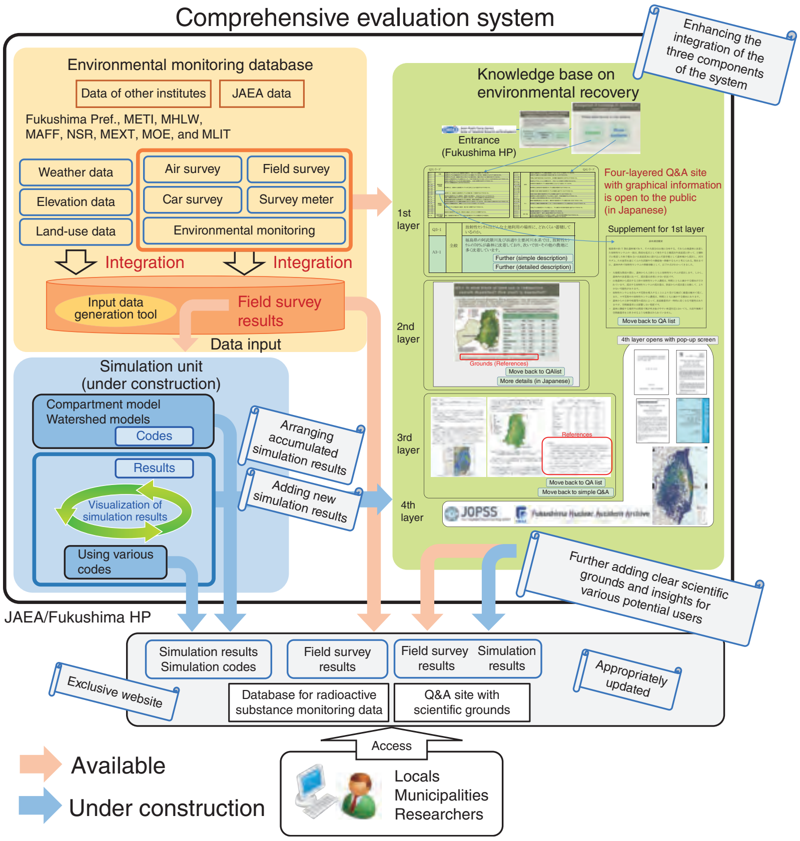

Fig.1-41 Concept of a comprehensive-evaluation system
The comprehensive-evaluation system consists of three components; an environmental-monitoring database, a simulation unit, and a knowledge base on environmental recovery.

Even now, radionuclides dispersed in the Fukushima environment by the accident at the TEPCO's Fukushima Daiichi NPS largely remain in forests. Over time, these radionuclides can pass out to the ocean and living environments under the action of wind and water flows. People are concerned with the potential risks that this poses to health and daily life.

In order to understand this issue in its entirety, evaluate its effects, and decide on countermeasures, JAEA and other research institutes have been conducting environmental monitoring since the accident. However, the findings of their studies are dispersed between various web pages, reports, research papers, pamphlets, and so forth. Therefore, it takes a great deal of time and effort for residents and local municipalities to gather all necessary information on the subject. We have gathered scientific findings on the migration of radioactive cesium and the recovery of the environment in Fukushima from various institutes. We have combined these with our own findings, and created a system to allow users to search easily for all relevant information. We are now enhancing this system so that evaluation of the environmental dynamics of radioactive cesium is possible. The system is called a comprehensive evaluation system (Fig.1-41).

The research results are arranged in a common format in the environmental-monitoring database. Visualization of the results is possible in this system. The system allows users to find various information on environmental-radiocesium dynamics with the description level matched to their needs (the knowledge base on environmental recovery), without referring to other media. For users who wish to know more details, the simulation unit gives access to simulation results on the transport of radioactivity in the environment, with land-use, topography, soil type, vegetation type, and initial radiocesium-deposition amounts taken into account. In addition, the various results have been summarized in an easy-to-understand Q&A format in the knowledge base on environmental recovery. Thus, the system provides information according to the needs of individual users.

It is recognized that understanding the re-circulation of radioactive cesium in forest environments and the sources of dissolved cesium discharged into rivers are important issues. We are therefore advancing research in these areas in response to concerns amongst local inhabitants. We will continue to update the system in accordance with the release of new research findings.

References

Tsuruta, T., Kitamura, A. et al., Status of Study of Long-Term Assessment of Transport of Radioactive Contaminants in the Environment of Fukushima – As a Part of Dissemination of Evidence-Based Information –, JAEA-Review 2017-018, 2017, 86p. (in Japanese).

Saito, H., Kitamura, A. et al., Comprehensive Evaluation System for Environmental Remediation of Fukushima – Toward Integration of Three Components as a Whole System –, JAEA-Review 2017-040, 2018, 34p. (in Japanese).

2

Nuclear Safety Research

Implementing Continuous Improvements in Safety

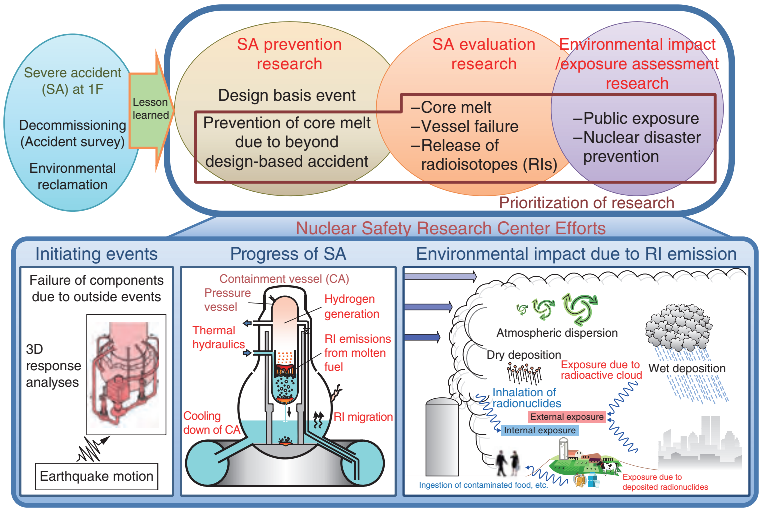

Fig.2-1 Directions of research at the Nuclear Safety Research Center
In accordance with the lessons learned from the accident at 1F, we have promoted studies on severe-accident prevention efforts and nuclear emergency-preparedness activities, such as environmental impact assessments and safety assessments for design basis events.

Basic design specifications

Maximum service pressure	1.5 MPa
Maximum temperature of injection gas	973 K
Test vessel height	11.2 m
Test vessel diameter	2.5 m
Equipment of pool and jacket for cooling	
Detailed instrumentation for temperature and concentration distribution	

Fig.2-2 Outline of the large-scale containment vessel test facility (CIGMA)
The CIGMA facility is designed to be able to simulate the behaviors of steam and hydrogen gas as well as having several measures for mitigating accidents.

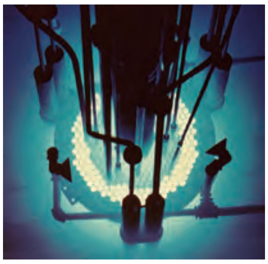

Fig.2-3 Nuclear safety research reactor (NSRR)
The experiment that simulates a rapid power increase during a reactivity-initiated accident can be safely performed.

The Nuclear Safety Research Center (NSRC) performs advanced safety research to provide a technical basis for nuclear regulatory authorities in terms of nuclear safety assessment. It also offers a long-term viewpoint through calculations, experiments, and measurement techniques. Through such research, we contribute to the development of safety criteria and support the creation of safety regulations with continuous improvement aimed at the highest level of safety.

We reviewed our previous research on design-based events prior to the accident at the TEPCO's Fukushima Daiichi NPS (1F). This was done in accordance with the lessons learned from the disaster, as shown in Fig.2-1. To reduce the risks associated with operating nuclear facilities, we have expanded the research on prevention and mitigation during the progression of severe accidents (SA), in preparation for and in response to emergency situations, on the consequences of radiation and the management of radioactive waste, and on the nuclear criticality safety assessment of fuel debris related to the 1F accident.

With regard to SA research, we intend to clarify the thermal-hydraulic phenomena that occur during SAs and develop effective measures to mitigate them. Therefore, we have conducted experiments at a large-scale containment vessel test facility called the Containment InteGral Measurement Apparatus (CIGMA), as shown in Fig.2-2. The experiments have focused on gas phase behaviors at high temperatures and the thermal-hydraulic behaviors of mixed gas, including hydrogen, which can cause containment vessel damage. With a view to upgrading SA evaluation methods, we intended to improve the accuracy of analyses using the computer codes for SA, employing knowledge obtained from the benchmark exercise on the 1F accident conducted by the OECD/NEA international cooperative project. By using the nuclear safety research reactor (NSRR) shown in Fig.2-3, we performed research that focused on the fuel failure limit, the effect of a fuel failure on the reactor during a reactivity-initiated accident, i.e., one of the design basis accidents for the safety evaluation of a nuclear reactor, and so on.

Moreover, we developed aircraft monitoring techniques using a manned helicopter to investigate the distribution of radionuclides in the atmosphere around 1F following the accident. We also performed background monitoring around the Kyushu Electric Power Company's Sendai NPS in response to emergency situations, according to the basic disaster management plan. In addition, a study on the ultra-trace analysis of nuclear materials for nuclear safeguards was conducted using a clean room facility.

This chapter presents the results of recent research on topics that include an investigation on post-boiling transition heat transfer in order to make models and validate thermal hydraulic codes (Topic 2-1), the influence of the air fraction in steam on the growth of the columnar oxide and α-Zr(O) layers (Topic 2-2), source term analysis considering the eutectic interaction of boron carbide with steel and oxidation during severe accidents (Topic 2-3), the development of a model for calculating the dose reduction effects of vehicles (Topic 2-4), the migration behavior of radioactive materials under boiling and drying accidents of high-level liquid waste (Topic 2-5), and the measurement of chemical states and isotope ratios in individual uranium particles using micro-Raman spectroscopy and other techniques (Topic 2-6).

Moreover, two topics related to the development of a topographical source model for air dose rate conversions in aerial radiation monitoring (Topic 1-11) and a simulation of the effect for reducing air dose rates by forest decontamination (Topic 1-16) are described in Chapter 1.

2–1 Prediction of the Cooling Capability of a Superheated Reactor Core

— Experiments for Modeling Post-Boiling Transition Heat Transfer —

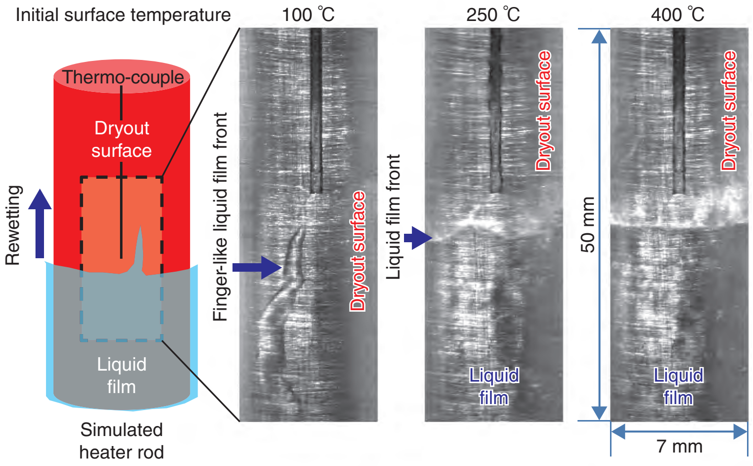

Fig.2-4 Visualization of liquid film front at rewetting
Visualized image of liquid film front obtained by high-speed camera with varying initial surface temperature. The liquid film front shape was finger-like when the initial surface temperature was relatively low, and it became almost uniform in the circumferential direction with an increase in the initial surface temperature. At high temperatures, many droplets dispersed from the liquid film front.

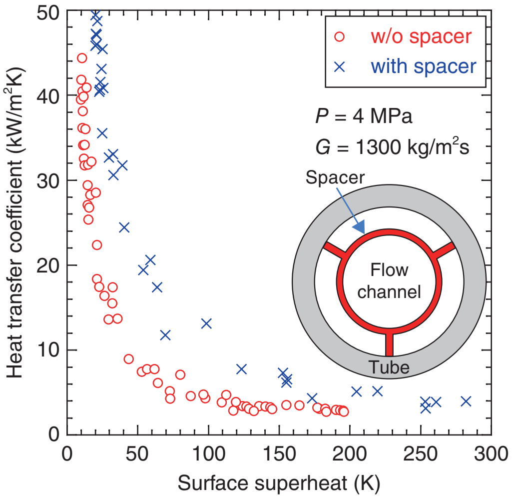

Fig.2-5 Spacer effect on heat transfer coefficient
Heat transfer coefficient on the dryout surface of a simulated fuel rod at a pressure of 4 MPa and mass flux of 1300 kg/m^{2}s. In the case where the tube was equipped with a spacer, the heat transfer coefficient increased over the entire temperature range.

If the core power abruptly increases for some reason in a light water reactor (LWR), there is a possibility that the surface of the fuel cladding will dry out. The increase of surface temperature caused by dryout should be suppressed to ensure fuel integrity. In the post-boiling transition (post-BT) standard of the Atomic Energy Society of Japan, the cladding temperature and dryout duration of fuel rods are used to evaluate the integrity of the dryout fuel. This standard was made on the basis of empirical correlations of the post-BT heat transfer to consider an anticipated operational occurrence (AOO). However, the new regulation established by the Nuclear Regulation Authority of Japan after the TEPCO's Fukushima Daiichi NPP accident requires a consideration for an anticipated transient without scram (ATWS), which is a more severe thermal-hydraulic condition than an AOO. The ATWS condition is characterized by high pressure, high mass flux, and high heat flux, and there has not been sufficient experimental research under such conditions. Because the ATWS condition can deviate from the applicable range of the correlations, new correlations need to be developed. For this purpose, we are conducting experimental research with use of various types of test sections from atmospheric pressure to high pressure, simulating an actual plant condition. The atmospheric pressure apparatus had a visualization test section to gain an understanding of the dominant factor of the phenomena. The facility was used in the high-pressure condition for experiments to obtain validation data for a semi-mechanistic model.

The visualization experiments aimed to determine the mechanism of rewetting, which is the re-establishment of solid–liquid contact on a dryout cladding surface by liquid film propagation. The rewetting velocity is the factor that determines the termination time of the dryout, and its prediction is much important for evaluating the cladding temperature and the duration of the dryout. The experimental apparatus could visualize the liquid film front in detail. Fig.2-4 shows the visualization image of the liquid film front obtained by a high-speed camera. It can be seen in this figure that the front shape was finger-like when the initial surface temperature was relatively low, and it became substantially uniform in the circumferential direction with an increase in the initial surface temperature. From these results, we elucidated that the film front shape and number of droplets dispersed at the film front varied depending on the initial surface temperature and the liquid–gas relative velocities. These phenomena could be significant factors that govern the rewetting velocity.

In high-pressure experiments, we investigated the spacer effect on heat transfer in the flow of a circular pipe. A fuel bundle of the LWR was equipped with spacers to maintain the gap space among fuel rods. Under the high mass flux and high heat flux condition during the ATWS, the existence of spacers was considered to strongly affect the post-BT heat transfer. Fig.2-5 shows the measured heat transfer coefficient on the dryout surface of the circular pipe. In the case that the pipe was equipped with a spacer simulating the ferrule spacer of a boiling water reactor, the heat transfer coefficient increased over the entire temperature range. The enhancement of heat transfer was caused by a phenomenon in which the steam flow including droplets (annular dispersed flow) was disturbed around the spacer and the disturbance increased the droplet deposition onto the dryout surface. From the results of the experiments under various pressure and mass flux conditions, it was clarified that the spacer effect was more significant under a relatively low-pressure and high-mass-flux condition.

Based on the above knowledge, we are developing a model that can precisely predict the post-BT heat transfer.

The present study was sponsored by the Secretariat of Nuclear Regulation Authority (NRA), Japan.

Reference

Satou, A. et al., Experimental Investigation of Post–BT Heat Transfer and Rewetting Phenomena, Proceedings of ANS International Conference on Best Estimate Plus Uncertainties Methods (BEPU 2018), Lucca, Italy, 2018, BEPU2018–270, 12p., in USB Flash Drive.

2–2 Evaluation of Fuel Integrity during Loss-of-Coolant Accidents

— Influence of Air Fraction in Steam during High-Temperature Oxidation of Fuel Cladding —

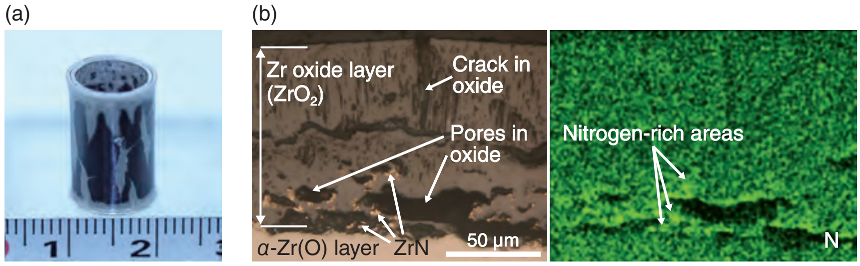

Fuel cladding

Optical micrograph

EDS mapping result of nitrogen

Fig.2-6 (a) Appearance and (b) optical micrograph (left side) and EDS mapping result of nitrogen (right side) of a cross-section of the specimen exposed to steam with a 70% air fraction at 1273 K for 2400 s
Zirconium nitrides (ZrN) and large pores can be observed near the interface between the oxide and *α*-Zr(O) layers.

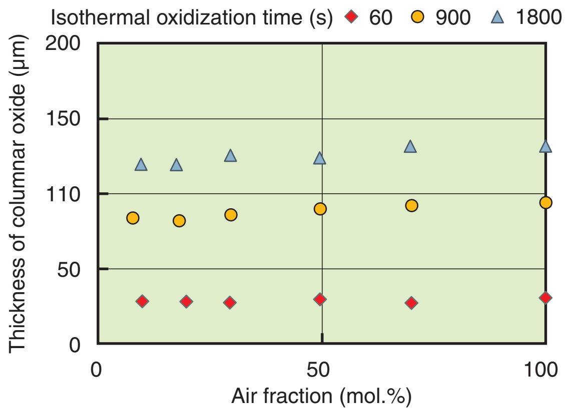

Fig.2-7 Dependence of the thickness of columnar oxide on the air fraction in steam at 1473 K
The thicknesses of the columnar oxide increases with the increasing air fraction in steam, irrespective of exposure time.

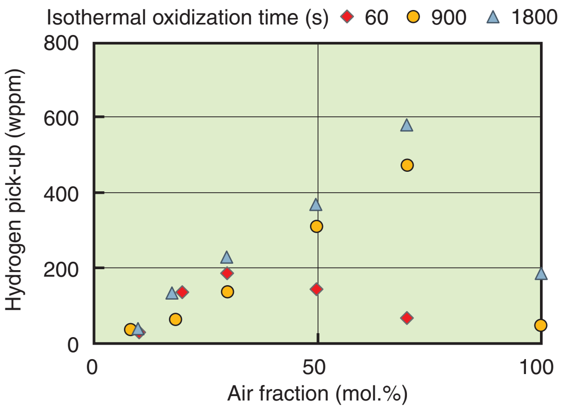

Fig.2-8 Dependence of hydrogen pick-up in the fuel cladding on the air fraction in steam at 1473 K
The amount of hydrogen pick-up increases with the increasing air fraction in steam. The steep decrease observed in the higher air fraction region is due to the lower partial pressures of steam.

The generation of heat and hydrogen from nuclear fuel during an accident is strongly affected by the atmosphere surrounding the fuel cladding. Whereas many data have been obtained regarding the behavior and rate of fuel cladding oxidation in high-temperature steam, there has been little knowledge gained in terms of the oxidation behavior under mixed steam-air conditions. In this study, the oxidation behavior of fuel cladding was investigated by heating it under mixed steam-air conditions at temperatures corresponding to loss-of-coolant accidents (LOCA) in the spent fuel pool and reactor core. Air can ingress the spent fuel pool and also the reactor core if emergency core-cooling systems fail during the postulated LOCA, resulting in a severe accident.

Current fuel cladding consists of a zirconium (Zr)-based alloy, and an oxide layer forms on its surface in a high-temperature oxidative atmosphere. An increase in the thickness of this oxide layer, however, may lead to cladding embrittlement and the subsequent fracture of fuel rods in the reactor core. On the other hand, it has been pointed out that nitrogen in the surrounding atmosphere could enhance the oxidation of Zr through nitride formation. In addition, hydrogen is generated during the steam oxidation of Zr at high temperatures. A part of this hydrogen would be absorbed into the metallic part of the oxidized fuel cladding, which would accelerate cladding embrittlement. The oxide layer formation and the acceleration of oxidation and hydrogen absorption into the metallic part by nitrogen would affect the integrity of the fuel rods.

In this study, we investigated the influence of the air fraction in steam on hydrogen absorption and the growth of columnar oxide at 1273 K and 1473 K, subjected to non-irradiated Zry-4 tube cladding. From the results of this study, it was found that the oxidation of the fuel cladding was accelerated by nitride formation near the interface between the oxide layer and metallic part, which is shown in Fig.2-6, and also by the effect of the air fraction in steam on the growth of columnar oxide, which is shown in Fig.2-7.

The amount of hydrogen absorbed into the fuel cladding during high-temperature oxidation is shown in Fig.2-8. It was found that hydrogen absorption was accelerated by an increase of the air fraction in steam. This is because the porosity of the oxide layer increased owing to nitride formation, and the hydrogen that was generated by the oxidation reaction could easily reach the metallic part. On the other hand, the amount of hydrogen absorption decreased in the higher air fraction region owing to the lower partial pressure of steam in the atmosphere, which generated a smaller amount of hydrogen.

We clarified the oxidation mechanism of fuel cladding in an atmosphere with a steam-air mixture at high temperatures.

Reference

Negyesi, M. et al., The Influence of the Air Fraction in Steam on the Growth of the Columnar Oxide and the Adjacent α–Zr(O) Layer on Zry–4 Fuel Cladding at 1273 and 1473 K, Annals of Nuclear Energy, vol.114, 2018, p.52–65.

2–3 Evaluation of the Environmental Release of Radionuclide Material in a SA

— Accident Analysis Considering Oxidation of BWR Control Material —

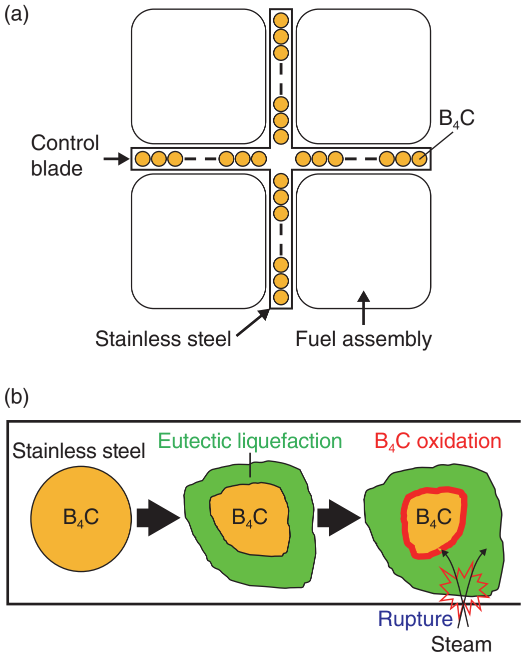

Fig.2-9 Melt progression of BWR control blade
(a) BWR control blade is made of boron carbide (B_4C) and stainless steel; (b) Oxidation of B_4C starts after the surrounding steel of the control blade is damaged by the progress of eutectic liquefaction.

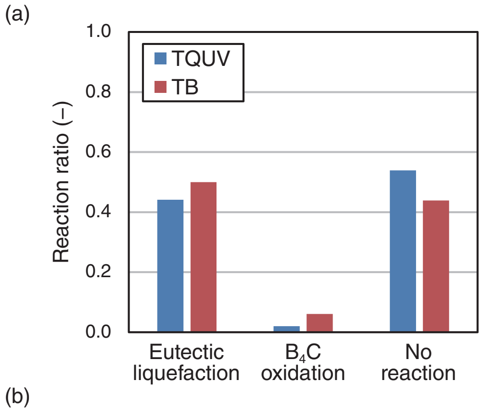

(b)

Product material by B_4C oxidation (mol)					
	B_2O_3	CO	CO_2	CH_4	H_2
TQUV[*1]	77.6	1.5	37.3	2.1×10^{-15}	331
TB[*2]	2140	273	797	2.0×10^{-13}	8353

[*1] TQUV : Accident of loss of core coolant injection
[*2] TB : Accident of station blackout

Fig.2-10 (a) Fraction of B_4C oxidation and (b) amount of products material
The models for B_4C/steel eutectic liquefaction and B_4C oxidation were developed and incorporated into the THALES2 code. In our analysis, core melt progression affected the behavior of B_4C oxidation. In particular, the fraction of B_4C oxidation was decreased in the TQUV sequence, in which the core damage progressed under the steam starvation condition.

For the purpose of obtaining technical knowledge to support nuclear safety regulations, research on source term evaluation, which focuses on the chemical reaction of fission products (FP) such as iodine and cesium, were carried out. Boron carbide (B_4C) was used as a neutron-absorbing material in a boiling water reactor (BWR) (Fig.2-9(a)), and boron species, which were produced from the reaction of B_4C oxidation, would affect the chemical reactions of FPs in the reactor coolant system (RCS) (Fig.2-9(b)). The interaction between the B_4C and the surrounding steel caused their liquefaction at a temperature lower than the melting point of either material. The reaction rate of B_4C oxidation was decreased by promoting eutectic liquefaction, which led to a decrease in the reaction area between the B_4C and steam. An integrated severe accident (SA) analysis code is needed to simulate these complex behaviors. The models for the eutectic interaction of B_4C with steel and B_4C oxidation were incorporated into the THALES2 code and applied to the source term analyses for a BWR with Mark-I-type containment. Two SA sequences with drywell failure by overpressure initiated by a loss of core coolant injection (TQUV sequence) and long-term station blackout (TB sequence) with and without a steam starvation condition in the core, respectively, were selected as representative accident sequences. Approximately half of the B_4C was predicted to melt in the analyses for the TQUV and TB sequences, as shown in Fig.2-10. On the other hand, a remarkable difference was found for the fraction of the B_4C oxidation between the two sequences. The B_4C oxidation was limited for the TQUV sequence under the steam starvation condition in the RCS due to the activation of reactor depressurization. Additionally, the oxidation of B_4C leads to the production of carbon dioxide (CO_2), which could greatly influence the pH of the water pool in the containment and the subsequent formation of volatile iodine species. Further studies are necessary for the FP chemistry in the RCS, taking into account the influence on pH variation and iodine chemistry in the water pool, to improve the predictability of the source term.

Reference

Ishikawa, J. et al., Source Term Analysis Considering B_4C/Steel Interaction and Oxidation during Severe Accidents, Proceedings of the 25th International Conference on Nuclear Engineering (ICONE25), Shanghai, China, 2017, ICONE25–67858, 7p.

2–4 Evaluating Radiation Exposure Difference Inside and Outside a Vehicle

— Development of a Vehicle Model for Radiation Transport Simulation and Its Application —

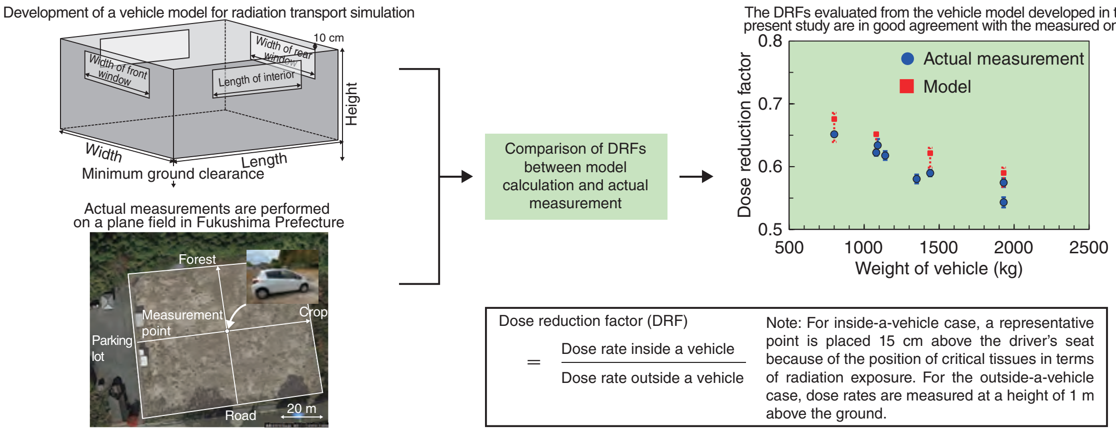

Dose reduction factor (DRF)

$$= \frac{\text{Dose rate inside a vehicle}}{\text{Dose rate outside a vehicle}}$$

Note: For inside-a-vehicle case, a representative point is placed 15 cm above the driver's seat because of the position of critical tissues in terms of radiation exposure. For the outside-a-vehicle case, dose rates are measured at a height of 1 m above the ground.

Fig.2-11 Development scheme of vehicle model for radiation transport simulation
We compared the DRFs, which were evaluated using the developed vehicle model with those obtained from the actual measurements. Consequently, it was confirmed that the DRFs evaluated from the vehicle model developed in the present study were in good agreement with the measured ones.

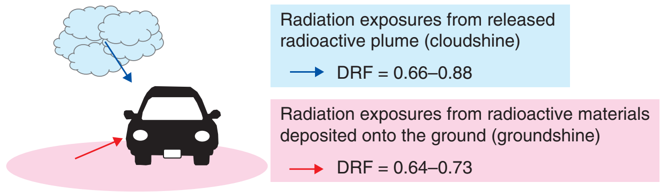

Radiation exposures from released radioactive plume (cloudshine)
→ DRF = 0.66–0.88

Radiation exposures from radioactive materials deposited onto the ground (groundshine)
→ DRF = 0.64–0.73

Fig.2-12 The DRFs for cloudshine and groundshine in a nuclear emergency
The DRFs were evaluated using the developed vehicle model. The DRFs varied with the weight of the vehicle and the photon energy of the cloudshine. We determined that the DRFs for cloudshine and groundshine were 10%–30% and 30%–40%, respectively.

Evacuation is one of the typical protective actions in a nuclear emergency. In Japan, in the response plans of local governments, private vehicles are widely used as a self-evacuation tool in a nuclear emergency. However, if the timing of evacuation is delayed or misjudged, evacuees cannot avoid passing through the radioactive plume or through areas contaminated by radionuclide deposits. Therefore, the potential doses from such exposure sources during evacuations have to be assessed and considered when optimizing the evacuation strategy in the case of a nuclear accident. However, a model for calculating the dose reduction factor (DRF) has not been developed up to now.

In the present study, we developed a vehicle model for calculating the DRF based on the actual shape and weight of Japanese vehicles:

$$M - M_0 = \rho \cdot d \cdot S$$

where M is the weight of the vehicle, M_0 is the weight of the ceiling and windows, ρ is the density of steel (7.8 g $\mathrm{cm^{-3}}$), d is the thickness of the vehicle model, and S is the surface area of the vehicle body, excluding the ceiling and windows. Here, the thickness of the ceiling of the vehicle body was assumed to be 0.08 cm based on information provided by a Japanese automaker.

To confirm the validity of this model, we performed actual measurements of radiation dose rates inside and outside the vehicles and evaluated the DRF of four types of vehicles in Japan. The measurements were performed on a plane field in Fukushima prefecture, in October 2015. Fig.2-11 shows a comparison of the DRFs from actual measurement versus the model calculations. As shown in this figure, the DRFs evaluated using the developed model had a similar tendency to the measured values. Consequently, it was confirmed that the DRFs evaluated from the vehicle model developed in the present study were in good agreement with the measured ones.

In addition, based on the developed vehicle model, we evaluated the DRFs for cloudshine and groundshine in the case of a nuclear accident. For groundshine, we used the photon energy values of 0.4, 1, and 1.5 MeV. Fig.2-12 shows the calculation results of the DRFs for cloudshine and groundshine. In the results, the DRFs depend on the photon energy and the weight of the vehicle. For cloudshine, the DRFs for the photon energies of 0.4, 1, and 1.5 MeV were 0.66–0.73, 0.78–0.85, and 0.82–0.88, respectively. For groundshine, the DRFs were 0.64–0.73.

However, it was noted that the effectiveness of an evacuation strategy could not be determined based only on the DRFs of the vehicles evaluated in this study. To make a more effective evacuation strategy, we have to consider not only the self-help behavior but also the combination of relevant protection actions. To achieve these aspects of optimization for an evacuation strategy, we must continue the optimization research on protective strategies for a nuclear emergency.

This work was sponsored by the Secretariat of the Nuclear Regulation Authority (NRA), Japan.

Reference
Takahara, S. et al., Dose–Reduction Effects of Vehicles Against Gamma Radiation in the Case of a Nuclear Accident, Health Physics, vol.114, no.1, 2018, p.64–72.

2–5 Evaluation of Confinement Performance at a Reprocessing Plant during Severe Accidents

— Experiment to Clarify the Migration/Deposition Behavior of Volatile Radioactive Ruthenium —

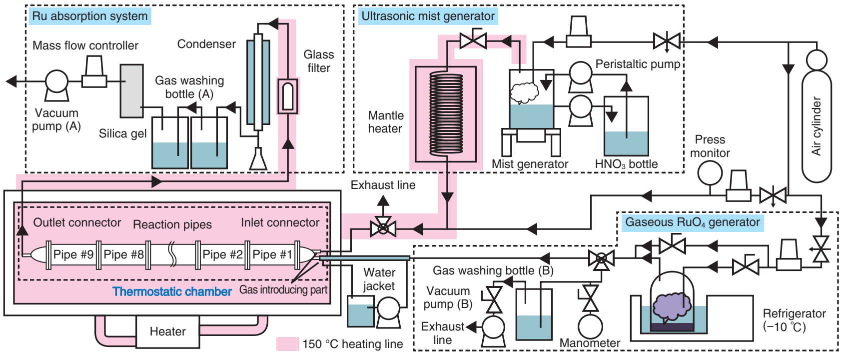

Fig.2-13 Schematic of experimental apparatus
This apparatus simulates the atmospheric conditions of the BDA. The migration behavior of Ru was evaluated by comparing the amount of Ru deposited in the glass pipes versus the Ru collected by the glass filter, and that absorbed in the condensate and gas absorbent.

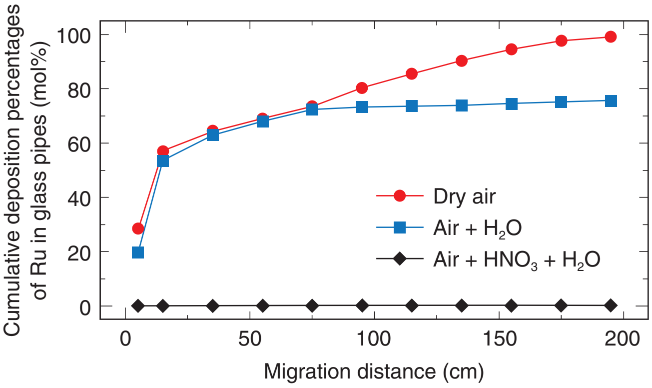

Fig.2-14 Comparison of cumulatively collected Ru under each atmospheric condition
In the experiment with dry air and water vapor, most of the gaseous Ru was decomposed and deposited on the glass pipes, whereas in the experiment with HNO_3 vapor, gaseous Ru passed through the glass pipes.

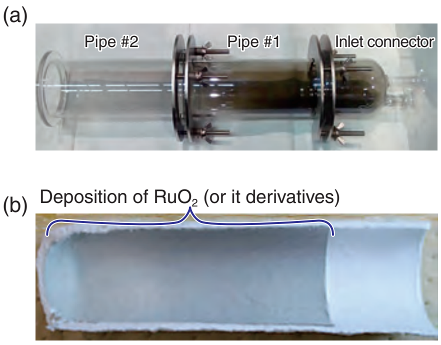

Fig.2-15 Photograph of deposited Ru on glass pipes and filter
In the experiment using dry air and water vapor, black deposits assumed to be the RuO_2 were observed in the glass pipes. In addition, Ru particles were collected in the glass filter in the experiment with water vapor.

To verify the safety of reprocessing plants (RP), it is important to evaluate severe accidents, which have a low frequency and large impact.

The high-level liquid waste (HLLW) in RPs is constantly cooled artificially because it is heated by the decay heat of the fission products. A shutdown of the cooling system from any cause may lead to the release of radioactive substances together with nitric acid and water vapor due to evaporation and the dryness of the HLLW. This accident, called a “boiling and drying accident” (BDA), is defined as one of the severe accident types in Japan’s nuclear safety standard for RPs.

Information on the behavior of radioactive substances in such an accident is essential to establish the management measures for a BDA. Ruthenium (Ru) is an important element from the viewpoint of public exposure assessment. It has higher radiotoxicity and a larger release fraction than other elements because it forms gaseous species such as ruthenium tetroxide (RuO_4).

We prepared an apparatus that partially simulated the volatilization and migration of the Ru in a BDA, and we conducted experiments to evaluate the interactions between gaseous Ru and coexisting gasses (Fig.2-13). Gaseous RuO_4 was supplied into glass pipes that simulated the migration pathway, and the migration behavior was evaluated from the deposition distribution of Ru in the apparatus. Experiments with dry air and water vapor were conducted as control experiments. Then, an experiment with HNO_3 + water vapor was conducted to simulate the atmospheric conditions of a BDA.

Fig.2-14 shows the cumulative deposition percentages of Ru in the glass pipes. Fig.2-15 shows photographs of the Ru deposition on the glass pipes for the dry air condition and in the glass filter after the experiment for the water vapor condition. Almost all of the supplied gaseous Ru was decomposed and deposited in the glass pipes in the dry air atmospheric condition. In the experiment for the water vapor condition, most of the Ru was deposited. However, approximately 30% of the supplied Ru was trapped in the glass filter. This result indicates that Ru aerosols were formed in the glass pipes. On the other hand, no deposition of Ru was observed for the HNO_3 + water vapor atmospheric condition. This result meant that HNO_3 vapor would have the effect of stabilizing gaseous Ru.

These results could to contribute to the improvement of accident management measures and safety assessment of a BDA.

Reference

Yoshida, N. et al., Migration Behavior of Gaseous Ruthenium Tetroxide under Boiling and Drying Accident Condition in Reprocessing Plant, Journal of Nuclear Science and Technology, vol.55, issue 6, 2018, p.599–604.

2–6 Deducing the Origin of Nuclear Materials by Analyzing Uranium Particles in Environmental Samples

— Determination of Chemical Forms and Isotope Ratios in Individual Uranium Particles for Nuclear Safeguards —

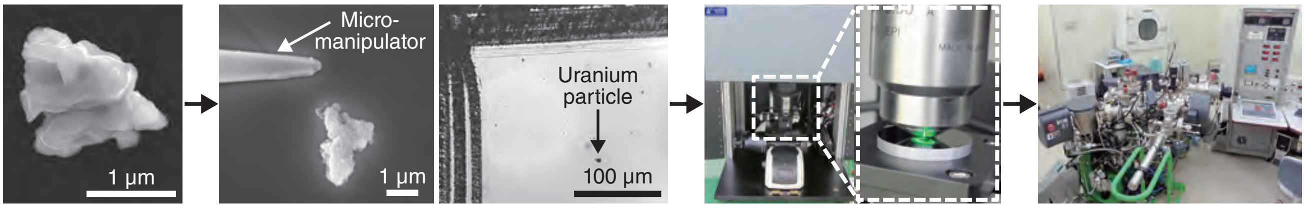

Uranium particle — Transfer onto another substrate — Micro-Raman spectroscopy Chemical form analysis — Secondary ion mass spectroscopy Isotope ratio analysis

Fig.2-16 Analytical flow for individual uranium particles
A novel technique for the analysis of individual uranium particles of micrometer size was developed using a combination of micro-Raman spectroscopy and secondary ion mass spectrometry.

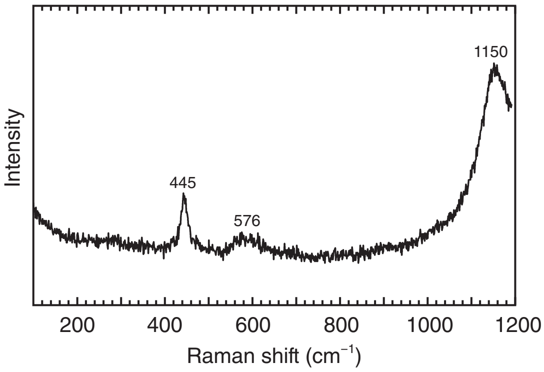

Fig.2-17 Raman spectrum of a uranium dioxide particle
Several Raman peaks assigned to the UO_2 structure were detected.

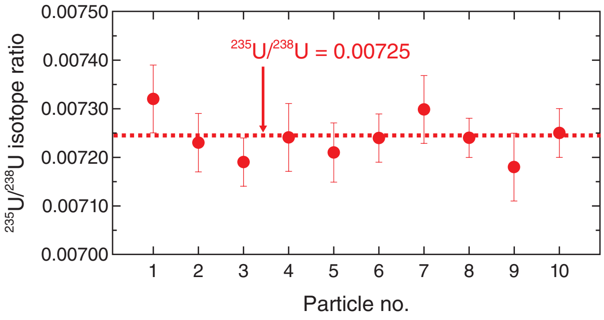

Fig.2-18 $^{235}U/^{238}U$ isotope ratios measured for individual uranium particles
The $^{235}U/^{238}U$ isotope ratios determined with the proposed method were consistent with that of natural uranium (indicated by a broken line).

Naturally occurring uranium consists of ^{234}U, ^{235}U, and ^{238}U isotopes. The uranium isotope ^{235}U is enriched to extract nuclear power effectively because it is the only fissile isotope of natural uranium. The abundance of ^{235}U is 0.72 % for natural uranium, 2 %–5 % for nuclear fuels for nuclear power plants, and over 90 % for the raw material for nuclear weapons. We routinely measure uranium isotope ratios in environmental samples, which are collected by International Atomic Energy Agency (IAEA) inspectors at nuclear facilities all over the world, to detect undeclared nuclear activities related to the production of nuclear weapons.

The nuclear fuel cycle is the progression of nuclear fuel through a series of processes. Various uranium compounds are used in the refining, conversion, enrichment, and fabrication processes, including triuranium octoxide in the refining process and uranium dioxide (UO_2) in the fabrication process. Investigation of the chemical states and isotope ratios of uranium particles may provide information on the origin of materials. However, there are few reports on the analytical techniques for obtaining both the chemical states and isotope ratios of individual uranium particles.

In this study, we developed a novel analytical procedure using micro-Raman spectroscopy (MRS) and secondary ion mass spectrometry (SIMS), as shown in Fig.2-16. Uranium particles on a substrate were identified by scanning electron microscopy and then transferred onto another substrate using a micro-manipulator. The chemical forms of uranium particles were analyzed by MRS, and the isotope ratios of the particles were determined by SIMS.

Fig.2-17 shows the Raman spectrum of a UO_2 particle in a natural uranium material. Characteristic Raman bands were observed at 445 cm^{-1}, 576 cm^{-1}, and 1150 cm^{-1}, which are the values assigned to the UO_2 structure. The uranium isotope ratios of individual UO_2 particles were determined by SIMS after the MRS measurement. Fig.2-18 shows the isotope ratios of ten individual UO_2 particles. The $^{235}U/^{238}U$ isotope ratios were highly consistent with that of natural uranium. We confirmed that the chemical states and isotope ratios of individual uranium particles could be analyzed by this proposed method.

The present study was sponsored by the Secretariat of the Nuclear Regulation Authority (NRA), Japan.

Reference

Yomogida, T. et al., Chemical State and Isotope Ratio Analysis of Individual Uranium Particles by a Combination of Micro–Raman Spectroscopy and Secondary Ion Mass Spectrometry, Analytical Methods, vol.9, issue 44, 2017, p.6261–6266.

3 Advanced Scientific Research

Advanced Science Pioneers the Future

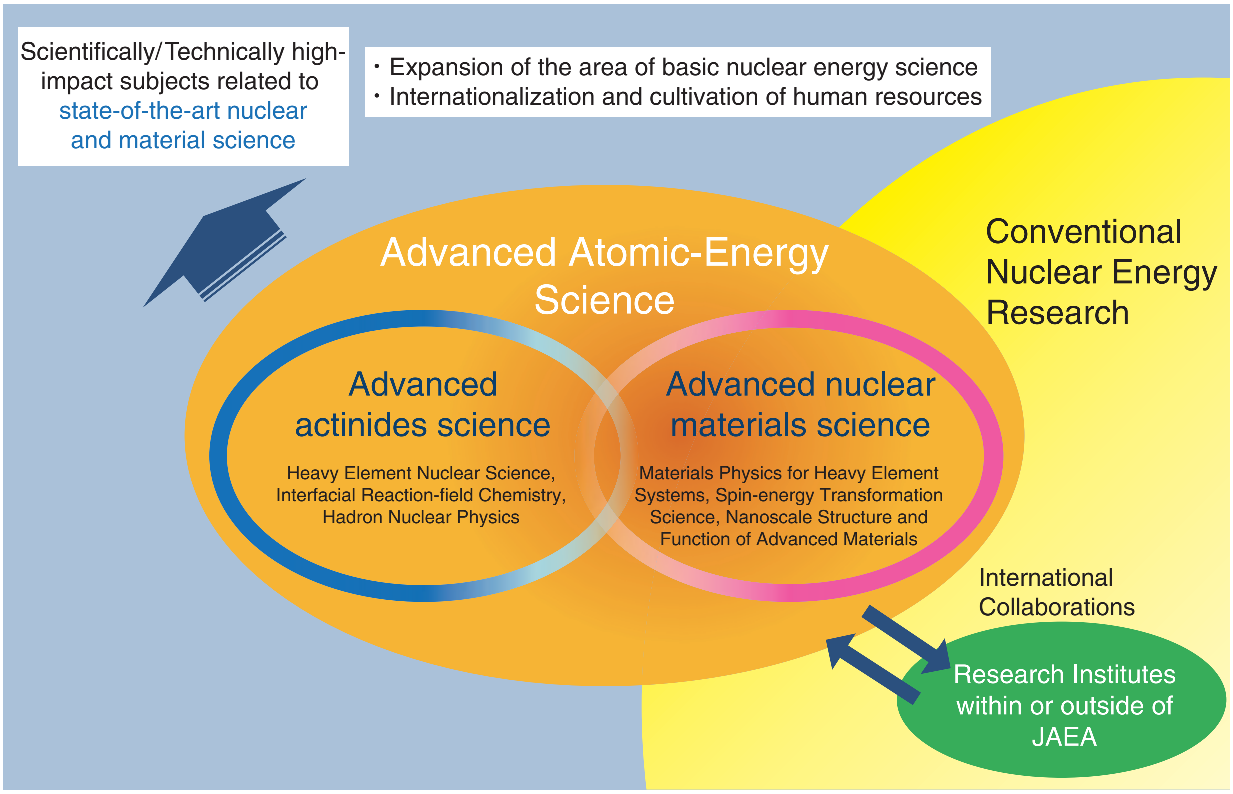

Fig.3-1 The role of advanced nuclear scientific research
In this study, we aim to perform high-impact scientific and technical studies related to state-of-the-art nuclear and material science.

A greater part of nuclear-energy-related technology is grounded on basic science. Besides seeking solutions to today's energy problems, future research must respond to the new stage of nuclear-energy development expected in the next few decades.

The Advanced Science Research Center (ASRC) explores the unlimited possibility of nuclear energy from the perspective of basic science. During this process, we aim to establish new research fields and further develop the existing science and technology.

We started our mid-term plan in FY2015, focusing on two main areas: advanced actinides science and advanced nuclear materials science. The former aims to conceptualize nuclear and heavy-element-based actinide science in a new way. In the latter research, we are investigating and developing new materials for nuclear-energy purposes. Through interactions between the two areas and collaboration with research institutes within and outside of JAEA, we are cultivating new fields of nuclear-energy science (Fig.3-1).

We have made numerous highlighted achievements during FY2017. Through our advanced actinides science, we elucidated the role of multi-chance fission at high energies in fission-fragment mass distributions measured in the JAEA tandem accelerator (Topic 3-1). This technique is expected to reduce nuclear waste by nuclear transmutation. In our biochemical research, we found an interesting relation between a novel complexation and the sorption of heavy elements on *Paramecium* cells (Topic 3-2). At J-PARC, we precisely measured new γ rays from a hypernucleus of fluorine (Topic 3-3). Hypernuclei measurements can uniquely probe the structures of nuclear matter, particularly those of neutron stars.

Substantial results have also been obtained by advanced nuclear materials science. A new electronic state was revealed by high-resolution nuclear magnetic resonance measurements at cryogenic temperatures (Topic 3-4). This result will likely provide guidelines for exploring practical superconductors. By investigating a special relativistic effect in materials (the so-called Rashba effect), we found that the magnetism direction in a special class of antiferromagnets differs between the inside and the surface of the sample. This property is potentially exploitable as a magnetic-anisotropy control of magnetic materials (Topic 3-5). Finally, in a neutron scattering experiment, we monitored the spin current in an insulator by measuring the magnon density of states (Topic 3-6).

The ASRC considers that developing human nuclear resources with expertise and demonstrating their total abilities via basic nuclear research are vital.

3–1 Capturing Various Nuclear Splits in Fission

— Toward the Reduction of Radiotoxicity of Nuclear Waste —

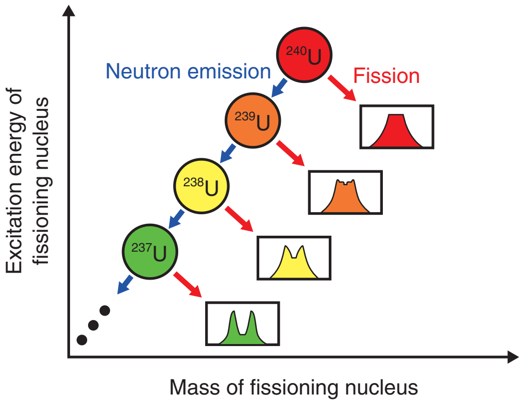

Fig.3-2 Competition between fission and neutron emission
A highly excited ^{240}U either decays via fission or produces a lower-excited ^{239}U via neutron emission. These competing processes continue until the excitation energy of the compound nucleus becomes sufficiently low. The observables in high-energy fission experiments are contributed by many nuclides that cannot be individually distinguished, which confuses the study of high-energy fission.

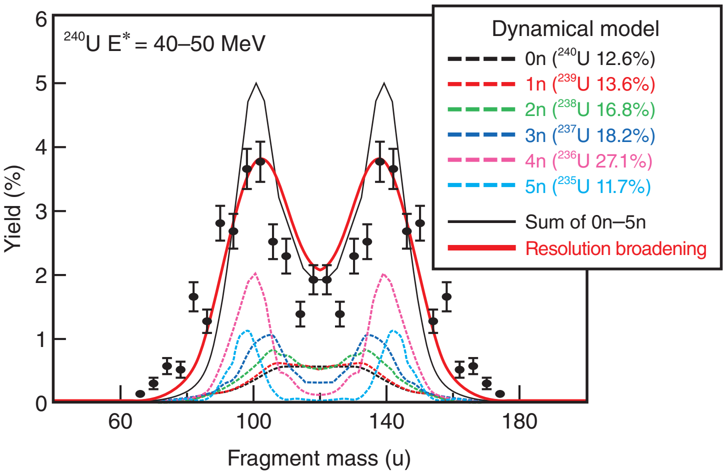

Fig.3-3 Nuclear splits in high-energy fission
The black plots show the observed nuclear splitting when a ^{240}U nucleus is produced in the excitation energy range of E* = 40–50 MeV. The spectrum is contributed by six $^{235\text{-}240}$U nuclides produced by the emissions of 0–5 neutrons (dashed lines). These calculated fission fragment mass distributions (FFMDs) sum to the red curve, which well reproduces the experimental result.

The management of radioactive wastes, such as transuranium accumulating in light water reactors, is among the most urgent issues in the use of nuclear power. Some of these nuclides survive irradiation with thermal neutrons in the light water reactor but can decay via fission when bombarded with higher-energy neutrons. Under this circumstance, a fissioning nucleus has a higher excitation energy compared with a fissioning nucleus in a light water reactor. To develop a fission-based nuclear transmutation technology, fission at high excitation energies must be clearly understood.

Nuclear fission is a process of a nucleus deforming gradually and finally splits into two lighter nuclei. This process can be investigated by observing the mass balance between the two daughter fragments, the so-called fission fragment mass distribution (FFMD). However, observing the FFMDs of highly excited nuclei has been prevented by an experimental difficulty, as described later. Thus, the fission mechanism at high energies remains poorly understood.

Herein, we produced a multitude of nuclides from the ^{18}O + ^{238}U reaction at the JAEA tandem accelerator facility and obtained their FFMDs over a wide range of excitation energies. A nucleus with a high excitation energy decays either by fission or by neutron emission. The latter creates a different nucleus with a lower excitation energy than the initial nucleus. Fig.3-2 demonstrates the competition between fission and neutron emission for the initial ^{240}U nucleus produced with a high excitation energy. The experimentally observed FFMDs are contributed not only by the ^{240}U nucleus but also by lower-excited $^{239, 238, 237,...}$U nuclei. The contributions from each nuclide cannot be separated, leading to the aforementioned experimental difficulty.

In this study, we separated these contributions by combining a dynamical fission model with the neutron emission before fission. Fig.3-3 presents an example of the obtained results. The closed circles plot the FFMD of the initial highly excited nucleus ^{240}U. As shown by the dashed curve, this FFMD comprised the FFMDs of six nuclides. We present the first *pure* FFMD at high excitation energies, i.e., the FFMD of ^{240}U (black dashed curve in Fig.3-3), which will promote high-energy fission research. To further understand the fission mechanism, we are planning to conduct measurements of prompt fission neutrons together with FFMDs. Such studies will help the evaluation of as-yet unmeasured nuclear data and the development of fission-based nuclear transmutation technology.

This study was supported by “Comprehensive study of delayed neutron yields for accurate evaluation of kinetics of high burn-up reactors” and “Development of prompt-neutron measurement in fission by surrogate reaction method and evaluation of neutron-energy spectra” by the Ministry of Education, Culture, Sports, Science and Technology (MEXT), Japan.

Reference

Hirose, K. et al., Role of Multichance Fission in the Description of Fission-Fragment Mass Distributions at High Energies, Physical Review Letters, vol.119, issue 22, 2017, p.222501-1–222501-6.

3–2 Protection from Metal Toxicity by a Protein?

— Binding of Heavy Elements to Soluble Glycoprotein on the *Paramecium* Cell Surface —

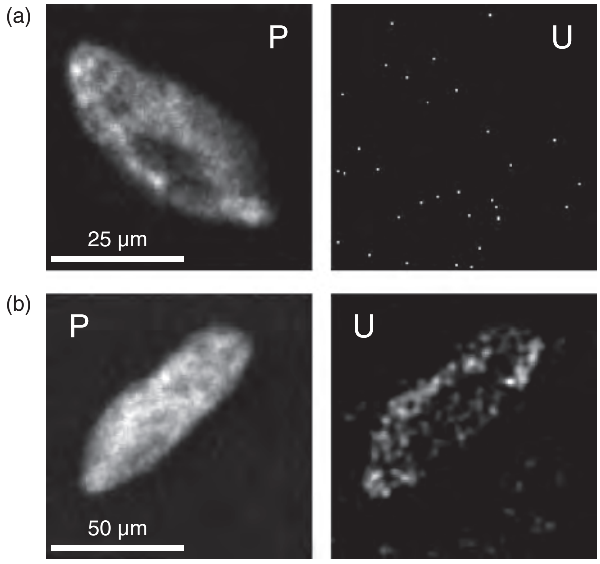

Fig.3-4 Adsorption of uranium on *Paramecium* cells
(a) Upper side figures are living cells. (b) Lower side figures are prekilled cells. *Paramecium* cells were exposed to aqueous uranium solutions, and the elemental distribution on the cells was measured via a non-destructive elemental analytical method, micro-PIXE. *Paramecium* cells were depicted using phosphorous, which is a major elemental component of cells.

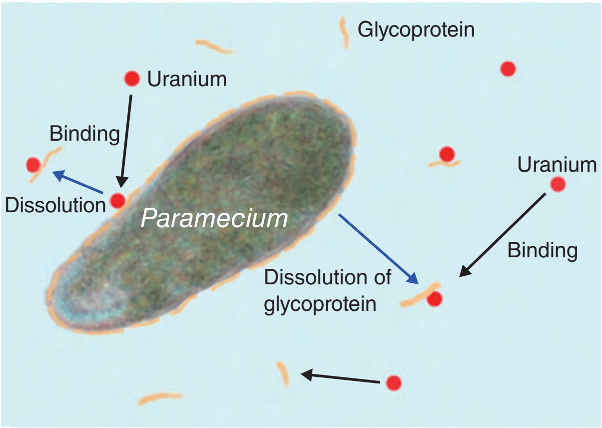

Fig.3-5 Binding of uranium to soluble surface glycoprotein of *Paramecium* cells
Uranium adsorption on living *Paramecium* cells might decrease via one or both of the two mechanisms: (1) when uranium binds to the surface glycoprotein, the uranium-bearing glycoprotein is subsequently dissolved, or (2) uranium binds to the dissolved glycoprotein.

The migration of metal elements (including radionuclides) through geological and aquatic environments is presumably influenced by the biological functions of bacteria, such as adsorption on cell surfaces, phosphate mineralization, reduction, and oxidation. Environmental bacteria lie at the bottom of the ecological pyramid (food chain) in environments co-inhabited by themselves and larger creatures. Bacteria are consumed by protozoa (e.g. paramecia, ameba, and euglena), single-celled microorganisms with lengths of tens to several hundreds of micrometers. These tiny organisms control the bacterial populations. However, the roles of protozoa on the environmental migration of metal elements have not been previously investigated. To elucidate these roles, this study investigates the interaction between a representative freshwater protozoan (*Paramecium* sp.) and a metallic element (uranium).

Paramecium cells were exposed to aqueous uranium solutions in the laboratory. Uranium adsorbed on living cells was hardly detected using an element analytical device but was clearly detected on dead cells analyzed via micro-particle induced X-ray emission (micro-PIXE). Here, the *Paramecium* cells were killed using chemicals (fixatives) before running the experiment (Fig.3-4). After the experiment, we probed the cause of this large difference by analyzing the liquid phase. We found that a fraction of the uranium was bound to an organic substance released from living *Paramecium* cells. This organic substance was a large soluble glycoprotein with an approximate molecular size of 250 kDa.

The characteristics of the organic substance accorded with those of the glycoprotein covering the entire cell surface of *Paramecium*. This finding strongly suggests that dissolution of the uranium-biding glycoprotein from the living cell surface reduced the level of the adsorbed uranium to below the detection limit of the micro-PIXE instrument (Fig.3-5). Meanwhile, the uranium on the prekilled cells remained because the surface glycoprotein was chemically fixed to the cells.

Paramecium is sensitive to and poorly resistant to metal elements. Although the role of glycoprotein on the *Paramecium* cell surface is only partially understood, it may protect the cell surface from metal toxicity.

This work was supported by the Japan Society for the Promotion of Science (JSPS) KAKENHI Grant-in-Aid for Scientific Research (C) (No.25420910).

Reference

Kozai, N. et al., Complexation of Eu(III), Pb(II), and U(VI) with a *Paramecium* Glycoprotein: Microbial Transformation of Heavy Elements in the Aquatic Environment, Chemosphere, vol.196, 2018, p.135–144.

3–3 Seeing Hypernuclei by γ rays

— Can Hidden “Strangeness” in Neutron Stars Be Disclosed? —

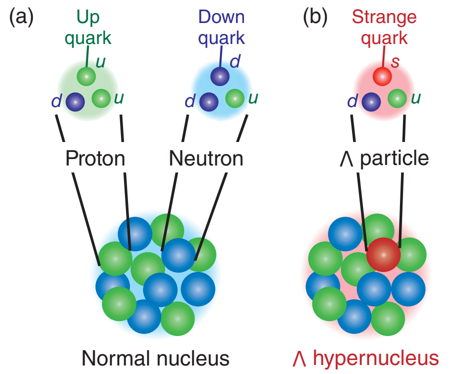

Fig.3-6 Normal nucleus and hypernucleus
(a) Normal nucleus composed of protons and neutrons only. (b) In hypernucleus, a Λ particle is added.

K1.8 beamline + SKS + Hyperball-J + Liquid carbon-tetrafluoride (CF_4) target
Data obtained in June 2015
J-PARC Hadron Experimental Facility

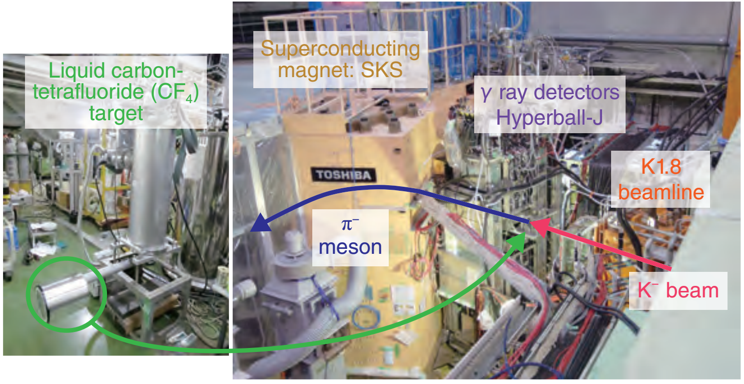

Fig.3-7 Experimental setup
Hypernucleus is produced by a reaction of K^- beam provided from J-PARC with the carbon-tetrafluoride (CF_4) target. At the same time, γ-rays emitted from the hypernucleus is detected by the γ-ray detectors (Hyperball-J) surrounding the target.

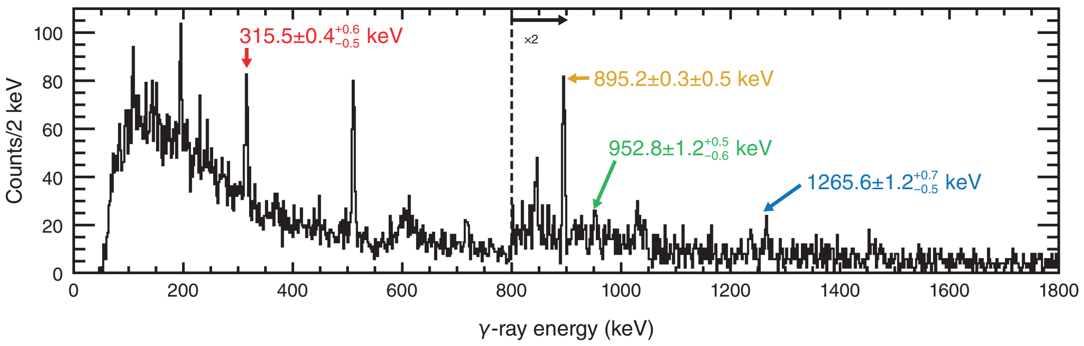

Fig.3-8 Obtained γ-ray spectrum
We succeeded to observe and identify four γ rays from florin-19-Λ (${}^{19}_{\Lambda}$F) hypernucleus. The first energy uncertainty is statistical and the second one is systematic. Several other peaks are also observed, but they are known to be from background sources other than ${}^{19}_{\Lambda}$F as they are also seen even when the hypernucleus is not produced.

Normal nucleus is composed of two constituents, namely, protons and neutrons (Fig.3-6(a)). At the level of quark, both are made of two kinds of quarks, up and down, but it is known there are six kinds of quarks in the nature. Then, how nuclei are changed if we change an up/down quark to another kind, for example, strange quark? Such special nuclei are called hypernuclei. Among them, those with a Λ particle (Fig.3-6(b)) have been actively studied.

There are many motivations to study hypernuclei, one of which is for neutron stars. It is expected that Λ particles exist in neutron stars, and therefore it is necessary to study Λ hypernuclei to understand neutron stars. Since neutron star is a huge hypernucleus, it is desirable to study as heavy hypernuclei as possible, but studies so far are mostly limited to light hypernuclei due to technical reasons.

We succeeded to produce florin-19-Λ (${}^{19}_{\Lambda}$F) hypernucleus and observe light (γ rays) emitted from it at Hadron Experimental Facility of J-PARC (Fig.3-7). It is the heaviest hypernucleus of which γ rays are observed so far. The result (Fig.3-8) is consistent with theoretical calculations using data from helium-4-Λ (${}^{4}_{\Lambda}$He) and lithium-7-Λ (${}^{7}_{\Lambda}$Li) hypernuclei we previously obtained. This indicates that heavier hypernuclei can be understood as well as light hypernuclei studied so far.

We will proceed such researches and investigate structures of even heavier hypernuclei. We expect to reveal the unknown internal structure of neutron stars by these studies.

This work was supported by the Japan Society for the Promotion of Science (JSPS) KAKENHI Grant-in-Aid for Scientific Research (A) (No.15H02079).

Reference

Yang, S. B., Tanida, K. et al., First Determination of the Level Structure of an *sd*-Shell Hypernucleus, ${}^{19}_{\Lambda}$F, Physical Review Letters, vol.120, issue 13, 2018, p.132505-1–132505-5.

3–4

Unraveling the Mechanism of Strong Superconductivity in a Uranium Compound Exposed to a Magnetic Field

— New Electronic State Revealed by High-Resolution Nuclear Magnetic Resonance Measurements at Cryogenic Temperatures —

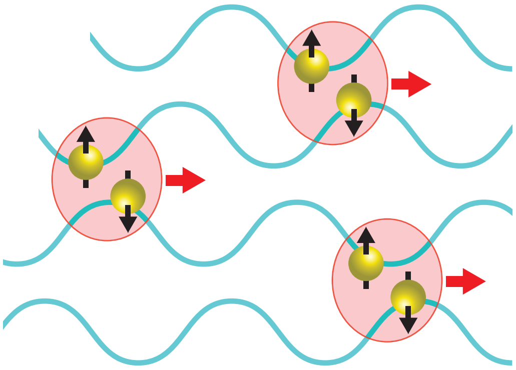

Fig.3-9 Schematic of superconductivity
Electrons (●) in material have a magnet-like character called electron spin (➡). At low energies, electrons are bound into so-called Cooper pairs (a pair is surrounded by the red circle) and become superconducting by flowing (➡) like a wave (~). The electron spins in a Cooper pair usually face each other in a staggered direction.

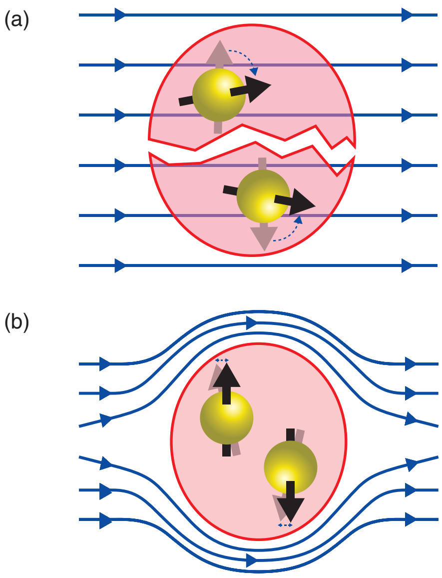

Fig.3-10 Behavior of Cooper pairs under a magnetic field (—)
(a) Under a magnetic field, the electron spin usually reorients in the magnetic field direction, and the Cooper pair breaks.
(b) In the uranium compound URu_2Si_2, the electron spins of the Cooper pair align in uniaxially alternating directions, maintaining the Cooper pairs even under a strong magnetic field.

Superconductivity, the state of zero electrical resistance and repulsion of magnetic fields, is expected to be exploited in a wide range of applications, such as superconducting (SC) power transmission and linear motor cars. However, superconductivity requires a very low temperature and is usually overcome and easily destroyed by a magnetic field. These properties inhibit the wider practical applicability of superconductivity. Therefore, many researches are pursuing superconductors with higher transition temperatures and stronger resistance to magnetic fields than standard superconductors.

We are actively researching the SC mechanism of the uranium compound URu_2Si_2, which is a superconductor with extreme strength against magnetic fields. However, as this compound is radioactive, sufficiently accurate experiments have been precluded by the stringent handling restrictions. At the JAEA facility, we synthesized an ultra-pure single crystal of URu_2Si_2 and formed it into a shape suitable for measurement. Thus, we measured (to the highest precision worldwide) the nuclear magnetic resonance in the SC state of the uranium compound at cryogenic temperatures. Nuclear magnetic resonance microscopically examines the electrons around nuclei through their magnet-like property (spin), thereby revealing the electronic states of the superconductivity.

Electrons in materials have a magnet-like property called electron spin, which is randomly oriented in the normal state. When an attractive force dominates between two electrons at low temperatures, the electrons form Cooper pairs with their spins coupled in antiparallel directions. Cooper pairs enter the SC state by creating aligned wave-like states (Fig.3-9). Under a strong magnetic field, the electron spins in a Cooper pair reorient in the direction of the magnetic field, breaking the pairing and hence the superconductivity (Fig.3-10(a)). However, our high-resolution nuclear magnetic resonance measurements of URu_2Si_2 demonstrated that in this compound, the uniaxial orientation of the electron spins is robust with respect to the magnetic field, meaning that the superconductivity survives in a strong magnetic field (Fig.3-10(b)). This achievement is expected to deepen our understanding of superconductivity and provide guidelines for exploring more practical superconductors.

This work was supported by the Japan Society for the Promotion of Science (JSPS) KAKENHI Grant-in-Aid for Young Scientists (B) (No.16K17757).

Reference

Hattori, T. et al., Evidence for Spin Singlet Pairing with Strong Uniaxial Anisotropy in URu_2Si_2 Using Nuclear Magnetic Resonance, Physical Review Letters, vol.120, issue 2, 2018, p.027001-1–027001-5.

3–5 Safer Memory Storage by “Antimagnets”

— A New Way of Controlling Antiferromagnetic Magnetization —

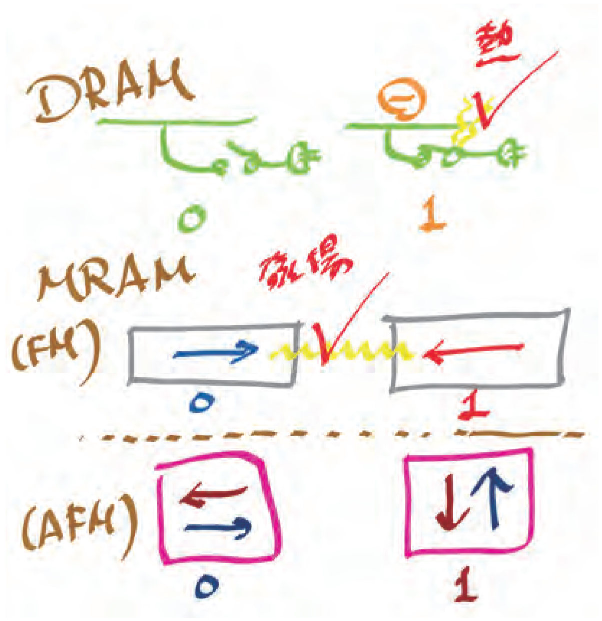

Fig.3-11 Semiconductor memory and magnetic memory
Binary data are stored in on/off electrical states in a semiconductor memory (DRAM) and in the magnetization direction in a magnetic memory (MRAM). However, DRAM and ferromagnetic-based MRAM are degraded by Joule heating (熱) and magnetic field (磁場) leakage, respectively. These problems can be solved using antimagnet MRAMs.

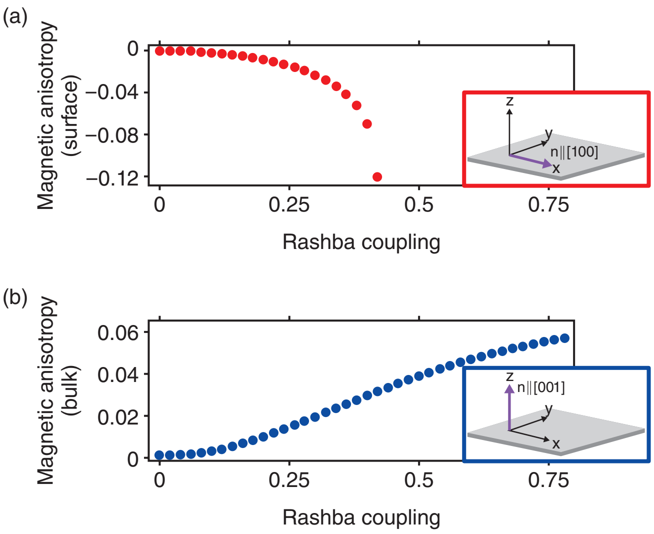

Fig.3-12 Rashba magnetic anisotropy in antiferromagnets
In a certain class of antiferromagnets, the preferential magnetization direction (magnetic anisotropy) is the in-plane direction (a) (negative value) at the sample surface/interface and the out-of-plane direction (b) (positive value) in the bulk. These properties can be modulated by adjusting the Rashba coupling parameters. The unit of the axes is eV.

The Internet, smart phones, and the forthcoming AI society are immersing us in digital data. The core of digital processing is the memory unit, which performs basic operations, such as writing, storing, and reading data, billions of times per second. Normally, these operations are realized by switching the electricity in semiconductor materials on and off. Such on/off switching modulates the flowability of the electricity and produces heat and waste energy. As the amount of digital data increases, the energy consumption of digital processing is becoming a major problem.

A promising candidate for negating this problem is a new type of memory device based on “magnetic memory”. Instead of turning electricity on and off, a magnetic memory device stores data in the direction of magnetism, greatly reducing the energy consumption (Fig.3-11). The basic unit of magnetic memory is a nanoscale magnet. Optimal materials for magnetic memory devices are being researched around the world. At the forefront of these researches is a material called “antiferromagnet” material.

An antiferromagnet (also called an “antimagnet”) has a magnetic property but does not generate a magnetic field and hardly responds to an external magnetic field. Antiferromagnets have superior characteristics that cannot be achieved using other magnetic materials. In memory chips, antiferromagnets are expected to reach today’s limit of integrability and data security because they cannot leak magnetic fields, and consequently, there is no crosstalk between the memory bits and no data leakage in principle.

We focused on the “magnetic anisotropy” property, which dictates the direction of magnetism in antiferromagnets. By analyzing a theoretical model incorporating the special relativistic effect (the Rashba effect) in materials, we revealed that in a special class of antiferromagnets, the direction of magnetism tends to differ between the inside and surface of the sample (Fig.3-12). Furthermore, by attaching different materials or applying an external voltage, we could tune the magnitude of the Rashba effect and the induced surface magnetic anisotropy.

These results are particularly important at the nanoscale because the surface effect magnifies as the size reduces. Therefore, antiferromagnets should realize energy-efficient magnetic memories.

This work was supported by the Japan Society for the Promotion of Science (JSPS) KAKENHI Grant-in-Aid for Scientific Research (C) (No.16K05424).

Reference

Ieda, J. et al., Magnetic Anisotropy by Rashba Spin-Orbit Coupling in Antiferromagnetic Thin Films, Journal of the Physical Society of Japan, vol.87, issue 5, 2018, p.053703-1–053703-4.

3–6 Spin Current Power Generation

— Magnon Density of States in $Y_3Fe_5O_{12}$ Determined via Neutron Scattering —

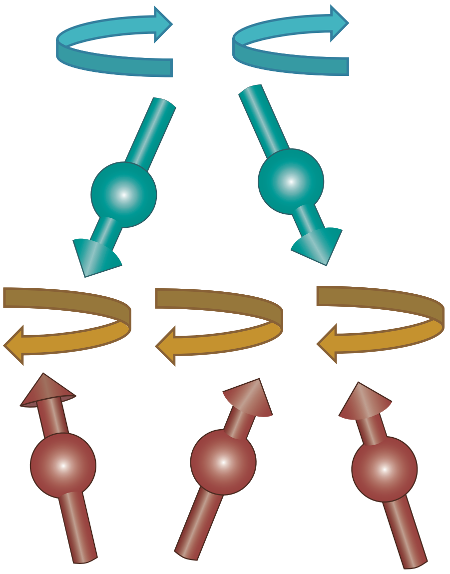

Fig.3-13 Low energy mode of spin waves in $Y_3Fe_5O_{12}$
Electrons (yellow spheres) in materials have a magnetic-like character called electron spin (black arrow). The schematic shows the anticlockwise rotational mode of five spins in a yttrium iron garnet (YIG) sub-lattice. This mode carries a spin current in one direction. The rotational direction in $Y_3Fe_5O_{12}$ is determined based on the crystallographic symmetry.

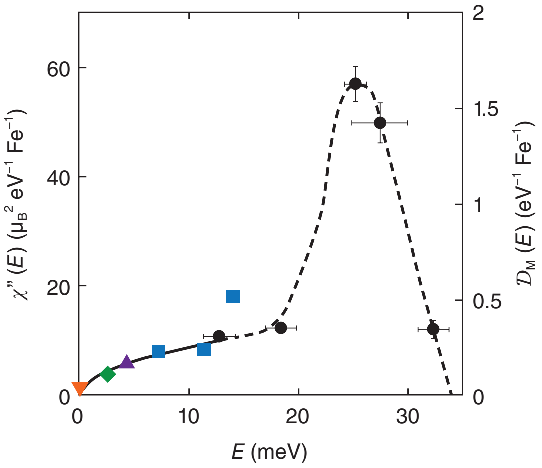

Fig.3-14 Magnon density of states in $Y_3Fe_5O_{12}$
The magnon density of states ($\mathcal{D}_M(E)$), obtained on an absolute scale by inelastic neutron scattering, is proportional to the imaginary part of the dynamical spin susceptibility ($\chi''(E)$). The magnitude is an important factor for spin current power generation.

Spin current defines the flow of spin-angular momentum. Spin current power is generated using a revolutionary method that produces electricity in an insulator. The spin current flows in the presence of a temperature gradient; i.e., it is a magnon flow. The flow establishes a voltage on the platinum electrodes via the inverse spin Hall effect. Spin power generation has been investigated in ferromagnetic materials such as yttrium iron garnet (YIG; composition $Y_3Fe_5O_{12}$). YIG exhibits up and down Fe^{3+} spins in a ratio of 3:2 (Fig.3-13), leading to a ferrimagnetic state. At low energies, both spins are limited to anticlockwise rotation and cannot freely rotate in three dimensions (Fig.3-13). Such restrictions are imposed by the crystallographic symmetry of the spins. Theoretical study confirmed that this rotation is closely related to the spin current in YIG and that mixing the clockwise and anticlockwise rotations decreases the efficiency. In YIG, both types of rotational energies are split by ~30 meV, implying that only the anticlockwise rotation in Fig.3-13 occurs at low temperatures. Furthermore, the magnitude of the spin current depends on the state number of the spin rotations (magnons), which determines the generation efficiency of the spin current power. The state number of the magnons can be measured as the magnon density of states (MDOS) via inelastic neutron scattering (INS). However, this measurement is difficult because the scattering intensity must be measured on an absolute scale. For this reason, the MDOS has never been directly determined, not even in the popular magnetic material YIG.

As shown in Fig.3-14, the MDOS in YIG has been newly detected over a wide energy range (three orders of magnitude) using three INS spectrometers (4SEASONS, AMATERAS, and DNA) in the Material and Life Science Experimental Facility of J-PARC Center.

Recently, highly efficient generation materials of spin current power have been extensively studied. A candidate ferrimagnetic material must meet the following conditions: “The clockwise and anticlockwise rotational modes do not overlap”, and “The MDOS in Fig.3-14 is high within the working temperature range (i.e., the low energy regime)”.

Whether a material satisfies these conditions can be studied via INS experiments. We suspect that magnon effects strongly interact with phonon effects. Therefore, our future study will investigate the effects of both magnons and phonons on the spin current by neutron scattering.

This work was supported by the Japan Society for the Promotion of Science (JSPS) KAKENHI Grant-in-Aid for Scientific Research (B) (No.25287094).

Reference

Shamoto, S. et al., Neutron Scattering Study of Yttrium Iron Garnet, Physical Review B, vol.97, issue 5, 2018, p.054429-1–054429-9.

4 Nuclear Science and Engineering Research

Fundamental Technologies for Innovation in Nuclear Energy

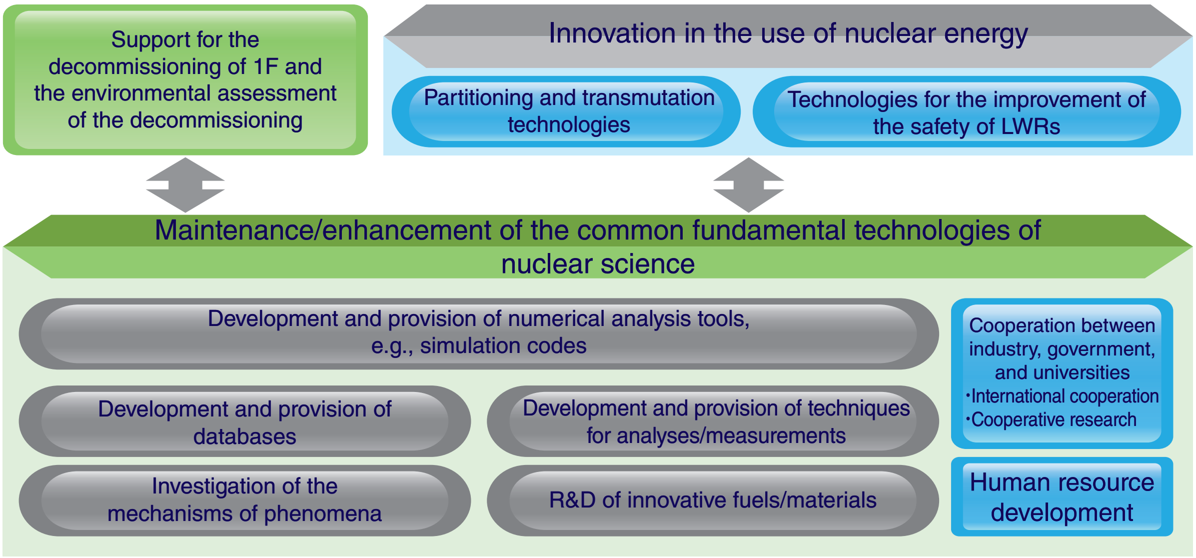

Fig.4-1 Overview of nuclear science and engineering research
The Nuclear Science and Engineering Center is maintaining and enhancing common fundamental technologies for the use of nuclear energy and radiation. The Center is also supporting the decommissioning, etc., of the TEPCO's Fukushima Daiichi NPS (1F) and contributing to the improvement of the safety of LWRs and the development of partitioning and transmutation technologies for reducing the impact of radioactive wastes.

Common fundamental technologies and knowledge, such as databases, codes for analyses/simulation, analytical technologies, and understanding of the mechanisms of phenomena, are necessary to support the use of nuclear energy and radiation. We always try to employ state-of-the-art technologies and frontier knowledge to improve commonly used technologies and further the available knowledge of nuclear science, and to provide industry, universities, and governmental agencies with the fundamental technologies and knowledge.

We are also contributing to improving the safety of light-water reactors (LWRs) and to developing partitioning and transmutation technologies for reducing the impact of radioactive wastes (Fig.4-1). In this section, recent results of our R&D activities are introduced.

Accuracy improvement of the neutron-capture cross sections of americium (Am): by applying the correction method to the measured thermal-neutron-capture cross sections of Am-241, as reported previously, we have succeeded in reducing discrepancies among the cross sections significantly (Topic 4-1).

Self-healing of ceramics under a radiation environment: we observed self-healing of a kind of ceramics, enabling them to restructure their atomic arrangement quickly after suffering damage using a novel method to observe nanometer-sized superfine structures created in ceramics irradiated with high-energy heavy particles (Topic 4-2).

Computational design of high-toughness alloys: we demonstrated the possibility that the toughness of an alloy is predictable by simulating the occupancy of solute elements on grain boundaries (Topic 4-3).

Research on solvent extraction of specific metals from radioactive wastes: we have determined the structure of europium ions on a boundary surface between organic/water phases using advanced laser spectroscopy (Topic 4-4).

Using a dynamic Monte Carlo code, we elucidated that extremely low-energy secondary electrons play a part in a new genetic transformation process through radiation (Topic 4-5).

We have developed a new model for estimating the therapeutic effect of boron neutron-capture-therapy (BNCT). A new computational method was established for the development using the Particle and Heavy Ion Transport code System (PHITS) (Topic 4-6).

When a severe accident (SA) happens at a nuclear power plant, release of radioactive substances to the environment may cause public exposure to radiation. In order to estimate how radioactive substances are released from nuclear fuels to the outside of the reactor, we have acquired detailed data concerning the chemical behavior of strontium by performing release/transport experiments simulating real conditions (Topic 4-7).

Evaluation of nuclear data of lead (Pb): we are evaluating experimental Pb nuclear data by performing measurements using an experimental criticality device and highly enriched uranium in the US. Pb is the coolant of the accelerator-driven system (ADS) and the accuracy of the reaction cross sections of Pb with neutrons is a key factor in the development of ADS (Topic 4-8).

We have developed a laser-charge-exchange system as an elemental technology for the development of ADS. We have demonstrated the extraction of a minute-power laser from the proton beam at J-PARC using the system (Topic 4-9).

We investigated the durability of mineral-insulated cables under the SA condition. We showed experimentally that a nickel-based alloy, NCF600, is promising (Topic 4-10).

4–1 Accuracy Improvement of Nuclear Data on Minor Actinides

— Evaluation of the Thermal-Neutron-Capture Cross Section Using Resonance Structure —

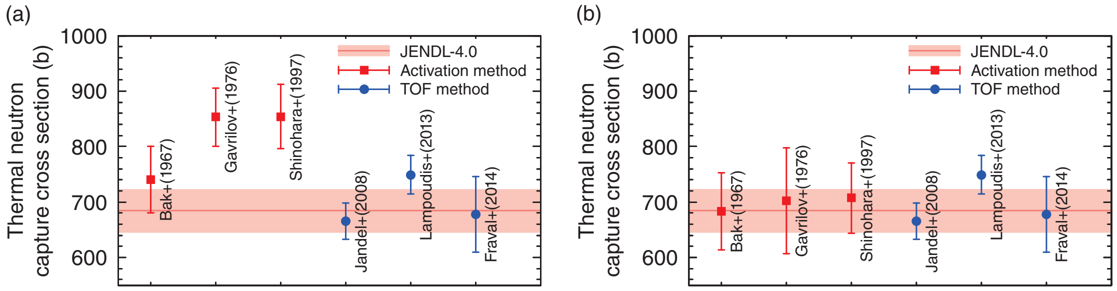

Fig.4-2 Comparison of thermal-neutron-capture cross sections of ^{241}Am

(a) Thermal NCCSs measured by an activation method (■) tend to be larger than TOF data (●). The thermal NCCS and uncertainty in the nuclear data library JENDL-4.0 are shown by horizontal line and band, respectively.
(b) By applying the developed correction method to activation data, the corrected data are consistent with the TOF data within their uncertainties.

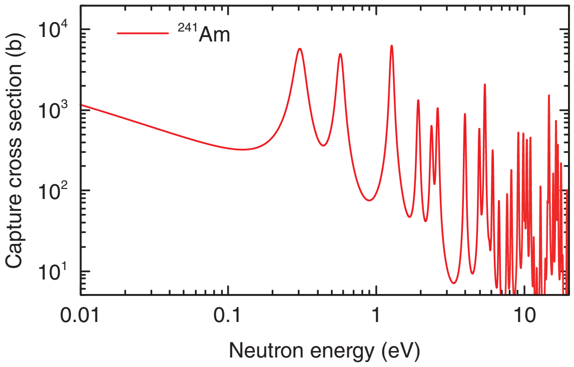

Fig.4-3 Neutron-resonance structure in the capture cross section of ^{241}Am

There are many MA nuclides like ^{241}Am, which have neutron resonances below 0.5 eV. These low-energy resonances are well-observed for not only MA nuclides, but also heavy nuclides like uranium and plutonium. We developed a strict correction method for thermal NCCSs by taking the neutron-resonance structure into account.

Minor actinides (MAs) are produced by nuclear reactions of uranium and plutonium in reactors and stored in nuclear spent fuels. It is necessary to properly manage and dispose of MAs in nuclear waste, since most of them have strong radiotoxicities. To reduce these burdens, nuclear-transmutation systems have been investigated. One basic dataset required for their system design is the neutron-capture cross section (NCCS). The NCCS at thermal energy is particularly important for accuracy improvement over the whole energy region since it is used to determine the absolute value of NCCS.

The thermal NCCSs have been measured by time-of-flight (TOF) and activation methods. The TOF method has the merit that NCCSs can be obtained not only at thermal energy, but also over a wide energy region. Nevertheless, a large uncertainty is likely to arise in an analytical procedure. In contrast, the activation method can easily derive an absolute value at a specific energy like the thermal one. Its accuracy is considered to be high.

It is known that the thermal NCCSs of MA nuclides derived by the TOF and activation methods have large discrepancies over their experimental uncertainties. Fig.4-2(a) shows the NCCSs of americium-241 (^{241}Am) at thermal energy measured by the two methods. Resolving such discrepancies is essential for increasing the accuracy of thermal NCCSs.

In this study, we focused upon the relationship between the neutron-resonance structure and the cadmium (Cd)-ratio method. Many MA nuclides have neutron resonances at low energy (Fig.4-3). Analyses of activation experiments have adopted the Cd-ratio method; a Cd filter is used to cut neutrons with energies below 0.5 eV. The thermal NCCS of a sample is derived by eliminating the neutron-resonance component from the difference in the sample irradiations with and without the Cd filter. The previous experimental analyses did not properly take account of neutron resonances below 0.5 eV. Thus, correction methods for these resonance components were developed using the neutron-resonance structure in the nuclear data library.

Fig.4-2(b) shows the results obtained by applying our method to the experimental thermal NCCSs of ^{241}Am. It is found that the contradiction between the thermal NCCSs measured with the two methods is fixed, and that both data are consistent within their uncertainties.

The correction method developed in the present study has high versatility, and thus, it is expected that the accuracy of thermal NCCS will be systematically improved by applying it to all nuclides with low-energy neutron resonances.

The present study includes the result of “Research and Development for accuracy improvement of neutron nuclear data on minor actinides” entrusted to JAEA by the Ministry of Education, Culture, Sports, Science and Technology (MEXT), Japan.

Reference

Mizuyama, K., Iwamoto, N. et al., Correction of the Thermal Neutron Capture Cross Section of ^{241}Am Obtained by the Westcott Convention, Journal of Nuclear Science and Technology, vol.54, issue 1, 2017, p.74–80.

4-2 Self-Healing of Ceramics in a Radiation Environment

— Result of Using a New Method for Observing Ceramic Surfaces —

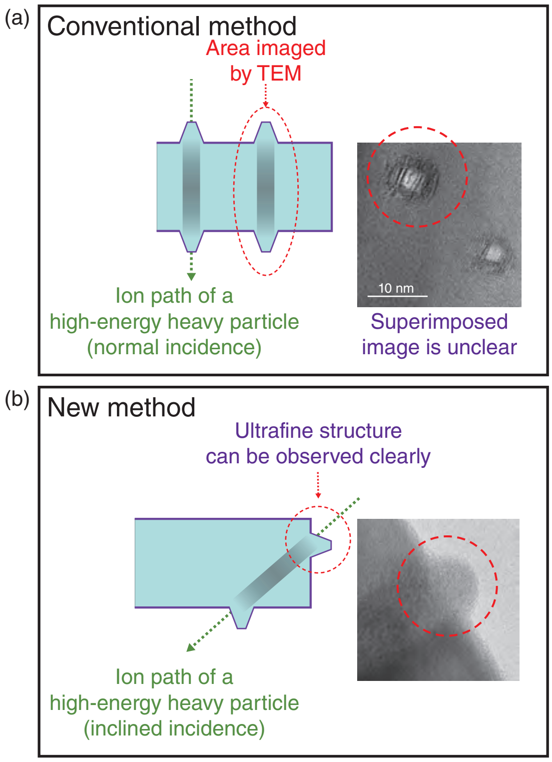

Fig.4-4 (a) Conventional method and (b) new method
(a) Image of ultrafine protrusion is unclear as long as the conventional method is used. (b) Clear image of ultrafine protrusion is obtained by the new method.

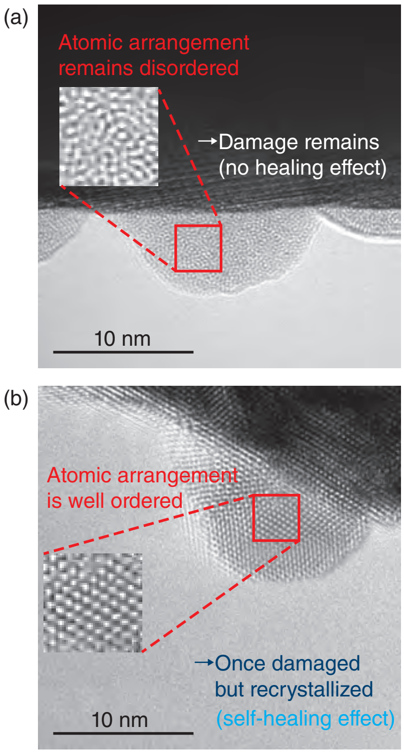

Fig.4-5 TEM images of ultrafine structure
(a) For normal ceramics (e.g. $Y_3Fe_5O_{12}$), the atomic arrangement after irradiation is disordered. (b) For particular ceramics (e.g. BaF_2), the self-healing effect by recrystallization is found.

Generally speaking, marked radiation damage is created when ceramics are irradiated by high-energy heavy particles. However, for particular ceramics such as barium fluoride (BaF_2) and uranium oxide (UO_2), irradiation creates less damage than expected. It is important to clarify the reason for the radiation-resistance of these ceramics.

When ceramics are irradiated with high-energy heavy-particle beams, nanometer-sized ultrafine structures are created at the surface. We speculated that the secret of radiation-resistance is hidden in this ultrafine structure, and have started to develop a new method for observing the details of the structure.

Fig.4-4 compares a conventional method of observation and a newly developed method. The nanometer-sized protrusion represents the ultrafine structure. As long as the conventional method is used, images of ultrafine protrusions and other structures are always superimposed, as shown in Fig.4-4(a), resulting in unclear images of the structure.

By irradiating at oblique incidence, we found that ultrafine protrusions were also created at the edge of the sample. As demonstrated in Fig.4-4(b), by improving the irradiation condition and using the transmission electron microscope (TEM), we found that high-resolution images of the ultrafine structure can be observed clearly.

Using the new observation method, the atomic arrangement inside the ultrafine structures of many ceramics (e.g., yttrium iron garnet ($Y_3Fe_5O_{12}$)) was found to be disordered after irradiation (Fig.4-5(a)). Conversely, when radiation-resistant ceramics (e.g., BaF_2 and calcium fluoride (CaF_2)) were irradiated, atomic arrangement was found to be well-ordered (Fig.4-5(b)). This means that the atomic arrangement eventually recovers, although it is temporarily disordered just after irradiation. This result suggests that radiation-resistant ceramics are likely to have a self-healing capability.

This work was supported by the Japan Society for the Promotion of Science (JSPS) KAKENHI Grant-in-Aid for Scientific Research (C) (No.16K06963).

Reference

Ishikawa, N. et al., Hillocks Created for Amorphizable and Non-Amorphizable Ceramics Irradiated with Swift Heavy Ions: TEM Study, Nanotechnology, vol.28, no.44, 2017, p.445708-1–445708-11.

4–3 Computational Design of High-Toughness Alloys

— Magnesium-Alloy Design from Electronic-Structure Calculations —

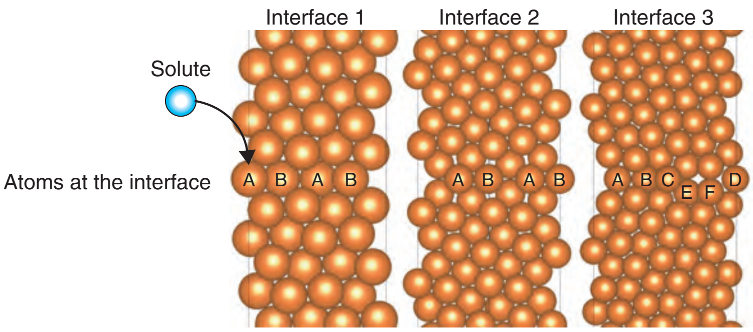

Fig.4-6 Atomic models of the interfaces
Relaxed atomic configurations of the (1) (1011), (2) (1012), and (3) (3032) TBs in pure Mg. Possible segregation sites used in the DFT calculations are shown by A to F in each interface.

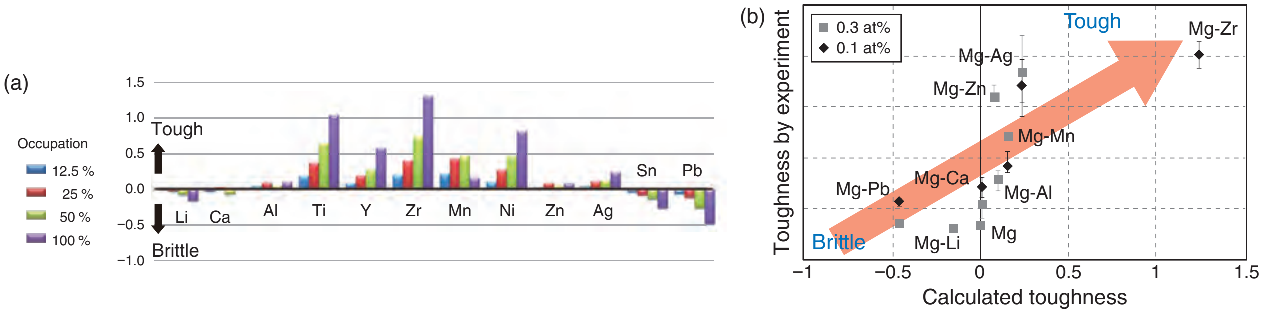

Fig.4-7 (a) Ideal work of interfacial-separation in terms of site occupation (12.5 %–100 %). (b) Fracture-toughness relationships between experiments and simulations
We investigated the effect of alloying elements on the toughness with respect to the occupation. The negative and positive values correspond to weakening and strengthening effect, respectively. The calculated values are in good agreement with the experimental ones. Thus, we can predict the potential candidate for alloying elements which improve the toughness.

Mg alloys are promising candidates for next-generation lightweight structural materials in terms of energy and environmental conservation, especially for use in transportation equipment. However, widespread application of wrought-Mg alloys is limited by their low formability at room temperature. This low formability is caused by their low ductility and fracture toughness. The former is because of their strong plastic anisotropy originating from their hexagonal close-packed (HCP) structure and the latter is attributed to the intrinsic features of their electronic structure.

An important property for improving formability is fracture toughness, because pure Mg is intrinsically brittle, with local strain concentration occurring at twin boundaries (TBs) and cracks mainly propagating along these boundaries. We have systematically investigated the fracture toughness of Mg-X binary alloys from the viewpoint of the effects of solute elements. In the present study, we introduce an electronic-structure-based approach combined with fracture mechanics to understand the effect of solute elements upon the interfacial fracture of Mg alloys. Rather than solely focusing upon the segregation energy at the surface and interface, we focus on the comprehensive mechanism caused by the electronic structure, which dominates cohesion or decohesion of the interfacial fracture.

Fig.4-6 shows atomic models of typical TBs observed in experiments. We constructed several types of TB configurations to investigate the effects of various solute elements upon the ideal work of interfacial separation. Three different TBs were constructed to investigate differences in the type of boundary, including energetically stable and unstable boundaries. The free-surface energy was evaluated, together with the interfacial energy and the energy-based Griffith criterion for crack propagation was applied.

The difference in the ideal work of interfacial separation between the Mg-M alloys and pure Mg in terms of the occupancy at the TB site for the (1012) TBs is summarized in Fig.4-7(a), with positive values corresponding to solutes with toughness. The values for Li, Ca, Sn, and Pb are very small or negative, indicating that these elements cause segregation-induced embrittlement at the interface. On the other hand, the other solutes show positive values and Zr has the highest among them. Finally, we compare the calculated values with experiments in Fig.4-7(b), where our prediction shows good agreement with the experimental values and the toughness is indeed improved by the Zr solute.

We conclude that the electronic interactions of both the bulk and the surface and their difference characterize the fracture toughness of binary alloys. We hope that computational simulations will play a more important role in the effective approach for new-alloy design.

This work was supported by the Japan Society for the Promotion of Science (JSPS) KAKENHI Grant-in-Aid for Scientific Research (C) (No.16K06714).

Reference

Tsuru, T. et al., Interfacial Segregation and Fracture in Mg-Based Binary Alloys: Experimental and First-Principles Perspective, Acta Materialia, vol.151, issue 1, 2018, p.78–86.

4–4 Toward Elucidation of Solvent Extraction Mechanism

— Observation of Metal Ions at an Interface Using a Laser —

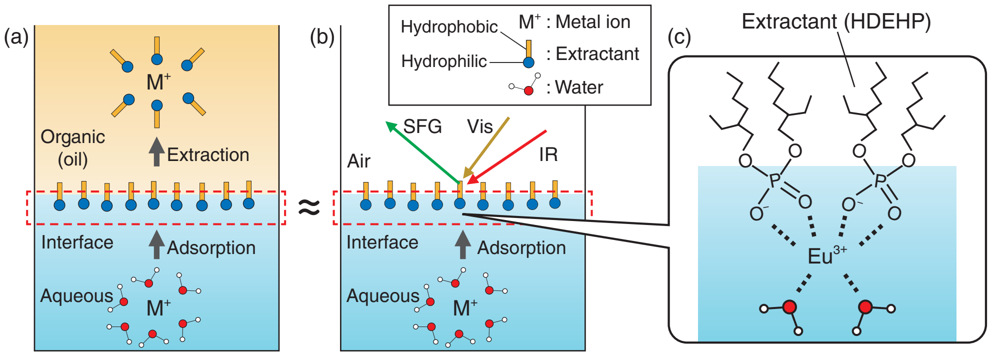

Fig.4-8 (a) Schematic of solvent extraction; (b) Diagram of the present research method; (c) Structure of a metal ion (Eu^{3+}) at the interface clarified in this study
Unlike the actual solvent extraction system (a), in the system without an organic phase (b), metal ions adsorbed to the interface are likely to stay there because no extraction takes place. The metal ions trapped at the interface were observed using sum frequency generation (SFG ➜) spectroscopy with visible (Vis ➜) and infrared (IR ➜) pulse lasers, and the structure of the metal ions present at the interface were revealed (c).

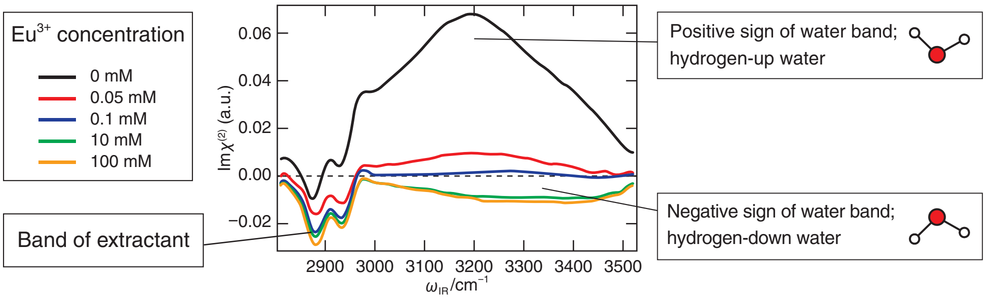

Fig.4-9 Vibrational spectra of the interface obtained by advanced laser spectroscopy: heterodyne-detected vibrational sum frequency generation spectroscopy
As the concentration of Eu^{3+} increases, the sign of the water band inverts from positive to negative. The sign of the water band corresponds to the direction of the water molecule present at the interface, and the interfacial water molecules showing negative sign point their hydrogen atoms downward. The hydrogen-down orientation of the interfacial water molecules is due to the bonding to Eu^{3+}, which adsorbs to the extractant (HDEHP) at the interface (Fig.4-8(c)).

Solvent extraction is a method for separation of metals. In solvent extraction, an aqueous phase dissolving metal ions and an organic phase dissolving a chemical called the extractant are brought into contact with each other, and metal ions are transferred from the aqueous phase to the organic phase (Fig.4-8(a)). Solvent extraction is one of the most important methods of treating radioactive waste generated by nuclear-power generation. Improving solvent-extraction technology is an important research topic.

In order to improve solvent extraction technology, fundamental research has conventionally focused upon the structure of metal ions in the aqueous and organic phases. On the other hand, the phase transfer mechanism of metals from the aqueous phase to the organic phase through the organic/aqueous interface remains poorly understood. Therefore, if the phase transfer mechanism occurring at the interface can be revealed, it is expected that new clues will be obtained for improvement of solvent extraction technology. However, it is generally difficult to observe metal ions at the interface.

In order to observe metal ions just before transfer from the interface to the organic phase, metal ions adsorbed at the interface between air and water (surface of the aqueous solution) were observed by advanced laser spectroscopy (Fig.4-8(b)). In the present study, extraction of europium ions (Eu^{3+}) using di-2-ethylhexyl phosphate extractant (HDEHP) was selected as a representative example of common solvent extractions, and the interface vibrational spectra of the system were obtained (Fig.4-9). As the concentration of Eu^{3+} increases, the positive sign of the water signal becomes negative. This indicates that interfacial water molecules pointing upward (hydrogen-up) change to a downward (hydrogen-down) orientation as Eu^{3+} is adsorbed to the interface. That is, interfacial water molecules are bonded to Eu^{3+} with hydrogen-down orientation (Fig.4-8(c)). The structure of Eu^{3+} sandwiched between HDEHP and water molecules has not been reported so far in the organic or aqueous phases, so that the Eu^{3+} structure at the interface is unique.

Based on the findings mentioned above, we proposed a reaction model for solvent extraction of Eu^{3+} using HDEHP as follows. In the aqueous phase, Eu^{3+} is surrounded by water molecules, but Eu^{3+} is sandwiched between HDEHP and water molecules at the interface; subsequently, Eu^{3+} is extracted in the organic phase and surrounded by HDEHP.

In future work, we will conduct studies that lead to improvement of the extraction rate, separation efficiency, etc., by clarifying what is happening at the interface in actual solvent extractions of radioactive waste.

This work was supported by the Japan Society for the Promotion of Science (JSPS) KAKENHI Grant-in-Aid for Young Scientists (B) (No.17K14919).

Reference

Kusaka, R. et al., The Structure of a Lanthanide Complex at an Extractant/Water Interface Studied Using Heterodyne-Detected Vibrational Sum Frequency Generation, Physical Chemistry Chemical Physics, vol.20, issue 4, 2018, p.2809–2813.

4–5 Elucidation of the Genetic-Transformation Process by Radiation

— Role of Extremely Low-Energy Electrons below 1 eV —

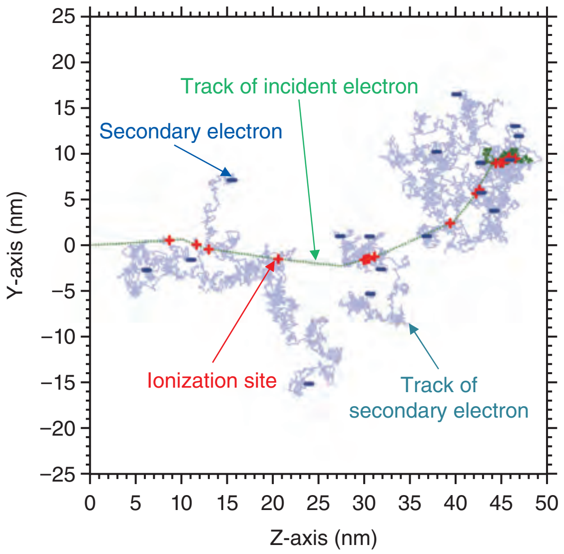

Fig.4-10 Electron tracks produced by an incident electron of 1 keV in water
DNA molecules were assumed to be located in the water, and the amount of DNA damage was estimated by the ionization and excitation sites. Clustered DNA-damage sites have been implicated in harmful biological effects such as cell death or mutation.

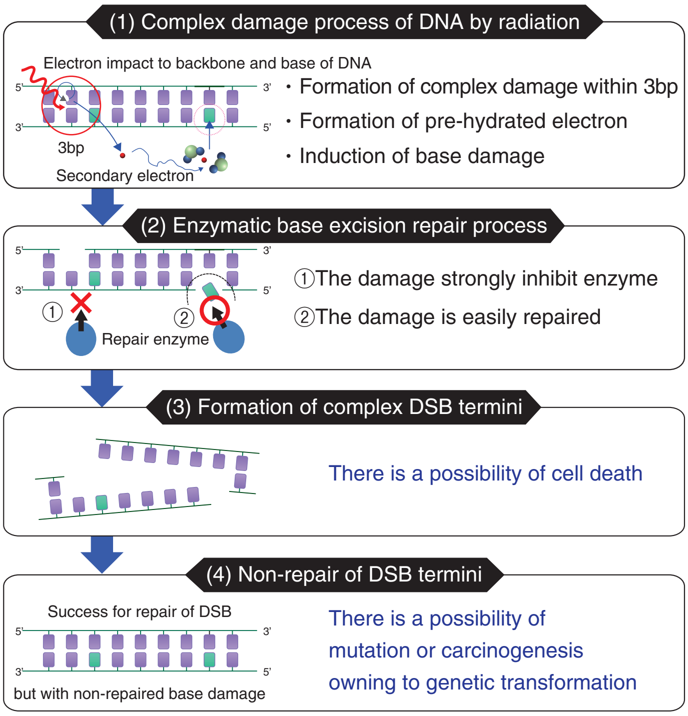

Fig.4-11 Relationship of DSB to base damage and biological effects
The figure shows the process by which DNA damage by radiation is converted to DSB by repair. In clustering the damage, the gene can be transformed by base damage remaining in the DSB termini.

When DNA in a living cell is exposed to ionizing radiation, single- or double-strand breaks (SSBs or DSBs) or base damage of the DNA may occur. Although most DNA damage can be removed, it has been found experimentally that the repair efficiency was extremely low for simultaneous damage within 1 nm (called “clustered damage”). Clustered damage has been implicated in inducing harmful biological effects. However, such damage is hard to detect using experimental techniques.

In this study, a dynamic Monte Carlo code is developed to simulate electron irradiation to DNA, taking into account the Coulombic force between ion pairs. Collisional interactions between electrons and the DNA sample were analyzed using the code. Fig.4-10 shows the ionization inductions (+ points) and secondary-electron positions (– points) arising from the incidence of an electron with an energy of 1 keV upon water including DNA. First, it was found that the yield of the clustered damage constructed by the SSBs and base damage within 1 nm was constantly induced. It was also found that the secondary electrons deaccelerated below 1 eV were finally distributed over a few nm from the ionization sites. The analyses also clarified that reductive damage was produced by electron attachment to DNA when the electrons were located near such molecules.

Based on these analyses, we predicted that complex DNA damage sites were composed of clustered damage produced by the electron incident upon the DNA, and that the isolated base-damage site involved extremely low-energy electrons (Fig.4-11(1)). The isolated damage sites could be converted to SSBs by the elimination capability of the repair enzyme (Fig.4-11(2)). The DSBs with base damage in their termini were consequently formed if additional SSBs were produced in the complementary strand (Fig.4-11(3)). In this case, biological effects may be induced by the remaining base damage, even if the DSB could be repaired (Fig.4-11(4)).

This analysis indicated that extremely low-energy secondary electrons were involved in genetic transformation. This is a significant insight into the initial factors behind mutation and cancer inductions.

This work was supported by the Japan Society for the Promotion of Science (JSPS) KAKENHI Grants-in-Aid for Young Scientists (B) (No.15H02823), (No.16H02959), and Grant-in-Aid for Scientific Research (C) (No.17K07022).

Reference
Kai, T. et al., A Significant Role of Non-Thermal Equilibrated Electrons in the Formation of Deleterious Complex DNA Damage, Physical Chemistry Chemical Physics, vol.20, issue 4, 2018, p.2838–2844.

4–6 Theoretical Estimation of the Therapeutic Effect of Boron Neutron Capture Therapy

— Development of a Mathematical Model Useful for Drug-Discovery Research and Treatment Planning —

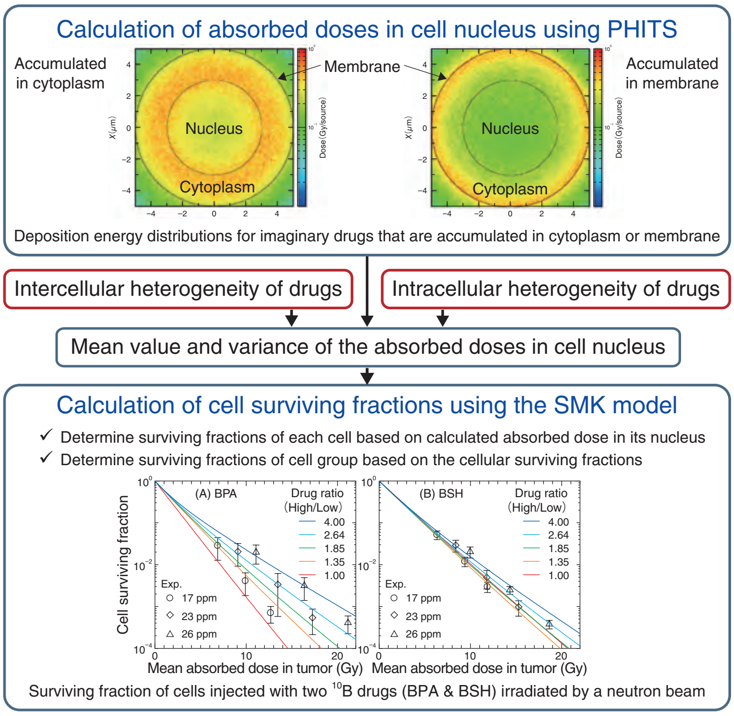

Fig.4-12 Flowchart of our developed model

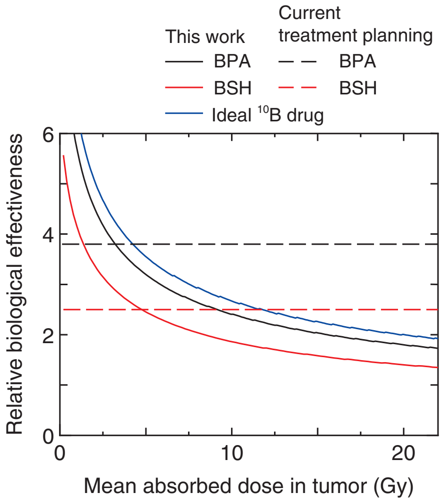

Fig.4-13 Relative biological effectiveness of the therapeutic effect of BNCT in comparison to X-ray therapy as a function of the mean absorbed doses in a tumor

The data for two ^{10}B drugs (BPA & BSH) currently used in BNCT, as well as for an ideal ^{10}B drug that has no intracellular heterogeneity, are shown in the graph.

Boron neutron capture therapy (BNCT) is a noninvasive therapeutic modality that uses a tumor-localizing drug containing ^{10}B. In BNCT, patients are injected with the drug and irradiated by neutron beams to cause ^{10}B(n,α)^{7}Li reactions within their bodies. The ranges of the generated α particles and ^{7}Li ions are equivalent to the size of a cell; thus, they can selectively kill tumor cells. Therefore, BNCT is particularly effective for treating locally invasive malignant tumors, and is under clinical trial for such tumors.

The therapeutic effect of BNCT is known to depend upon the concentration and type of the drugs used in the treatment, even when the absorbed doses are the same. However, the mechanism behind this dependence has yet to be elucidated. We therefore developed a mathematical model for estimating the therapeutic effect of BNCT based upon the Particle and Heavy Ion Transport code System (PHITS) coupled with the stochastic microdosimetric kinetic (SMK) model.

Fig.4-12 shows the flowchart of our developed model. First, the absorbed doses in the cellular nucleus are calculated for imaginary drugs that are accumulated only within the cell-nucleus, cytoplasm, cell membrane, or extracellular space using PHITS. Then, those for the actual drug are estimated from the calculated data, considering the intracellular and intercellular heterogeneity in the drug distribution. The surviving fractions of each cell and cell group are successively determined based on the mean value and variance of the calculated absorbed doses within the cellular nucleus. The accuracy of the calculated surviving fractions turns out to be well-validated by the animal-experimental data. Using this model, we estimated the dose dependences of the therapeutic effect of BNCT in comparison to X-ray therapy, and found that current treatment plans may underestimate and overestimate the therapeutic effect for lower- and higher-dose irradiations, respectively, as shown in Fig.4-13.

Two conclusions are derived from this study. (1) For improving the therapeutic efficacy of BNCT, it is important to develop drugs that accumulate in tumor cells with less intercellular heterogeneity. (2) It is desirable to consider the dose dependence of the relative biological effectiveness in treatment planning of BNCT. The developed model can theoretically estimate the therapeutic effect of BNCT, which used to be evaluated only in an empirical way. Thus, it can play important roles not only in treatment planning, but also in drug-discovery research for future BNCT.

This work was supported by the Japan Society for the Promotion of Science (JSPS) KAKENHI Grant-in-Aid for Scientific Research (C) (No.26461900).

Reference

Sato, T. et al., Microdosimetric Modeling of Biological Effectiveness for Boron Neutron Capture Therapy Considering Intra- and Intercellular Heterogeneity in ^{10}B Distribution, Scientific Reports, vol.8, issue 1, 2018, p.988-1–988-14.

4–7 Radioactive-Material Behavior during a Severe Accident

— Evaluation of the Release and Transport of Radioactive Materials in a Reactor —

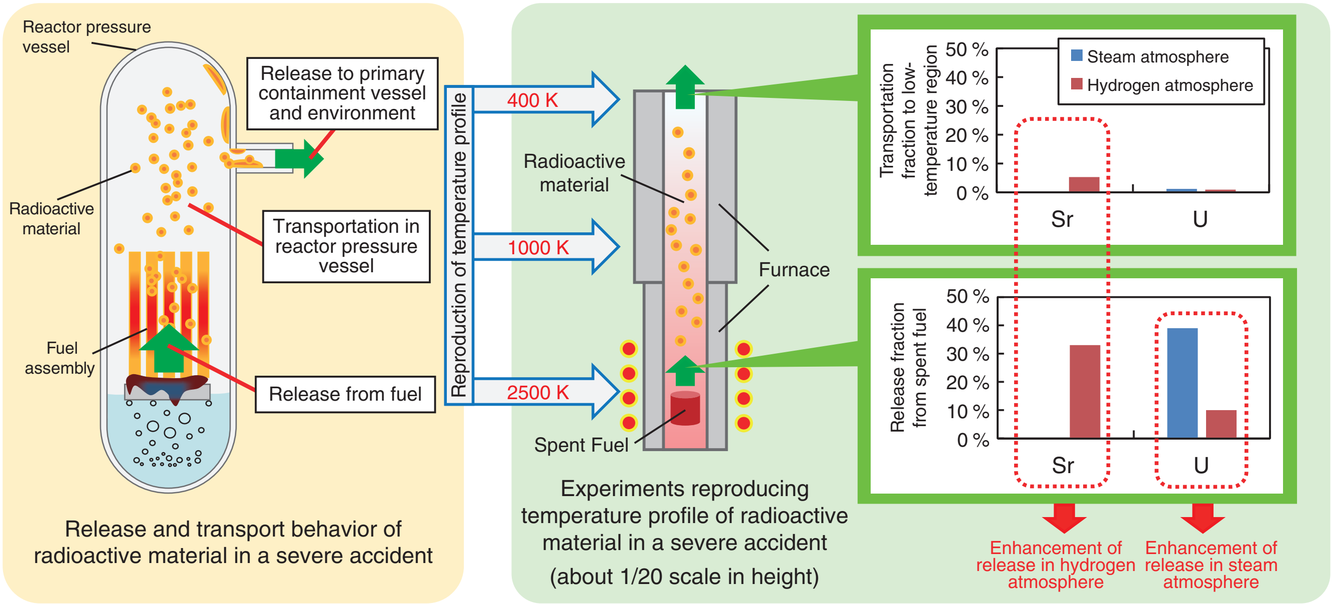

Fig.4-14 The Sr and U fractions of release from spent fuel and of transport to the low-temperature region in experiments reproducing the temperature profile during transportation in a SA

The Sr and U fractions of release from spent fuel and of transport to the low-temperature region were derived based on the results of the heating test of actual spent fuel under SA conditions. Sr and U were believed to be negligible under SA based on limited information. The results show that the Sr and U releases can be enhanced under hydrogen and steam atmospheres, respectively. Moreover, Sr was found to be transported to the low-temperature region, implying the possibility that Sr may be transported to the primary containment vessel under a hydrogen atmosphere.

With the aim of enhancing light-water-reactor safety, public exposure should be evaluated more accurately through detailed estimation of radioactive-material behavior during severe accidents (SAs). Such behaviors include those during release from nuclear fuel and transport into the environment through the high-temperature region of the reactor pressure vessel and primary containment vessel (hereafter, release and transport behavior). The release and transport behavior is also important for estimating the distribution of radioactive materials in a reactor. This information can be reflected in planning the decommissioning and dismantling of the TEPCO's Fukushima Daiichi NPS (1F). It is well-known that the release and transport behaviors of radioactive materials are significantly influenced by their chemical behavior, namely the kinds of reactions that take place and the chemical forms. We have conducted a fundamental study toward the construction of databases and models of chemical behavior for radioactive materials.

Cesium and iodine are important nuclides from the viewpoint of public exposure at SAs. On the other hand, although strontium (Sr) and ulanium (U) releases are believed to have been negligible, they were released from 1F. Consequently, they should be paid more attention due to their decay heat, radiotoxicity, and so on. Therefore, data on their release and transport behaviors have been acquired through international collaborative experiments.

Attention was focused upon the experimental atmosphere. Atmospheres considered in this experiment included not only those containing steam (hereafter, steam atmosphere), but also hydrogen (hereafter, hydrogen atmosphere) because of its significant effect upon chemical behavior. Hydrogen is generated by the oxidation of structural materials in reactors. In addition, in order to reproduce the actual conditions of an SA, actual spent fuel was used and the temperature profile during transportation was simulated (Fig.4-14). The spent-fuel sample was heated up to 2500 K and the released Sr and U were collected for quantitative analysis in the furnace. This analysis allowed the release fraction from the spent fuel and the transport fraction to the low-temperature region to be calculated.

The results showed that large amounts of Sr and U were released in hydrogen and steam atmospheres, respectively (Fig.4-14). This enhanced release can be well explained with the aid of chemical-equilibrium-calculation results, which revealed that Sr and U could exist in spent fuel as volatile chemical forms such as metallic Sr and UO_3. Moreover, Sr was found to be transported further to the low-temperature region. This implies the possibility that Sr may be transported to the primary containment vessel under a hydrogen atmosphere.

We will continue to obtain detailed data concerning chemical reactions during release and transport for continuous upgrading of the database.

Our research was accomplished as the collaborative study with the French Alternative Energies and Atomic Energy Commission (CEA).

Reference

Miwa, S. et al., Release and Transport Behaviors of Non-Gamma-Emitting Fission Products and Actinides in Steam and Hydrogen Atmospheres, Nuclear Engineering and Design, vol.326, 2018, p.143–149.

4–8 Improving the Reliability of Nuclear-Characteristics Prediction for Accelerator-Driven Systems

— Critical Experiment to Validate Nuclear-Data for Lead-Coolant on a Critical Assembly in the United States —

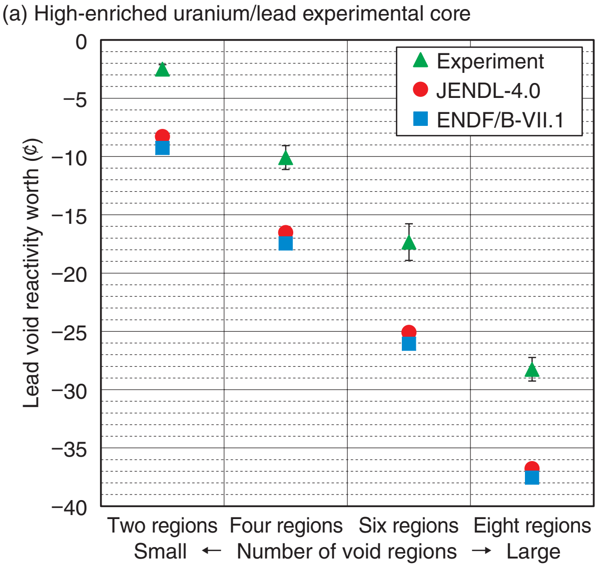
(a) High-enriched uranium/lead experimental core

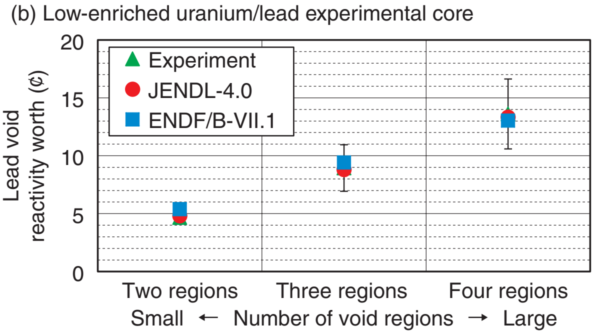
(b) Low-enriched uranium/lead experimental core

Fig.4-15 Comparison of experimental and calculated lead-void-reactivity worths

The results of the present experiment appear as green triangles (▲). The analytical results using the evaluated nuclear-data library developed by JAEA (JENDL-4.0) and the United States (ENDF/B-VII.1) are indicated as red circles (●) and blue squares (■), respectively. In the low-enriched uranium/lead experimental core, the experimental and analytical results overlap, indicating good agreement.

The high-level radioactive waste (HLW) remaining after removal of uranium (U) and plutonium (Pu) by reprocessing spent fuel emitted from nuclear power plants contains long-lived nuclides that continue to emit strong radiation for a long period of time. Thus, it must be buried in a stable stratum deeper than several hundred meters, so as not to affect the human living environment. In order to reduce the environmental burden of HLW, we have investigated a fast neutron system dedicated to transmutation (accelerator-driven system: ADS) that is capable of converting partitioned long-life nuclides with strong radiotoxicity into stable or short-lived nuclides by fission as a nuclear reaction with neutrons. We have considered using chemically stable lead bismuth for the ADS as a highly safe coolant. However, Japan has no experience with the use of lead bismuth as a nuclear reactor coolant, and the characteristics of the nuclear reaction (nuclear-reaction cross section) of lead have not been sufficiently verified. Therefore, in this research, we obtained new experimental data to validate the nuclear-reaction cross section of lead in fast neutron cores using a critical assembly in the United States.

In the ADS, fast neutrons generated by the spallation reaction of lead bismuth are gradually moderated by nuclear reaction with lead-bismuth coolant, leading to fission after being absorbed. Fast neutrons generated by nuclear fission are also used for the next fission reaction through a similar moderation process (fission chain reaction). Therefore, in order to correctly predict the neutron-mediated fission chain reaction in the ADS, it is important to accurately evaluate the nuclear-reaction cross section with lead in the coolant for neutron moderation. Moreover, the fission chain reaction exhibits different tendencies for different types of fuel. Therefore, we constructed two typical experimental cores (a high-enriched uranium (HEU)/lead-experimental core rich in ^{235}U and a low-enriched uranium (LEU)/lead-experimental core rich in ^{238}U) in this experiment. By removing (voiding) the lead from these experimental cores, we measured the influence (lead-void-reactivity worth) of the decrease in the amount of neutrons moderated by lead upon the fission chain reaction in the fast-neutron systems. Thus, the accuracy of the reaction between lead and neutrons can be verified by evaluating the change of the nuclear-fission chain reaction under the presence or absence of lead in each experimental core.

In the HEU fuel containing a large amount of ^{235}U, neutrons moderated by lead generally have a higher probability of fission than unmoderated fast neutrons. Therefore, the removing lead from the HEU/lead experimental core decreases the amount of moderated neutrons and then the fission chain reaction becomes less likely to occur. This resulted in a negative lead-void-reactivity worth in that core (Fig.4-15(a)). In the LEU-fuel rich in ^{238}U, on the other hand, unmoderated fast neutrons have a higher probability of fission than neutrons moderated by lead. Therefore, removing lead from the LEU/lead experimental core makes it easy for the fission chain reaction to occur: the lead-void-reactivity worth was observed to be positive (Fig.4-15(b)). In addition, these measurements were compared with the calculation values of lead-void-reactivity worth using nuclear-reaction cross-section data (nuclear data) developed by Japan and the United States. It was found that, in the LEU/lead experimental core, the calculation results well reproduced the experimental ones. In the HEU/lead experimental core, however, the calculation results overestimated the experimental values.

By this experiment, we acquired effective data for multidirectional validation of the nuclear-reaction cross sections of lead under changes to the type of fuel. We will continue cooperation between Japan and the United States to advance the research and the development on transmutation technology by expanding the experimental data for validating the nuclear-reaction cross section of lead in the fast-neutron system.

This study is a part of the collaborative result with the Los Alamos National Laboratory in the United States.

Reference

Fukushima, M., Oizumi, A. et al., Lead Void Reactivity Worth in Two Critical Assembly Cores with Differing Uranium Enrichments, Nuclear Science and Engineering, vol.189, issue 1, 2018, p.93–99.

4–9 A New Technique for Extracting Low-Power Proton Beams with a Laser

— Establishment of the Elemental Technology Required for the TEF —

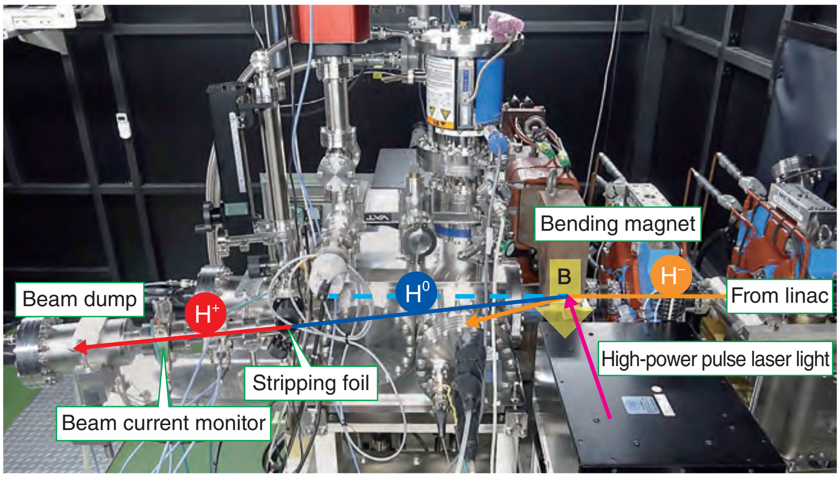

Fig.4-16 New type of laser-charge-exchange (LCE) device
LCE devices were installed at the end of the linac with an energy of 3 MeV. We performed laser injection (pink arrow) and beam bending (yellow arrow) in one bending magnet.

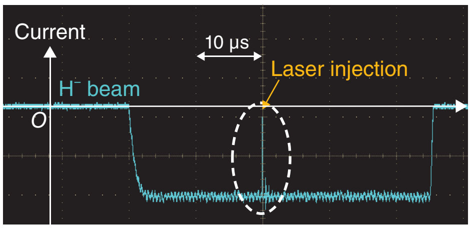

Fig.4-17 Disappearing current waveform of the H^- beam by the laser
When the laser is injected into the H^- beam (light-blue line) in the bending magnet, the H^- beam is neutralized and moves in a straight line. Then, the current of the H^- beam becomes zero and the current waveform disappears.

For the purpose of reducing the amount of high-level radioactive waste and toxicity to humans and the environment, we propose an accelerator-driven system (ADS) for transmuting long-lived nuclides into short-lived or stable ones. Since the ADS is a hybrid system of the proton linear accelerator (linac) and the nuclear reactor, various issues are inherent to research and development of the ADS. To conduct fundamental research on the ADS, we consider the Transmutation Experimental Facility (TEF) at J-PARC. At TEF, spallation-target technology is being developed using a high-power negative-hydrogen (H^-, 400 MeV/250 kW) beam. By extracting a low-power proton (H^+, 10 W or less) beam from the high-power H^- beam and introducing the H^+ beam to a zero-power critical assembly (i.e., a low-power nuclear reactor), nuclear characteristics related to the feasibility of ADS can be studied. Extraction of the low-power H^+ beam with long-term power stability is indispensable because the extracted H^+ beam drives the nuclear reactor and its safety. For a traditional beam-extraction system using a pulse electromagnet and/or stripping foil, unexpectedly high-power beam extraction occurs due to the abnormality of the electromagnet and the deformation of the stripping foil. It is difficult to extract a very weak proton beam stably. To extract a low-power H^+ beam with long-term power stability, we developed a new type of laser-charge-exchange (LCE) device and conducted the extraction experiment.

To eliminate the background protons, we performed laser injection and beam bending in one bending magnet, and LCE devices were installed at the end of the linac with an energy of 3 MeV (Fig.4-16). For the experiment, we set target values from the request of TEF, i.e., the power of the extracted H^+ beam was 5–10 W equivalent and the beam-power stability was within 5 %. Furthermore, in order to match with the operation schedule of J-PARC linac, the target value of the extraction time was 7 d (total: 56 h) or more. To produce such an H^+ beam, we have newly developed a high-power pulse-laser source (1.6 J/pulse, 25 Hz) synchronized with the repetition rate (25 Hz) of the H^- beam. We have also developed a laser-light-transport system capable of maintaining the irradiation position with high accuracy.

Using this system experimentally, we succeeded in extracting an H^+ beam of about 8 W equivalent for about 8 d (total 65 h) with a beam-power stability within about 3 % (Fig.4-17), achieving our initial goal. Thus, we established an elemental technology required for the TEF, i.e., the foundations of control technology for the extraction of the low-power H^+ beam from the high-power H^- beam at J-PARC with long-term power stability.

Reference

Takei, H. et al., Beam Extraction by the Laser Charge Exchange Method Using the 3–MeV LINAC in J-PARC, Plasma and Fusion Research, vol.13, special issue 1, 2018, p.2406012-1–2406012-6.

4–10 Plant-Safety-Measurement Enhancement

— A Study of Sheath Materials for Use on MI Cables during Severe Accidents —

Table 4-1 Evaluation of the damage time for sheath materials used in MI cables under air or air/H_2O mixtures at 1015 °C

Since the oxidation rate depended upon the parabolic path, it was calculated from the conservative initial exposure. Damage time was predicted based on the oxidation rate and the thickness of the sheath material of the MI cables. Thus, it was confirmed that the NCF600 damage time was four times longer than that of SUS316 at 1015 °C.

Material		SUS316		NCF600	
Condition		Air	Air/H_2O	Air	Air/H_2O
Oxidation time (mg/cm^2/h)		2.4	6.9	0.6	1.6
Damage time (h)	ϕ1.6 mm (thickness of sheath material : 0.23 mm)	77	27	325	122
	ϕ3.2 mm (thickness of sheath material : 0.32 mm)	107	37	453	170

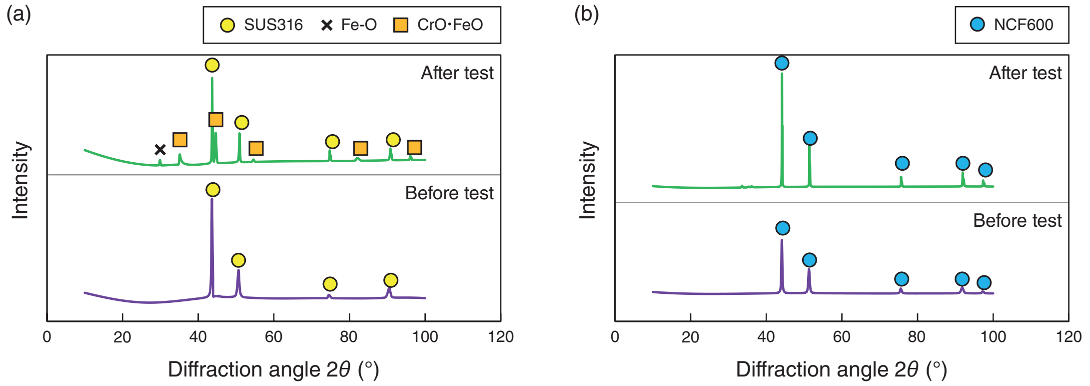

Fig.4-18 XRD analysis of specimen surfaces after exposure to mixed-gas atmosphere ($I_2/CO/O_2/H_2O$) at 800 °C for 96 h

The results show that there were constituent elements of the Fe-O and CrO·FeO matrix metals on the surface of SUS316 (a). Conversely, the oxides were not observed on the surface of NCF600 (b).

Polymeric materials are used to insulate and sheathe low-voltage cables in nuclear power plants. Lessons learned from the accident at the TEPCO's Fukushima Daiichi NPS show that it is necessary to develop new monitoring systems to prevent injuries during severe accidents (SAs). The reactor-vessel environment during an SA is thought to be complex, having high temperature, Fission Products (FPs), and atmospheric exposure; there is concern that damage to sheath materials will occur prematurely due to corrosion. Therefore, we started to research and develop that mineral-insulated (MI) cables with metal sheaths are capable of withstanding as signal cables for monitoring systems to be used in the case of SAs from based on knowledge of measurement technology development at the Japan Materials Testing Reactor (JMTR).

MI cables comprise insulators, core wires, and sheath materials. Among these, 316 stainless-steel (SUS316) or nickel-based (NCF600) alloys are selected as sheath materials because these withstand high temperatures and pressures, water vapor, oxidizing atmospheres, and high versatility.

First, in order to evaluate corrosion characteristics in an atmosphere without FP, the weight change was measured under air and a mixture gas of air and water vapor (air/H_2O), and the oxidation rate was calculated. From the oxidation rate and the thickness of the sheath material for the MI cable, the damage time of the NCF600 was found to be about 4 times longer than that of the SUS316, sufficient for performing measurements until the SA had passed (Table 4-1).

Second, when simulating the environment containing the FP of iodine gas (temperature 800 °C, exposure time 96 h), corrosion products were unevenly formed upon the surface of SUS316, and it was confirmed that peeling occurred readily. This result suggests that this environment has more complex corrosion characteristics than atmospheric air or an air/H_2O mixture. Conversely, a uniform oxide film was formed on the surface of NCF600; however, it was confirmed to be thin enough to be detected by X-ray-diffraction (XRD) analysis (Fig.4-18). Thus, NCF600 is expected to be a good material to use during SA.

From these findings, comprehensive evaluation of such features as the electrical characteristics under the radiation environment must be carried out to determine the basic specifications of the MI cable, and the applicability to the nuclear power plant must be examined.

The present study was a part of result of the R&D program for Plant Safety Enhancement "Research and development of high-performance monitoring systems for safety measurement of LWRs", supported by the Agency for Natural Resources and Energy under the Ministry of Economy, Trade and Industry (METI), Japan.

Reference

Nakano, H. et al., High-Temperature Oxidation of Sheath Materials Using Mineral-Insulated Cables for a Simulated Severe Accident, Mechanical Engineering Journal, vol.5, issue 2, 2018, p.17-00594-1–17-00594-12.

5 Applied Neutron and Synchrotron-Radiation Research and Development

Contributions to Developments in Science, Technology, and Academic Research Using Neutron and Synchrotron Radiation

In accordance with the Science and Technology Basic Plan formulated by the Government of Japan, we aim to contribute to the advance of science and technology and the promotion of industry in Japan through the production of innovative results using neutron and synchrotron radiation. We are utilizing the high-intensity proton accelerator at the Japan Proton Accelerator Research Complex (J-PARC) and the JAEA synchrotron-radiation beamlines at Super Photon ring-8 GeV (SPring-8) as well as upgrading neutron facilities and devices and pursuing world-leading research in fields such as nuclear energy and materials sciences that utilize neutron and synchrotron radiation.

(1) Research and development at J-PARC

J-PARC comprises a series of three proton accelerators, namely a linear accelerator (LINAC), a 3-GeV rapid cycling synchrotron (RCS), and a 50-GeV synchrotron, as well as three experimental facilities. The facilities include the Materials and Life Science Experimental Facility (MLF) for a wide range of research fields using neutron and/or muon beams, the Hadron Experimental Facility for nuclear and particle physics experiments using K-mesons and other particles, and the Neutrino Experimental Facility for T2K particle-physics experiments using neutrinos. All of these experimental facilities are open to users from across the globe (Fig.5-1).

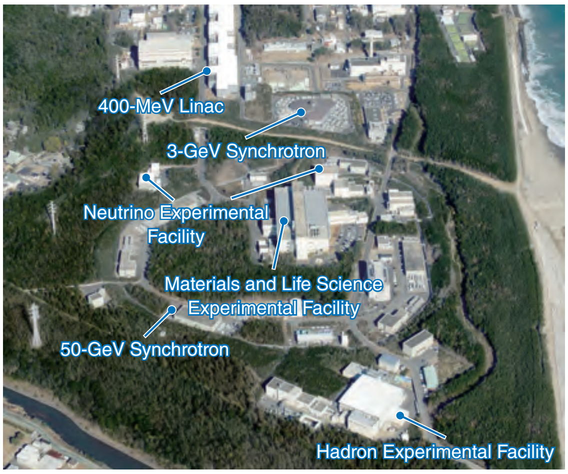

Fig.5-1 Japan Proton Accelerator Research Complex

In the accelerators, successive tests and component improvements were conducted to realize stable operation with a 1-MW beam. In the LINAC, the ion source achieved stable operation with an extraction-beam current of 40 mA for approximately 200 days. The RCS has been successfully used to test high-intensity proton-beam acceleration using multi-harmonic-beam loading by taking advantage of the frequency characteristic of the magnetic alloy (Topic 5-1).

In FY2017 at the MLF, the user program for eight scheduled run cycles (176 days) was successfully accomplished at 200–400 kW with an availability of over 90 %. The International Neutron & Muon School (49 people from 13 countries participated) were conducted using the neutron instruments and muon beamlines for materials and life-sciences researchers. With the BL19 TAKUMI Engineering Materials Diffractometer, the *in-situ* tensile-deformation behavior was successfully analyzed for lath martensitic steel containing a high dislocation density in order to elucidate the high-strength steel-material-reinforcement mechanism (Topic 5-2). To obtain a high-quality beam with a short pulse width and short decay time, the absorber material (Au–In–Cd alloy) was developed and its processing/bonding properties were demonstrated to further develop research on the structure, phase transition, and residual stress of materials (Topic 5-3).

(2) Research and development at the Materials Sciences Research Center (MSRC)

The MSRC aims to create innovative results and to seed research in a wide range of scientific, technological, and academic fields by developing and improving neutron and synchrotron-radiation instruments for advanced structural and functional analysis in Tokai (JRR-3 and J-PARC) and Harima (SPring-8).

In FY2017, we have established two new analytical methods using neutrons. One is a new way to determine the phase fraction in steel materials using the accelerator-driven compact neutron source, RANS, in collaboration with RIKEN and Tokyo City University. This method is expected to be used for basic research and development as well as quality-control procedures for steel materials without requiring large neutron experimental facilities such as J-PARC and JRR-3 (Topic 5-4). The other method is a demonstration experiment to simultaneously determine both atomic and spin-structures in materials by analyzing a neutron-transmission spectrum with Neutron Beamline for Observation and Research Use at BL10 of the MLF (Topic 5-5). We will commence a feasibility study using RANS because this method doesn't need intense neutrons. This development has been made in collaboration with J-PARC Center and the National Institute for Materials Science.

X-ray-absorption fine structure (XAFS) and imaging XAFS analyses (Fig.5-2) elucidated the chemical state of Rh, which was strongly affected by the distribution of Ru near Rh (Topic 5-6). This is useful for the secure manufacture and storage of waste glass, including platinum-group elements. *In-situ* and precise XAFS analysis, combined with cyclic voltammetry (CV), revealed the catalytic reaction at the electrode–electrolyte interfaces for fuel cells (Topic 5-7). Such operando measurements as CV-XAFS are becoming increasingly popular for materials science.

Fig.5-2 Experimental hutch No.3 at JAEA beamline BL22XU, SPring-8

5–1 High-Intensity Proton Acceleration Using a Broadband RF Cavity

— Investigation of Beam Instability Caused by Higher Harmonics —

Fig.5-3 RF Cavity for J-PARC 3-GeV Synchrotron
The cavity employs magnetic-alloy cores cooled by pure water directly, realizing a very high field gradient of 22 kV/m, which is more than twice as high as the conventional one. Furthermore, the cavity is driven by multi-harmonic RF voltages, owing to the broadband characteristics of the magnetic alloy.

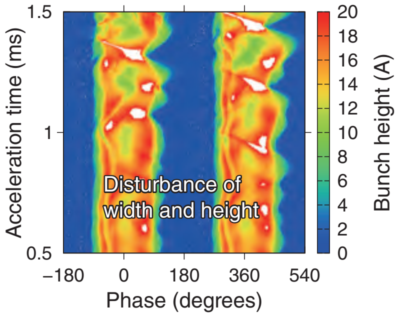

Fig.5-4 Observation of beam instability by a beam monitor
The bunch width becomes wider and narrower and the height alternates between becoming higher and lower just after acceleration commences. This phenomenon is considered instability.

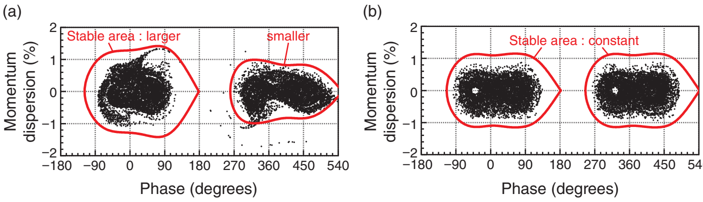

Fig.5-5 Observation of beam instability by a beam monitor
(a) The particle-tracking simulation suggests that the area which captures the beam stably alternatively becomes wider and narrower, causing beam instability. (b) The area is kept constant without instability.

J-PARC 3-GeV rapid cycling synchrotron (RCS) accelerates high-intensity protons with a repetition rate of 25 Hz. The proton beam is accelerated by an RF voltage generated at an acceleration cavity. We have developed a magnetic-alloy (MA)-loaded cavity (Fig.5-3) instead of a Ferrite one because the field gradient must be more than twice as high as the conventional one. Furthermore, we have realized multi-harmonic RF-voltage generation in a single cavity because of the broadband characteristics of the MA, and this is the first trial for the high-intensity proton synchrotron.

However, beam instability is observed with a beam loss when the beam power is close to 1 MW, which is the design value of the RCS. Fig.5-4 shows the mountain plot of the beam monitor. The RCS accelerates two bunches, and it can be seen that the width and height of these bunches oscillate in alternation. Analysis of the beam measurement suggests that the growth time of the instability is less than one tenth of that calculated by the well-known instability theory.

We think that this unknown instability may be caused by the cavity, which has broadband characteristics. The high-intensity beam generates a “wake voltage” at the cavity. The voltage disturbs the original acceleration voltage and causes beam loss. Although the compensation system for the wake voltage already has been prepared, it is believed that cancelling the main harmonics of the wake voltage will be enough for stable acceleration. However, the particle-tracking simulation suggests that the harmonics that were considered to be negligible in fact grow rapidly.

Fig.5-5 shows the simulation results. The protons are shown as dots and the stable acceleration area is shown as a red line. The upper graph indicates the case of instability. The stable area becomes larger and smaller in alternation and some protons are spilled out. The lower graph indicates the stable case, and the area is unchanged. We have confirmed that the broadband characteristics of the cavity cause this newly observed instability with the minor harmonics.

We have prepared a compensation system for the minor harmonics, and finally, we have achieved 1-MW beam acceleration.

Reference

Yamamoto, M. et al., Observation of Simultaneous Oscillations of Bunch Shape and Position Caused by Odd–Harmonic Beam Loading in the Japan Proton Accelerator Research Complex Rapid Cycling Synchrotron, Progress of Theoretical and Experimental Physics, vol.2017, issue 11, 2017, p.113G01–1–113G01–24.

5–2 Elucidation of the Strengthening Mechanism of High-Strength Steels by Pulsed-Neutron Analysis

— Dislocation Evaluation during Deformation of Lath Martensitic Steel —

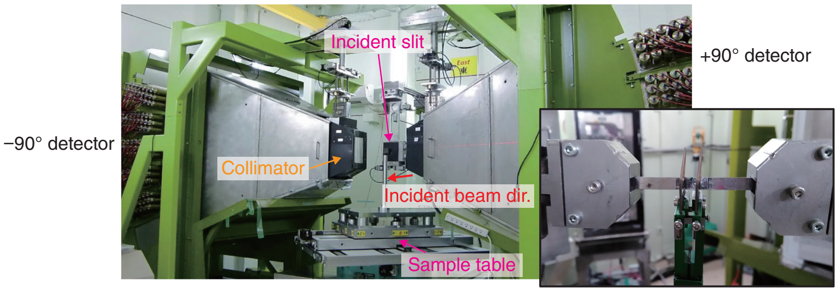

Fig.5-6 J-PARC high-resolution neutron diffractometer “TAKUMI”
The current status of TAKUMI and the setting for *in-situ* neutron diffraction during tensile deformation (photograph at the bottom right).

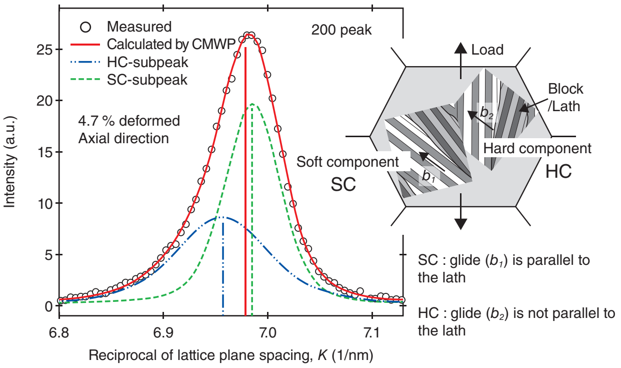

Fig.5-7 Typical diffraction profiles in the axial direction under tensile plastic deformation
The diffraction profile with good symmetry prior to plastic deformation becomes asymmetric after plastic deformation, owing to the presence of SC and HC, which behave differently.

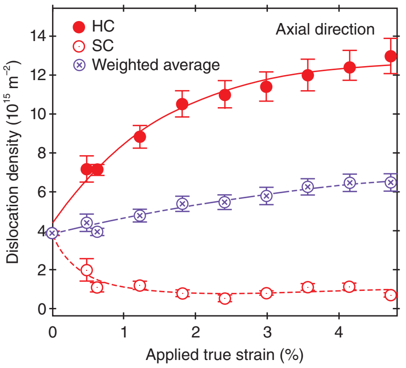

Fig.5-8 Change in dislocation density with respect to the strain amount of tensile deformation
The dislocation density decreases in the SC, along with work softening by the progress of deformation. On the other hand, the dislocation density in the HC increases, resulting in the work hardening.

When an Fe-C based alloy (steel) is quenched to room temperature from a high-temperature region wherein the austenite structure is stable, a rapid phase transformation occurs to form a martensite structure, accompanied by the high-density generation of defects called dislocations. This steel is called a martensitic steel and is well-known as a high-strength structural material. There are four forms of martensite: lath, butterfly, lens, and thin-plate-shape, which are produced depending on the content of carbon and the generation-temperature range. Among these, lath is most important for practical use as heat-treated steel. Lath is a band (lamellar) region of several tens of nanometers. Some laths form blocks, and blocks with the same orientation form packets. Lath martensitic steel shows a very large strength increase (work hardening) at the initial stage of plastic deformation. However, since the dislocation density is very high and the microstructure is fine in lath martensitic steel, the observation of microstructure variation by deformation using the electron-microscope technique is difficult, and the mechanism of large work hardening has yet to be elucidated.

We have developed a dislocation-evaluation method utilizing the high resolution of J-PARC neutron diffractometer “TAKUMI” (Fig.5-6) and applied this method to the analysis of data obtained from the neutron-diffraction experiment during tensile deformation of lath martensitic steel. The variations of dislocation density and dislocation arrangement during tensile plastic deformation were quantified to elucidate the mechanism of the large work hardening. Fig.5-7 shows the diffraction profile in the tensile direction under tensile plastic deformation. We found that the diffraction profile with good symmetry before deformation becomes asymmetric after plastic deformation. We succeeded in separating the asymmetrical peak in the dislocation-evaluation analysis using the so-called CMWP method into contributions from two subpeaks related to two different packets with different slip systems for plastic deformation. That is, we discovered the existences of soft packets (soft component: SC) and hard packets (hard component: HC) for dislocation gliding.

Through further detailed analyses, we also found that stress, dislocation density, and dislocation arrangement were distributed between the two packets. For example, in Fig.5-8, despite the already large dislocation density before deformation, that during deformation increased in HC and work hardening occurred, resulting a large increase in the stress. On the other hand, in SC, the dislocation density decreased and softening occurred. This indicates that HC plays an important role in work hardening. These results clarify the large work hardening in plastic deformation of lath martensitic steel.

Further improvements of this dislocation-evaluation-analysis method and TAKUMI will assist not only the development of advanced steel and other metallic materials but also in elucidating ancient metallurgical techniques such as the forging of Japanese swords by analyzing the crystallographic microstructures and dislocation properties.

Reference

Harjo, S. et al., Work Hardening, Dislocation Structure, and Load Partitioning in Lath Martensite Determined by *In Situ* Neutron Diffraction Line Profile Analysis, Metallurgical and Materials Transactions A, vol.48, no.9, 2017, p.4080–4092.

5–3 Supplying Pulsed Neutron Beams with Narrow Width and Short Decay

— Development of a Low-Activation Thermal-Neuron Absorber for Neutron-Beam-Pulse Shaping —

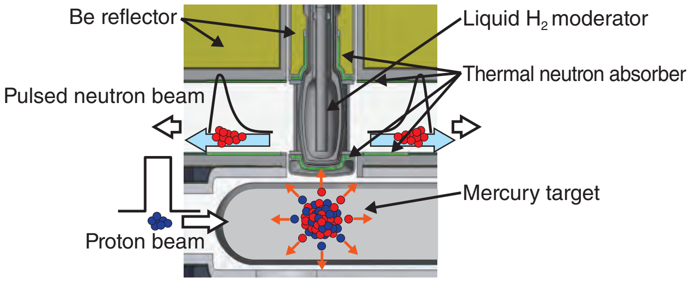

Fig.5-9 Cross section of a spallation neutron source
A thermal-neutron-absorber material is installed, encapsulating the moderator walls other than the neutron-emission surface to stop late-arriving slow neutrons from entering into the moderator.

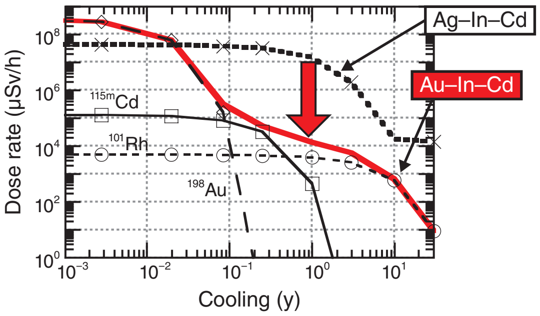

Fig.5-10 Radiation-dose rate of Au–In–Cd after 6 MW·y operation
Radiation-dose rate of Au–In–Cd decreases about three orders of magnitude lower than that of Ag–In–Cd at 1 m from surface after 1 year cooling after 6 MW·y operation.

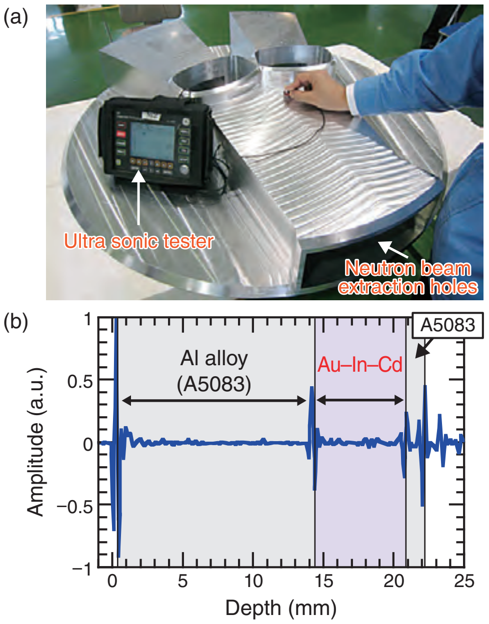

Fig.5-11 Photograph of the machined parts of the reflector after an HIP process (a) and a typical result of the ultrasonic test between the Au–In–Cd and A5083 plates (b)
Reflections were confirmed to be observed for all HIP boundaries of Au–In–Cd and A5083, respectively, around neutron-beam-extraction holes in ultrasonic-inspection measurement, yielding good bonding between Au–In–Cd and A5083.

In the 1-MW spallation-neutron source at J-PARC, cold and thermal neutrons are created by slowing of the fast neutrons produced by injection of high-intensity pulsed protons into a mercury target. These neutrons are provided to investigate material structure and properties. In particular, narrow pulsed neutron beams with short tails are important for high-resolution neutron experiments, such as identifying slight changes in the diffraction peaks caused by small changes in residual stress. Thermal-neutron-absorber materials, which absorb late-coming slow neutrons far from the moderator during neutron-slowing-down processes, can be effective for producing narrow-pulsed neutron beams with short tails. Such materials are installed to encapsulate the moderator walls aside from the neutron-emission surface as well as along the inner surface of the neutron-extraction-beam holes in a reflector assembly, as shown in Fig.5-9.

For a 1-MW neutron source, a combination of materials with different neutron-capture-resonance energies, such as silver (Ag), indium (In), and cadmium (Cd), was successfully implemented as the original thermal-neutron absorber, resulting in a new world record for resolution in powder-diffraction measurements. However, there is a disadvantage to using Ag–In–Cd alloy for periodic replacement of spent moderator and reflector, because it produces high residual radioactivity under neutron irradiation, such as ^{110m}Ag (half-life ($T_{1/2}$): 250 days) and ^{108m}Ag ($T_{1/2}$: 418 years) after every 6 MW·y operation, which correspond to a lifetime of structural material of moderator and reflector.

Alternative materials that offer lower residual activities have been investigated. As shown in Fig.5-10, we identified gold (Au), which was found to result in a residual radioactivity three orders of magnitude lower than that of Ag without sacrificing neutronic performance in terms of peak intensity, pulse width, and pulse tail. We also succeeded in developing a homogeneous ternary gold–indium–cadmium (Au–In–Cd) alloy.

The Au–In–Cd alloy needs to be bonded tightly to the aluminum alloy A5083, which is one of the structural materials of the moderator and reflector, because the installed regions are exposed to high heating under 1-MW operation. To form an effective thermal and structural bond between the Au–In–Cd and A5083 alloys, a hot-isostatic-pressing (HIP) method was applied. We found the optimal HIP conditions (a temperature range of 530–540 °C at the bonding surface and a 1-hour holding time under 100 MPa) for a small test size (c.a. 100 g), resulting in a bonding strength three times higher than required. However, there were still critical engineering issues to be resolved, including the fabrication of large Au–In–Cd-alloy pieces and their bonding to full-sized structural materials needed in the reflector assemblies. The large heat capacity of the actual reflector parts with a total weight of 500 kg (as opposed to the small test pieces) would affect their internal-temperature profiles during the HIP process, and would ultimately fail to satisfy the optimal HIP condition in the bonding area between the Au–In–Cd and A5083 alloys. We performed thermal analysis to achieve optimal conditions in the bonding area for actual-sized pieces and confirmed the internal temperature profiles experimentally. Finally, bonding between Au–In–Cd and A5083 alloys was successfully achieved by applying the results shown in Fig.5-11.

New developments of Au–In–Cd thermal-neutron absorbers will contribute not only to easing the handling and disposal of spent moderators and reflectors by reducing residual radioactivity but also to the development of research based on high-resolution experiments using pulsed neutron beams on such subjects as material structure, phase transitions, and residual stress.

Reference

Teshigawara, M. et al., Implementation of a Low-Activation Au-In-Cd Decoupler into the J-PARC 1 MW Short Pulsed Spallation Neutron Source, Nuclear Materials and Energy, vol.14, 2018, p.14–21.

5–4 Establishment of a Novel Analysis Technique for High-Performance-Steel Development

— Application of an Accelerator-Driven Compact Neutron Source in the Manufacturing Industry —

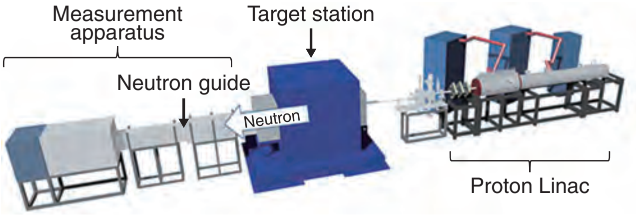

Fig.5-12 RIKEN accelerator-driven compact neutron source (RANS)
Neutrons are produced by a low-radiation-energy nuclear reaction through the collision of protons with a Be target in the RANS target station.

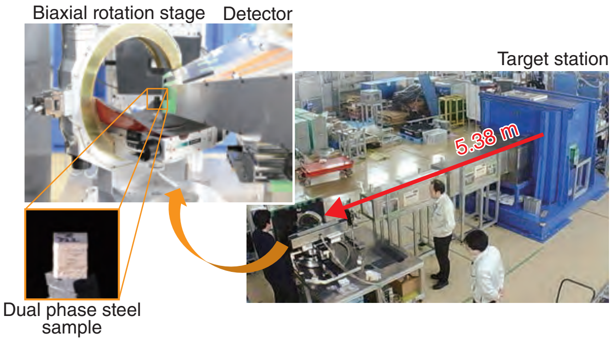

Fig.5-13 Diffractometer settled at RANS
A compact diffractometer composed of a biaxial rotation stage and neutron detectors is settled 5.38 m downstream from the RANS target station.

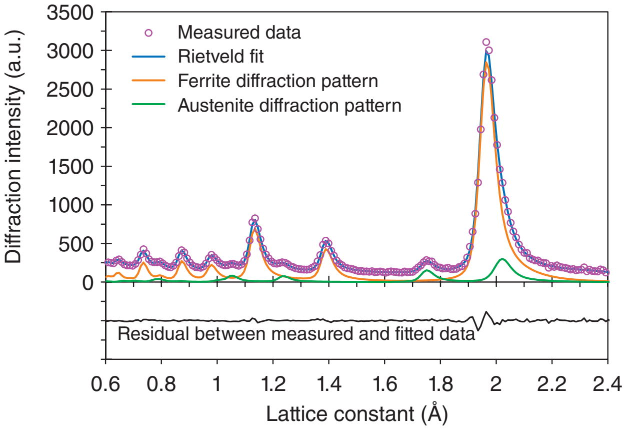

Fig.5-14 Diffraction pattern of a typical austenite/ferrite dual-phase-steel sample measured by RANS
The measured diffraction pattern (◯) is fitted to a theoretical diffraction pattern (—) by Rietveld analysis, and the volume fractions of ferrite (—) and austenite (—) phases in the sample are evaluated by comparing the intensities of their diffraction patterns.

The emission of greenhouse gases, including carbon dioxide (CO_2), must be reduced significantly to address the problem of global warming. It is therefore very important to increase vehicle fuel efficiency by reducing automobile-body weights. The application of high-tensile-strength steels is widely known as a solution to this problem, with their good balance with press/drawing formability, which is essential for such high-valued engineering materials. The retained austenite phase in steels is an important ductile microstructure for improving the bulk formability; thus, it is necessary to control and optimize the volume fraction of the austenitic phase for novel high-tensile-strength steels. Neutron diffraction is a highly statistical characterization technique for measuring the bulk-average volume fraction of steel because of the high penetrability of the neutron beam. However, a compact neutron source has not yet been used for this purpose, since the neutron flux is significantly lower than that of a large-scale neutron facility attached to a nuclear reactor or a proton accelerator. In this study, we have made great progress toward realizing neutron diffraction by a compact neutron source using the RIKEN accelerator-driven compact neutron source (RANS) shown in Fig.5-12, and to measure the volume fraction of the retained austenite.

A dual-phase steel sample with ferrite and austenite was utilized in this study as a reference material. A neutron-diffraction pattern can provide the necessary crystal-structure information concerning the ferrite and austenite phases, together with the austenite volume fraction by comparing the intensities of their diffraction peaks. In the construction of the diffractometer in RANS, the background noise is carefully eliminated to detect as many diffraction peaks as possible with low neutron-beam flux. In addition, the diffractometer is downsized to assure a high accessibility to the investigated sample and the optical apparatus on the diffractometer. Furthermore, a biaxial-rotation technique is employed to collect neutron-diffraction patterns from all stereographic directions of a sample, as shown in Fig.5-13. Using the above measurement system, the neutron-diffraction patterns of austenite and ferrite phases from all directions of the sample were reliably orientation-averaged over about 5 hours, as shown in Fig.5-14. As a result, the volume fraction of the austenite phase measured by RANS was 13.1 %, indicating only 1-2 % discrepancies with the 13.9 % value obtained by a well-established large-scale neutron facility (J-PARC TAKUMI). These comparisons suggest that neutron diffraction using RANS is viable for quantitative analysis of the volume fractions of crystal phases, revealing the bright application prospects of an in-house compact neutron source for the raw-material manufacturing industry, the automobile industry, etc.

In the future, the improvement of the neutron source and an increase in the neutron-detector area are expected to improve the measurement accuracy and shorten the measurement time. This neutron-diffraction-measurement technique using a compact neutron source may contribute to not only the rapid development and strict quality management of novel high-valued steels but also to the creation and optimization of other advanced structural and functional materials.

This research was accomplished as a collaborative study among RIKEN, Tokyo City University, and JAEA.

Reference

Ikeda, Y., Suzuki, H. et al., Development of On-Site Measurement Technique of Retained Austenite Volume Fraction by Compact Neutron Source RANS, Tetsu-to-Hagané, vol.104, no.3, 2018, p.138–144 (in Japanese).

5–5 Characterization of Spin Arrangement by Neutron Transmission

— For Observation under Extreme Environments and Mapping of Spin Arrangements —

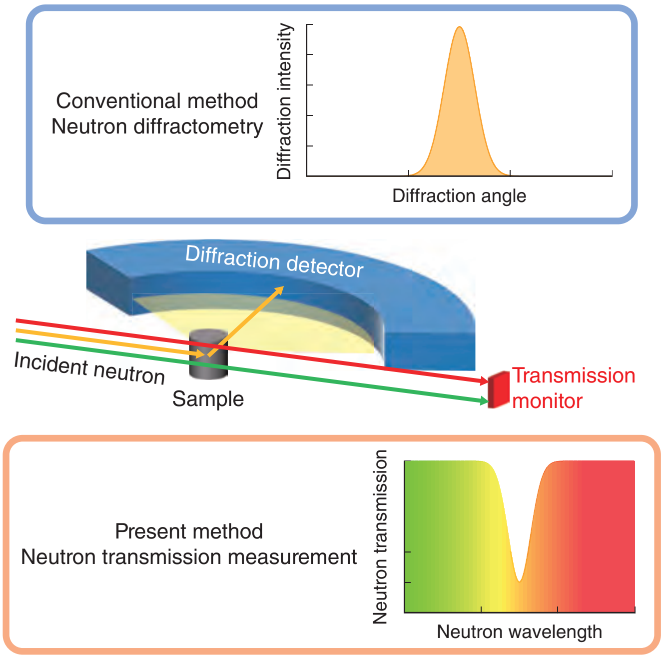

Fig.5-15 Scheme of comparison of neutron diffraction and neutron transmission
Neutron diffractometry requires a wider neutron-beam-path angle to detect diffracted neutrons, whereas only a small window is necessary for neutron-transmission measurement.

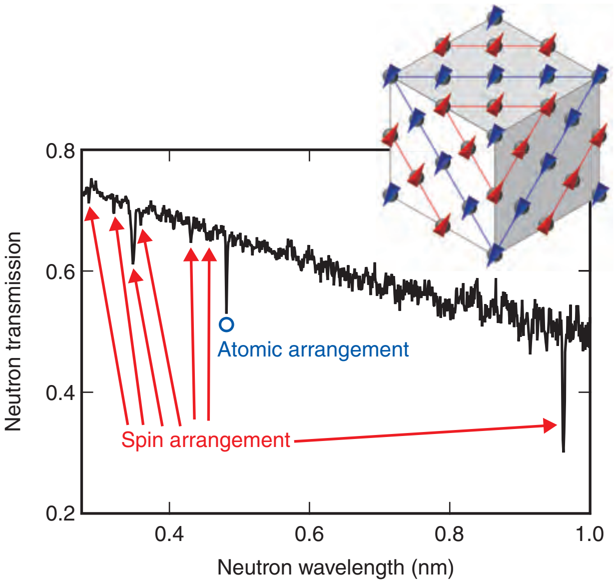

Fig.5-16 Neutron-transmission spectrum of single-crystal nickel oxide
The blue circle (○) shows the dip caused by an atomic arrangement. The dips indicated by red arrows (→) cannot be explained by the atomic arrangement, but are attributed to the anti-ferromagnetic-spin arrangement. The inset on upper right illustrates the anti-ferromagnetic spin arrangement in nickel oxide. Red (▲) and blue (▲) triangles represent upward and downward spins, respectively.

Neutron diffractometry is a powerful technique for characterizing atomic and spin arrangements from Bragg-diffraction patterns (Fig.5-15). Generally, the diffraction patterns are measured over a wider range of diffraction angles. On the other hand, the wavelength dependence (spectrum) of neutron transmission is also effective for characterizing the atomic and spin arrangements. The Bragg diffraction appears as dips in the neutron-transmission spectrum. Neutron-transmission measurement has an advantage in that it can be measured with only small windows. The neutron-transmission measurement is used to determine the atomic arrangements and is also applied to their imaging measurements.

Based on those previous studies using neutron transmission, we hypothesized that neutron transmission must also be useful for determining spin arrangements. For demonstration purposes, we performed neutron-transmission measurements for a typical spin arrangement. Fig.5-16 shows the neutron-transmission spectrum of a single crystal of nickel oxide (NiO), which is a typical anti-ferromagnet. The neutron-transmission spectrum of NiO exhibits several dips (Bragg dips) due to the spin arrangement (→), as well as the atomic arrangement (○). Similarly, the neutron-transmission spectrum of NiO powder shows step-like decreases called Bragg edges, which are caused by the anti-ferromagnetic spin arrangement (not shown).

These results reveal that neutron-transmission measurement is useful for characterizing spin arrangements. In particular, it is suitable for measurements under extreme sample environments, such as high pressure, high magnetic field, and ultra-low temperature, which often limit the window size for the diffracted neutron and thus prevent the neutron-diffraction pattern for the wide diffraction angle from being obtained. Furthermore, neutron-transmission measurement can be applied to imaging measurements of the spin arrangements inside magnetic-recording media.

Reference

Mamiya, H., Oba, Y. et al., Magnetic Bragg Dip and Bragg Edge in Neutron Transmission Spectra of Typical Spin Superstructures, Scientific Reports, vol.7, 2017, p.15516-1–15516-8.

5–6 Clarifying the Chemical State of Platinum-Group Elements in Borosilicate Glass

— Advanced Analysis of Correlations between Constituent Elements Using Imaging XAFS —

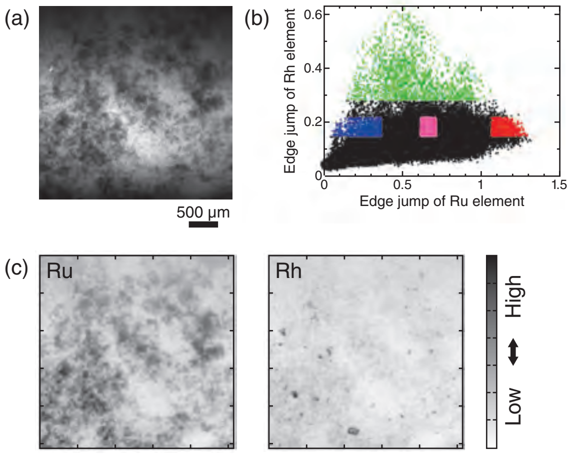

Fig.5-17 Distribution correlation between Ru and Rh elements in borosilicate glass
Imaging XAFS signals are obtained from the transmission X-ray image (a). The X-Y plot of absorption edge jumps corresponding to them (b) and the gray-scale mappings (c) are calculated from the imaging XAFS.

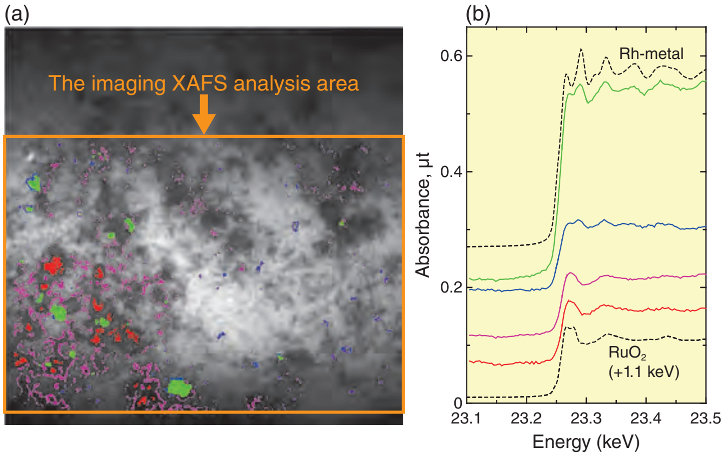

Fig.5-18 Imaging XAFS spectra derived based on the distribution correlation
The imaging XAFS spectra (b) are calculated from each area (a) selected based on the correlation information in the Fig.5-17(b). Comparison with the spectra of standard materials shows that the chemical form of Rh is oxide in a highly concentrated Ru area (Red), but it is metallic in the low-Ru-distribution area (blue).

The high-level liquid waste (HLLW) created by reprocessing spent nuclear fuel is mixed with molten borosilicate glass at high temperature inside a glass melter. Geological disposal of vitrified radioactive waste is planned after intermediate storage in Japan. Because there are more than 30 kinds of elements in the vitrified waste, some of their compounds are not contained stably in the borosilicate glass. It is very important to investigate the chemical state and coordination structure of these elements for safe management of vitrified waste. Synchrotron radiation-based X-ray absorption fine structure (XAFS) analysis, which offers high selectivity of specific elements and high sensitivity to diluted components, has been widely used in the chemical analysis of simulated vitrified waste. We have developed and used the imaging XAFS technique, which offers position sensitivity in addition to elemental selectivity. The distribution of each element and the XAFS signals corresponding to selected pixels on the transmission X-ray image are obtained through imaging XAFS analysis. It is known that platinum-group metals (PGM; Ru, Rh, and Pd) are aggregated in borosilicate glass because of their low solubility: they settle down and are deposited at the bottom of the glass melter. This is a typical problem in the vitrification process. Therefore, we study the behavior of PGM elements in borosilicate glass using the imaging XAFS technique in cooperation with the TRP Decommissioning Center.

Fig.5-17 shows imaging XAFS analysis results for borosilicate glass containing simulated HLLW components. It is clear from the two mapping figures that the distributions of Ru and Rh elements are not uniform but are rather aggregated in the glass sample. This behavior is already documented and need not be investigated using a synchrotron facility. The additional remarkable feature of this study is that the imaging XAFS spectrum was obtained separately based on correlation information of the Ru and Rh distributions. The chemical state of Rh in borosilicate glass is usually a mixture of Rh metal and its oxides. It has been reported that the only Rh oxide detected was RhO_2, while the Rh_2O_3 that was expected thermodynamically was not detected in the borosilicate glass.

The X–Y plot of the absorption edge jump values for Ru and Rh, as obtained he from the XAFS spectra for each pixel on the transmission X-ray image, are shown in Fig.5-17(b). We selected three areas in the figure: (1) the red area, where a lot of Ru is distributed; (2) the blue area, where little Ru is distributed; and (3) the green area, where a lot of Rh is distributed. Since each point of the X–Y plot and pixel on the image form a pair, we can identify pixels corresponding to the selected area shown in Fig.5-18(a). The imaging XAFS spectra obtained from the X-ray intensities of the three selected areas (red, blue, and green) are shown in Fig.5-18(b). Imaging XAFS analyses showed that the chemical form of Rh was mainly RhO_2, where the concentration of Ru was very high (red area) and metallic when the Ru concentration was low (blue area). In the very highly concentrated Rh area, its chemical form was metallic.

These results suggest that the chemical form of Rh is basically metallic in the borosilicate glass but becomes RhO_2 where its distribution accords with that of Ru. The chemical state of Rh in the vitrified waste is more strongly controlled by the distribution correlation with Ru elements, rather than the thermodynamic properties of Rh compounds. We will use the imaging XAFS technique to clarify the complicated chemical behavior in the vitrified waste and contribute to the advancement of vitrification technology.

This work was supported by the Japan Society for the Promotion of Science (JSPS) KAKENHI Grant-in-Aid for Scientific Research (C) (No.15K04739).

Reference

Okamoto, Y. et al., Chemical State Analysis of Rhodium in Simulated Waste Glass by Synchrotron-Radiation-Based XAFS and Imaging XAFS Techniques, Transactions of the Atomic Energy Society of Japan, vol.16, no.4, 2017, p.180–190 (in Japanese).

5–7 Change of the Oxidation State of Fuel Cell Catalysts during Reactions

— Surface Structure of Metal Nanoparticles Revealed by Synchrotron X-ray Absorption Spectroscopy —

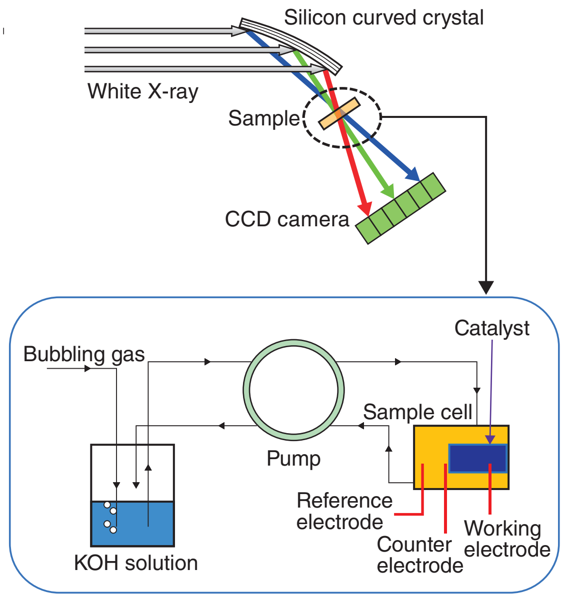

Fig.5-19 Schematic pictures of X-ray-absorption spectroscopy system
X-rays are produced over a wide energy band when a polychromator is illuminated by white X-rays. This system enables us to observe X-ray-absorption spectra in a short time. We have succeeded in determining the structure change of catalysts during reactions with sample cells that can control the electric potential of electrocatalysts in solution.

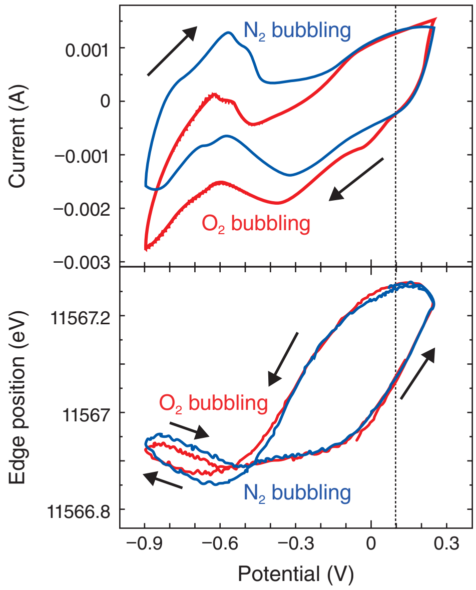

Fig.5-20 Simultaneous observation results of electric current and X-ray-absorption-edge position
The electric current and X-ray-absorption-edge position during a potential sweep are displayed. The current change demonstrates the manner of the electrocatalytic reaction and the X-ray-absorption-edge position indicates the surface-oxidation state of platinum-nanoparticle catalysts. This simultaneous observation reveals the surface-oxidation state of platinum catalyst during a catalytic reaction.

Fuel-cell development has attracted a great deal of attention for a long time. Fuel cells have the advantage of not discharging any carbon dioxide at all during power generation; however, they also have some drawbacks, such as using precious platinum metals as electrocatalysts. Platinum is considered to be degraded by oxidation and it is important to investigate how platinum-metal catalysts are oxidized during fuel-cell operation.

X-ray-absorption spectroscopy is an element-selective technique, which means that only structural information about platinum can be obtained among all electrode components. The oxidation state is determined by the position of the X-ray-absorption edge. Fig.5-19 shows the outlines of the dispersive X-ray-absorption-spectroscopy-observation system, as well as the sample setting adopted in this study. While we have to change X-ray energy by moving the monochromator in the normal case, the displayed system can detect absorption spectra without any mechanical-motion process; this means that absorption spectra can be measured within a short time. We have utilized this system for high-speed observation of time-resolved X-ray-absorption spectroscopy with a sweeping electric potential in order to reveal the oxidation states of the platinum-metal catalyst during electrocatalytic reactions.

The oxygen-reduction reaction is considered to be a rate-limiting process for fuel-cell operation. In this experiment, oxygen bubbling was applied to the solution in which the electrode was immersed to realize the oxygen-reduction reaction, and compared with the result of nitrogen bubbling that purges oxygen gas. Fig.5-20 shows the electric current caused by the catalytic reaction and the absorption-edge-position of platinum determined by X-ray-absorption spectroscopy measured at the same time. As the potential is reduced from the high-potential side, the current with oxygen bubbling increases in the negative direction under 0.1 V. This is due to a new current caused by the oxygen-reduction reaction. At this reaction-onset potential, the position of the X-ray-absorption edge retains a relatively high value, indicating that the surface of the platinum catalyst is covered by the oxide layer when the oxygen-reduction reaction starts, because the higher the position of the absorption edge, the more that the platinum catalyst is oxidized. It was also found that the reduction reaction of the oxide layer of the platinum-catalyst surface was inhibited by the presence of oxygen gas. The absorption-edge positions decrease as the potential is lowered, but the oxygen-bubbling case shows a gentler slope.

This study has revealed the oxidation state of the platinum catalyst at the reaction-onset potential. We believe that these results will lead to the development of a high-performance catalyst that expands the oxygen-reduction reaction to the higher-potential side.

This work was supported by the Japan Society for the Promotion of Science (JSPS) KAKENHI Grant-in-Aid for Young Scientists (B) (No.16K17540).

Reference

Kusano, S., Matsumura, D. et al., Study of Catalytic Reaction at Electrode–Electrolyte Interfaces by a CV–XAFS Method, Journal of Electronic Materials, vol.46, issue 6, 2017, p.3634–3638.

6 HTGR Hydrogen and Heat Application Research

Research and Development of HTGR, Hydrogen Production, and Heat Application Technologies

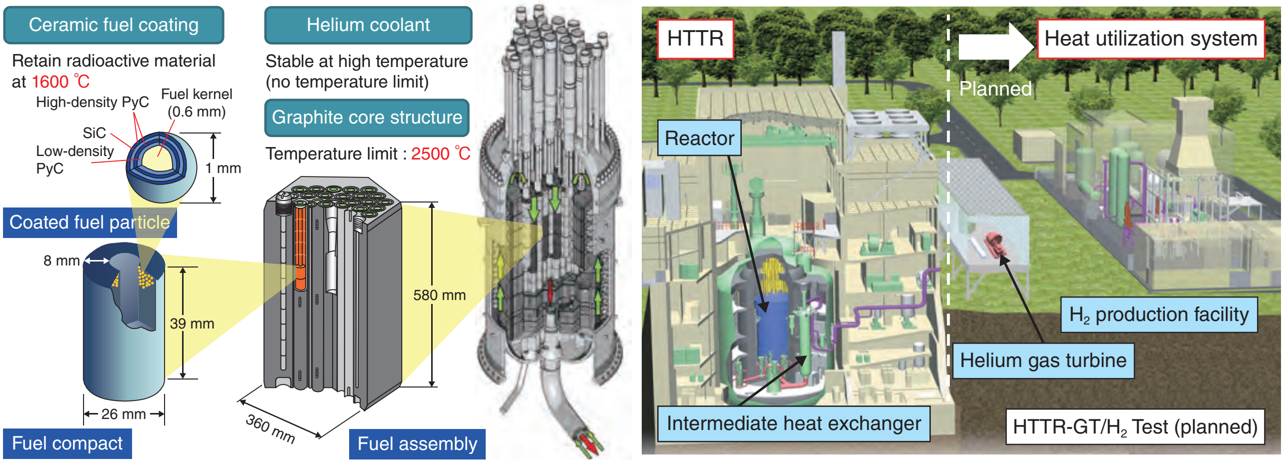

Safety

- Ceramic-coated fuel with excellent heat resistance
- Mild temperature transient in accident with graphite moderator
- Helium gas with chemical inertness

No core meltdown occurs in principle with these features

Economy

Waste heat reduction by cascaded heat utilization (heat utilization ration : 80 %)

Simple and highly efficient system by gas turbine (efficiency : 50 %)

Environmental load reduction

Small amount of waste by high burn-up fuel and highly efficient power generation

Control of global warming by CO_2-free hydrogen production

Fig.6-1 Features of HTGR
The HTGR is a helium gas-cooled, graphite-moderated thermal-neutron reactor with excellent inherent safety features.
The HTGR meets various heat application requirements such as hydrogen production and power generation.

Japan's energy–supply–demand structure is fragile because of its excessive dependence on imported fossil-fuel resources. To remedy this situation while simultaneously reducing the greenhouse-gas emissions that cause global warming, Japan is advancing the use of safe nuclear energy. The High Temperature Gas-cooled Reactor (HTGR) is a nuclear reactor with various industrial uses, such as high efficiency power generation by a helium gas turbine, hydrogen production, and seawater desalination (Fig.6-1). "Chapter 3. Promotion of technology development, 2. Technical challenges to be addressed" of the 5th Energy Basic Plan, which was decided by the Cabinet in July 2018, mentions that "Under international cooperation while looking at overseas market trends, GOJ also facilitates R&D of nuclear technologies that serves the safety improvement of nuclear use, such as HTGRs which are expected to be utilized in various industries including hydrogen production and which has an inherent safety".

The industry, academic body and government council established by the Ministry of Education, Calture, Sports, Science and Technology (MEXT) is developing strategies for commercializing HTGRs and deploying Japanese HTGR technologies overseas. Last year, a cooperation policy and domestic organization structure was established for an experimental and commercial reactor in Poland. We aim to maintain the most advanced HTGR technology in the world, cultivated through the design, safety review, construction, operation, maintenance, and safety evaluation of Japan's first HTGR in Oarai Town. These operations will follow Japan's new regulation standards for the High Temperature engineering Test Reactor (HTTR). The plant will be constructed by overseas projects and returned to our country in future.

The HTTR, constructed using domestic technology, is the only HTGR worldwide that can extract 950 °C heat from the reactor. The HTTR attained a reactor outlet temperature of 950 °C in 2004 and continuously operated at that reactor outlet temperature for 50 days in 2010. The inherent safety features of the HTGR were also confirmed in a loss-of-forced-cooling test in 2010, without inserting the control rod. In these tests, the reactor intrinsically shut down and maintained a stable state.

Currently, JAEA is conducting an accident progression analysis of the HTGR during extreme seismic events, studying the reduction of radioactive waste using the HTGR characteristics, testing the ZrC coating for oxygen sequestering, developing a passive-radiative cooling facility for the HTGR, and improving the neutron-startup source exchange work of HTGR (Topics 6-1–6-5). The heat from the HTGR has been utilized in iodine, sulfur and hydrogen production by a thermochemical water-splitting process (Topic 6-6). Finally, an HI decomposition membrane reactor that improves the hydrogen production efficiency has been developed, and its applicability has been evaluated on industrial materials (Topic 6-7).

Owing to the inherent safety features of HTGR, the HTTR is expected to restart its operation without confirming compliance with the new regulation standards, and without large-scale modification or reinforcement. We are now steadily making the final preparations before restarting the HTTR operation.

6–1 Exploring High Temperature Gas-Cooled Reactor Safety

— Accident Progression Analysis of HTGR during Extreme Seismic Events —

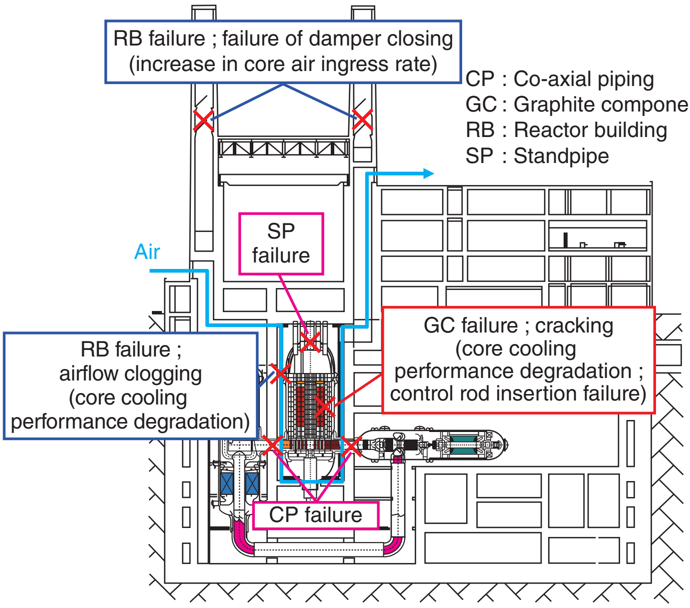

Fig.6-2 The worst accident scenario induced by seismic events
We consider failures in coaxial piping (CP) and standpipes (SPs), the core air ingress, and degradation of the core cooling performance due to a reactor building (RB) failure. We also examine core-cooling degradation and failure of control rod insertion caused by graphic component (GC) failure.

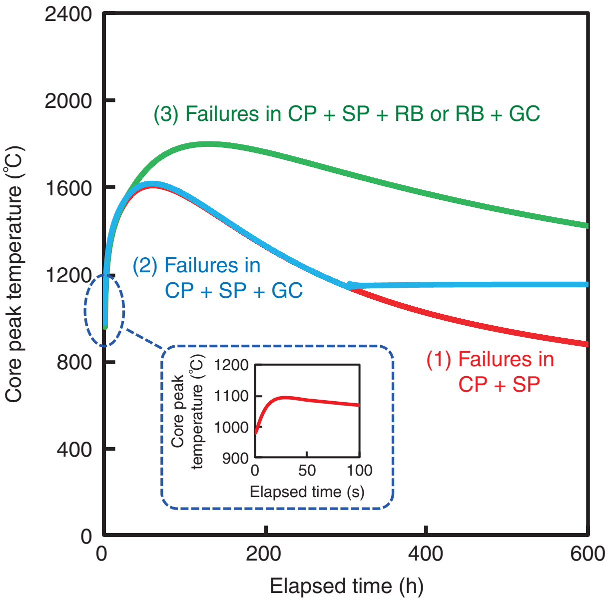

Fig.6-3 Core peak temperature behavior during failures in RB and GC
Increase in core peak temperature caused by degradation of core cooling performance due to a RB failure (3). Curves (1) and (2) show the core cooling behavior without a RB failure. In (2), the core peak temperature remained constant after the advent of re-criticality because the rod insertion was prevented by a GC failure.

Towards commercial deployment of High Temperature Gas-cooled Reactor (HTGR), it is necessary to confirm safety for high-consequence, low-probability accidents. To identify the cliff-edge effect, a severely abnormal plant behavior caused by an abrupt transition from one plant status to another following a small deviation in a plant parameter, we investigate the worst accident scenario for public dose at the site boundary.

We select simultaneous failures in the co-axial piping (CP) and the standpipes (SPs), cylindrical structures containing the control rods. This scenario maximizes the air ingress rate into the core. We also assume that the situation is compounded by multiple failures in the reactor building (RB) and graphite component (GC) (Fig.6-2). The control rod floats due to blow down of the reactor coolant through the SP failure points, and air enters the RB because the damper does not close. The flow path inside the RB which is installed for passive reactor cooling is clogged. Subsequent cracking in the graphite components prevents insertion of control rods and degrades the cooling performance of the reactor.

By analyzing the accident progression in the above scenario, we showed that the reactor automatically shuts down for a short duration after the power escalation, limiting the core-temperature increase to below 120 °C (Fig.6-3). Initially, the decay heat gradually increases the peak core temperature, but is eventually dissipated into the atmospheric air and/or the earth by thermal conductance and radiation through structures. During several dozens to hundreds of hours after the accident, the peak core temperature monotonically decreases (Fig.6-3(1) and (3)) because the dissipation heat rate exceeds the decay heat generation rate of the core. The peak core temperature never reaches 1900 °C, the temperature at which the fuel integrity was experimentally confirmed to be maintained, even during an RB failure (3). After the advent of re-criticality, which occurs a few hundred hours after an accident causing a GC failure (2), the summed heat generation rates of decay and the fission reaction balance the core thermal dissipation rate, so the core peak temperature remains constant. The amount of radionuclide released from the top of the RB is the same in each case. On the other hand, the quantity of radionuclide released by RB leakage at the ground level is higher during a RB failure than the case without failure. According to the integrated value of public dose for three-months, the duration to the reactor cold condition, is approximately six times higher for the case with failure (3) than in the case without failure ((1) and (2)) because the high peak core temperature increases the diffusivity of the radionuclides in the fuel coating. However, no cliff-edge effect is observed even in the worst-case scenario.

The present study was a part of result of the “Probabilistic Risk Assessment Method Development for High Temperature Gas-cooled Reactors”, supported by the Ministry of Education, Culture, Sports, Science and Technology (MEXT), Japan.

Reference

Sato, H. et al., Probabilistic Risk Assessment Method Development for High Temperature Gas–Cooled Reactors (1) Project Overviews, Proceedings of 2017 International Congress on Advances in Nuclear Power Plants (ICAPP 2017), Fukui and Kyoto, Japan, 2017, paper 17078, 7p., in CD–ROM.

6–2 Environmental Burden Reduction by High Temperature Gas-Cooled Reactor

— Study on Reducing Radioactive Waste by Utilizing the Characteristics of HTGR —

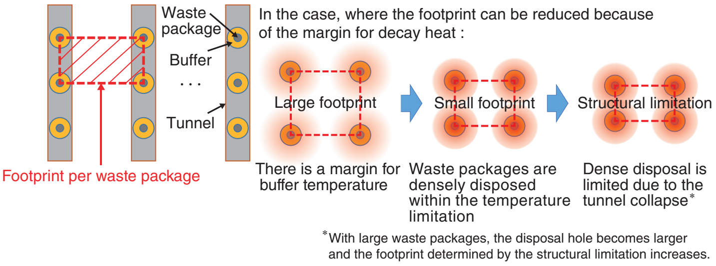

*With large waste packages, the disposal hole becomes larger and the footprint determined by the structural limitation increases.

Fig.6-4 Concept of repository footprint
The repository footprint can be reduced by densely arranging the disposal within the range where buffer temperature does not exceed 100 °C. Meanwhile, the footprint reduction is structurally limited. In direct disposal, the footprint is enlarged by the large canister.

Table 6-1 Comparison of number of high-level radioactive waste generations per 1 TWeh electricity generation and repository footprint
The waste package generation and footprint of HTGR and LWR are compared during direct disposal and disposal with reprocessing. In these cases, the repository footprints are determined by structural limitations and depend on the size of canister.

Reactor specification	LWR (PWR)	HTGR	Superiority
Burn-up (GWd/t)	45.0	119.5	3 times
Thermal efficiency (%)	34.5	45.6	+32 %
Direct disposal	LWR (PWR)	HTGR	Superiority
Number of waste packages generated (canister/TWeh)	2.92	1.20	−59 %
Repository footprint per waste package (m^2/canister)	192 (structural)*	204 (structural)*	–
Repository footprint (m^2/TWeh)	560	244	−56 %
Vitrified waste (reprocessing)	LWR (PWR)	HTGR	Superiority
Number of waste packages generated (canister/TWeh)	3.40	2.32	−32 %
Repository footprint per waste package (m^2/canister)	90 (structural)*	90 (structural)*	–
Repository footprint (m^2/TWeh)	306	209	−32 %

* Structural limitation.

Table 6-2 Optimization of HTGR radioactive waste and disposal method
We optimized HTGR waste disposal shown in Table 6-1 to reduce the waste volume and footprint. The repository footprint is significantly reduced by 50 % in direct disposal, by 80 % in disposal with reprocessing, and by 90 % in disposal with partitioning.

Direct disposal	Representative	Optimized case	Superiority	–	
Disposal method	Vertical	Horizontal	–	–	
Cooling time (year)	54	94	–	–	
Repository footprint per waste package (m^2/canister)	204 (structural)*[1]	104	−49 %	–	
Repository footprint (m^2/TWeh)	244	125	−49 %	–	
Reprocessing	Representative	Optimized case	Superiority	Partitioning	Superiority
Disposal method	Vertical	Horizontal	–	Horizontal	–
Duration before reprocessing (year)	4	5.5	–	4	–
Cooling time (year)	54	94	–	154	–
Number of waste packages generated (canister/TWeh)	2.32	1.77	−23 %	0.83*[2]	−64 %
Repository footprint per waste package (m^2/canister)	90 (structural)*[1]	20 (structural)*[1]	−78 %	29*[3]	−68 %
Repository footprint (m^2/TWeh)	209	36	−83 %	24	−88 %

*[1] Structural limitation.
*[2] It includes vitrified waste and Sr-Cs waste.
*[3] Sr-Cs waste is determined by structural limitation, and vitrified waste is determined by decay heat from Minor Actinoid (MA).

Waste problems are important in nuclear power generation. The safety of waste disposal is ensured by limiting the public dose leaked from corroded waste packages. However, reducing waste volume is important for reducing required repository footprint.

The Fission Products (FPs) of electricity generation by High Temperature Gas-cooled Reactor (HTGR) is approximately 70 % of that generated by Light Water Reactor (LWR), because the high-temperature characteristics of HTGR confer excellent thermal efficiency. Exploiting these advantages, we aim to reduce the waste volume and hence the environmental burden of the reactor. After direct disposal, the coated particle fuel can highly confine the FPs and have high-temperature resistance; these are advantageous for cooling during storage as well.

The vitrified waste is placed into a canister (hereafter referred to as waste package), surrounded by buffer materials and disposed of into the geology. A similar disposal procedure is assumed for spent fuel. To prevent the buffer material from deteriorating under the decay heat from the waste, the temperature must be maintained below 100 °C. For this reason, the pitch between waste packages is reduced within a range not exceeding the limit temperature, and the repository footprint is also reduced (Fig.6-4).

The waste package generation per unit of electricity generation is shown in Table 6-1. The footprints per waste package are determined by structural limitations, so are proportional to the canister size. The number of waste package generations and the repository footprint of HTGR is approximately 60 % lower in direct disposal, and 30 % in disposal with reprocessing, than in LWR. In disposal with reprocessing, the waste generation is reduced by the excellent thermal efficiency; in direct disposal, it is reduced by the nuclear characteristics, which reduce the generation of TRansUranium (TRU) element per energy release.

Next, we investigated the optimum conditions of waste volume and footprint reduction by referring to HTGR waste generation. We adopted a horizontal emplacement to avoid the structural limitation. In direct disposal, the footprint can be reduced by half, with 94 years cooling time before disposal (Table 6-2). After the period, FPs with short half-life decay. the decay heat is dominated by TRU with a long half-life, so extending the cooling time is ineffective. In disposal with reprocessing, delaying the reprocessing by only 1.5 years reduces the number of vitrified waste packages by 20 %. After cooling for 94 years (reaching the structural limitation), the footprint of disposal is reduced by 80 %. Finally, we investigated a group partitioning technology. Sr–Cs separation generates another waste product, but reduces the number of waste packages (including the Sr–Cs waste) by 60 %. After 154 years of cooling, the footprint is reduced by 90 %.

In this way, we confirmed that HTGR dramatically reduces the waste volume, and hence the environmental burden.

Reference

Fukaya, Y. et al., Optimization of Disposal Method and Scenario to Reduce High Level Waste Volume and Repository Footprint for HTGR, Annals of Nuclear Energy, vol.116, 2018, p.224–234.

6–3 Enhancing the Safety of Plutonium Burner High Temperature Gas-Cooled Reactor

— Test of ZrC Coating as an Oxygen Getter —

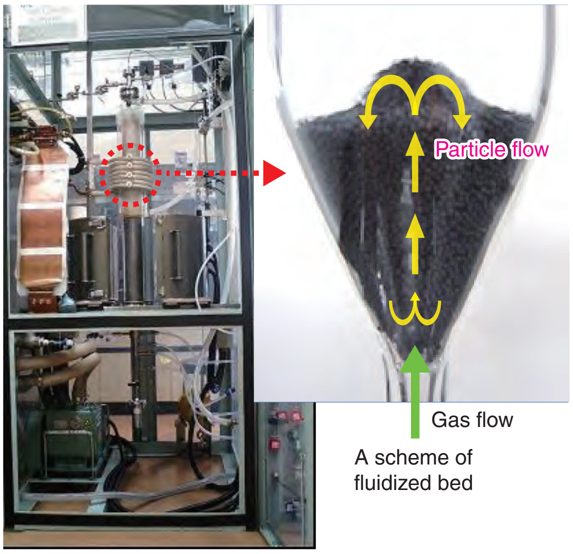

Fig.6-5 ZrC coater constructed by JAEA
A ZrC layer with a C/Zr ratio of 1.0 is directly coated onto particles in a fluidized bed under zirconium bromide and methane source gases. The coating method is chemical vapor deposition at above 1300 °C.

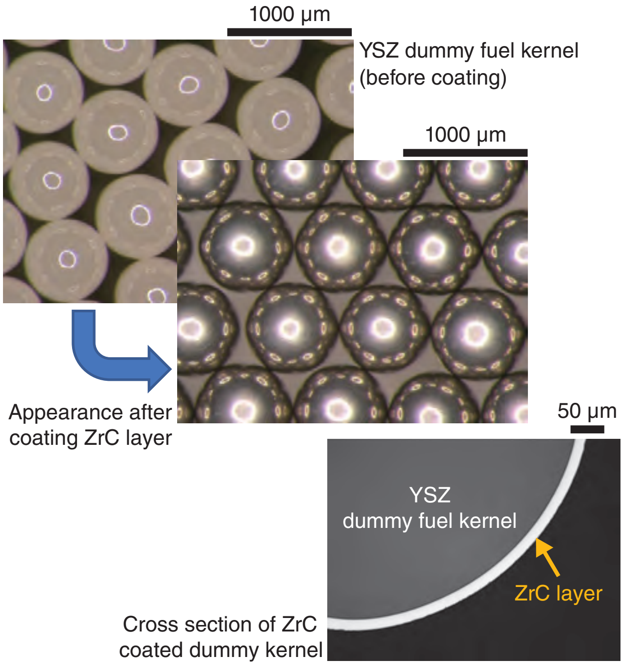

Fig.6-6 Appearance and cross section of ZrC layer obtained by coating test
The ZrC surface has a metallic appearance, unlike SiC and other carbide ceramics.

Plutonium (Pu) extracted by reprocessing from the spent fuel of the light water reactor (LWR) is planned for reuse as MOX fuel in both the LWR and the fast breeder reactor. With its inherent safety features, the High Temperature Gas-cooled Reactor (HTGR) is expected to reduce Pu safely, reduce the risk factors of core melting accidents. On the other hand, the burnup of reprocessed Pu fuel comprising more than 60 % fissile material is 600 GWd/t, one order of magnitude higher than that of conventional uranium fuel. From a nuclear security and safety perspective, resistance to nuclear proliferation and maintenance of integrity under very high burnup conditions is important when applying Pu as an HTGR fuel.

The HTGR uses characteristic coated fuel particles (CFPs) with diameters below 1 mm. Each particle consists of a fuel kernel with an approximate diameter of 0.5 mm covered by quadruplet ceramic layers made from carbon (C) and silicon carbide (each 25–45 μm thick). The Pu is very difficult to reprocess, as it is dispersed in an inert matrix of yttria-stabilized zirconia (YSZ) which greatly increases the nuclear security over conventional oxide fuels. However, the free oxygen generated by fission increases the internal gas pressure, causing additional CFP failure that inhibits the extended burnup of the CFP. Therefore, the CFP should be maintained intact under very high burnup conditions.

To enhance the safety of Pu burner HTGR fuel (3S-TRISO fuel) under extended burnup, we developed a technology that directly coats zirconium carbide (ZrC) on the fuel kernel. The refractory ZrC sequesters free oxygen, preventing the increase of partial pressure of oxygen in the CFP, and controlling the compositions of carbon and zirconium. Most importantly for obtaining stoichiometric ZrC, the C/Zr ratio is controlled at 1.0. Thus, we have been investigating the chemical vapor deposition conditions of ZrC by the bromide method. The ZrC coater developed by JAEA was evaluated in several coating tests, as shown in Fig.6-5.

To optimize the conditions of the stoichiometric ZrC coating, we first needed to improve the conventional condition, which is optimized to reduce excess free-carbon in ZrC coated on C coating. Here, we studied the temperature distributions in the reactor using particles coated with different ZrC compositions. The coating tests were conducted under carefully controlled conditions in a fluidized bed. The desired output (600 GWd/t) was achieved by YSZ dummy fuel kernels twice coated with a stoichiometric ZrC layer (approximate thickness: 21 μm; target value: 10 μm), as shown in Fig.6-6.

Hereafter we will fabricate a new dummy fuel kernel containing cerium (which has similar chemical properties to Pu), and evaluate it in ZrC coating tests. Based on the results, we will develop the fundamental technologies for 3S-TRISO fuel fabrication.

The present study was sponsored by the Ministry of Education, Culture, Sports, Science and Technology (MEXT), Japan.

Reference

Ueta, S. et al., Development of Security and Safety Fuel for Pu–Burner HTGR: Part 5 — Test and Characterization for ZrC Coating, Proceedings of the 25th International Conference on Nuclear Engineering (ICONE 25), Shanghai, China, 2017, ICONE25–67530, 4p.

6–4 Development of a Passive Radiation Cooling System for High Temperature Gas-Cooled Reactors

— Conceptual Development of a Decay Heat Removal Method during Accidents —

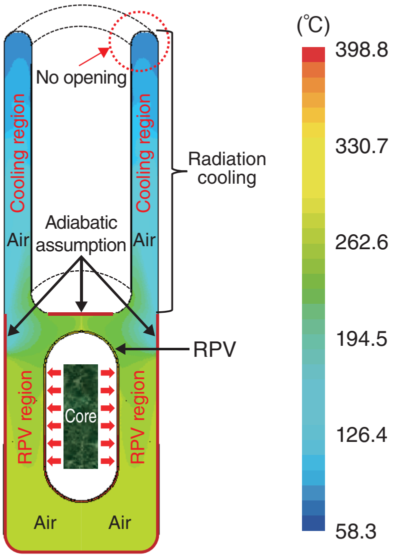

Fig.6-7 Analytical model and the analyzed temperature distribution
Except in the reactor core itself, the structures and the cooling system including the reactor pressure vessel (RPV) never exceed the temperature limit (550 °C) of 2¼Cr-1 Mo steel during an accident, with a safety margin of approximately 151 °C. After adjusting the adiabatic boundary condition in future work, we will also increase the removable heat flux from the RPV region.

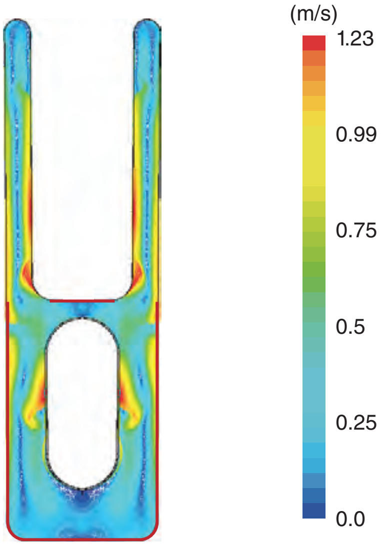

Fig.6-8 The analyzed velocity distribution
The air velocity in the cooling system is sufficiently low (approximately 1.2 m/s at most), negating the need to promote natural convection through ducts (which create a chimney effect).

The disaster at the TEPCO's Fukushima Daiichi NPS raised the expectations of High Temperature Gas-cooled Reactors (HTGRs). An HTGR avoids core meltdown (core melting) and a passive cooling system (which indirectly removes the heat from the reactor core) plays a crucial role during accidents. The High Temperature engineering Test Reactor (HTTR) located at JAEA is installed with a vessel cooling system (VCS) that removes the heat released from the RPV by pump-forced circulation of the coolant (water).

However, if the power supply is interrupted, the pump system cannot be driven, risking a significant reduction in the heat removal activity. In such cases, the HTGR avoids fuel failure but the RPV temperature could exceed the limit temperature. Therefore, we studied a heat removal method that minimizes the heat dissipation during normal operation and passively removes the decay heat during accidents without requiring active components and an emergency power supply. We also conducted a feasibility study of the heat removal method in a scale model (a heat-transfer test apparatus).

A cooling system based on passive natural atmospheric circulation is a likely candidate for commercial HTGRs. However, when the atmospheric inlet duct becomes stuck through incidents such as bird-strike, the heat removal activity of this type of cooling system is significantly compromised.

To resolve this difficulty, we propose a novel cooling system with a containment vessel, which relies on radiation cooling as far as possible. To double the number of surfaces in the radiation cooling region, we adopt a doughnut shape with inner, upper and outer surfaces (Fig.6-7). The heat-exchange area is further increased by machining each surface of the doughnut and adding structures such as fins. During normal operation of the HTTR, the RPV releases 1.2 to 2.5 kW/m^2 of heat. In this research, the targeted heat release for commercial HTGRs is 3 kW/m^2.

We first evaluated the thermal-hydraulics phenomena of the cooling system in detail. Even at an atmospheric temperature of 40 °C, the temperatures of the structures (except in the reactor core itself) and the cooling system including the RPV never exceeded the temperature limit of 2¼Cr-1 Mo steel (550 °C) during accidents. This result clarified the passive removal of heat from the RPV (Fig.6-7). The adiabatic boundary conditions were set to retain the heat in the RPV region, where the temperature is most severe, as much as possible. After adjusting the adiabatic boundary condition in future work, we will also increase the removable heat flux from the RPV region. Specifically, we will study the heat dissipation from the RPV region to the ambient environment such as ground. We will also reduce the temperature of the concrete, carbon steel and other materials around the RPV as far as possible, and consider the non-insulated heat transfer paths.

Because the air does not stagnate in the curved shape, the air velocity in the cooling system is approximately 1.2 m/s at most (Fig.6-8). This low velocity negates the need to promote natural convection through ducts via the chimney effect. Conversely, promoting natural convection can further promote the heat removal capacity.

In addition, when the reduction ratio of the scale model to the actual cooling system is x^{-1}, the radiation cooling and natural convection of the actual cooling system can be simultaneously reproduced when the air in the scale model is pressed up to $x^{1.5}$ times.

In summary, we conceptualized a novel decay-heat removal method for nuclear reactors during accidents, and demonstrated its feasibility in quantitative analyses.

Based on the analytical results of this research, we developed a scale model for further tests. Currently we are engaged in collaborative experimental research with Kyushu University.

This work was supported by the Japan Society for the Promotion of Science (JSPS) KAKENHI Grant-in-Aid for Scientific Research (C) (No.15K06676).

Reference

Takamatsu, K. et al., New Reactor Cavity Cooling System (RCCS) with Passive Safety Features: A Comparative Methodology between a Real RCCS and a Scaled–Down Heat–Removal Test Facility, Annals of Nuclear Energy, vol.96, 2016, p.137–147.

6–5 Improvement of Neutron-Startup-Source Exchange Work of the High Temperature Gas-Cooled Reactor

— Downsizing of Transportation Container Adjusting with Exchange Processes —

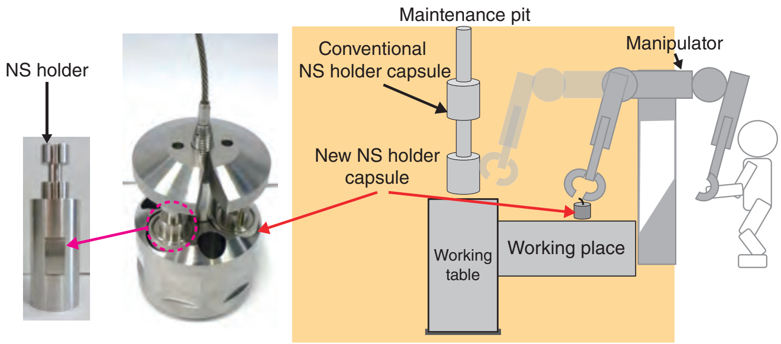

Fig.6-9 Schematic of NS exchange work after improvement
The holder capsule of the neutron startup source (NS) was downsized from its initial dimensions (diameter = 155 mm, height = 1285 mm) to a diameter and height of 75 mm and 135 mm, respectively. The downsizing omits the pulling of the NS holder from the NS holder capsule and transporting it to the working place.

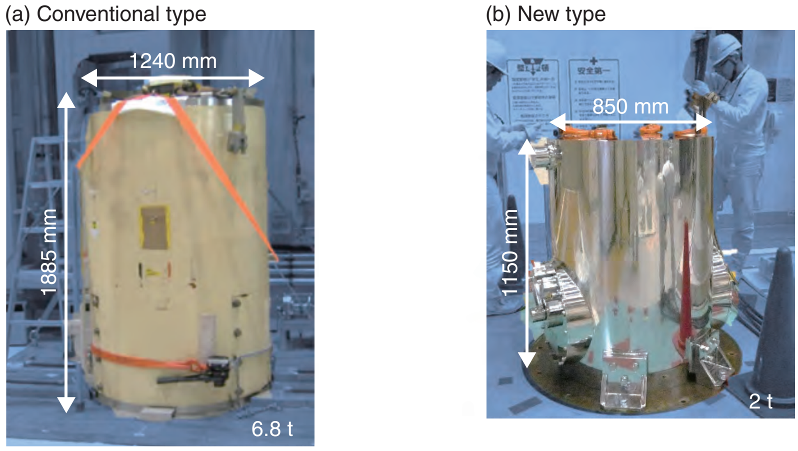
(a) Conventional type
(b) New type

Fig.6-10 Transportation containers
Comparison of a conventional container (a), and the new transportation container (b). The dimensions and weight of the new container are downsized by 2/3 and 1/3, respectively. The aseismic performance is improved by changing the structure from belt lashing to bolt fixing. The downsizing also improves the work of transporting the container by an overhead crane in the reactor building of the HTTR.

For commercializing High Temperature Gas-cooled Reactors (HTGRs), we must accumulate, continuously improve, and upgrade the maintenance technologies of the High Temperature engineering Test Reactor (HTTR).

The HTTR has three neutron startup sources (NSs) in the reactor core. The NSs are used not only for start-up, but also to confirm the integrity of the in-core neutron detector (wide-range monitor) after a reactor shutdown.

The NS (^{252}Cf) is placed in the NS holder (diameter 30 mm, height 100 mm) of the HTTR (Fig.6-9). Approximately, every seven years, NS is exchanged by a remote handling manipulator in the maintenance pit of a concrete cell.

The above-described exchange mechanism is afflicted by two problems: (1) Difficulty of handling the small-sized NS holder by manipulator, and (2) insufficiency of the aseismic performance of the transportation container structure.

To solve the above problems, we propose two solutions: (1) Moving the handling position to nearby the manipulator operator, which eases the handling and improves the safety, and (2) improving the aseismic performance of the transportation container by downsizing and installing a bolt-fixing structure.

Based on these proposals, we developed a new NS holder capsule and transportation container.

The conventional NS holder capsule was too large to place near the manipulator operator (Fig.6-9). Therefore, it was necessary to pull the NS holder from the NS holder capsule and transport it to the working place. As the working place was far from the holding capsule, the NS holder was at risk of falling. However, after downsizing the NS holder capsule, the NS could be transported to the working place without such handling errors. The transportation container (Fig.6-10(b)) was also downsized from the conventional transportation container (Fig.6-10(a)). Moreover, the bolt-fixing structure improved the aseismic performance.

As mentioned above, we improved the safety of the NSs exchange work by developing a new transportation container. The downsizing resolves the technical issues recognized in previous NSs exchange works.

By continuously improving the maintenance technologies and accumulating knowledge of the HTTR, we can contribute to the commercialization of HTGRs.

Reference
Shimazaki, Y. et al., Improvement of Neutron Startup Source Handling Work by Developing New Transportation Container for High–Temperature Engineering Test Reactor (HTTR), Journal of Nuclear Science and Technology, vol.54, issue 2, 2017, p.260–266.

6–6 Toward Efficient Hydrogen Production via the IS Process

— Promotion of HI Decomposition by a Membrane Reactor —

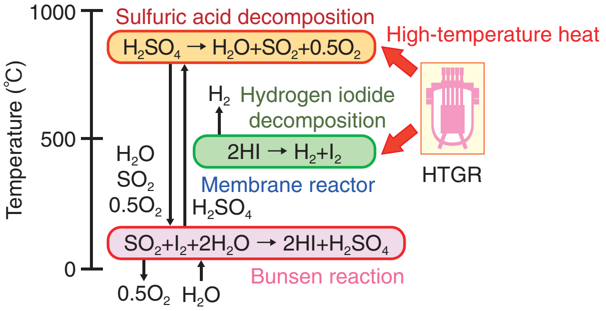

Fig.6-11 Schematic of the IS process

In the IS process, iodine and sulfur dioxide are added to water in an exothermic reaction that creates sulfuric acid (H_2SO_4) and hydrogen iodide (HI). The H_2SO_4 can be decomposed at about 850 °C, releasing oxygen and recycling sulfur dioxide. The HI can be decomposed at about 400 °C, releasing hydrogen and recycling iodine.

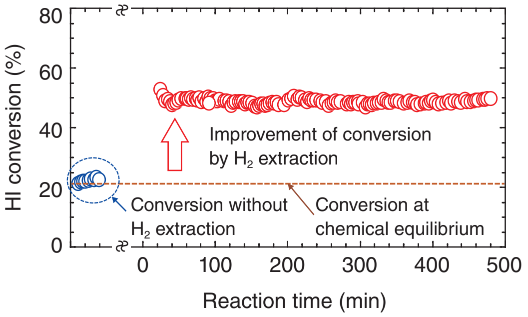

Fig.6-13 Enhancement of HI decomposition conversion by the membrane reactor

Without the membrane, the attained conversion (○) was almost identical to the equilibrium conversion of HI decomposition. After incorporating the membrane, the hydrogen was successfully extracted, and the conversion was boosted to approximately 50 % (○).

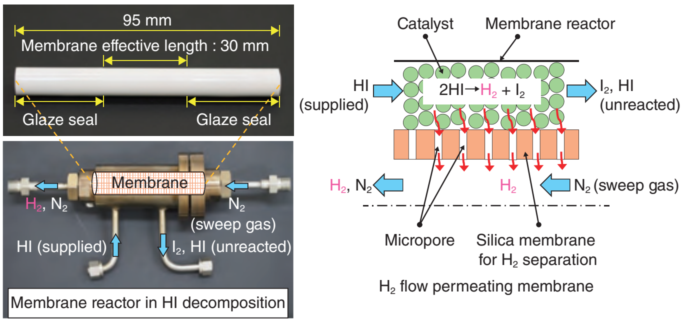

Fig.6-12 Schematic of the membrane reactor equipped with a hydrogen-separation silica membrane in HI decomposition

The gaseous HI catalytically decomposes into hydrogen and iodine within the membrane reactor. Under the pressure difference created by the nitrogen sweep gas, the hydrogen is selectively separated through the pores of the membrane, enhancing the HI decomposition conversion.

With the aim of contributing to a low-carbon society, we are researching and developing a thermochemical IS process for hydrogen generation, which uses the heat generated by a High Temperature Gas-cooled Reactor (HTGR). This thermochemical IS process uses water as its raw material, and iodine (I) and sulfur (S) in its reaction processes (Fig.6-11). As the entire process requires only water and nuclear heat and releases only hydrogen and oxygen, it is expected as a future CO_2-free hydrogen production technology.

Since the IS process converts thermal energy into chemical energy of hydrogen, an improvement of the process efficiency is one of the important tasks. The efficiency-determining step in this process is the HI decomposition, owing to its low conversion at chemical equilibrium (approximately 20 % at 400 °C). This low-decomposition conversion increases the amount of recycled materials, e.g., iodine and HI, thereby increasing the thermal burden and decreasing the thermal efficiency of the total process.

The HI conversion can be improved by a membrane reactor that extracts hydrogen from the reaction field. Removing the hydrogen from the membrane reactor improves the reaction efficiency. To this end, we have been developing elemental technologies of the membrane reactor for HI decomposition.

The membrane is the heart of the membrane reactor. The high decomposition temperature (> 400 °C) and highly corrosive HI environment exclude the use of common hydrogen-separation membranes such as polymers and palladium membranes. A promising candidate is silica membrane.

We have fabricated high performance silica membranes by chemical vapor deposition on porous alumina supports (Fig.6-12). Fig.6-13 shows the results of the membrane HI decomposition test. The HI conversion was increased from 20 % at equilibrium to approximately 50 %. Removing the hydrogen shifted the reaction equilibrium, promoting the HI conversion. Currently, the expected hydrogen production efficiency of the IS process is approximately 40 %. The targeted efficiency is 50 % in future developments. We are working to improve the thermal efficiency by developing large-scale HI membrane reactor.

The present study was supported, in part, by the Council for Science, Technology and Innovation, Cross-ministerial Strategic Innovation Promotion Program (SIP), “Energy Carrier”, funded by the Japan Science and Technology Agency (JST).

Reference

Myagmarjav, O. et al., Hydrogen Production Tests by Hydrogen Iodide Decomposition Membrane Reactor Equipped with Silica–Based Ceramics Membrane, International Journal of Hydrogen Energy, vol.42, issue 49, 2017, p.29091–29100.

6–7 Applicability Evaluation of Metallic Materials in Hydrogen Production by the IS Process

— Corrosion Resistance of Nickel-Based Alloy in a Practical Gaseous HI Decomposition Environment —

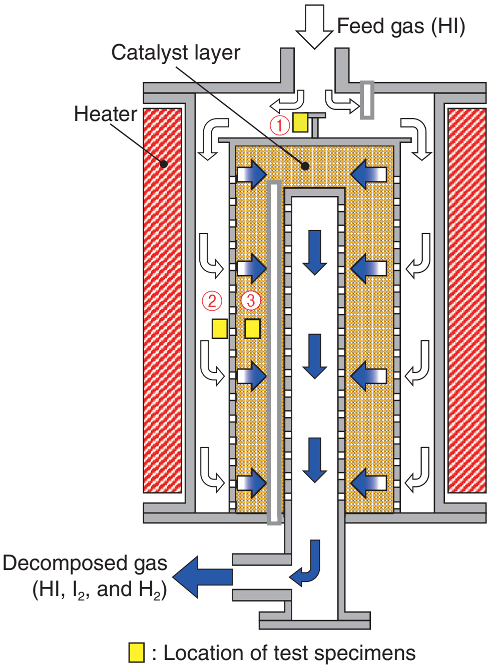

Fig.6-14 Corrosion test for gaseous HI decomposition environment
Gaseous HI fed from the top of the reactor was decomposed into I_2, H_2, and undecomposed HI through the catalyst layer. Test specimens were placed in three regions; ① inlet of the reactor, ② upstream of the catalyst layer, and ③ inside the catalyst layer.

Material	Before corrosion test	After corrosion test ①	②	③
HC-276				
SUS316				

Fig.6-15 External appearance of the test specimens
The specimen placed at ① partially retained its original surface. The surfaces of the specimens placed at ② and ③ were uniformly roughened, confirming overall corrosion. HC-276 shows a smoother surface than SUS316.

Table 6-3 Corrosion rates of test specimens
Corrosion rates were determined by weighing the original and corroded test specimens, and calculating the weight difference. The HC-276 specimen was measurably corrosion- resistant.

Material	Position	Temp. (℃)	Gas composition	Corrosion rate (mm/y)
HC-276	①	110	HI	0.01
	②	500	HI	0.52
	③	500	$HI+I_2+H_2$	0.75
SUS316	①	110	HI	0.37
	②	500	HI	6.53
	③	500	$HI+I_2+H_2$	5.76

Structural materials with high corrosion resistance are required in the iodine–sulfur (IS) thermochemical process of water-splitting hydrogen production, which occurs in a corrosive liquid or gaseous environment over a wide temperature range. Although ceramic materials such as SiC and glass are highly resistant to corrosive environments, they are difficult to fabricate for large-scale reactors. Therefore, metallic materials are preferred in commercial large-scale H_2 production.

Previous studies confirmed that nickel-based alloy is corrosion resistant in a gaseous HI environment with water vapor. However, the corrosion resistance of this material in the practical dry gaseous environment of HI decomposition, where dry HI is decomposed into I_2 and H_2 with a catalyst at 500 °C, has not been clarified. Especially, as I_2 can form metal iodides, it might corrode the metallic alloy. To evaluate this possibility, we performed a corrosion test of the nickel-based alloy Hastelloy C-276 (HC-276) in the practical environment.

The test specimens were placed in the HI decomposer (Fig.6-14) and their corrosion rates were determined from their weight changes after the corrosion process. Considering that the corrosion rate obeyed a parabolic rate law in the coexistence of water vapor (as determined in previous studies), the exposure time was conservatively decided as 100 h. For comparison with the candidate material HC-276, we also tested the corrosion resistance of JIS-SUS316. The test specimens were placed in three regions: ① the reactor inlet, ② upstream of catalyst layer, and ③ inside the catalyst layer.

After the test, the specimens showed uniform surface roughening consistent with general corrosion (Fig.6-15). Table 6-3 summarizes the average corrosion rates. Neither specimen was seriously corroded at position ① due to the low temperature in this region. At positions ② and ③, the corrosion rate of JIS-SUS316 was approximately 6 mm/y, meaning that this material cannot withstand the corrosive environment. On the contrary, the HC-276 specimen showed good corrosion resistance (at most 0.75 mm/y), though it is suggested that the specimen was corroded at a rather higher rate in the catalyst by I_2.

In future work, we will clarify the development of the corrosion rate in longer corrosion tests, and will try to improve the corrosion resistance of HC-276 by forming protective oxide layers. This will be attained by pre-oxidizing HC-276 and adding water vapor to the HI decomposition environment.

Reference
Kamiji, Y. et al., Corrosion Resistance of Nickel–Based Alloy to Gaseous Hydrogen Iodide Decomposition Environment in Thermochemical Water–Splitting Iodine-Sulfur Process, Proceedings of 5th International Conference on Chemical and Biological Sciences (ICCBS 2018), Bucharest, Romania, 2018, p.51–54, in USB Flash Drive.

7 Research and Development of Fast Reactors

Research and Development of Fast Reactor Cycle Technology

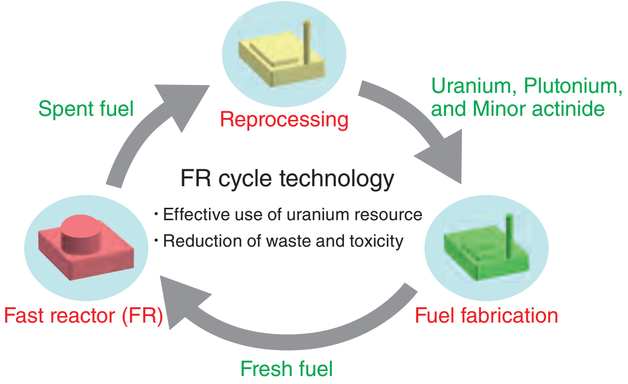

Fig.7-1 Fast reactor cycle
The fast reactor cycle is a nuclear system in which fuel is burned to generate electricity with a fast reactor and spent fuels are reprocessed for extraction of uranium or plutonium. Extracted fuel is then burned again for recycling.

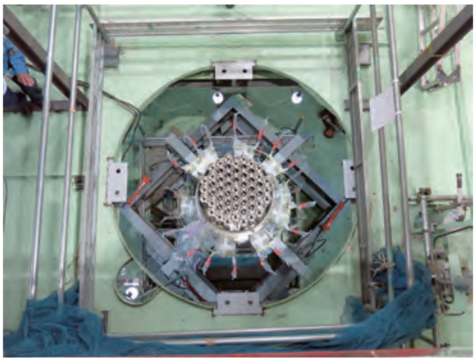

Fig.7-3 A test section simulating the core
Sodium natural-circulation-cooling tests are conducted using a simulated core with an electric heater.

A fast reactor cycle can dramatically increase the utilization efficiency of uranium resources for long-term nuclear-energy utilization (Fig.7-1). Our intension is to make the fast reactor cycle technology accepted to society. This technique aims to maximally decrease the risk of nuclear disasters that heavily release radioactive materials, such as the TEPCO's Fukushima Daiichi NPS (1F) accident, and thus have the potential to facilitate the acceptance of nuclear technology in society. Moreover, we widely simulate the root causes of severe accidents including natural disasters and create an enhanced-safety concept through design with enhanced prevention and mitigation measures.

●Starting the test with the plant-dynamics test loop

Reactor-core-cooling technology that does not use active devices such as pumps has been developed to ensure cooling performance during accidents. Cooling tests for the core by natural circulation with a plant-dynamics test loop (PLANDTL which stands for PLANt Dynamics Test Loop) in Oarai (Fig.7-2), have been undertaken using a test section simulating the core of a sodium-cooled fast reactor (SFR) (Fig.7-3). These results show that the core can be cooled without fail, even in conditions of complete emergency-power loss, and these results can contribute to improving the safety of SFRs.

Fig.7-2 Plant-dynamics test loop
Tests for the cooling core in case of an emergency have been started in order to ensure cooling technology.

●Introduction to R&D results in each field

Measures to ensure high safety for SFRs are the same as those used in light-water reactors. Our objectives are to prevent severe accidents such as 1F by thoroughly pursuing stopping and cooling of reactors and confinement of radioactive materials, even during accidents, and to preform firm maintenance to prevent of failures or trouble based on an accurate understanding of reactor properties.

Regarding the safety of FRs, we have been preparing global standards and design guidelines in cooperation with all of the countries of the world (Topic 7-1). In these works, our objective is to enhance the safety of SFRs around the world.

We measure the properties of mixed-oxide fuels with plutonium and uranium, and perform studies to predict fuel behavior inside the reactor (Topics 7-2–7-4). From these results, the prediction accuracy of the safety or performance of reactors will be improved.

Maintenance technologies for preventing failure or trouble have also been developed. The study of maintenance program is being proceeded to be established, in which the degree of importance of each system and device for the safety is taken into account (Topic 7-5). From this study, rational inspection can be feasible for ensuring safety. This result, which is recognized as the standard of the American Nuclear Society, contributes to improving the safety of FRs around the world. Moreover, an inspection technology for maintenance of the heat-transfer tubes that serve as cooling-system components in steam generators has also been developed (Topic 7-6). This technology allows the finer defects of heat-transfer tubes to be detected with the expectation of preventing accidents or failure in advance.

As study for "confinement", study for evaluating the phenomena of sodium contacting to concrete in the building in case of accidents is underway (Topic 7-7). Thus, the influence of the chemical reaction of sodium and concrete can be evaluated precisely, and confinement performance will be ensured.

7–1 Safety-Design Guidelines for Generation-IV Sodium-Cooled Fast Reactors

— To Achieve Its Adoption into Leading-Edge Fast Reactors —

Table 7-1 Examples of Gen IV SFRs in the world
Japan and France have a wealth of experience in breeding technology, and their current major goal is to develop measures to deal with spent fuel and radioactive wastes. Meanwhile, Russia, India, and China have selected SFRs among other reactor concepts considering energy security, and are developing them toward early full-scale use.

Country	Reactor name	Electric power (MWe)	Development stage
Japan	Japanese SFR	750	Demonstration
France	ASTRID	100–200	Demonstration
Russia	BN-1200	1220	Commercial
India	CFBR	600	Commercial
China	CFR1000	1000	Commercial

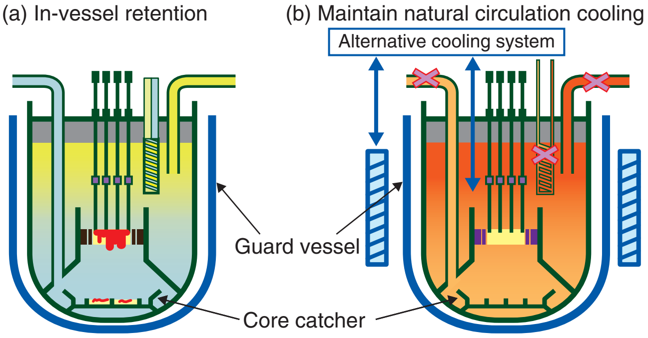

Fig.7-4 Images of design measures to prevent and mitigate severe accidents recommended by SDC and SDG
(a) Molten cores are retained and cooled within the RV, even if the core is damaged due to failure of reactor shutdown.
(b) The core is maintained in sodium to remove heat by means of a decay-heat-removal system that uses the natural circulation of sodium and alternative heat-removal techniques.

Under the Generation IV International Forum (GIF), JAEA is playing a leading role in developing the Safety Design Criteria (SDC) and the Safety Design Guidelines (SDG) based on experiences from the design, construction, and operation of JOYO and MONJU, and from efforts toward the commercialization of sodium-cooled fast reactors (SFRs). The SDC will constitute the international de-facto standard requirements for SFR, while the SDG will provide recommendations to support designers operating under the SDC. These documents, disseminated by the GIF and IAEA, are being increasingly introduced into advanced SFR designs throughout the world. Currently, the SDC and SDG are being revised based on feedback from regulatory bodies and international organizations.

Table 7-1 exemplifies Generation IV (Gen IV) SFRs now under development. The SDC and SDG are being used in those projects to implement safety measures, especially for preventing and mitigating severe accidents according to their design characteristics, such that plant safety can be ensured.

In particular, the SDC and SDG recommend “in-vessel retention (IVR)”, where molten-core materials are retained and the accident is controlled within the reactor vessel (RV) (Fig.7-4(a)). An SFR should be equipped with a power-reduction function utilizing inherent reactivity feedback and passive mechanism so as to avoid core damage. In addition, the documents state that the failure of the reactor-coolant boundary must be prevented, even if core damage is postulated to achieve IVR. Passive-design measures are being considered among design options in some advanced SFRs. For example, the French ASTRID, Russian BN-1200, and Indian CFBR reactors are examining passive-shutdown system using hydraulic pressure and/or Curie-point electromagnets. The installation of a core catcher in the RV is positively considered to achieve the goal.

An SFR uses sodium, which brings safety benefits—e.g. sodium with a high boiling point provides sufficient time for coolant boiling, enabling core damage to be avoided. Moreover, natural circulation is easily achievable, and the coolant level can be maintained using static components. As described in the SDC and SDG, SFRs maintain their cooling ability by ensuring an intact RV and guard vessel (GV), by enhancing decay-heat-removal systems, and by using alternative and independent cooling systems such that the total loss of cooling can be practically eliminated. Designers of advanced reactors are striving to improve measures to prevent core damage. Examples include a GV covering the entire primary coolant system, a diversified decay-heat-removal system, and the use of the natural circulation of sodium (Fig.7-4(b)).

Safety measures in Gen IV SFRs are being enhanced in compliance with the SDC and SDG. JAEA is leading the safety of SFR by establishing the SDC and SDG as international standards.

The present study was supported includes the result of a technical-development program for a fast-breeder reactor, etc., by the Agency for Natural Resources and Energy, Ministry of Economy, Trade and Industry (METI), Japan.

Reference

Kubo, S. et al., Study on Safety Design Concept for Future Sodium–Cooled Fast Reactors in Japan, Proceedings of International Conference on Fast Reactors and Related Fuel Cycles: Next Generation Nuclear Systems for Sustainable Development (FR17), Yekaterinburg, Russia, 2017, IAEA-CN245-164, 10p., in USB Flash Drive.

7–2 Evaluate the Mechanical Properties of MOX

— Young's Modulus Analyzed by the Sound Speeds of MOX Measured by the Ultrasound Method —

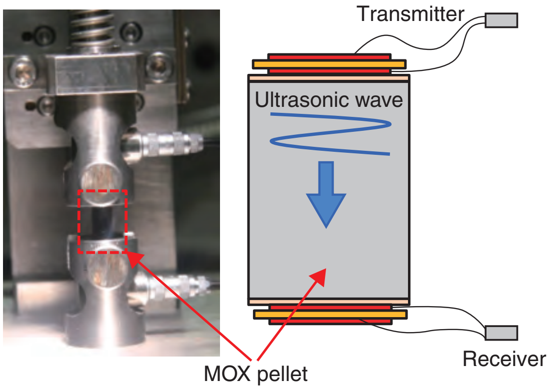

Fig.7-5 Outline of measurement by the ultrasound method
A MOX pellet is indicated by the red frame in the left- photo. As shown in the right image, an ultrasound pulse is transmitted from the top and received at the bottom of the MOX pellet. The sound speeds of the longitudinal and transversal waves are calculated using the distance and the time over which the ultrasound wave travels.

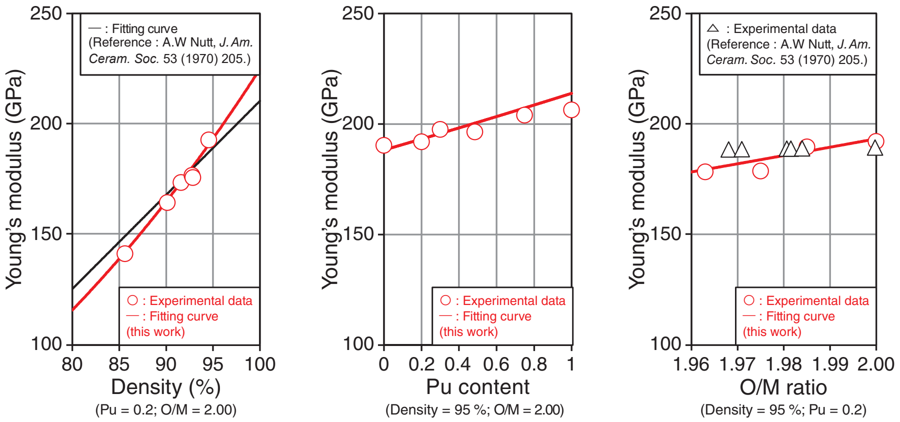

Fig.7-6 The effect of density, Pu content, and O/M ratio upon the Young's modulus
The Young's modulus can be calculated from the measured sound speeds. The effects of density, Pu content, and O/M ratio upon the Young's modulus were evaluated.

To secure the soundness of fuel pins during irradiation, these pins must be designed to prevent raptures brought about by fuel-and-cladding mechanical interaction (FCMI). Mechanical properties such as the Young's modulus of the uranium-plutonium mixed-oxide (MOX) fuel are used to evaluate the FCMI behaviors. The Young's modulus of MOX fuel is known to be influenced by various factors such as density and plutonium (Pu) content. Moreover, the oxygen-to-metal (O/M) ratio is expected to influence on the Young's modulus. However, no report has yet evaluated or formulated the effects of all factors.

In this study, various MOX pellets of different densities, Pu contents, and O/M ratios were prepared and the sound speeds of longitudinal and transversal waves in the pellets were measured by the ultrasound method. This measurement is outlined in Fig.7-5. By this method, the time taken for an ultrasound wave traveling from the transmitter to the receiver is measured. The sound speeds are calculated by the time and the distance over which the ultrasound travels. Then, mechanical properties such as Young's modulus can be derived from the sound speeds.

The results of the Young's modulus are shown in Fig.7-6. The measurement and the evaluation revealed that the Young's modulus decreased significantly as the density decreased. For lower densities, the decrease of the cross section capable of taking stress is considered as the reason for the decrease of the Young's modulus.

The Young's modulus was enhanced for MOX with a higher Pu content. It has been reported that this was the case because the interatomic bonding force is stronger for higher Pu contents. The effect of the O/M ratio was obtained such that Young's modulus decreased along with O/M, and the reason for this may also be the effect of the interatomic-bonding force.

The fitting equations for calculating mechanical properties such as Young's modulus as functions of density, Pu content, and O/M ratio were proposed from the experimental results. The equations can offer accurate properties for evaluating FCMI, which contributes to the development of MOX fuel design.

As a future plan, we will further study science-based models of MOX properties by integrating various properties on top of the mechanical ones obtained in this work.

Reference

Hirooka, S. et al., Sound Speeds in and Mechanical Properties of (U,Pu)O_{2-x}, Journal of Nuclear Science and Technology, vol.55, issue 3, 2018, p.356–362.

7–3 Evaluation on Cesium Behavior in a Fast-Reactor Fuel Element

— Development of an Analytical Method for Fast-Reactor MOX-Fuel Elements —

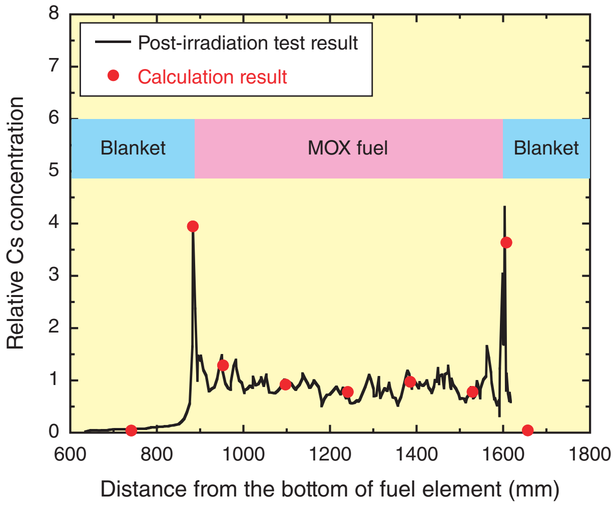

Fig.7-7 Axial distribution of the Cs concentration in a fuel element
Local Cs-concentration peaks are at the upper and lower boundaries between the MOX and blanket-fuel columns. We developed an analytical model for Cs behaviors, making use of past research results. The model describes Cs migration by two processes: Cs thermal diffusion in a fuel pellet, and Cs evaporation and condensation between adjacent fuel pellets. The model was incorporated into the calculation code CEDAR, which enabled the reproduction of the measured Cs axial distribution in an irradiated fuel element.

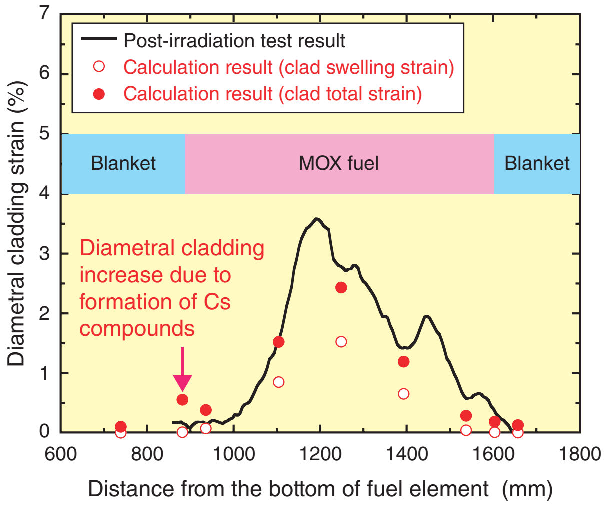

Fig.7-8 Axial distribution of the diametral cladding strain of a fuel element
Large diametral-cladding increase in the MOX-fuel-column region of the irradiated fuel element was governed by cladding swelling, while little diametral increase was seen at either the upper or lower ends of the fuel column where Cs was significantly concentrated. In the CEDAR calculation, accumulated Cs–U–O compounds at the lower end of the MOX fuel column induced expansion of blanket pellets to the extent of causing mechanical interaction with the cladding, yet this interaction was not significant and the calculated cladding-diametral increase was very small.

In mixed-oxide (MOX)-fuel elements irradiated in fast reactors, as fuel burnup proceeds, a Fission Products (FPs), cesium (Cs), migrates to the lower-temperature regions of the fuel elements and may interact with other FPs to form chemical compounds, thereby affecting the fuel-pellet temperature and dimensional stability of the cladding. We have developed a model for analyzing Cs behaviors and incorporated it into the calculation code CEDAR, which predicts changes in the temperatures and dimensions of a fuel element. This allowed for the Cs behaviors and their impact upon the integrity of the fuel element under irradiation to be predicted.

Thermal diffusion and evaporation–condensation processes are the base of the analysis model of Cs behaviors, the idea of which was inspired by the past relevant research results. The radial and axial Cs migrations in the fuel element were calculated by applying the temperature distributions of CEDAR to these processes. Fig.7-7 shows the axial distribution of the Cs concentration in the fuel element irradiated to high burnup in the prototype fast reactor Phenix in France. The calculation of CEDAR including the Cs-behavior model showed that Cs accumulates at the upper and lower ends of the MOX-fuel column as a result of its migration in the fuel element during irradiation, thereby reproducing the actual results of locally increased Cs concentrations.

We developed a model for predicting the formation of various Cs compounds based on the calculations of chemical-equilibrium reactions between Cs and oxygen (O), uranium (U) and other FPs such as molybdenum (Mo). This model also uses temperatures and the amount of oxygen in the fuel pellets calculated by CEDAR.

The analysis of the high-burnup-fuel element showed that Cs compounds were accounted for by the Cs–Mo–O and Cs–U–O systems. The Cs–Mo–O compound is known to accumulate as a medium in the gap between the fuel pellet and the cladding, thereby decreasing the fuel-pellet temperature; it was predicted to be formed in the gap over the entire MOX-fuel-column region, which was consistent with the actual distribution of this compound. The Cs–U–O compounds are known to be formed at the parts where Cs is concentrated and, because of their lower density, may cause contact between the pellets and the cladding. In the analysis, Cs–U–O compounds accumulated at the lower end of the MOX-fuel column caused contact between blanket pellets and cladding, yet the effect of the contact pressure upon the cladding diameter was sufficiently small. As shown in Fig.7-8, the calculation by the code adequately reproduced the measured cladding-diametral strain.

Reference

Uwaba, T. et al., Coupled Computer Code Study on Irradiation Performance of a Fast Reactor Mixed Oxide Fuel Element with an Emphasis on the Fission Product Cesium Behavior, Nuclear Engineering and Design, vol.331, 2018, p.186–193.

7–4 Evaluation of the Irradiation Behavior of Fast-Reactor MOX Fuel

— O/M-Ratio Dependence of Fuel Restructuring and Fuel Temperature —

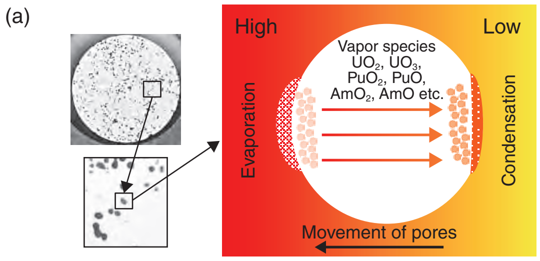

Fuel pellet (before irradiation)

Evaporation and condensation of pores during irradiation

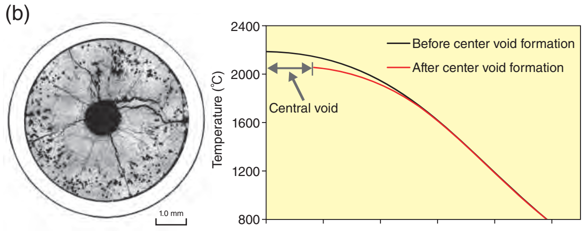

Fuel pellet (after irradiation)

Temperature distribution before and after center void formation

Fig.7-9 Mechanism of central-void formation
Oxide fuel is manufactured at a theoretical density of ~85 %–95 % TD and contains many pores (a). These pores move toward the fuel center and form the central void by evaporation–condensation during irradiation (b).

(a) Difference in center void diameter due to the difference in O/M ratio (Pu content : 31 wt%, Am content : 2.4 wt%)

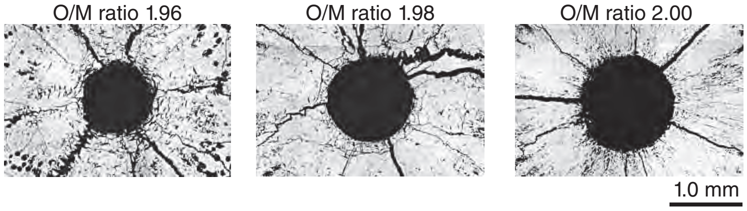

(b) Analysis result of fuel temperature and vapor pressure

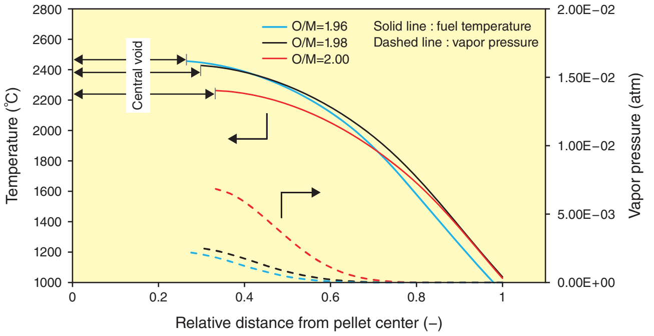

Fig.7-10 Difference in central-void diameter according to O/M ratio and analysis result
Samples with an O/M ratio of 2.00 had larger central-void diameters than those with O/M ratios of 1.96 and 1.98 (a). The calculation showed that the fuel-center temperature was lower for O/M 2.00 by about 200 °C than for O/M 1.96 and 1.98. The central-void diameter becomes larger in the sample with an O/M ratio of 2.00 because the vapor pressure is high (b).

In order to ensure safety, fast-reactor fuel must be designed to prevent fuel melting. It is known that the oxide–metal (O/M) ratio of mixed-oxide fuel (MOX fuel) affects the thermal conductivity, melting point, and vapor pressure. Therefore, it is necessary to confirm the O/M ratio's influence upon the irradiation behavior and to reflect this influence in the fuel design. In addition, research and development on minor actinides (MAs) bearing MOX fuel for the fast reactor has been proceeding from the viewpoint of reducing radioactive waste. In order to develop MA-bearing MOX, it is indispensable to clarify the influence of MA-addition upon irradiation behavior.

This study evaluated the influence of the O/M ratio upon the irradiation behavior based on the irradiation-test result of MA-MOX fuel.

Because the fuel-center temperature decreases with the formation of the central void, fuel restructuring is one of the most important behaviors from the viewpoint of evaluating the fuel's thermal behavior. Fig.7-9 shows the mechanism of central-void formation. As shown in this figure, the existing pores in the as-fabricated MOX-fuel pellet move toward the fuel center by evaporation–condensation processes under a radial temperature gradient. This pore migration causes fuel restructuring. Vapor pressure is one of the most important physical properties for evaluating the fuel restructuring caused by this process.

Fig.7-10 shows the O/M-ratio dependence of the central-void diameter and fuel temperature. As shown in this figure, the central-void diameter of the O/M 2.00 sample was larger than that of samples with O/M 1.96 and 1.98. In order to evaluate the difference in the central-void diameter due to this O/M ratio, the relationship between this ratio and vapor pressure was evaluated based on the latest knowledge and a new pore-migration model was developed. Moreover, since MAs such as Am also influence the vapor pressure, MAs were also considered as vapor species in this improved model. The results of this evaluation are shown in Fig.7-10; the central-void diameter of the O/M 2.00 sample was larger than those of the O/M 1.96 and 1.98 samples. However, the fuel temperatures in the O/M 2.00 sample were evaluated to be lower than those in O/M 1.96 and 1.98. The reasons were as follows: the fuel temperature decreased due to the high thermal conductivity at stoichiometry, and the pore-migration velocity increased since the total vapor pressure was increased by the vapor pressure of UO_3, whose increase was derived from the high oxygen potential at stoichiometry.

Thus, by considering the influence of the O/M ratio of the vapor pressure, it was possible to evaluate fuel restructuring. Moreover, since the irradiation test of MA-MOX fuel is small, developing a pore-migration model that considers MAs was a major achievement.

Reference

Ikusawa, Y. et al., Oxide-Metal Ratio Dependence of Central Void Formation of Mixed Oxide Fuel Irradiated in Fast Reactors, Nuclear Technology, vol.199, issue 1, 2017, p.83–95.

7–5 Determining Inspections Necessary for Maintaining Fast Reactor Performance

— Development and Standardization of a Determination Method for In-Service Inspection of Fast Reactors —

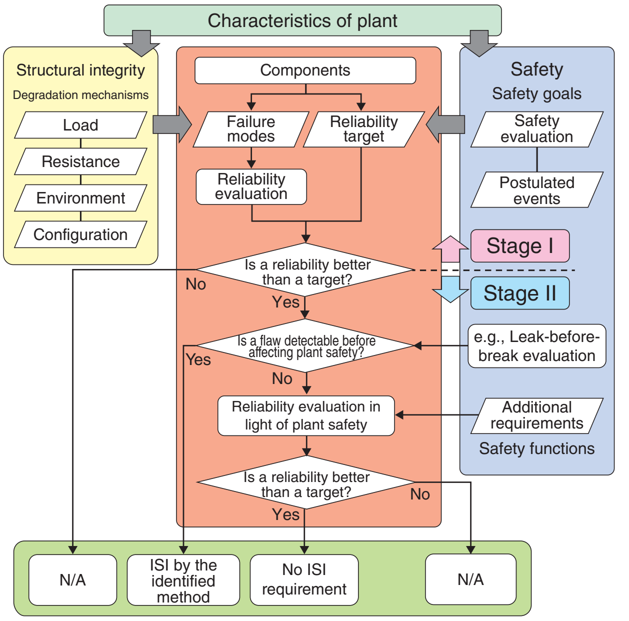

Fig.7-11 Flow for determining ISI
Two-stage evaluation in light of plant safety and the structural integrity of components is conducted to determine ISI suitable for fast reactors.

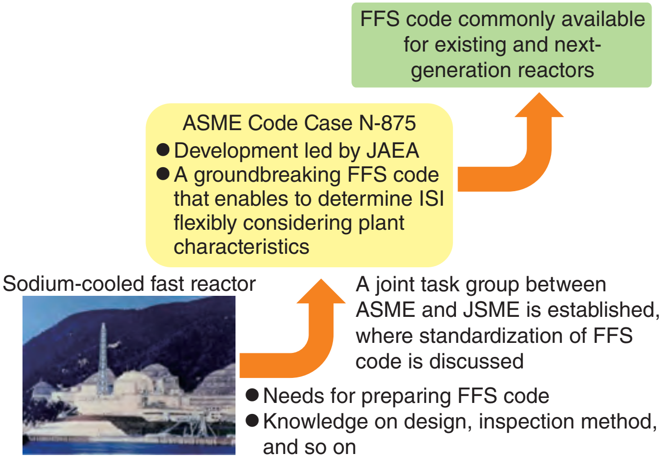

Fig.7-12 International standardization process for the proposed method
The proposed determination method of ISI for fast reactors has been issued in the ASME code, which is one of the most recognized international standards. Now, in ASME, application of the proposed method is being discussed as a basic concept applicable to any type of reactor.

In nuclear power plants in Japan, in-service inspection (ISI) is conduced according to the fitness-for-service (FFS) code issued by the Japan Society of Mechanical Engineers (JSME) to maintain the performances of components required for operation. However, the scope of the code is limited to light-water reactors and no FFS code exists for fast reactors in Japan. Taking a look at overseas situations, there is an FFS code for liquid-metal reactors, which is intended for application to sodium-cooled fast reactors in the American Society of Mechanical Engineers (ASME) code, but the code has not been completed. More than 30 years have passed and some important requirements remain undeveloped, and so the code is not practically available. An FFS code is of course important for maintaining performance during operation; even during the plant-design and development stage, it is important for achieving design while taking inspection properties such as accessibility into consideration.

Therefore, we decided to develop a method for determining ISI for fast reactors based on the System Based Code (SBC) concept, which is aimed at rational maintaining the structural integrity of components by setting reliability targets and design and maintenance requirements to meet these targets.

Fig.7-11 shows the proposed flow for determining ISI. The flow consists of two stages. In Stage I, we focus upon the structural integrity of the components. Potential active degradation mechanisms are considered based on conditions including the material and service environment, and then the reliability of the specified component is evaluated. If the reliability meets a target value, it is possible to proceed to Stage II, in which plant safety is the focus. The detectability of defects before they grow to an unacceptable size is assessed in consideration of plant safety. If there is any feasible way to reliably detect degradation, it is adapted as an ISI. Otherwise, structural-integrity evaluation is required while employing a sufficiently conservative hypothesis. If the result meets the target value, ISI is not required. Thus, the proposed flow can determine ISI suitable for fast reactors by taking key characteristics, including the importance of components in light of plant safety, material, environment, and inspection properties, into consideration.

As examples, ISI requirements are investigated for a guard vessel and a core support structure of the fast breeder prototype reactor, MONJU, according to the proposed flow. In Stage I, fatigue-creep-interaction damage and fatigue damage are specified as potential active degradation mechanisms for the guard vessel and the core support structure, respectively; it is then confirmed that their structural reliabilities meet target values through reliability evaluation. In Stage II, the reliability levels of the components are evaluated assuming initial fully circumferential cracks with a depth equal to 10 % of the thickness as additional requirements, because there is no available inspection method for the components. It is shown that both components had sufficient reliability even with the additional requirement based on the conservative hypothesis. The failure occurrences of these components are practically eliminated. Hence, it is concluded that no ISI requirements are needed for these components.

Results concerning the development of an ISI determination method suitable for fast reactors, including this study, have been provided for discussion on the fitness-for-service code for liquid-metal reactors in ASME, and the proposed method was standardized as Code Case N-875 in July 2017. Now, ASME is discussing applying the proposed method as a basic concept applicable to any type of reactor (Fig.7-12).

Reference

Takaya, S. et al., Determination of In-Service Inspection Requirements for Fast Reactor Components Using System Based Code Concept, Nuclear Engineering and Design, vol.305, 2016, p.270–276.

7–6 Advanced Inspection Technology for JSFR SG Tubes

— Development of a Hybrid Eddy Current Sensor for Small Defects —

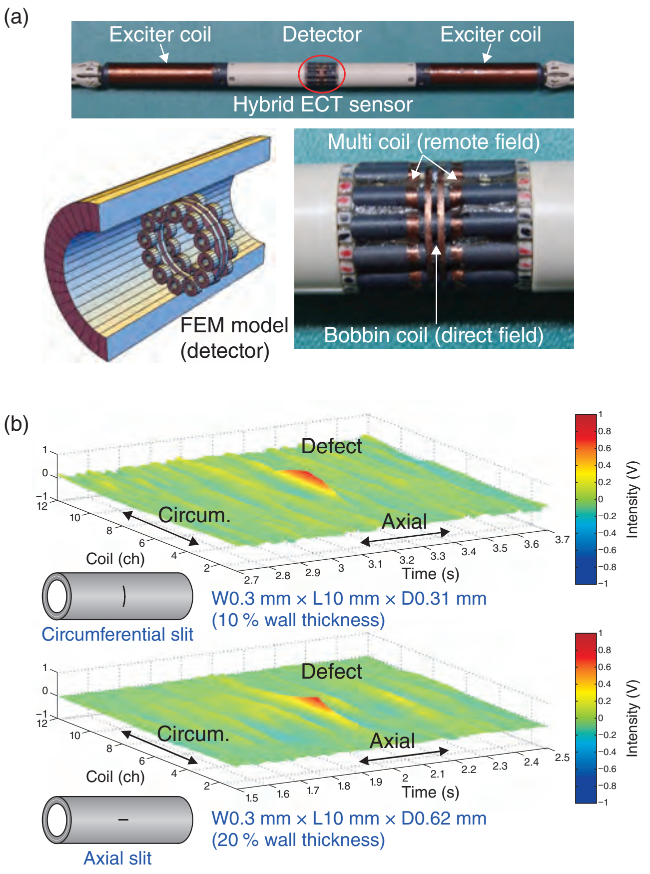

Fig.7-13 Hybrid ECT sensor (a) and detection of EDM defects (circumference and axial slit) (b)

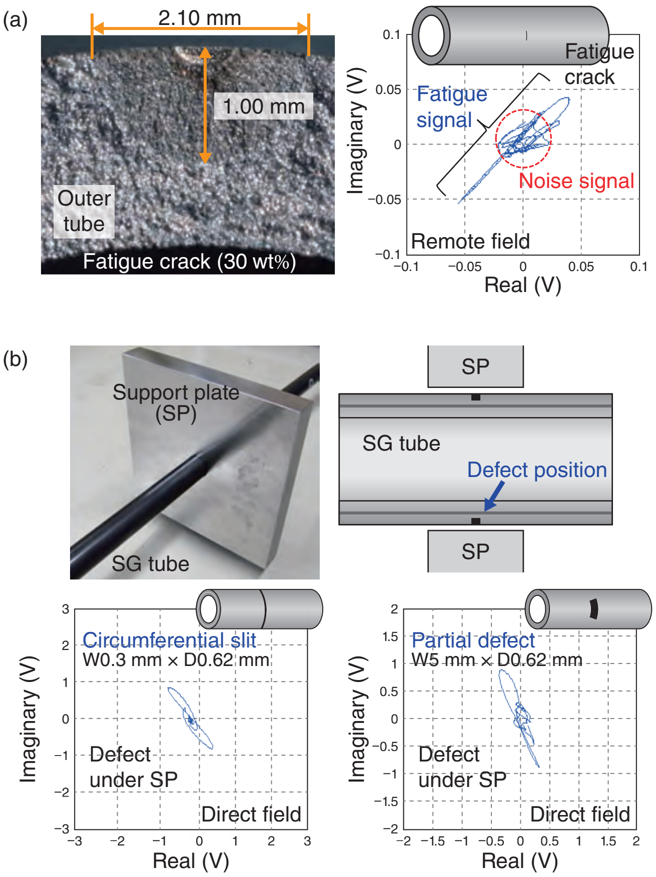

Fig.7-14 Detection of a fatigue crack by a multi-coil sensor (a) and defects under the support plate by a bobbin coil (b)
$X = \sin(\omega t)$, $Y = \sin(\omega t + 90°)$

A hybrid eddy current testing (ECT) sensor is being developed based on a combination of direct and remote magnetic fields to detect small defects near and under the support plate (SP) of the steam generator (SG) tubes of JSFR. Since SG tubes are thinner (19 mm outer diameter and 12 mm inner diameter) and made of 9Cr-1Mo steel, they are more difficult to be inspected than light water reactor tubes. A hybrid ECT sensor is required for having the accuracy and sensitivity to detect small defects for further evaluation of their size and depth and prediction of their growth. Development of this technology started with a multi-coil sensor that could be made more sensitive to small defects on the outer surface of the SG tubes by optimizing coils arrangement, number, and size using FEM numerical simulations. An increased eddy current flow on the surface of the SG tubes resulted in a higher sensitivity to small defects, as shown in the experimental data. Fig.7-13 shows the hybrid ECT sensor detecting a slit (0.3 mm wide and deep). A C-scan of the measured signal shows the defect position on the tube surface. Ferrite cores improve the electromagnetic characteristics of the designed hybrid ECT sensor to detect a fatigue crack (under 10 μm wide and 1 mm depth) (Fig.7-14(a)).

In the past, the sizes and positions of defects in ferromagnetic tubes were distinguished using two sensor units (ECT and RF-ECT). Because of their differing lift-off noise distributions and spatial separation, it was difficult to use sensor-combination signals to suppress noise levels and correlate their signals to defect locations. In the new approach, the sensors are combined in the same location and differentiate the defect position while maximizing sensor sensitivity to reduce interference signal between them. The hybrid ECT sensor has both magnetic field systems integrated into a single unit. Fretting wear defects were created on the outer surface of a tube under the SP. Fig.7-14(b) shows the performance of an ECT sensor for defects under tube SP. The measurements demonstrate the feasibility of this approach, resulting in a higher S/N ratio for detecting both defects.

In the future, to shorter the inspection time, we plan to inspect SG tubes without draining the sodium.

Reference

Yamaguchi, T. et al., Development of a Hybrid ECT Sensor for JSFR SG Double-Wall Tubes, Journal of Nuclear Science and Technology, vol.54, issue 11, 2017, p.1201–1214.

7–7

Evaluation of Chemical Reaction Behavior during Severe Accidents in Fast Reactors

— Chemical Reaction Dynamics between Concretes and Sodium —

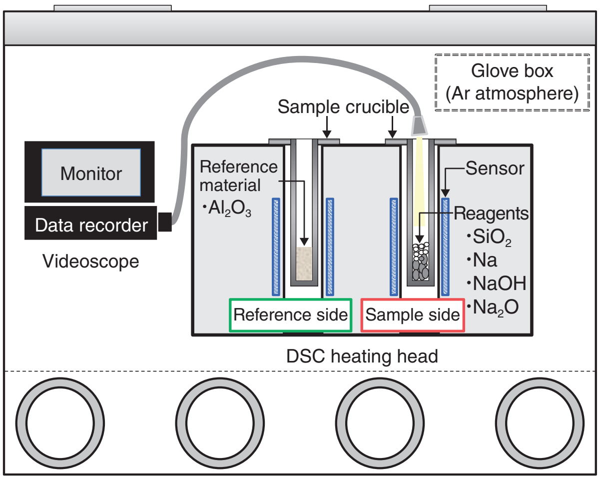

Fig.7-15 Experimental apparatus and situation
Thermal analysis was performed at different heating rates to determine the rate of each reaction assumed between sodium and concrete. Videoscope is capable of observing the sample surface during the reaction.

(a) DSC curves

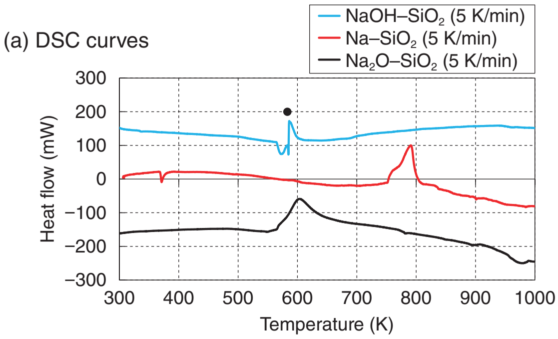

(b) Sample surface state during reaction of NaOH–SiO_2

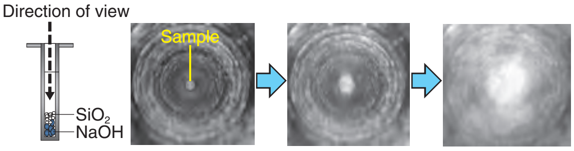

Fig.7-16 Comparison of DSC curves and observations during a reaction
Thermal analysis of each reaction assumed to take place between sodium and concrete was performed to confirm the reactivity. The onset temperature and kinetic behavior for each reaction were confirmed from the DSC curves (a). Moreover, the sample surface during the reaction was observed.

As a countermeasure against sodium leaks in sodium-cooled fast reactors (SFRs), a steel liner is built to protect against the chemical reaction caused by direct contact of liquid sodium with structural concrete. However, if considering severe accidents such as a breach of this steel liner by an intensive sodium leak, a sodium–concrete reaction (SCR) may occur. SCR may result in ablation of structural concrete with exothermic heat and the release of hydrogen gas. Thus, it is important to evaluate the behavior of SCR. Though various experimental studies on SCR have been performed in many countries to obtain findings on this subject, these have not been sufficient to elucidate the mechanism behind SCR due to complex and composite phenomena arising from the thermal and chemical effects. Therefore, a mechanistic evaluation method has been developed by identifying the dominant chemical reaction from the viewpoint of chemical reaction dynamics.

In this study, thermal analysis of silica (SiO_2) (one of the major compositions of structural concrete) with sodium (Na) was performed to obtain fundamental information concerning reaction behavior. Based on the obtained data, kinetic evaluation was performed. For thermal analysis, a Differential Scanning Calorimetry (DSC) instrument placed in a glove box with an argon (Ar) atmosphere was used because sodium is chemically reactive (Fig.7-15). Sample mixtures of SiO_2 with Na, sodium hydroxide (NaOH), or sodium monoxide (Na_2O) as byproducts were used and heated at different heating rates of 3–10 K/min in the temperature range of 298–1073 K.

Fig.7-16(a) compares the DSC curves of reactions of Na–SiO_2, NaOH–SiO_2, and Na_2O–SiO_2. The DSC curves for reactions of NaOH–SiO_2 and Na_2O–SiO_2 indicate that those onset temperatures are less than 600 K. In the case of a NaOH–SiO_2 reaction, an intensive exothermic peak (●) caused by the solid (SiO_2)–liquid (NaOH) reaction was observed right after the NaOH melting, indicating intensive reaction-kinetic behavior. Rapid blowout of the sample was observed during intensive exothermic behavior (Fig.7-16(b)). This phenomenon can be explained by the occurrence of the rapid NaOH–SiO_2 reaction and accidental blowout of the reacting system caused by the water vapor produced by the cited reaction. On the other hand, the Na–SiO_2 reaction occurs at a temperature more than 100 K higher than the NaOH–SiO_2 and Na_2O–SiO_2 reactions, indicating that the kinetic behavior of the Na–SiO_2 reaction is slower than that of the NaOH–SiO_2 reaction. In cases of reactions of Na–SiO_2 and Na_2O–SiO_2 at different heating rates of 3–10 K/min, the DSC exothermic peaks systematically shift to higher temperatures with increasing heating rate. Based on this kinetic characterization, activation energies for reactions of Na–SiO_2 and Na_2O–SiO_2, as estimated by the kinetic method, were approximately 231 and 106 kJ/mol, respectively. Thus, the Na–SiO_2 reaction was slower than the Na_2O–SiO_2 reaction. Moreover, the NaOH–SiO_2 reaction was dominant and significantly faster than other reactions such as Na–SiO_2 and Na_2O–SiO_2.

As a next step, we are implementing thermal analysis of reactions between sodium or sodium compounds with major compositions of structural concrete except SiO_2 and developing a mechanistic evaluation method for chemical reaction behavior.

This study was conducted in collaboration with the Hiroshima University.

References

Kikuchi, S. et al., Application of Thermal Analysis in Research and Development of Sodium-Cooled Fast Reactor, Netsu Sokutei, vol.43, no.1, 2016, p.11–18 (in Japanese).

Kikuchi, S. et al., Thermal Behavior of Sodium Hydroxide-Structural Concrete Composition of Sodium-Cooled Fast Reactor, Journal of Thermal Analysis and Calorimetry, vol.131, issue 1, 2018, p.301–308.

8 Research and Development on Fuel Reprocessing, Decommissioning, and Radioactive Waste Management

Toward the Decommissioning of Nuclear Facilities and Radioactive Waste Management

JAEA formulated the "Medium- and Long-Term Management Plan of our Facilities" (issued on April 1, 2017, amended on April 1, 2018) as a comprehensive plan which detailed the following three points:

– Selection and consolidation of facilities,
– Safety measures,
– Management of back-end issues.

In the plan, 44 nuclear facilities were chosen to be decommissioned.

JAEA submitted an application for the permission to proceed with the decommissioning of MONJU and the Tokai Reprocessing Plant (TRP) to the Nuclear Regulation Authority (NRA), which led to NRA granting this permission for MONJU on March 28, 2018, and for TRP on June 13, 2018.

To ensure a safe and appropriate nuclear facility decommissioning and radioactive waste management, it is necessary to introduce new technologies and knowledge and to promote the development of technologies for advanced safety and cost reduction. We have been comprehensively developing technologies for the safe and effective dismantling of nuclear facilities, minimization and stabilization processing of radioactive waste, and the disposal of radioactive waste (Fig.8-1). Our disposal project will be able to be applied to low-level radioactive waste from research facilities of universities and private organizations as well as our own.

The results of the technological development in this fiscal year are as follows:

– Integrated evaluation of radioactivity in waste from multiple facilities,
– Study of common evaluation methods for radioactivity in waste from research reactors (Topic 8-1).

In addition, the following results of the research and development (R&D) related to the accident at the TEPCO's Fukushima Daiichi NPS, are also introduced in Chapter 1: Characterization of Waste Generated by Contaminated Water Treatment (Topic 1-5).

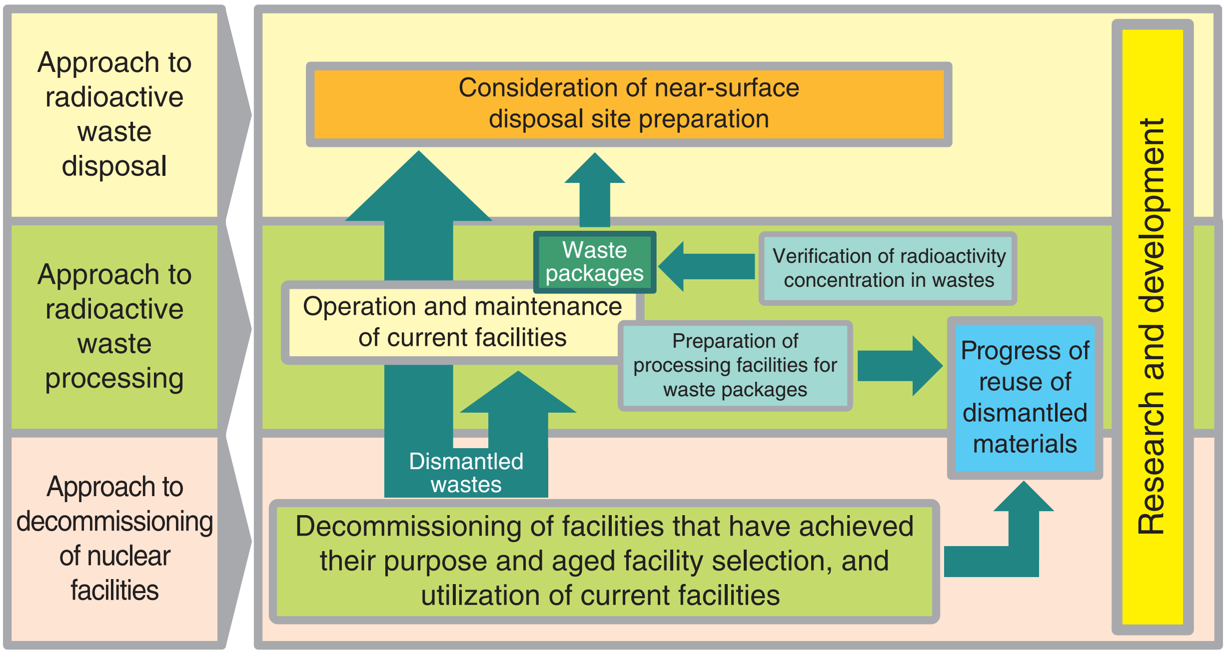

Fig.8-1 Outline of low-level radioactive waste management
We are steadily promoting the research and development of the decommissioning of nuclear facilities and the processing of radioactive waste, including waste treatment and waste characterization.

R&D to Improve Technology and Reliability of Geological Disposal in Japan

Geological disposal is one of the methods for the long-term isolation of high-level radioactive waste (HLW) produced during the generation of nuclear power from human environments. This is a critical issue which the present generation must approach sensibly, and it will remain crucial irrespective of any revision to the national nuclear energy policy.

In Japan, fuel spent in power reactors is reprocessed to extract the reusable uranium and plutonium for power generation. The liquids separated from the spent fuel during chemical reprocessing are solidified into a stable glass form. Under the Japanese disposal concept, vitrified waste is then encapsulated in a thick steel overpack, surrounded by highly compacted bentonite, and placed in a stable geological environment at a depth of more than 300 m below surface (Fig.8-2).

The process of implementing methods for the geological disposal of HLW is a long-term project that will last over 100 years. The project begins with the site selection and continues with the repository construction and operation, which is followed by backfill for repository closure. It is a national responsibility and of great importance to proceed efficiently with the project, continuously improving its sound technical basis and applying these attitudes to its implementation, regulatory activities, and also to the enhancement of public confidence. For this reason, to improve the technologies used for reliable geological disposal in Japan, we have made and will continue to make steady progress in the R&D in various fields such as geoscience, repository engineering, and safety assessment (Fig.8-3).

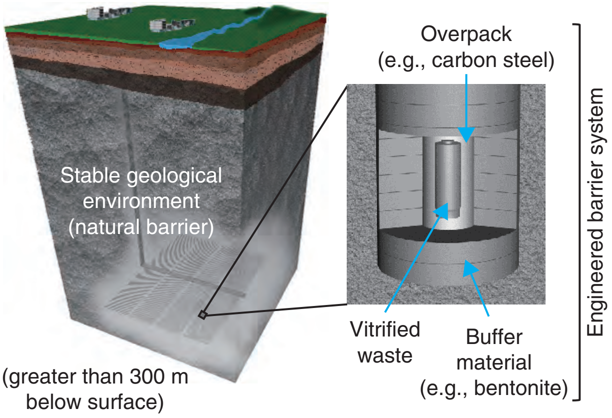

Fig.8-2 Schematic view of the basic concept for the geological disposal of high-level radioactive waste in Japan

Underground Scientific Research

At present, our R&D focuses particularly on projects at two underground research laboratories (URLs)–one at Mizunami, where crystalline rocks are examined, and the other at Horonobe, where sedimentary formations are examined (Topics 8-2–8-6).

In addition, to evaluate the long-term stability of geological environments in Japan (Topic 8-7) at the Toki Geochronology Research Laboratory (TGR), studies on topics such as tectonics, volcanic and faulting activities, and similar are currently in progress.

Research and Development of Geological Disposal Technologies

Together with the mentioned geoscientific efforts, to expand our knowledge on geological disposal, we are conducting an extensive study to assess the performance of the disposal system, engineered barrier systems, and long-term chemistry and migration of radionuclides at Tokai (Topic 8-8). These studies exploit the data and information on geological environments that were obtained through geoscientific research at both mentioned URLs.

Results of the R&D activities have been summarized as a web-based report (CoolRep), which has been made available on JAEA's public website (CoolRep:https://kms1.jaea.go.jp/CoolRep/english.html).

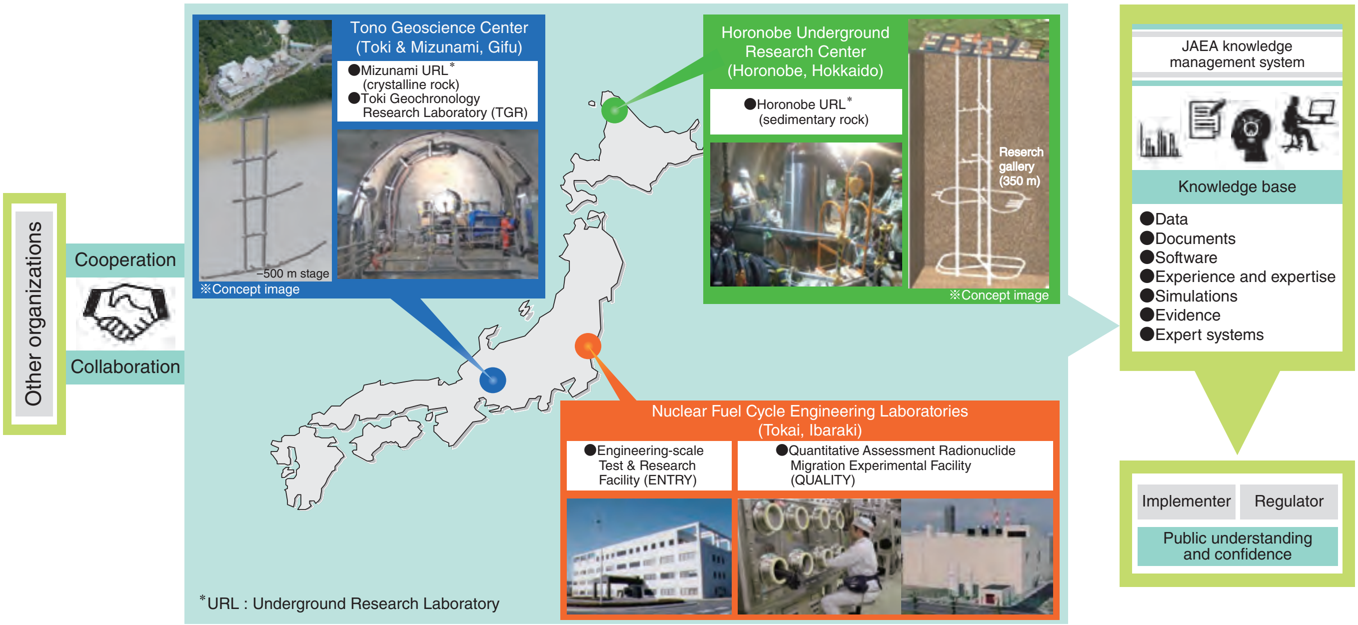

Fig.8-3 Structure of JAEA R&D activities

Improvement of Safety and Fuel Reprocessing Technologies

The decommissioning plan for TRP received approval from the NRA in June 2018, and TRP has entered a new stage of decommissioning. We have been promoting the vitrification of high-level radioactive liquid waste, with a primary focus on safety and the risk reduction of the radioactive material stored as a solution. Vitrification of the high-level radioactive liquid waste is scheduled to be completed by the 2028 Japanese fiscal year. We have also developed advanced vitrification techniques as well as solidification techniques for low-level radioactive liquid waste. The development of our solidification techniques, the nitric acid decomposition treatment, and the new cement solidification techniques is ongoing.

We are improving vitrification techniques from various viewpoints, such as the observation of the behavior of platinum group particles. To reduce the amount of vitrified waste, we are investigating more advanced methods and different ratios of the glass components. In our examination, we use non-radioactive isotopes as simulants and carry out theoretical calculations to estimate the thermal behavior of the vitrified waste. We are also studying alternatives for the borosilicate glass (Topic 8-9).

8–1 Integrated Evaluation of Radioactivity in Waste from Multiple Facilities

— Study of a Common Evaluation Method for Radioactivity in Research Reactor Waste —

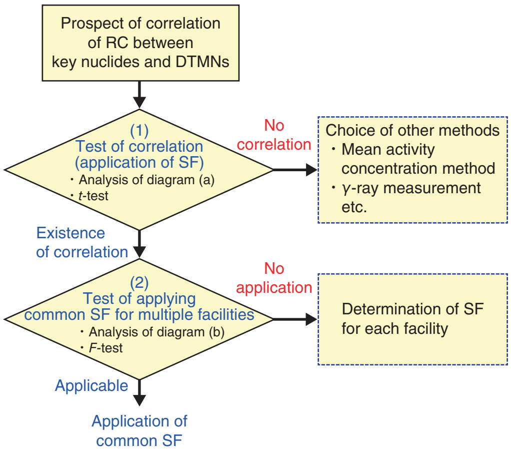

Fig.8-4 Common SF for multiple facilities
(1) Correlation between the radioactivity concentration (RC) of key nuclides and difficult-to-measure nuclides (DTMNs); (2) Common SF for multiple facilities.

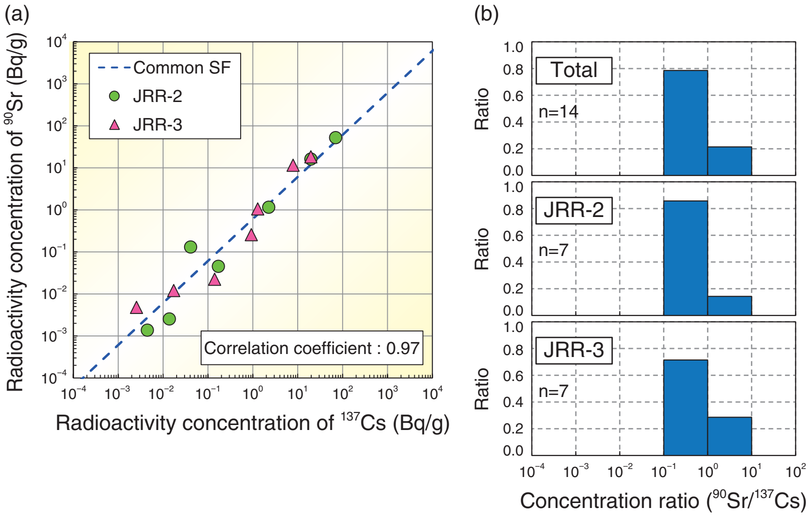

Fig.8-5 (a) Scatter diagram of the RCs of ^{90}Sr and ^{137}Cs in waste from the JRR-2 and the JRR-3; (b) RC ratio distribution for ^{90}Sr/^{137}Cs per facility
At JRR-2 and JRR-3, the correlation between the waste RCs of ^{137}Cs and ^{90}Sr is presented by a scatter diagram and the t-test (a). Their RC ratios are examined by the F-test (b). The result shows that the common SF for both JRR-2 and JRR-3 could be applied as shown in (a).

We have planned the near surface disposal of low-level radioactive waste generated by research, industrial, and medical facilities. It is necessary to confirm that the waste radioactivity concentrations (RCs) of each nuclide are smaller than the acceptable concentrations. However, a lot of effort is needed to collect the waste samples and perform radiochemical analysis to evaluate the RCs of difficult-to-measure nuclides (DTMNs). Therefore, it is important to establish more efficient methods for waste evaluation.

For waste generated by a research reactor, the scaling factor (SF) method has already been used because of its efficiency in evaluating the RCs of DTMNs by using the RC ratios of DTMNs and easy-to-measure nuclides (key nuclides). However, it is impractical to attempt to determine waste SFs for each reactor, because various types of research reactors exist in Japan.

Therefore, the applicability of the common SF for waste from both Japan Research Reactor-2 (JRR-2) and Japan Research Reactor-3 (JRR-3) has been examined based on the RCs of 19 DTMNs (^{90}Sr, etc.) and the key nuclides (^{60}Co and ^{137}Cs) in metal waste. Both research reactors comprise a heavy-water coolant and have similar characteristics in terms of the nuclide production mechanism and nuclide waste transport behavior, even though their fuel composition and reactor operating history differ.

By following the examination flow (Fig.8-4), the correlation of the key nuclides and the DTMNs in waste from both JRR-2 and JRR-3 was examined by a statistical analysis of the scatter diagram (Fig.8-5(a)) and a calculation of the t-test. Upon confirmation of a correlation, an observation of the concentration ratios (Fig.8-5(b)) and a calculation of the F-test were performed to examine whether the common waste SFs from JRR-2 and JRR-3 were applicable.

As a result, the RC correlation between ^{90}Sr and ^{137}Cs was confirmed by the t-test (significance level = 1 %) and its correlation coefficient was determined to be 0.97. Moreover, an application of a common waste SF from JRR-2 and JRR-3 was established by performing the F-test (significance level = 1 %). Similar results were obtained for the SFs of ^{63}Ni/^{60}Co, ^{152}Eu/^{60}Co, and ^{239}Pu+^{240}Pu/^{137}Cs. These results indicate that common waste SFs of these five DTMNs at JRR-2 and JRR-3 can be applied.

The RCs of 14 DTMNs showed no correlation with the RCs of the key nuclides. Therefore, these will be reevaluated after an increase in RC data, or we will examine the application of the mean activity concentration method of DTMN.

Based on these results, RC data for waste from other nuclear facilities will be collected, after which we will consider to extend to the facilities for which the common evaluation method can be applied.

Reference

Hayashi, H., Izumo, S. et al., Study on the Evaluation Methodology of the Radioactivity Concentration in Low-Level Radioactive Wastes Generated from JRR-2 & JRR-3, JAEA-Technology 2018-001, 2018, 66p. (in Japanese).

8–2 Ultratrace Analysis of Rare Earth Elements in Groundwater

— Improvement of the Onsite Extraction Method for the Study of Underground Redox Conditions —

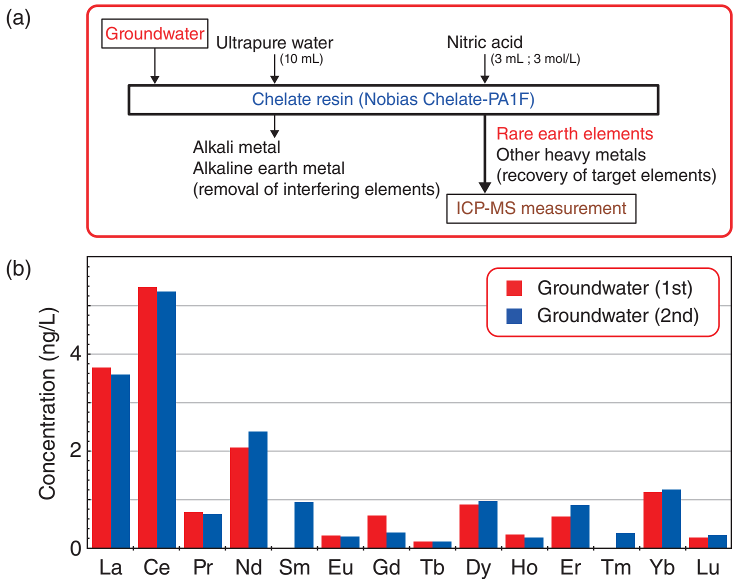

Fig.8-6 Flowchart for the analysis of rare earth elements (REEs) and REE content in groundwater samples by onsite extraction methods
(a) Outline of the REE analysis with a chelate resin. After the onsite extraction, REE content was measured by the ICP-MS at JAEA. We improved the preparation method for the ultratrace analysis of REEs in groundwater (less than 0.1 ng/L). (b) Reproducibility of the REE analysis confirmed for groundwater by a chelate resin.

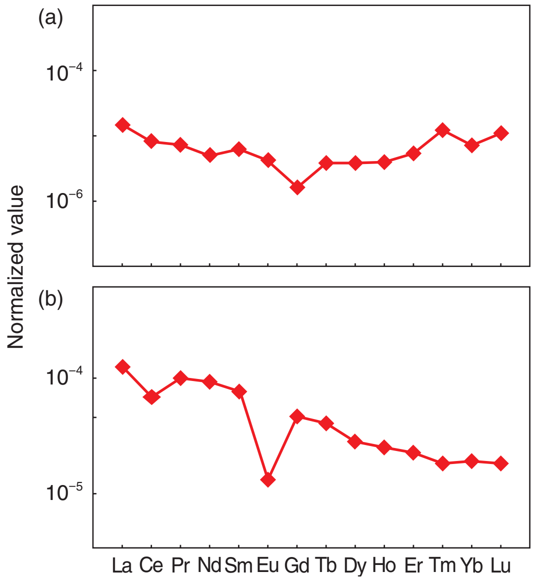

Fig.8-7 REE patterns in groundwater samples from onsite extraction methods
(a) Chondrite-normalized REE patterns in groundwater from the Gifu prefecture. (b) REE patterns in samples from the Yamanashi prefecture. The anomalous negative trend for Eu was observed, indicating redox conditions or material sources from the environment.

Geochemical properties such as the redox potential play an important role in the material cycles that occur in geological environments, so understanding their properties is crucial issue for successful geological disposal. The distribution and behavior of rare earth elements (REEs) and other chemical elements found in nature will indicate the process of evolution of the chemical conditions, as well as the sources of these materials. However, a quantitative analysis of REEs in natural samples is made complicated by their extremely low concentration in such samples, as well as by mass interference from other elements (e.g., Ba).

In this study, analyses (Fig.8-6) were performed using onsite solid-phase extraction and preconcentration methods for REEs, using a chelate resin comprising the iminobisacetic acid and the ethylenediaminetriacetic acid (Nobias Chelate PA1, Hitachi High-Tech Fielding Corporation). The chelate resin has previously been used to preconcentrate micronutrients in seawater and salt water samples; however, the application of the chelate resin to the REE analyses of groundwater and river water samples has rarely been reported. Standard reference materials and natural groundwater samples were used to evaluate these methods. The concentrations of REEs and other chemical elements were measured three times for each sample by using an inductively coupled plasma mass spectrometer (ICP-MS) at JAEA.

Using the chelate resin, background levels of REEs were found to be smaller than 0.3 ng/L, while their recovery rates (REEs, 1 ng/L) were discovered to be more than 90 % of those of artificial surface water. Barium contents were lower than the detection limit after extraction. Additionally, repeat analyses were performed to confirm the reproducibility of the onsite extraction (Fig.8-6). The REE patterns were observed for groundwater samples upon performing an onsite solid-phase extraction using the chelate resin (Fig.8-7). The observed REE data in natural water samples were in good agreement with those obtained using the previous method. Therefore, onsite solid-phase extraction using the chelate resin was demonstrated to be a rapid and simple preparation technique for REE analyses.

This work was a part of the result of the “R&D program supporting the development of technology for geological disposal of high-level radioactive waste”, supported by the Agency of Natural Resources and Energy (ANRE), the Ministry of Economy, Trade and Industry (METI), Japan.

Reference

Watanabe, T. et al., Onsite Chelate Resin Solid–Phase Extraction of Rare Earth Elements in Natural Water Samples: Its Implication for Studying Past Redox Changes by Inorganic Geochemistry, Limnology, vol.19, issue 1, 2018, p.21–30.

8–3 What Will Happen to Groundwater When Closing the Underground Drift?

— World's First On-Site Observation of Groundwater Chemistry in a Closure Drift —

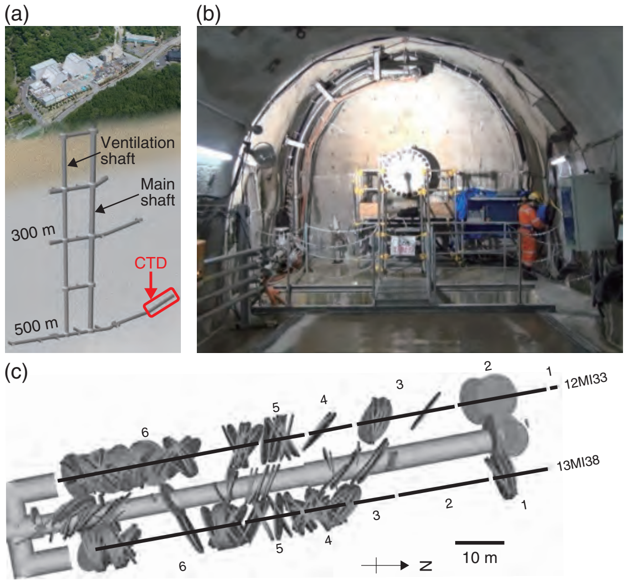

Fig.8-8 Schematic illustration of the Mizunami Underground Research Laboratory (MIU) and photograph of the water plug
(a) Schematic illustration of the MIU. The red square denotes the location of the Closer Test Drift (CTD). (b) Photograph of the water plug. (c) Positional relation between the CTD and the boreholes. Numbers along both boreholes denote the monitoring numbers.

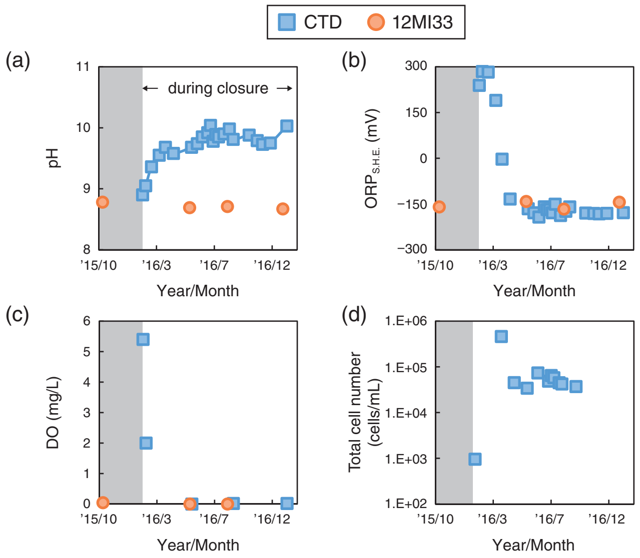

Fig.8-9 Variation of groundwater chemistry in the CTD and the monitoring borehole (12MI33)
(a) pH; (b) ORP; (c) DO; (d) total cell number. The square (■) and the circle (●) denote the CTD and the 12MI33, respectively. The gray area represents the period of operation of the CTD (until January 2016).

It is assumed that the groundwater properties in and around a drift (water pressure and underground chemistry) at a deep level change due to an artificial factor, such as its pumping, ventilation, and the use of cement during the construction and the maintenance period of a drift. Changes to groundwater chemistry after the closure of the drift have never been observed in-situ. It is important to clarify the types of process that influence the change of the groundwater environment in a closed drift. In January 2016, we constructed a water plug made of reinforced concrete to close the Closure Test Drift (CTD; Fig.8-8(a)) drilled in the Toki granite at a depth of 500 m (Fig. 8-8(b)). We observed a change in the groundwater chemistry in and around the CTD. Prior to the construction of the CTD, we excavated a borehole at a distance of 5 m from the CTD (12MI33; Fig.8-8(c)) and observed the groundwater chemistry.

The groundwater pH in the CTD was not greater than 9 before closure, but it changed to a value of 10 approximately 6 months from closure. However, the pH of the groundwater in the 12MI33 continued to be lower than 9 (Fig.8-9(a), exemplifying the result of Section 2). The increase in the groundwater pH in the CTD appears to be caused by a reaction between the CTD groundwater and the minerals in the shotcrete (such as calcium hydroxide). On the other hand, calcite, which was precipitated from the reaction on the shotcrete interrupted the reaction between shotcrete and the groundwater. In this test, alkaline groundwater in the CTD leaked into the open part of the gallery (outside of the water plug). However, if the drift is backfilled with solid material, the alkaline groundwater would probably spread broadly into the surrounding rock.

The initial redox potential (ORP) of the groundwater in the CTD indicated an oxidized condition (around +300 mV) because the CTD was filled with seepage from the open gallery. However, the ORP plunged to the original baseline value (−150 mV; Fig.8-9(b)) in three months. The concentration of dissolved oxygen also decreased at the same time as the ORP (Fig.8-9(c)). In addition, the number of microorganisms in the groundwater consistently increased with these changes (Fig.8-9(d)). Based on the microbiological study, the increased number of microorganisms mainly contained aerobic microorganisms. From these result, it can be inferred that the microorganisms consumed oxygen in the groundwater and promoted the recovery to the original reductive state.

By testing on a real drift, we revealed that the change in the groundwater environment accompanying the excavation, operation, and closure of the drift was caused by the groundwater flow, oxygen invasion, a reaction between groundwater and minerals, and a microbial reaction.

This result represents an important insight for the safety assessment in an actual geological disposal. In the future, it is necessary to monitor the changes in the groundwater environment when closing larger drifts and to confirm the importance of various processes.

Reference

Hayashida, K., Murakami, H. et al., Evaluation of Hydrogeochemical Processes Provoked by Tunnel Excavation and Closure Based on Simulated Experiment in a Mock-Up Test Drift, Chikyukagaku, vol.52, issue 1, 2018, p.55–71 (in Japanese).

8–4 Development of a Method to Infer Fault Connectivity

— A New Ductility Index Including the Mechanical Properties of Rocks —

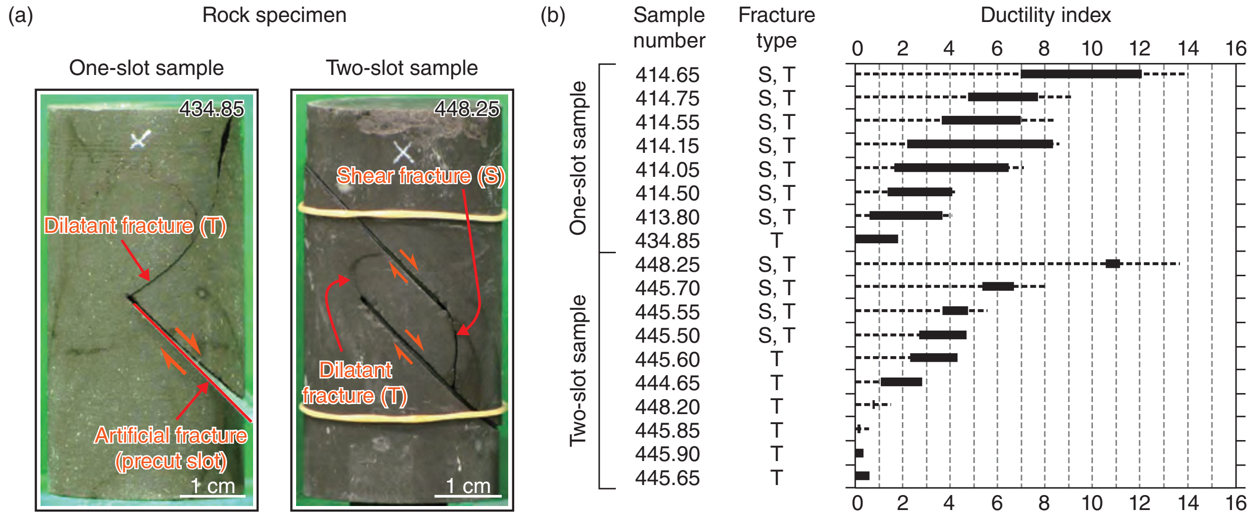

Fig.8-10 (a) Relationship between the types of fractures propagating from faults (modeled by artificial fractures) in the rock failure experiment and (b) the ductility index
A dilatant fracture (T) is a fracture with evidence of tensile failure. A shear fracture (S) is a fracture that exhibits only the evidence of shear failure, without tensile failure.

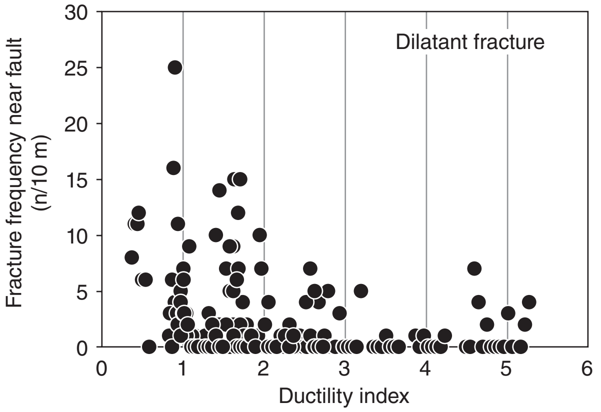

Fig.8-11 Relationship between the frequency of dilatant fractures observed near natural faults in a drill core and the ductility index

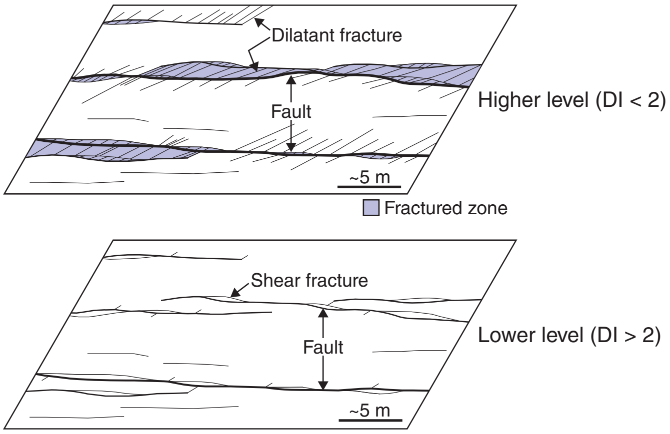

Fig.8-12 Relationship between fault connectivity and the ductility index
Dilatant fractures facilitate linking among neighboring faults at higher levels.

Faults lengthen by linkage with other faults. Even though the manner of linkage may vary, faults tend to link if dilatant fractures (Fig.8-10(a)) propagate from faults as secondary fractures. However, the process by which mechanical conditions facilitate the propagation of dilatant fractures from faults has not yet been appropriately described.

This study investigated the mechanical conditions that facilitated the propagation of dilatant fractures from faults by using a new indicator, the ductility index (DI), and performing a theoretical analysis, a laboratory experiment, and field observations. The DI is defined as the effective mean stress divided by the tensile strength of the rock, and it is lower at shallower areas. The theoretical analysis revealed that dilatant fractures tend to propagate from faults when the DI is smaller or equal to 2. This result is consistent with the results of rock failure experiments that used rock specimens and the observations of natural fractures in a drill core. These experiments showed that only the dilatant fractures preferentially propagate from faults (modeled by artificial fractures) when the DI is smaller or equal to 2 (see the samples 434.85, 448.20, 445.85, 445.90, and 445.65 in Fig.8-10(b)). The core observation showed that dilatant fractures are more developed near faults where the DI smaller or equal to 2 (Fig.8-11). These results suggest that the connectivity of faults differs between shallow and deep levels even within the same formation, depending on the DIs (Fig.8-12). This is a result of vital importance to the reliable assessment of the groundwater flow during the site selection for radioactive waste disposal.

Reference

Ishii, E., Far–Field Stress Dependency of the Failure Mode of Damage–Zone Fractures in Fault Zones: Results from Laboratory Tests and Field Observations of Siliceous Mudstone, Journal of Geophysical Research: Solid Earth, vol.121, issue 1, 2016, p.70–91.

8–5 Accumulation of Heavy Metals in Biofilms in a Deep Subsurface Environment

— Evaluation of Heavy Metal Sorption in Groundwater Interaction Systems of Microbes, Rocks, and Groundwater —

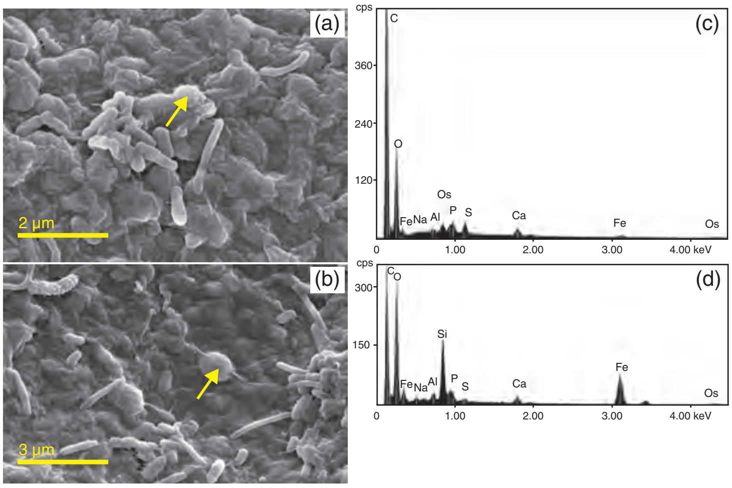

Fig.8-13 Field-emission scanning electron microscope micrograph of biofilms and energy-dispersive X-ray spectroscopic (EDS) analysis
(a) Biofilm formed in sedimentary rock groundwater. (b) Biofilm formed in granite groundwater. (c) Result of the EDS analysis of the allowed point in the biofilm of sedimentary rocks. (d) Result of the EDS analysis of the allowed point in the biofilm of granite rocks. The elements Fe, Ca, S, etc. were detected in the biofilms.

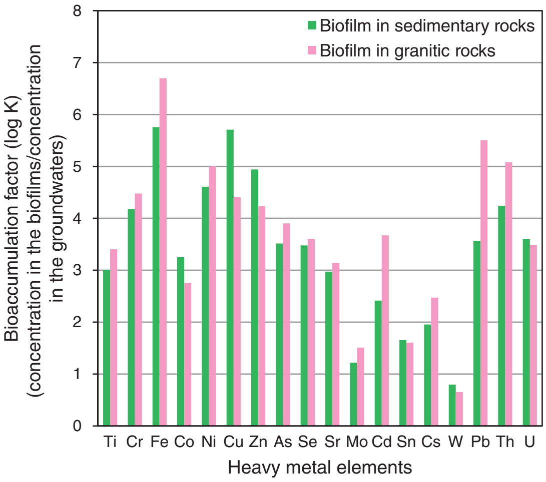

Fig.8-14 Bioaccumulation factor for heavy metals in groundwaters and biofilms
Chemical analyses demonstrated that high amounts of heavy metals such as Cr, Fe, Ni, Cu, Zn, Pb, and Th accumulated in the biofilms.

Research has shown that microbial ecosystem in subsurface environments appear to be far more extensive and metabolically and phylogenetically complex. Planktonic and attached microorganisms are present in nature and attached microorganisms comprise diverse cells embedded within slimy extracellular polymeric substances, or biofilms. It is thought that microorganisms form biofilms in subsurface environments, but their existence, metabolic function, and interaction with metals in subsurface are not well known. In biofilm environments, heavy metals, including radionuclide pollutants, interact by a variety of mechanisms such as biosorption, bioaccumulation, biotransformation, biomineralization, precipitation, metabolic redox reactions, and production of complexing agents. To evaluate microbial effects in performance assessments of geological disposal sites, it is important to understand the interactions between biofilms and heavy metals, including the radioactive elements in subsurface environments.

In this study we characterized the geochemical and microbial structures of biofilm samples that formed in groundwater in the subsurface environment at the Tono Uranium Mine area, Japan. The biofilm samples were collected from the insides of teflon tubes that were used to sample anaerobic groundwaters in a borehole drilled in the Tono area of Japan, in order to understand their effects on the migration behavior of heavy metals in subsurface environments. Examination of the biofilms using a field-emission scanning electron microscope (FE-SEM) demonstrated that the presence of an organic matrix could be observed throughout their structures (Fig.8-13). Microbiomes of the derived biofilms, as well as those of the ambient bacterioplankton, were characterized based on DNA analysis, and their heavy metal sorption properties were examined with reference to the geochemical features of the groundwaters.

The results showed that the community structure lacked diversity in the biofilm samples in both sedimentary and granitic rocks. The predominant phylotype (78 % of the biofilm) in the biofilm library for sedimentary rock groundwater was closely related to *Methylobacillus flagellatus* (96.5 % similarity), classified as an obligate methylotroph. In the granitic groundwater, the most predominant phylotype (77 % of the granitic biofilm) was closely related to *Ignavibacterium album*, which is strictly anaerobic and grows fermentatively. Biofilms were also characterized with accumulation/sorption of heavy metals such as Cr, Fe, Ni, Cu, Zn, Pb, and Th. From the calculation of the bioaccumulation factor for the concentration of heavy metals, we found different sorption properties of each element and each groundwater sample between sedimentary rocks and granite (Fig.8-14). Saturation indices were calculated using the chemical composition and redox conditions. It was found the metal sorption properties varied between biofilms. Presumably, this occurred because of the influences of co-occurring Fe-hydroxides and sulfide minerals under the redox conditions in the subsurface environments.

The biofilm–mineral interaction provides an implication for the possible retardation of radionuclide migration in subsurface hydrology, which is of practical interest in geological disposal systems for high-level radioactive waste.

Reference

Amano, Y. et al., Characteristics of Naturally Grown Biofilms in Deep Groundwaters and Their Heavy Metal Sorption Property in a Deep Subsurface Environment, Geomicrobiology Journal, vol.34, issue 9, 2017, p.769–783.

8–6 Characterization of Mass Transport Paths in Mudstone with a Fracture

— Establishing an In Situ Tracer Test Method for Groundwater Saturated with Dissolved Gas —

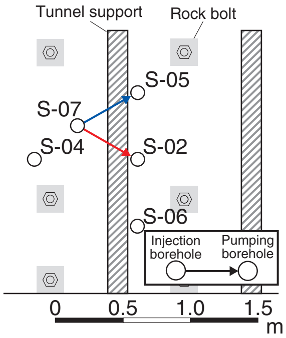

Fig. 8-15 Layout of tracer migration tests
Each borehole is drilled to a depth of approximately 3 m, in a substantially horizontal direction from the gallery wall. The arrows show the flow directions in preliminary tests (→) and the tracer test (→).

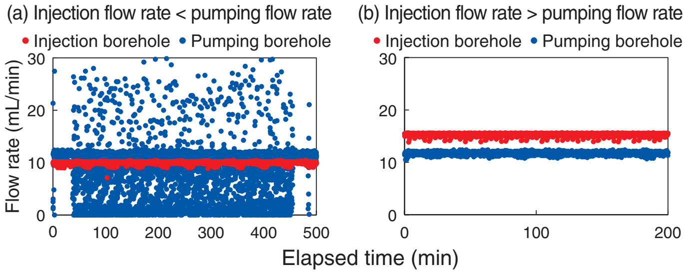

Fig.8-16 Relationship between the test condition and degassing
(a) Flow rate for an injection flow rate of 10 mL/min, a pumping flow rate of 12 mL/min, and with degassing. (b) Flow rate for an injection flow rate of 15 mL/min and reduced degassing. The test condition of the injection flow rate being larger than the pumping flow rate is ideal to reduce degassing.

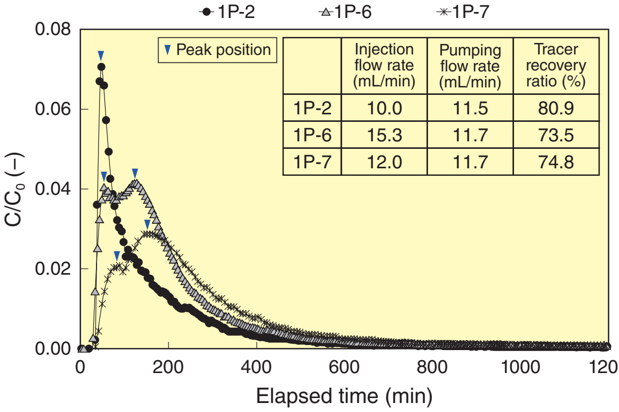

	Injection flow rate (mL/min)	Pumping flow rate (mL/min)	Tracer recovery ratio (%)
1P-2	10.0	11.5	80.9
1P-6	15.3	11.7	73.5
1P-7	12.0	11.7	74.8

Fig. 8-17 Relationship between the test condition and the tracer recovery ratio
Tracer recovery ratios for the test case of 1P-6 and 1P-7 (the injection flow rate being larger than the pumping flow rate) are relatively low, because the tracer migrates through a relatively large number of paths, contributing to some of the peaks in the breakthrough curve. The test condition of the pumping flow rate being larger than the injection flow rate is ideal to achieve a large tracer recovery ratio.

In situ tracer tests are valuable to directly evaluate the solute transport phenomena in a rock mass under field conditions (e.g., groundwater flow, groundwater chemistry). However, few in situ tracer tests focused on fractures in sedimentary rocks have been conducted thus far. Therefore, it is necessary to develop techniques for conducting in situ trace tests and to obtain the input data of mass transport analyses for the safety assessment of geological disposal.

In situ tracer tests with pore pressure change have to be conducted while reducing the degassing, which results in flow paths being unsaturated because methane and carbon dioxide, which are dissolved in groundwater in a pressurized environment around mudstone in the Horonobe Underground Research Center, are degassing when pressure released. The tracer recovery ratio, which is a quality indicator for tracer tests, should also be made as large as possible to ensure a good quality of tests. As the test conditions of the injection flow rate and the pumping flow rate were varied, in situ tracer tests and preliminary tests using water without tracers were performed. We evaluated the effects of the test conditions by observing the degassing occurrence and the tracer recovery ratio. The layout of these tracer tests is shown in Fig.8-15.

Results of the preliminary test showed that the flow rate in a pumping borehole varied widely. This is a result of measurement errors caused by the gas bubble penetration degassing from the groundwater when the pumping flow rate (●) is larger than the injection flow rate (●), as shown in Fig.8-16(a).

On the other hand, these variation do not occur when the injection flow rates are larger than the pumping flow rates (Fig.8-16(b)). Therefore, an injection flow rate larger than that of the pumping flow rate leads to a reduction in the effects of degassing. However, the results of tracer tests (conducted using uranine) with pumping flow rates larger than injection flow rates (1P-2), show good tracer recovery ratios (Fig.8-17). These results are better than those obtained by tests of 1P-6 and 1P-7, which are conducted with injection flow rates larger than the pumping flow rates. The lower tracer recovery ratios of 1P-6 and 1P-7 are due to tracer migration, which results from a large injection flow rate and occurs via larger flow paths. Therefore, these results reveal that, to simultaneously reduce degassing and increase tracer recovery in tracer tests in groundwater saturated with gasses, an injection flow rate slightly larger than the pumping flow rate is ideal.

Based on this study, we established a method of in situ tracer tests which targets fractures in mudstone flowing in gas-saturated groundwater. This method enables a reduction of the effects of degassing and provides high-quality data.

Reference
Takeda, M. et al., Evaluating Test Conditions for in situ Tracer Migration Test in Fractured Siliceous Mudstone Involving Groundwater with Dissolved Gas, Journal of Nuclear Fuel Cycle and Environment, vol.25, issue 1, 2018, p.3–14 (in Japanese).

8–7 Efficient Analysis of Rock Mineral Content Ratio

— Modal Analysis Using X-ray Maps and Image Processing —

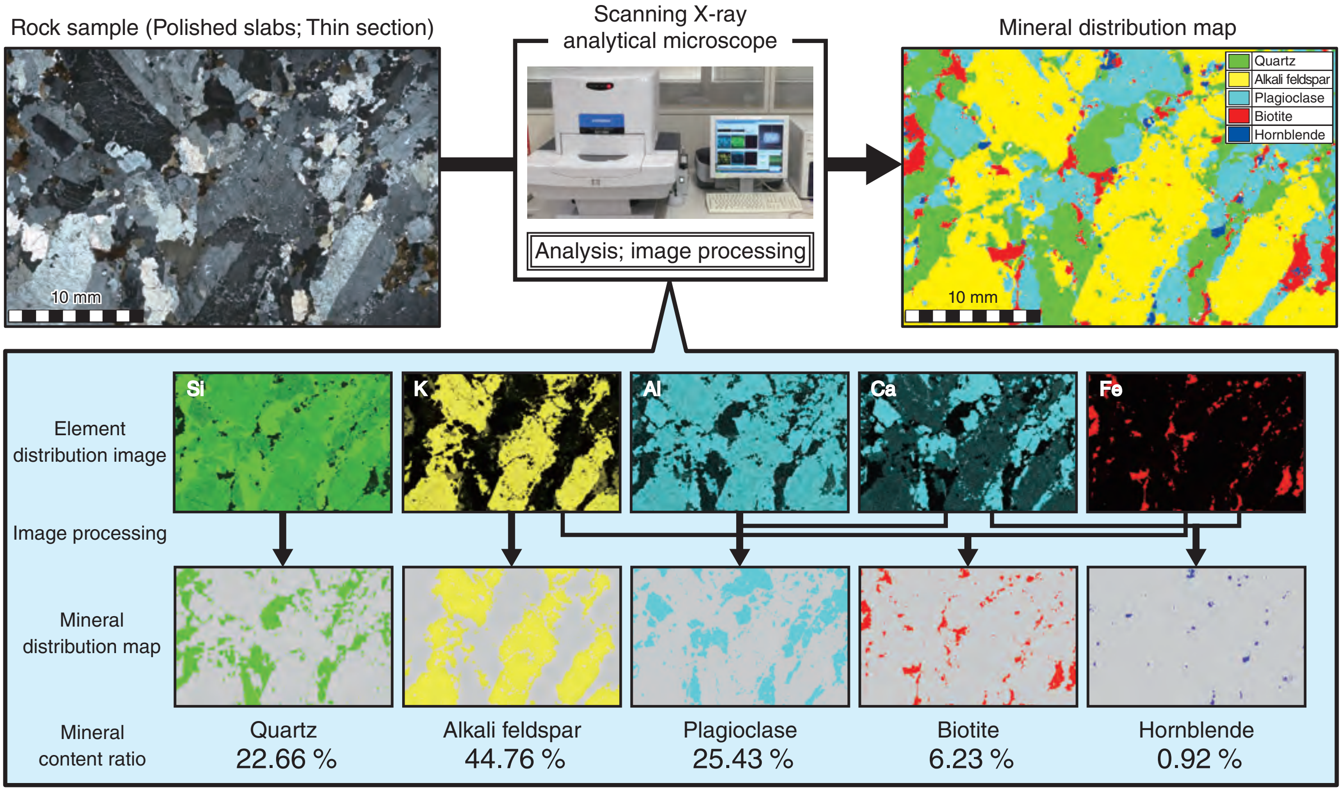

Fig.8-18 Analysis overview
A mineral distribution map is produced by elemental measurements performed using a scanning X-ray analytical microscope and image processing. The mineral content ratio is calculated based on the mineral distribution map.

The modal composition (mineral content ratio) of a rock is the principal characteristic for its petrological study and it is generally analyzed by the point-counting method on a thin section (a sliced and polished rock sample adhered to a piece of glass), observed using a polarizing microscope. However, this method is time-consuming and depends on the user’s mineral identification ability. Therefore, a quicker and simpler method, which would be blind to the user’s ability, is required. Here we introduce an alternative method employing a scanning X-ray analytical microscope (SXAM) and image processing software. We apply this method to granitic rocks composed of quartz, alkali feldspar, plagioclase, biotite, and hornblende.

In this new method, we first scan a rock sample (using a thin section or a polished slab) using SXAM to obtain element distribution images (Fig.8-18). SXAM is a device that can measure surficial element concentration using X-ray irradiation. Automatic measurement is performed for approximately 18 hours to obtain distribution images of the major elements found in granitic rocks (Si, K, Al, Ca, and Fe). We developed a suitable superposing technique using commercially available software for image processing to create the mineral distribution map (Fig.8-18). Then, the mineral content ratio is calculated based on the obtained map using other software. The image analysis of the map provides the spatial distribution of each mineral, after which the modal composition can be calculated (Fig.8-18). This method can be established as a routine, and the actual work time needed to complete the process is between 30 and 60 minutes.

The modal composition calculated by this method is almost completely equal to that of the point-counting method performed on the same sample by an expert. By using this method, the quantitative modal composition based on element concentration can be obtained efficiently in a short time, regardless of individual ability for mineral identification. In addition, this method can be applied not only to granitic rocks, but also to other plutonic rocks and hypabyssal rocks, so long as the rocks are composed of multiple kinds of minerals with a grain size larger than 100 μm and with different chemical compositions.

This work was a part of the result of the “R&D program supporting the development of technology for geological disposal of high-level radioactive waste”, supported by the Agency of Natural Resources and Energy (ANRE), the Ministry of Economy, Trade and Industry (METI), Japan.

Reference

Ueki, T. et al., Modal Analysis Using Scanning X-ray Analytical Microscope and Image Processing and Analyzing Softwares, The Journal of the Geological Society of Japan, vol.123, issue 12, 2017, p.1061–1066 (in Japanese).

8–8 Transport of Radionuclides in Specific Surface Environments

— Application of an Open Data Method to Assess Sediment Transport —

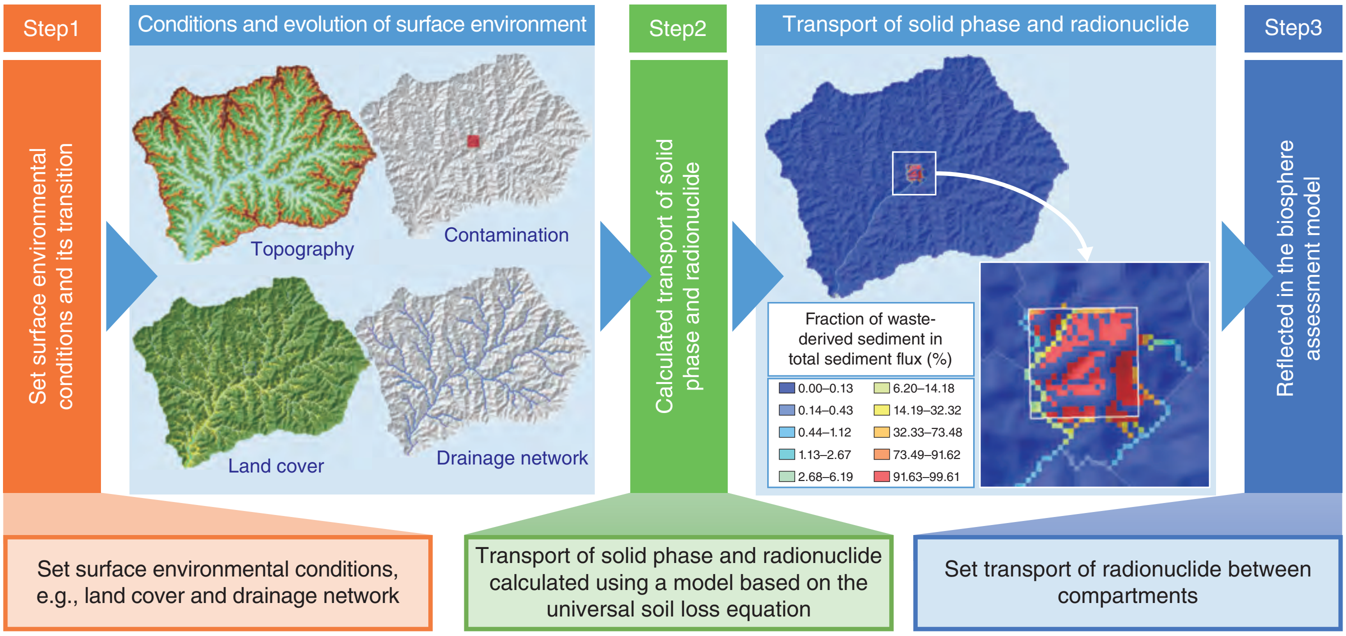

Fig.8-19 Example of the relationship between the transport of sediment/radionuclides and a biosphere assessment
Various surface environmental conditions such as its topography, land cover, drainage network, and contamination were set (Step1) to calculate the sediment transport and the corresponding radionuclide transport (Step2). This method paves the way for a more realistic biosphere assessment, which reflects the features of radionuclide transport according to sediment transport (Step3).

The safety assessment of geological disposal of radioactive waste requires an evaluation of the exposure dose for humans in the surface environment (known as the biosphere assessment). For this calculation, an assessment is made for the transport process of radionuclides from the repository to the surface environment and the process in the surface environment. The transport processes of radionuclides within a surface environment are primarily controlled by the transport of a liquid (water) and a solid phase (sediment, etc.), and the intake of radionuclides by drinking water is considered to be the main exposure process. Those transport and human-exposure processes are heavily affected by the conditions of the surface environment, such as its topography and land cover. In the tectonically active and pluvial setting of Japan, such surface environmental conditions evolve with time. One of the typical processes relating to the evolution of the surface environmental conditions is sediment transport followed by erosion. However, it is extremely difficult to precisely predict this evolution over hundreds of thousands of years, which is the length of time possibly required for the safety assessment of geological disposal.

For that reason, widely used methods rely on generalized biosphere assessment models, in which the configuration of the surface environment is represented as a combination of homogeneous compartments, while various radionuclide transport processes are simply represented as a transfer of water and sediment between those compartments.

Because of that, the purpose of this research is to enable the calculation of radionuclide transport in the surface environment according to sediment transport followed by erosion as realistically as possible. In this calculation, erosion and sediment transport processes are modeled by applying the universal soil loss equation and simple hydraulic equations, while the available published data (open data) such as topography, land covers, and precipitations are used as input. By using this calculation, broad distributions of radionuclides and the discharge of radionuclides from main catchments in the surface environment can be estimated. This methodology has also been applied to calculate the radionuclide transport at an off-site environment of the TEPCO’s Fukushima Daiichi NPP accident. Fig.8-19 shows an example of various surface environmental conditions set in Step1 and the calculated sediment transport from Step2. This example shows a significant dilution of sediment from a specific area that is assumed to be a discharge area for radionuclides from the underground repository.

It is expected that the results obtained for the radionuclide transport from the transport of the sediment using this method can be applied to define parameter values to present the movement of sediment and radionuclides between compartments. These parameters are of prime importance in the biosphere assessment model, and should be determined as best as possible for specific surface environmental conditions.

Reference

Yamaguchi, M. et al., Predicting the Long-Term ^{137}Cs Distribution in Fukushima after the Fukushima Dai-Ichi Nuclear Power Plant Accident: A Parameter Sensitivity Analysis, Journal of Environmental Radioactivity, vol.135, 2014, p.135–146.

8–9 Vitrification Technology for Radioactive Elements

— Search for an Appropriate Glass Medium —

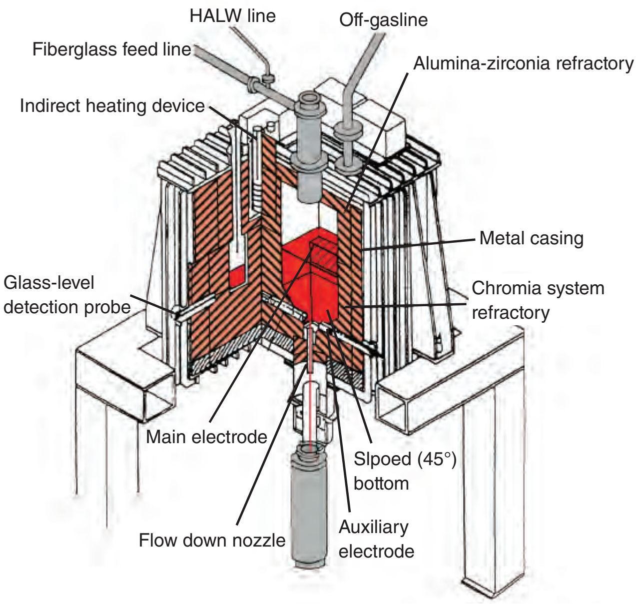

Fig.8-20 Conceptual structure of the melter at the TVF
Conceptual structure of the glass melter at the Tokai Vitrification Facility (TVF). The fiber cartridge (70 mmφ × 70 mmL), which can absorb the highly active liquid waste (HALW), is used for this melter. The cartridge-impregnated HALW is melted in the melter by the application of direct current and the melt is flown into a canister. This vitrification method is called the liquid-fed Joule-heated ceramic melter (LFCM).

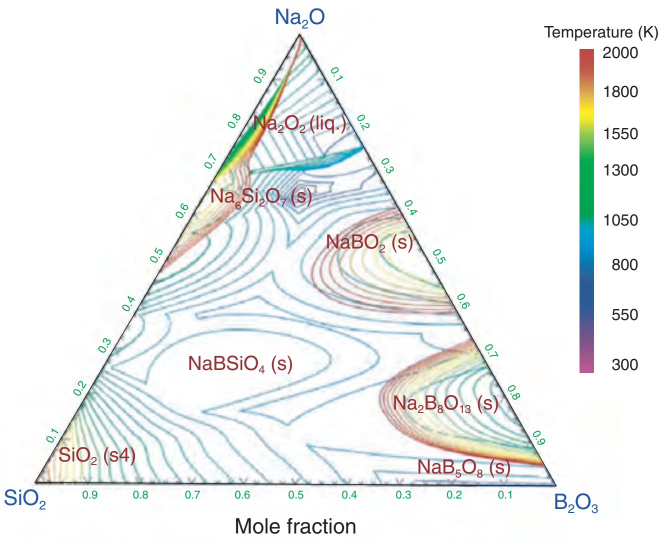

Fig.8-21 Liquidus surface projection for the SiO_2-B_2O_3-Na_2O ternary system
The glass phase diagram can be constructed using our established thermodynamic database. This figure shows the SiO_2-B_2O_3-Na_2O ternary system in air with an oxygen concentration of 20.95 %, which is called the liquidus surface projection. The relation between the glass composition and the liquidus point can easily be estimated using this figure.

The highly active liquid waste generated by the reprocessing of spent fuel is vitrified with using a glass melter at the vitrification facility, as shown in Fig.8-20. The obtained stable vitrified waste is called high-level radioactive waste (HLW) and it is stored until final disposal.

Glass is an amorphous solid that exhibits the glass transition phenomenon with rising temperature (its fluidity increases with a rapid decrease of its rigidity and viscosity). Glass is generally considered to be a fragile material, but it has a high rigidity and a viscosity almost equal to that of crystal when it doesn't have any defects on its surface. Therefore, in theoretical terms, glass is regarded as one of the toughest materials. Since before the 13th century, borosilicate glass (BSG) has been known to possess a lower thermal expansion, a superior acid resistance, good rigidity, and chemical stability. By the end of the 19th century, BSG was used commercially due to the development of optical glass. As the glass used in HLW production requires the aforementioned properties, BSG is commonly used as the vitrified medium because of the existence of already established technology for its use in HLW production.

Currently, more advance methods are being investigated for the purposes of removal of some fission products (FPs) before vitrification, or to change the ration of glass components, in order to decrease vitrified waste. To minimize radioactivity and the generation of radioactive waste, stable isotopes are commonly used as simulants in vitrification experiments instead of the high-level radioactive FPs, which can lead to the possibility to obtain more data. Before performing the experiment under high temperature, theoretical calculations were used to estimate the thermal behavior of the vitrified waste. As thermodynamic properties are necessary for these theoretical calculations, some missing properties were estimated by computational analysis. The ternary phase diagram shown in Fig.8-21 was constructed as an example.

The search for an enhanced glass medium is carried out gradually with the research and development of vitrification technology. The iron phosphate glasses are an enhanced glass medium which may be able to load various elements and which could prove to be a suitable medium for low-level radioactive waste.

References

Amamoto, I. et al., Research on Vitrification Technology to Immobilize Radioactive Sludge Generated from Fukushima Daiichi Power Plant: Enhanced Glass Medium, Journal of Nuclear Science and Technology, vol.53, issue 10, 2016, p.1467–1475.

Amamoto, I., Vitrification Technology for Radioactive Wastes, Journal of the Society of Inorganic Materials, Japan, vol.24, no.391, 2017, p.393–401 (in Japanese).

9 Computational Science and E-Systems Research

Computational Science for Nuclear Research and Development

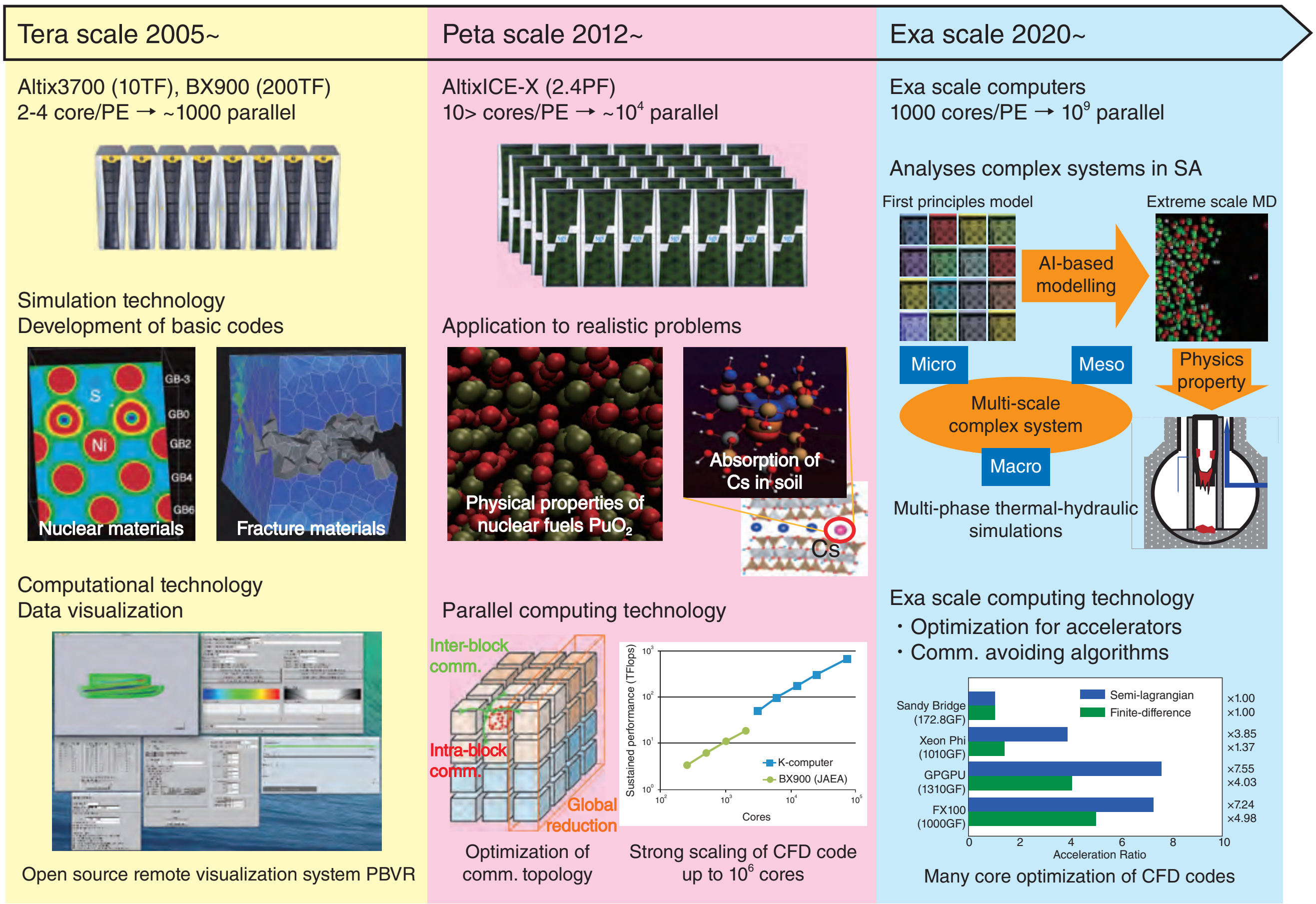

Fig.9-1 Computer-science research at the Center for Computational Science and e-Systems
To analyze complex systems in nuclear research and development, exascale simulations are being developed by advancing the simulation and computational technologies that were originally devised for tera/petascale simulations.

Simulation techniques for analyzing the complex phenomena comprising various physical effects are essential for resolving issues created by the accident at the TEPCO's Fukushima Daiichi NPS, such as the environmental dynamics of radioactive substances, the volume reduction of polluted soil, and the study of severe accidents (SAs). These techniques are also required for research and development of future nuclear systems. For example, severe-accident analyses require not only macroscale thermal-hydraulic simulations for the melt-relocation behavior of nuclear fuels and structural materials but also state-of-the-art multiscale and multiphysics simulation technologies, which enable AI-based integration of mesoscale simulations for evaluating complicated interface formation owing to mixing of molten debris and fracture events such as crack growth as well as microscale quantum simulations for estimating diffusion, chemical reactions, and phase transitions in extreme environments at high temperature and pressure. In addition to these new simulation technologies, computational technologies that support high-performance computing on future exascale machines are required.

Thus far, we have developed simulation techniques such as quantum and fluid simulations, which form the basis for analyzing complex phenomena as well as computational technologies such as numerical algorithms and visualization systems. We further advance these techniques and address the development of new simulation and computational technologies that enable exascale analyses of complex phenomena (Fig.9-1). Such simulation techniques for complex phenomena will form a common foundation for general nuclear research and development.

In FY2017, as a computer-science contribution to the reconstruction and revitalization of Fukushima prefecture, we disclosed mechanisms for cesium absorption on various clay surfaces in soil via first-principles-based simulations (Chapter 1, Topic 1-18). In addition, in the following three topics, various micro and mesoscale simulations that are needed for the analyses of complex phenomena were improved:

1. AI-based acceleration of quantum Monte Carlo simulations for quantum many-body systems in strongly correlated electron systems such as heavy-isotope compounds (Topic 9-1).
2. Kinetic Monte Carlo simulations of the condensation mechanism of impurities at grain boundaries in steel (Topic 9-2).
3. Establishment of a new materials' radiation-damage formula that accounts for damage recovery due to atom-relocation processes observed in MD simulations (Topic 9-3).
4. Development of a new in-situ visualization system that enables interactive visualization of extreme-scale simulations at runtime (Topic 9-4).

We are steadily promoting research on simulation and computational techniques, which form a common foundation for nuclear research and development and are providing them to the community.

9–1 Challenges of Solid-State Physics with AI Technology

— Machine Learning Accelerates Quantum Simulations —

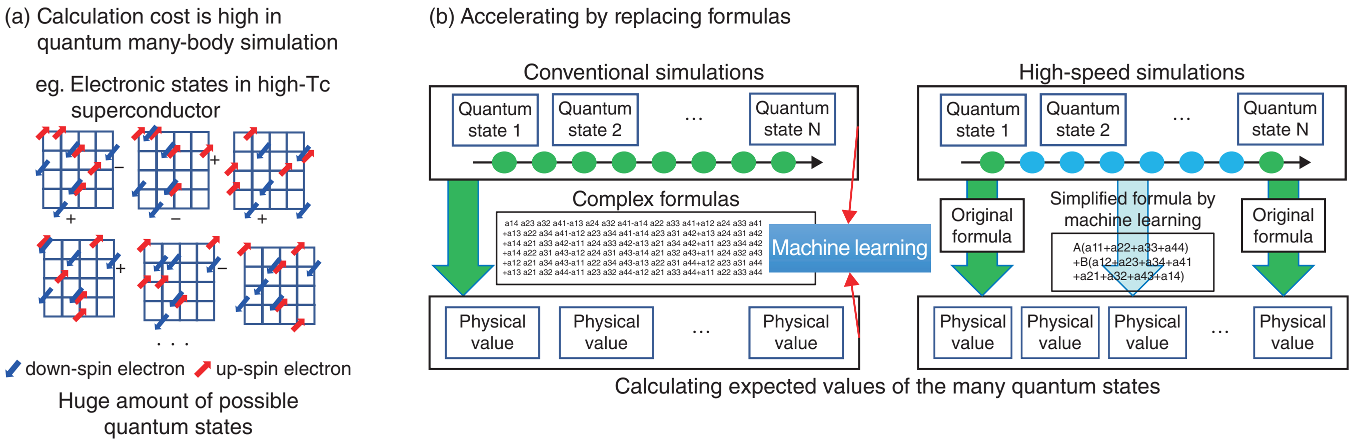
(a) Calculation cost is high in quantum many-body simulation

(b) Accelerating by replacing formulas

Fig.9-2 Schematic figure of the quantum manybody system calculation (a) and the Monte Carlo method (self-learning Monte Carlo method) using machine learning (b)
High speed is achieved by replacing complex expressions that require huge calculations in conventional simulation with simpler expressions found by machine learning.

Many of the properties of matter are explained by the behavioral differences of the electrons in the material. In particular, materials such as copper oxide high-superconducting-transition-temperature (high-Tc) superconductors and heavy element compounds including uranium etc. are called strongly correlated electron systems in which electrons strongly interact with each other. Understanding of electron behavior in these materials is one of the important problems in modern solid-state physics. In order to accurately simulate the behavior of these electrons, quantum simulation that takes quantum mechanical properties of electrons is necessary. For example, in the superconducting state where the resistance becomes zero, it is known that electrons move in pairs, but in the copper oxide high-temperature superconductor at a high temperature above the liquid nitrogen temperature, the behavior of the electrons has not been fully understood and its superconducting mechanism is one of the big mysteries of solid-state physics. There are many quantum simulation, theoretical analysis, and experiments.

However, in quantum simulation, when the number of electrons increases, the number of electron states that we have to consider increases exponentially. Thus, the calculation cost is very high and even if the latest supercomputer is used. It is difficult to fully understand strongly correlated electron systems (Fig.9-2(a)). Therefore, many researchers all over the world are trying to develop highly accurate and fast calculation methods.

In this research, we focused on “Machine Learning”, which has been developing rapidly in the field of computational science in recent years. From a huge amount of data, machine learning can find patterns are difficult for human beings to find. In this research, we succeeded in developing a faster method (self-learning Monte Carlo method) by creating an effective model by extracting its essence using machine learning in quantum Monte Carlo simulation which is a highly accurate quantum simulation method.

In Markov chain Monte Carlo simulation, we calculate the physical quantity (such as electron density) by using stochastic process called Markov chain made by target model. However, to calculate the transition probability of Markov chain, it is necessary to calculate using a very complicated expression reflecting the complexity of the quantum system. Therefore, we execute traditional simulation as a trial simulation, gather learning data on this complicated calculation formula, and finding out the pattern behind it by machine learning to construct an effective model represented by a simple calculation formula. In this simulation, it is possible to calculate the physical quantity at a high speed (up to 10000 times) by sandwiching the simulation with this effective model (Fig.9-2(b)).

Using this high-speed method, it becomes possible to deal with complicated models reflecting the structure of more realistic substances, and it is expected to elucidate the variety of physical properties of materials which have been a mystery until now.

Reference

Nagai, Y. et al., Self–Learning Monte Carlo Method: Continuous–Time Algorithm, Physical Review B, Rapid communication, vol.96, issue 16, 2017, p.161102–1–161102–6.

9–2 Elucidation of Embrittlement of Steels from Analysis of Atomic-Diffusion Behavior

— Evaluation of the Diffusion Coefficient by Kinetic Monte Carlo Simulation Based on First-Principles Calculation —

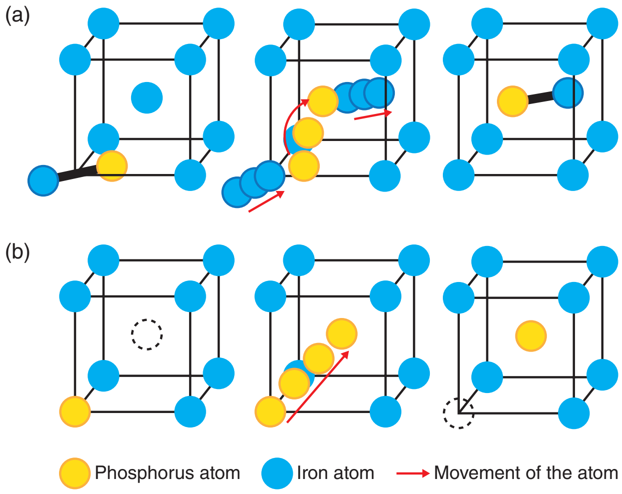

Fig.9-3 Movement mode of the phosphorus atom
(a) Moving by exchanging the pair atom. (b) Moving to the position of an adjacent vacancy. The left and right figures show the atomic state before and after the movement, respectively. The central figure shows the transition state of the movement.

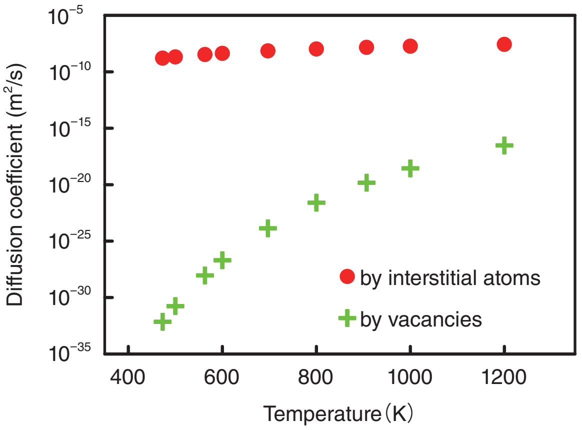

Fig.9-4 Temperature dependence of the diffusion coefficient evaluated by the simulation
As temperature increases, phosphorus atoms diffuse faster in both cases. It is seen that the movement by interstitial atoms is several orders of magnitude faster than that by vacancies.

Neutron irradiation at high temperature during reactor operation causes iron atoms in the stable positions of the crystal lattice in steels covering reactor cores to be repelled and move around. Along with this phenomenon, impurity atoms also start to gather at grain boundaries where the crystal lattice structure is in disorder, thereby weakening these boundaries. This phenomenon is called embrittlement, and it may eventually lead to cracking. Therefore, to safely operate nuclear reactors, it is important to estimate the amount of impurities at grain boundaries by evaluating how impurity atoms migrate and how fast they gather at these boundaries.

Phosphorus is one impurity that causes embrittlement at grain boundaries in steels. A phosphorus atom pairs with an interstitial iron atom moving via a gap between lattice nodes and can move by exchanging its partner to another atom (Fig.9-3(a)). On the other hand, the lattice node previously occupied by an expelled iron atom becomes a vacancy, and this vacancy moves when it is filled by an adjacent iron atom. When a vacancy moves to the node next to a phosphorus atom, this atom can move by jumping to the node of the vacancy (Fig.9-3(b)). These movements become more active as temperature rises. The moving mode of phosphorus atoms shown in Fig.9-3 can be found by consideration based on the energies of various configurations of atoms obtained from the first-principles calculation. However, one cannot know the diffusion speed from only the movement mode. Therefore, in this study, the movement of atoms was simulated by the kinetic Monte Carlo technique based on Fig.9-3, the time and distance of the movement of phosphorus atoms was measured, and the diffusion coefficient at various temperatures was calculated to evaluate the diffusion speed (Fig.9-4). Thus, it was confirmed that the movement by interstitial atoms is several orders of magnitude faster than that by vacancies. This result is useful for predicting the amount of phosphorus at grain boundaries under various conditions of temperature and irradiation as well as for evaluating the embrittlement of steels.

This method, which aims at evaluating macroscopic embrittlement based on atomic-level behavior that is difficult to measure experimentally, is called the multiscale modeling and is an effective computer-research method. In the future, we hope to contribute to the evaluation and prediction of nuclear-structural-material embrittlement by further improving this method.

The present study was partly supported by the Japan Society for the Promotion of Science (JSPS) KAKENHI Grant-in-Aid for Scientific Research (C) (No.15K06429).

Reference

Ebihara, K. et al., Modeling of Phosphorus Transport by Interstitial Dumbbell in α–Iron Using First–Principles–Based Kinetic Monte Carlo, Materials Transactions, vol.58, no.1, 2017, p.26–32.

9–3 Proposing a New Standard for Radiation Damage to Nuclear Materials

– Establishing a Radiation-Damage-Evaluation Formula Based on Numerical Simulations –

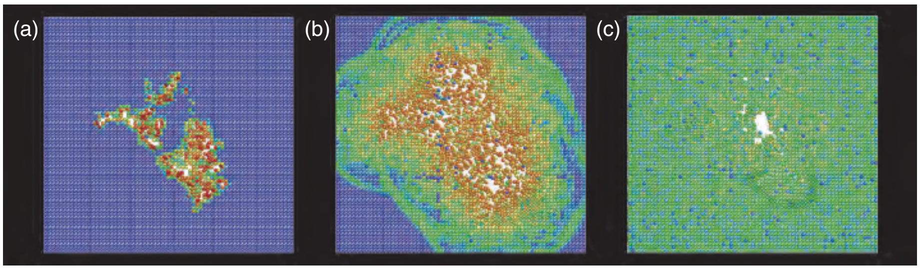

Fig.9-5 Displacement-damage MD simulation in materials
Atoms in solids are displaced by high-energy particles. First, defects are generated roughly by the conventional evaluation formula prediction (a). Subsequently, the influence spreads and the number of defects surpasses the conventional prediction (b), and after the cooling process, the number of surviving defects becomes lower than that conventionally predicted (c). (CREDIT: Andrea Sand)

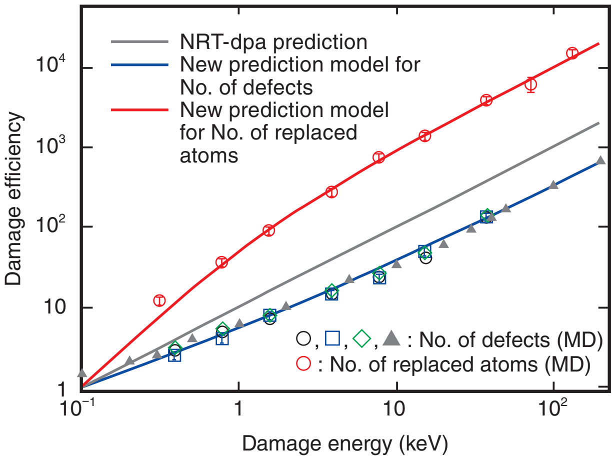

Fig.9-6 Comparison between our new radiation-damage-evaluation formula and MD results
The average number of displaced atoms per high-energy particle is called the damage efficiency. This value increases along with the particle energy (damage energy). The conventional NRT model is neither a good formula for evaluating the number of atoms whose position is replaced nor for evaluating the number surviving as defects. On the other hand, the new prediction model seems to accurately reproduce the number of defects simulated by the high-precision MD simulations.

When a solid's atoms are irradiated by high-energy particles such as electrons, neutrons, and protons, a large amount of energy is given to the primary knock-on atom, which is displaced from its original position in the solid; in some cases, chain reactions of atomic displacements take place, leaving many lattice defects (Fig.9-5). We call this phenomenon displacement damage. As this phenomenon disrupts crystal structure, the original properties of solids undergo changes. Nuclear materials exposed to severe radiation thus change their properties such as dimension and strength during the operation, causing deterioration of safety and efficiency. However, accurate prediction of such changes allows us to cope with such deterioration proactively. Thus, we need to predict how many particles will be displaced by specific irradiation. To date, this has been done using a damage-evaluation formula proposed by three scientists–Norget, Robinson, and Torrens–in the 1960s, called the NRT model. This formula simply evaluates the number of atoms displaced by a particle in proportion to that particle's energy. Although it is easy to use, many scientists and engineers have issues with it, as it reproduces the results of neither radiation experiments nor high-precision molecular-dynamics (MD) simulations.

In 2011, the Working Party on Multiscale Modelling of Fuels and Structural Materials for Nuclear Systems was launched as part of OECD/NEA activities, and three JAEA computational materials scientists participated. At the experts' meeting on primary radiation damage, they concluded that a new irradiation-damage-evaluation formula would be appropriate, and an international project for this purpose was launched: first, they determined the form of the equation by physical investigation; secondly, they determined the coefficients of the equation by fitting it to the result of the high-precision MD displacement-damage simulation. This method not only enables the formula to reproduce the MD results but also allows each term to retain some physical meaning. In addition, this method enables an evaluation formula to be established even for materials for which there are no experimental data.

As can be seen in the right pane in Fig.9-5, a majority of atoms once displaced will return to lattice positions. This 'retuning' effect was considered in the new evaluation formula. As shown by the blue line in Fig.9-6, the new formula reproduces the number of surviving defects.

Although the primary damage process is completed within 1 ns, the defects continue moving slowly at a finite temperature; this causes the defects to further disappear and to be clustered over a long period of time. Without knowledge of such kinetics, it is not possible to properly model the experimentally observed displacement damage. A study of this long-term behavior by JAEA experts was referenced in the OECD/NEA final report.

Reference

Nordlund, K., Suzudo, T. et al., Improving Atomic Displacement and Replacement Calculations with Physically Realistic Damage Models, Nature Communications, vol.9, 2018, p.1084-1–1084-8.

9–4 Development of Visualization Technology for Large-Scale Simulation at Runtime

— *In-Situ* Visualization Using Particle-Based Volume Rendering —

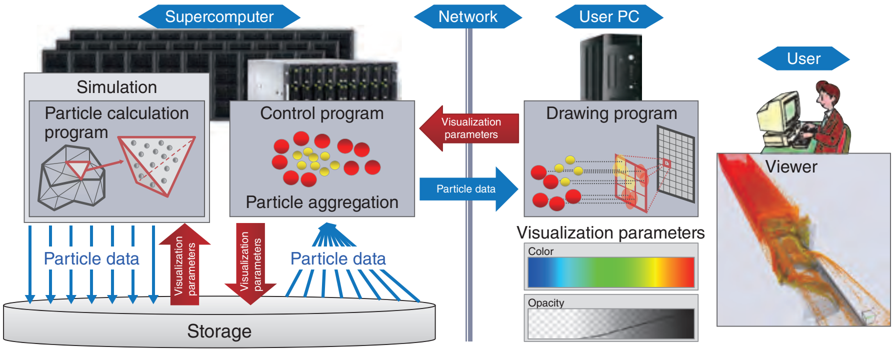

Fig.9-7 Constitution of In-Situ PBVR framework
The particle-calculation program coupled with the simulation on the supercomputer generates particle data for visualization and outputs it on the storage. The control program aggregates particle data and transfers it to a user's PC via the internet. The drawing program on the user's PC displays the visualization of the particle data on the viewer screen. The user observes the visualized image and adjusts visualization parameters such as color and opacity. The adjusted visualization parameters are output to the storage via the control program. The particle-calculation program reads visualization parameters from the storage and uses it for particle generation.

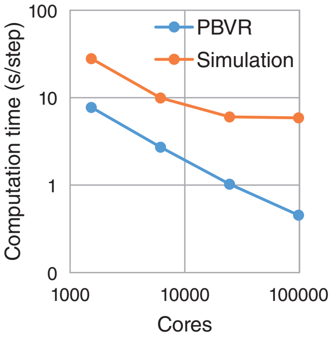

Fig.9-8 Performance on Oakforest-PACS
The problem size was fixed at 240 × 240 × 1920 (about 100 million lattices) and about 10 million particles (about 250 Mbyte) were used for visualization. The horizontal axis is the number of computing units (number of cores) and the vertical axis is the computation time for a single step.

A supercomputer is formed when a large number of computing units are combined. It can execute a large-scale simulation by communicating calculation data among the computational units and generates data as a calculation result. Conventionally, the data are output to storage, and visualization analysis of the data is performed after simulation. However, the storage speed required for such an input/output process cannot keep up with the drastic improvement of supercomputer performance in recent years, and it has become difficult to apply conventional visualization methods to huge datasets (~ petabyte order). To avoid the data input/output problem, *in-situ* visualization, which executes visualization processing simultaneously with simulation and outputs a compressed visualization image (~ megabyte), is becoming increasingly prominent.

However, conventional *in-situ* visualization suffers from two drawbacks. First, every time the viewpoint is changed, communication between a large number of computing units occurs in order to render the anteroposterior relation of the polygons in the correct order. This communication time often exceeds the calculation time of the simulation and hinders it. Secondly, in conventional *in-situ* visualization, it is necessary to set the visualization parameters, namely viewpoint position, color, opacity, etc., beforehand, meaning that numerous simulations are needed to adjust these parameters.

To solve these problems, we have developed a new *in-situ* visualization framework "In-Situ PBVR" using particle-based volume rendering (PBVR) (Fig.9-7). PBVR converts simulation result data to particle data for visualization and drawing. Unlike polygon data, the order of PBVR's particle data does not need to be rearranged; i.e., communication between computing units is unnecessary and the data size is extremely small. Utilizing this fact, we performed particle calculation without disturbing the simulation, with a viewpoint position that can be changed interactively by drawing particle data independent of the viewpoint on the user's PC. Additionally, we created a mechanism that reflects visualization parameters that have been interactively adjusted by the user's PC in the particle calculation via the supercomputer's storage, and realized *in-situ* visualization that can adjust the visualization parameters interactively during the simulation's runtime.

We combined the In-Situ PBVR with the heat-flow simulation inside the reactor pressure vessel and investigated the processing performance using the state-of-the-art supercomputer Oakforest-PACS. As shown in the performance evaluation in Fig.9-8, the particle-generation speed continued to accelerate even when the computing unit was increased from about 1500 to about 100000, and was suppressed within 8 %–28 % of the simulation speed. Particle data were transferred from Oakforest-PACS via the Internet, realizing interactive visualization.

This method won the 28th term Visualization Information Society Thesis Award.

References

Kawamura, T. et al., Performance Evaluation of Runtime Data Exploration Framework Based on In–Situ Particle Based Volume Rendering, Supercomputing Frontiers and Innovations, vol.4, no.3, 2017, p.43–54.

Kawamura, T. et al., Algebraic Design of Multi–Dimensional Transfer Function Using Transfer Function Synthesizer, Journal of Visualization, vol.20, issue 1, 2017, p.151–162.

10 Development of Science & Technology for Nuclear Nonproliferation

Development of Technology and Human-Capacity Building in the Nuclear-Nonproliferation and Nuclear-Security Fields to Support the Peaceful Use of Nuclear Energy

The Integrated Support Center for Nuclear Nonproliferation and Nuclear Security (ISCN) has been conducting the following activities on technology and human-resources development related to nuclear nonproliferation and security, cooperating with affiliated domestic and overseas institutions toward a world without treats of nuclear weapons and nuclear terrorism (Fig.10-1).

Technology Development for Japanese and International Applications

We have been developing technologies to strengthen nuclear nonproliferation and security in accordance with domestic and international trends. We are addressing the development of new technologies that enable the nuclear material measurement although it is difficult to measure nuclear material by conventional means. Examples of our projects include non-destructive assay technology (NDA) to quantify the nuclear materials in fuel debris at the TEPCO's Fukushima Daiichi NPS, nuclear material detection and measurement technologies, for uses such as detecting nuclear materials in heavily shielded containers using nuclear-resonance fluorescence analysis and NDA to measure nuclear material with fission products through irradiation with an external pulsed neutron source. Recently, we have begun developing evaluation metrics for the attractiveness of nuclear or radioactive material for nuclear security in collaboration with the US. Furthermore, we have been improving the accuracy and expediting the analysis of nuclear forensics technologies which can identify the origin and processing history of nuclear materials used in criminal acts. We have also commenced development of nuclear forensics technology for use following a nuclear-terrorism event. Topic 10-1 outlines a study on a new uranium-age-dating technique, which is one of the most important elements of nuclear forensics to be developed by JAEA/ISCN.

Support Government Policymaking Based on Our Technological Expertise

We conducted policy research on the synergistic effects of nuclear-nonproliferation safeguards and nuclear security (collectively called the 2Ss) measures in nuclear-fuel-cycle facilities. To enhance and promote both 2Ss, we first clarified not only specific measurement and surveillance technologies, equipment, tools, and information but also declared possible fuel-cycle facilities and their processes to enable the maximization of 2S's synergistic effects. Then, challenges and possible solutions for the feasibility and applicability of future nuclear-fuel-cycle facilities were analyzed and evaluated.

Support for Human-Capacity Development

Following Japan's national statement at the April 2010 Nuclear Security Summit, ISCN has conducted capacity-building support activities targeting Asian countries since 2011. As of March 2018, about 3800 individuals from Asian countries including Japan have participated in seminars and training related to nuclear nonproliferation, safeguards, and nuclear security, as organized by ISCN. ISCN's capacity-building-support activities have contributed to human-resource development in Asia in particular and have drawn high praise from the US and Japanese governments.

Contributions to the International Verification Regime for CTBT

To establish a global verification regime for nuclear testing, we have been provisionally operating the facilities of the international monitoring system of the Comprehensive Nuclear-Test-Ban Treaty (CTBT) and a national data center. After the 6th nuclear test conducted by North Korea in September 2017, JAEA reported the results of analysis and evaluation of data observed at the CTBT radionuclide-monitoring stations to the national government in a timely manner, thereby contributing to evaluation by the national government based on the CTBT national-operation system of Japan.

Support for JAEA's Nuclear-Fuel Transportation and Procurement of Research Reactor Fuels

We support the nuclear transportation being performed by our research and development centers. We have coordinated the procurement of fresh fuels and the disposal of spent fuels for our research reactors. Through these activities, we contribute to the Global Threat Reduction Initiative (GTRI), which has been strengthening global nuclear security by promoting the systematic return of highly enriched uranium to the US.

Efforts to Promote Understanding

ISCN contributes to promote understanding of this field for domestic and overseas by investigating and analyzing international trends related to nuclear nonproliferation and nuclear security and by delivering the ISCN News Letter, holding an International Forum on Peaceful Use of Nuclear Energy, among other activities.

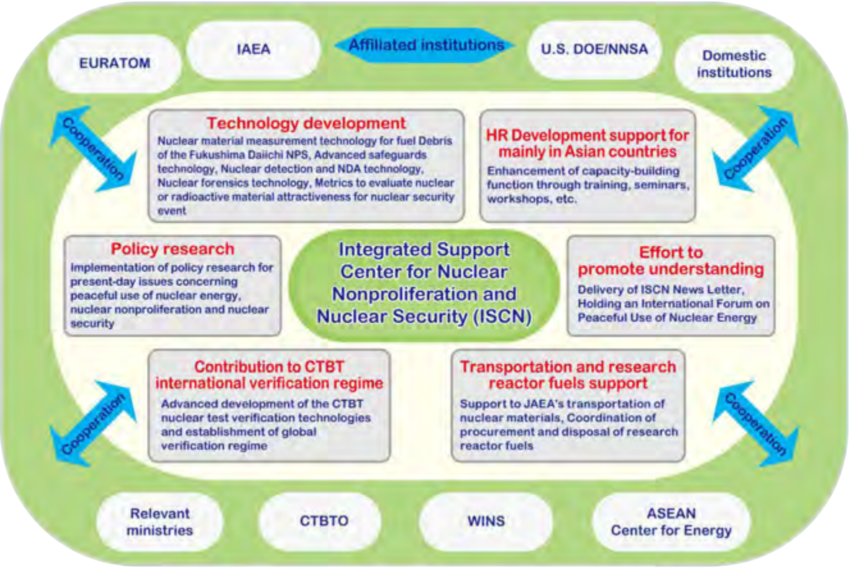

Fig.10-1 ISCN activities and affiliated institutions
We have been playing an active role in strengthening nuclear nonproliferation and nuclear security in cooperation with affiliated domestic and overseas institutions.

10–1 Development of a New Method for Age Determination

— Reduction of Analytical Time Using the Secular Equilibrium State in a Sample —

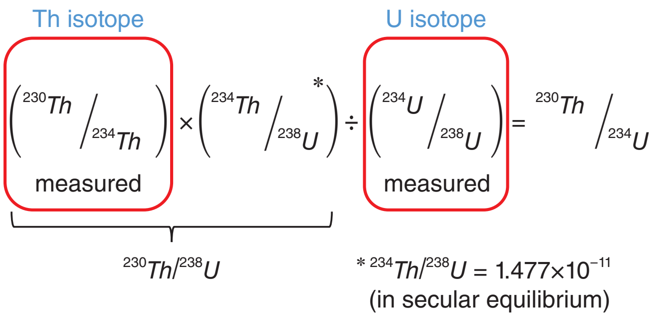

Fig.10-2 Equation for age determination without isotopic certified reference materials (spike solution)
The isotopic ratio of ^{234}Th/^{238}U in secular equilibrium can be calculated from the half lives of these isotopes. Using the measured isotopic ratios of ^{230}Th/^{234}Th and ^{234}U/^{238}U and this equation, the ^{230}Th/^{234}U isotopic ratio for age determination can be calculated.

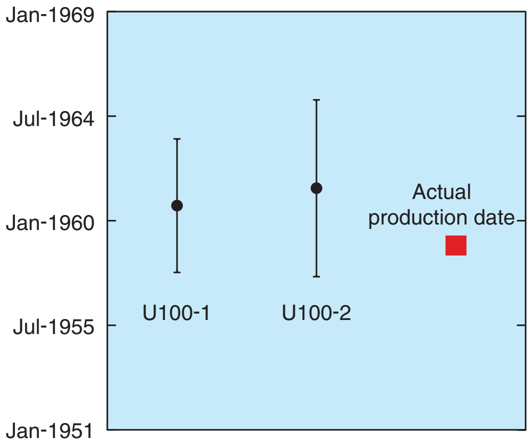

Fig.10-3 Age determination results for the uranium certified reference material (U100)
Applying the proposed method for age determination to the uranium certified reference material (U100), model-production dates that agree with the actual production date are obtained.

Each state is considered to have a responsibility to reinforce nuclear security to combat terrorism using nuclear and radioactive materials. Nuclear forensics is a technical measure for analyzing and assaying the origin, history, route of transportation, and objective of nuclear and radioactive materials. Each state is developing techniques and a framework for nuclear forensics as an important component of nuclear security. In particular, age determination is used to demonstrate the production date of nuclear material and is therefore believed to be essential information in nuclear forensics.

The principle of uranium (U) age determination can be described as follows. In U production processes, other elements are eliminated and the produced material does not contain its daughter nuclide of thorium (Th). As time progresses, Th is produced again at a constant rate in purified U materials. Consequently, the production date can be estimated to measure the ratio of U and Th in materials. To measure the amount of U and Th in the sample, the isotope-dilution mass-spectrometry (ID-MS) method is widely used; this method requires the addition of certified reference materials (spike solution). Accurate measurement of U and Th isotopes using the ID-MS method requires precise weighing of a sample and spike solution, as well as strictly controlled preparation of the spike solution at its concentration. In this study, to establish a concise method for U age determination, a new method is developed using the ^{230}Th/^{234}Th and ^{234}U/^{238}U ratios in the sample and the calculated ^{234}Th/^{238}U ratio in secular equilibrium (Fig.10-2). According to this new method, U and Th in the U sample solution are separated by two steps of anion exchange. The isotope ratios of U and Th are then determined by a thermal-ionization mass spectrometry. The ID-MS method requires three days for performing the analytical procedure; the new method reduced this time to six hours, thereby completing the process rapidly. Applying the new method for age determination to the uranium certified reference material (U100), we obtained model-production dates that agree with the actual production date (Fig.10-3). Joint research between JAEA and the European Commission, Joint Research Center is underway for the comparison between the ID-MS method and our new method, which is applied for radioactive measurements.

Reference

Okubo, A. et al., Uranium Age-Dating Using In-Situ Isotope Ratios by Thermal Ionization Mass Spectrometry for Nuclear Forensics, Journal of Radioanalytical and Nuclear Chemistry, vol.314, issue 1, 2017, p.231–234.

About the Design of the Cover

The cover is designed with white hexagons similar to the pattern in a tortoise shell, an ancient Japanese symbol of people's wish for longer lives. Coincidentally, this shape is the same as that of core fuel assemblies for both the prototype fast breeder reactor "MONJU" and the high temperature engineering test reactor "HTTR".

The images on the cover show detailed molten materials accumulation behavior inside the pedestal by mechanistic numerical simulation code, JUPITER (top left) and visualization result of radioactive substances inside the turbine building of the TEPCO's Fukushima Daiichi NPS (1F) Unit 3 (bottom right).

The top left image shows the detailed molten materials accumulation behavior inside the pedestal. Melt relocation and accumulation behavior of the main component of core internals such as UO_2, SUS and Zry are inflowed and are calculated mechanistically by JUPITER (Chapter 1, Topic 1-1, p.11).

The bottom right image shows the color image of the radioactive substances obtained using the compact Compton camera in the 1F building, which is the high-dose rate environment. We detected the local contamination near the hose crawled on the floor surface (Chapter 1, Topic 1-7, p.17).

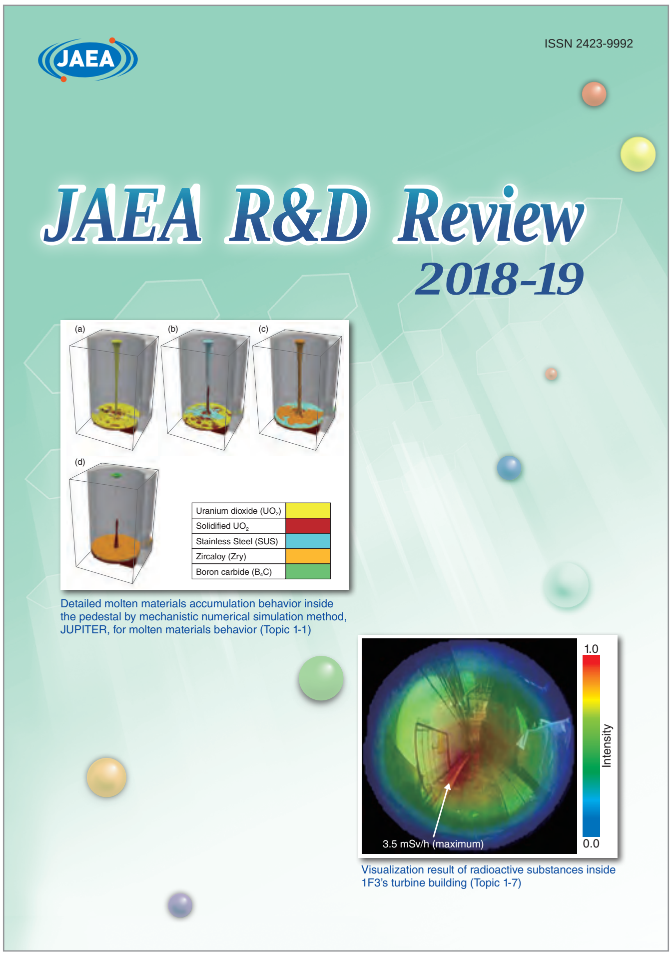

ISSN 2423-9992

JAEA R&D Review

2018-19

Uranium dioxide (UO_2)	🟨
Solidified UO_2	🟥
Stainless Steel (SUS)	🟦
Zircaloy (Zry)	🟧
Boron carbide (B_4C)	🟩

Detailed molten materials accumulation behavior inside the pedestal by mechanistic numerical simulation method, JUPITER, for molten materials behavior (Topic 1-1)

Visualization result of radioactive substances inside 1F3's turbine building (Topic 1-7)

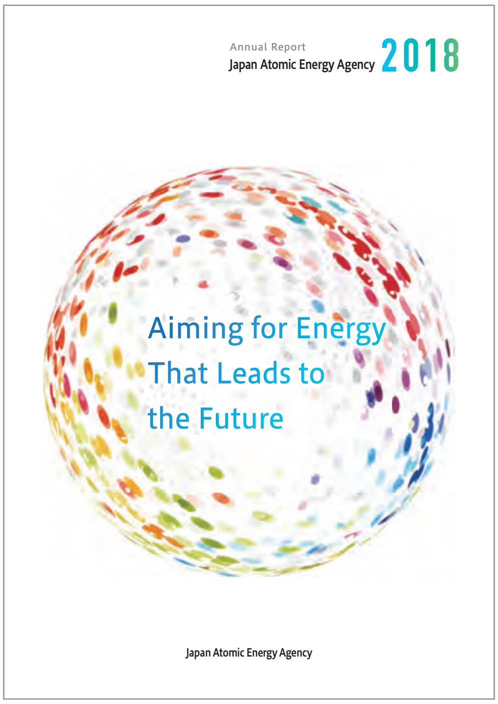

About the activity status of the whole agency
including CSR, see the annual report
Japan Atomic Energy Agency 2018

JAEA R&D Review 2018-19

Published by
Japan Atomic Energy Agency in January 2019

This publication is issued by Japan Atomic Energy Agency (JAEA) on a yearly basis.
Inquiries about availability and/or copyright of the contents in this publication should be addressed to Institutional Repository Section, Intellectual Resources Management and R&D Collaboration Department, Japan Atomic Energy Agency (JAEA).

Address: 2-4 Shirakata, Tokai-mura, Naka-gun, Ibaraki-ken 319-1195, Japan
Phone: +81-29-282-6387, **Facsimile:** +81-29-282-5920, **e-mail:** ird-seika_shi@jaea.go.jp